

COMBINED DIGITAL BREAST TOMOSYNTHESIS AND NEAR-INFRARED  
SPECTRAL TOMOGRAPHY FOR BREAST LESION CHARACTERIZATION

A Thesis

Submitted to the Faculty

in partial fulfillment of the requirements for the

degree of

Doctor of Philosophy

by

KELLY E. MICHAELSEN

Thayer School of Engineering

Dartmouth College

Hanover, New Hampshire

April 2014

Examining Committee:

Chairman \_\_\_\_\_  
Keith D. Paulsen

Member \_\_\_\_\_  
Brian W. Pogue

Member \_\_\_\_\_  
Venkataramanan Krishnaswamy

Member \_\_\_\_\_  
Steven P. Poplack

Member \_\_\_\_\_  
Andrew Karellas

\_\_\_\_\_  
F. Jon Kull  
Dean of Graduate Studies



## **Abstract**

Annual screening mammograms are recommended for all women above 40 years of age for early detection of breast cancer, and are known to improve cancer mortality rates. However, mammography is hampered by low sensitivity and a high rate of false positive results that can lead to invasive and possibly unnecessary biopsies. Digital breast tomosynthesis (DBT) is a recently approved screening method that takes multiple X-ray images at different positions relative to the breast, rendering excellent three-dimensional anatomic detail of the breast. Near-infrared spectral tomography (NIRST) was added into a DBT system, to provide co-localized information about the metabolic status of the tissue, specifically quantification of blood content, oxygen saturation, water and lipid levels. When used alone, NIRST is hampered by low spatial resolution. The hypothesis in this work was that noninvasive differentiation between malignant and benign lesions can be more accurately obtained by combining spatial information from DBT and functional information from NIRST in a single exam.

To this end, the NIRST hardware has been integrated into an existing DBT unit, allowing completely co-registered X-ray and optical data. Early simulation work demonstrated the potential of this synergistic combination, optimized for short scanning time, low cost and complexity. The system was built and tested to obtain both clinical quality DBT scans and high fidelity NIRST data. Breast-mimicking phantoms assessed size, contrast and depth resolution as well as chromophore recovery. A total of 32 normal subjects were examined and the recovered tissue metabolic markers were analyzed with respect to patient demographics. Finally, 13 women with abnormal mammographic findings were

imaged prior to biopsy and the results demonstrate correlation between hemoglobin content and histo-pathological diagnosis. The addition of NIRST imaging to DBT could aid in clinical decision making and decrease the number of biopsies which are performed with negative results, improving patient experience.

## **Acknowledgements**

I would like to thank all of the people who have made my time at Thayer such a worthwhile learning experience. Without the individuals acknowledged here, this work would not have been possible and I cannot thank them enough.

Despite attending Dartmouth as an undergraduate, I rarely ventured over to the engineering school but I did have the opportunity to meet Prof. Keith Paulsen once during that time and was excited about the work that he was doing at Thayer. Keith has been a dedicated mentor, taking time out of his busy schedule to meet me to talk about any and all sorts of issues. His assistance during the F30 grant application process was particularly noteworthy, going above and beyond in reading documents and advising me through the process. Working with Keith has had a tremendous effect on my education and I truly appreciate all his patience, knowledge, understanding and guidance.

I first heard about Prof. Brian Pogue while interviewing at M.D./Ph. D. programs at other institutions. Mentioning my interest in medical imaging and prior attendance, they inquired if I had met him, and I decided to seek him out. Working with him has been very helpful; his strong focus on student learning has led to improvements in my oral and written communication skills and understanding of the subject matter on which this thesis is based. His willingness to help and excitement about research have been a very positive influence on my work.

Prof. Venkataramanan Krishnaswamy was absolutely essential to this Ph. D, as there would be no imaging system without him. His close mentorship early on in my studies was incredibly helpful. His instruction on the basics of instrumentation and

willingness to discuss the project anytime has led to many fruitful conversations and new research directions.

I want to thank Prof. Steven Poplack for being a part of my committee as well. His enthusiasm has been essential in recruiting women to participate in our study. His dedication, attention to detail and patience in teaching has made him a great asset to our team and a wonderful mentor.

I express gratitude to Prof. Andrew Karellas for serving on my committee and collaborating on this project. Along with his colleagues Srinivasan Vedantham and Linxi Shi, they developed the segmentation methods essential for the work described here.

I appreciate the help of everyone in the Optics in Medicine lab for their willingness to help, collaborate and have fun doing it. Shudong Jiang and Michael Mastanduno have worked especially closely with me to do patient exams and solve problems respectively. Adele Shenoy and Emily Jordan, two undergraduates who have worked in the lab for the past three years, have been hugely helpful in phantom and patient studies. I also want to thank all the members of the research team at DHMC for their flexibility and dedication to the biopsy cohort recruitment.

Finally, I'd like to thank all my amazing friends and family for providing encouragement, support, understanding during the more challenging times and fun and entertainment when breaks were needed. Over the course of my Ph. D., I feel I have learned and grown a lot and have all of these people to thank for it.

This work was funded by NIH R01CA139449 and NIH F30CA168079.

## Table of Contents

Acknowledgements .....	iv
List of Tables .....	xv
List of Figures .....	xvii
List of Abbreviations .....	xxxvii
Chapter 1: Introduction .....	1
1.1. Project Overview .....	1
1.2. Current State of Clinical Breast Imaging .....	2
1.3. Role of DBT in Breast Cancer Management and Detection .....	4
1.4. NIRST Imaging of the Breast .....	5
1.5. Combining NIRST and DBT .....	6
1.6. Overview of this Thesis .....	8
Chapter 2: Imaging the Breast with Diffuse Light.....	10
2.1. Introduction.....	10
2.2. Spectroscopic Imaging .....	11
2.3. Imaging Types .....	13
2.4. System Design .....	16
2.4.1. Simulations of Proposed System and Optical Scattering Study .....	16
2.4.1.1. Methodology .....	17
2.4.1.2. Sample Patient Simulations .....	20
2.4.1.3. System Simulations.....	22
2.4.2. Development of a combined NIRST-DBT imaging system .....	23

2.4.3.	Light Delivery .....	25
2.4.4.	Light Collection .....	27
2.5.	Integration of NIRST and DBT .....	27
2.5.1.	Materials Characterization for NIRST-DBT Interface .....	27
2.5.2.	Stray Light .....	35
2.6.	System Calibration .....	37
2.6.1.	Source Calibration .....	37
2.6.2.	Detector Calibration .....	38
2.6.3.	Attenuator Calibration .....	40
2.6.4.	Source/Detector Localization .....	41
2.7.	Conclusions .....	43
Chapter 3:	Image Formation Methods .....	45
3.1.	Image Formation .....	45
3.1.1.	Optical Properties .....	46
3.1.2.	Diffusion Modeling and Other Methods .....	48
3.1.3.	Finite Element Modeling .....	51
3.2.	Image Reconstruction .....	53
3.2.1.	Forward Problem .....	53
3.2.2.	Inverse Problem .....	53
3.2.3.	Spectral Reconstructions .....	57
3.2.4.	Inclusion of Anatomic Spatial Priors .....	60
3.3.	Image Segmentation Methods .....	64

3.3.1.	DBT Image Formation .....	64
3.3.2.	DBT Image Post Processing .....	70
3.3.3.	Adipose and Fibroglandular Segmentation.....	73
3.3.4.	Lesion Segmentation.....	78
3.3.5.	DBT Segmentation Assessment.....	83
3.4.	Mesh Creation .....	86
3.4.1.	DBT Segmented Image Post Processing.....	87
3.4.2.	Meshing.....	89
3.5.	Conclusion .....	91
Chapter 4:	Phantom Experiments .....	93
4.1.	Introduction.....	93
4.1.1.	Calibration Phantoms.....	94
4.1.2.	Anthropomorphic Phantoms .....	95
4.2.	Phantom Calibration .....	96
4.2.1.	Characterization of Reference Phantom .....	96
4.2.2.	Prior Calibration Methods.....	97
4.2.3.	Direct Data Calibration Techniques.....	99
4.2.4.	Single Wavelength Reconstructions .....	101
4.3.	Spectral Slice Phantom .....	102
4.3.1.	Phantom Design.....	102
4.3.2.	Procedure .....	103
4.3.3.	Depth-Dependent Contrast Recovery .....	107

4.3.4.	Inclusion Volume Mischaracterization .....	108
4.3.5.	Discussion .....	112
4.4.	Hemoglobin Phantoms .....	114
4.4.1.	Phantom Design .....	114
4.4.2.	Results .....	115
4.5.	Water and Lipid Anthropomorphic Phantoms .....	117
4.5.1.	Composition .....	119
4.5.2.	Procedure .....	119
4.5.2.1.	Fully Anthropomorphic Phantoms .....	121
4.5.2.2.	The Imaging System .....	122
4.5.2.3.	Data Reconstruction .....	123
4.5.3.	Results .....	124
4.5.3.1.	Creation of Optimal Phantoms .....	124
4.5.3.2.	Contrast Sensitivity .....	126
4.5.3.3.	Reproducibility .....	127
4.5.3.4.	Durability .....	128
4.5.3.5.	Anthropomorphic Test Case .....	129
4.5.4.	Discussion .....	131
4.6.	Conclusions .....	135
Chapter 5:	Methods for Combined NIRST-DBT .....	138
5.1.	Introduction .....	138
5.2.	Exam Workflow .....	139

5.2.1.	NIRST-DBT.....	140
5.2.2.	DOSI .....	142
5.3.	LABVIEW Interface.....	145
5.3.1.	Setting Source Strength.....	146
5.3.2.	Real Time Exam Monitoring .....	146
5.3.3.	Output .....	147
5.4.	MATLAB Analysis Tools .....	147
5.4.1.	Phantom GUI .....	148
5.4.2.	Source/Detector Pair Identification.....	149
5.5.	Data Dropping and Adjustments.....	150
5.5.1.	Detector Output Thresholding .....	151
5.5.2.	Tissue Geometry Data Dropping .....	152
5.5.3.	Slope-Based Data Removal .....	154
5.6.	Data Analysis Tools .....	156
5.7.	Image Formation.....	158
5.8.	Conclusions.....	158
Chapter 6:	Healthy Volunteers.....	162
6.1.	Introduction.....	162
6.2.	Normal Subject Imaging Summary .....	163
6.2.1.	System Improvements.....	164
6.2.2.	Reconstruction Algorithm Adjustments .....	166
6.2.3.	Patient Considerations .....	168

6.3. NIRST Results .....	168
6.4. Patient Characteristics and NIRST Results.....	170
6.4.1. Breast Density .....	172
6.4.2. Bra Cup Size .....	173
6.4.3. Thickness .....	175
6.4.4. Body Mass Index .....	177
6.4.5. Fibroglandular Percent.....	178
6.5. Assessing NIRST Data .....	179
6.5.1. Comparing Adipose and Fibroglandular Regions.....	180
6.5.1.1. Results.....	181
6.5.1.2. Discussion .....	181
6.5.2. Comparing CC and MLO Views .....	182
6.5.2.1. Results.....	182
6.5.2.2. Discussion .....	184
6.5.3. Comparing Compressed and Uncompressed NIRST.....	185
6.5.3.1. Results.....	186
6.5.3.2. Discussion .....	188
6.6. Comparison of NIRST and DOSI Results .....	189
6.6.1. Results.....	190
6.6.2. Discussion .....	191
6.7. Conclusions.....	191
Chapter 7: NIRST-DBT Lesion Characterization Methods.....	195

7.1. Introduction.....	195
7.2. Biopsy Patient Logistics .....	196
7.2.1. Patient Recruitment.....	197
7.2.2. DBT Image Analysis.....	199
7.2.3. Pathological Results.....	200
7.2.4. Patient Characteristics.....	202
7.3. Increasing Sensitivity of Small Lesions.....	204
7.4. Lesion Characterization Using NIRST-DBT.....	210
7.4.1. Experimental Design.....	211
7.4.2. Case Examples .....	211
7.4.3. Patient Summary .....	214
7.5. Discussion.....	216
7.6. Conclusions.....	217
Chapter 8: The Role of Scattering in NIRST of the Breast .....	219
8.1. The Importance of Scattering Information .....	219
8.2. Simulation Results .....	220
8.3. Normal Subject DOSI Imaging.....	223
8.3.1. Patient Characteristics.....	223
8.3.2. Using Group Estimates .....	224
8.4. Normal Subject X-Ray Imaging .....	227
8.4.1. Phantom Calibration .....	228
8.4.2. Slope-Based Calibration .....	232

8.5. Conclusions.....	236
Chapter 9: Conclusions and Future Directions .....	239
9.1. Completed Work.....	239
9.1.1. System Design and Instrumentation .....	239
9.1.2. Image Formation Methods.....	240
9.1.3. Phantom Imaging .....	242
9.1.4. Methods for Combined NIRST-DBT Imaging .....	243
9.1.5. Imaging Healthy Volunteers .....	244
9.1.6. NIRST-DBT Lesion Characterization Methods .....	245
9.1.7. The Role of Scattering in NIRST of the Breast .....	246
9.2. Future Directions .....	248
9.2.1. Hardware Developments.....	248
9.2.1.1. New Detector Panel .....	248
9.2.1.2. Clinical Unit Attachment .....	250
9.2.1.3. Source Strength Measurement .....	251
9.2.1.4. Elimination of Breast Shroud.....	252
9.2.2. Software Developments.....	253
9.2.2.1. Regularization, Noise and Lesion Size .....	254
9.2.2.2. Estimation of Optical Scattering.....	254
9.2.2.3. Inclusion of Chest Wall Data .....	255
9.2.2.4. Source Position and Scan Optimization.....	256
9.2.2.5. Distributed Sources and Detectors.....	256

9.2.3. Phantom Experiments .....	256
9.2.4. Final Remarks .....	257
Appendices.....	259
Appendix A: Original Settings for DBT Images .....	259
Appendix B: Modified Settings for DBT Images .....	260
Appendix C: Patient Imaging Checklist .....	261
Appendix D: Detailed Steps for Patient Imaging .....	263
Citations .....	268

## List of Tables

Table 1: Important quantities, their symbols, units, and relationships in diffusion-based on NIR transport theory <sup>61</sup> .....	11
Table 2: Material qualities of plastics tested for detector case <sup>91,92</sup> .....	31
Table 3: Prototype DBT vs. Mammography–Quantra (MQ) § indicates paired t-test; * indicates statistical significance <sup>143</sup> .....	85
Table 4: Comparison of two views of the same breast, * indicates statistical significance <sup>143</sup> .....	86
Table 5: Correlation between breast density and hemoglobin, oxygen saturation, water and lipids. Bold values indicate statistical significance (p<0.05).....	172
Table 6: Correlation between bra cup size and hemoglobin, oxygen saturation, water and lipids. Bold values indicate statistical significance (p<0.05).....	174
Table 7: Correlation between breast thickness and hemoglobin, oxygen saturation, water and lipids. Bold values indicate statistical significance (p<0.05).....	175
Table 8: Correlation between BMI and hemoglobin, oxygen saturation, water and lipids. Bold values indicate statistical significance (p<0.05) .....	177
Table 9: Correlation between fibroglandular content and hemoglobin, oxygen saturation, water and lipids. Bold values indicate statistical significance (p<0.05).....	179
Table 10: Correlation between DOSI properties and NIRST for hemoglobin, oxygen saturation, water and lipids. Bold values indicate statistical significance (p<0.05) .....	190
Table 11: BIRADS and pathology results from subjects in the biopsy cohort imaged to date.....	201



## List of Figures

- Figure 1: Workflow diagram of breast cancer screening, diagnosis, and treatment. Each circle in the diagram represents one woman. If the results from the screening are suspicious or inconclusive, women go on to diagnostic mammography or ultrasound and may be recommended for a breast biopsy. Each step along the path is more time consuming and expensive, and more likely to incur side effects than the previous step. .... 4
- Figure 2: Region-guided reconstruction of NIRST data involves segmentation of DBT slices creating images from which a volume mesh is generated. The prediction of the forward diffuse transport data is simulated on the finite element mesh and used in iteratively reconstructing a co-registered volume of the optical properties of the breast with the mesh regions as a template..... 7
- Figure 3: Absorption and scattering as a function of wavelength in the visible and NIR regime for major tissue chromophores in breast tissue<sup>62</sup> ..... 12
- Figure 4: Different spectroscopy methods for probing tissue, to obtain absorption and scattering information used in diffuse optical imaging: continuous wave, time domain, and frequency domain<sup>65</sup> ..... 14
- Figure 5: Software procedures used in simulation are shown as a flow chart. Lower left shows source and detector configurations for the FD (left) and CW (right) data for a given patient study on the breast mesh/volume<sup>84</sup> ..... 18
- Figure 6: Illustrative example of a patient simulation with a malignant lesion is shown with (a) scattering amplitude, (b) oxy-hemoglobin ( $\mu\text{m}$ ), (c) water fraction (percent), (d) scattering power, (e) deoxy-hemoglobin ( $\mu\text{m}$ ), and (f) lipid content

(percent). Exact (simulated) distributions are shown on the left while the corresponding recovered images are shown on the right for each quantity<sup>84</sup> ..... 21

Figure 7: Illustrative example of a patient simulation with a benign lesion is shown, with (a) scattering amplitude, (b) oxy-hemoglobin ( $\mu\text{m}$ ), (c) water fraction (percent), (d) scattering power, (e) deoxy-hemoglobin ( $\mu\text{m}$ ), and (f) lipids content (percent). Exact (simulated) distributions are shown on the left while the corresponding recovered images are shown on the right for each quantity<sup>84</sup> ..... 21

Figure 8: (a) Schematic of the NIRST-DBT imaging system. (b) Photograph of the fully assembled NIRST-DBT system installed at the Dartmouth-Hitchcock Medical Center (DHMC). (c) Photograph of the 2- axis galvanometric scanning mirror assembly mounted adjacent to the X-ray emission port on the DBT scanner. The source unit allows arbitrary positioning and scanning of laser light beams onto the compressed breast surface without obstructing the X-ray field-of-view<sup>68</sup> (d) Photograph showing the silicon photodiode detector panel inserted into the custom designed cassette assembly to allow easy insertion and removal of the panel during sequential NIRST-DBT scans..... 24

Figure 9: (a) Close up of the 2-axis galvanometric scanning mirror assembly mounted adjacent to the X-ray emission port on the DBT scanner; red arrows show how the light is reflected off mirrors and onto the tissue, depicted in the bottom schematic. (b) Photograph of the fully-assembled NIRST optical cart installed at the Dartmouth-Hitchcock Medical Center (DHMC). (c) Photograph showing the patient interface for the combined NIRST-DBT system (d) Photograph of NIRST detector panel without the cassette assembly..... 25

Figure 10: (a) Attributes of possible detector case designs for the detector panel. (b) Single X-ray frame from a DBT scan showing attenuation from a thin fiber plate. (c) Depiction of a detector case model with windows over the locations of the detectors. (d) X-ray frame from DBT scan indicating attenuation of a panel with windows<sup>91</sup>. ..... 29

Figure 11: Photograph of the plastic materials tested in this study. Top row (from left to right) is polycarbonate, polypropylene, acrylic, high-density polyethylene, and polycarbonate with a diffusive sticker. Bottom row (from left to right) is acetal, acetal resin, polytetrafluoroethylene and sandblasted polycarbonate<sup>91</sup>. ..... 30

Figure 12: (a) Photograph of the detector case developed for the combined NIRST-DBT system. (b) Detector case with the detector panel inserted. (c) Depiction of light channeling in the detector case. (d) Graph illustrating the effects of light channeling on the acquired NIRST data. (e) Raw 660 nm data acquired from a homogeneous resin phantom when placed directly on top of the detectors (in blue) relative to when imaged with the detector enclosed in the case (red). (f) Agar inclusion phantoms with increasing hemoglobin contrast (background in blue, inclusion in red) when imaged on a thin plastic film above the detectors (dots) and when imaged on the detector case (Xs)<sup>91</sup>. ..... 32

Figure 13: Light blocking materials used in patient exams. (a) Light blocking fabric draped over the DBT unit. (b) Light blocking skirt surrounding the breast compression paddle during phantom experiments. (c) Patient in position for NIRST-DBT exam (d) Raw data acquired from a homogeneous phantom imaged through the detector case with (in red) and without (in blue) the light blocking

precautions. (e) Light blocking breast shroud used during patient exams (f) Patient positioning with the breast shroud. .... 35

Figure 14: Each graph shows a single wavelength of light coupled to an optical phantom and measured at 20 different detectors over two days. Significant variation in detector sensitivity is noted, but source strength measured on two different occasions showed variations ranging from less than 1% (for 660 nm) to nearly 5% (for 905 and 940 nm). .... 38

Figure 15: (a) Schematic showing the calibration puck positioned over an individual detector element in the detector panel. (b) Schematic drawing of the calibration puck showing a square notch on top that allows repeatable positioning over each detector element. (c) Correction factor for each of the 75 detector elements showing variations in individual detector response (certain detector channel numbers are unused). (d) Raw tomographic projection data plotted as a function of source-detector separation acquired from a homogeneous test phantom at 660 nm and 785 nm wavelengths. (e) Processed data showing the removal of known signal artifacts and noisy data<sup>68</sup>. .... 39

Figure 16: Graph of attenuator calibration showing the log of the laser's output power vs. attenuator setting in the LABVIEW control software for all the wavelengths of the system. .... 40

Figure 17: (a) DBT processed image slice from the source plane with several metal BB's located at the four corner source positions and central position, all shown in a darker color, with green circles highlighting the source and corresponding BB location. The red pixels indicate the locations of the point sources applied to the

mesh for the NIRST reconstructions and the dark points are the BB locations. (b) DBT-processed image slice from the plane of the detector panel. The red pixels indicate the locations of the point detectors applied to the mesh for the NIRST reconstructions. (c) DBT-processed image slice from the plane including the photodiode detectors with red pixels indicating the locations of point detectors and blue pixels indicating the location of point sources. .... 41

Figure 18: Absorption coefficient of different components of tissues at different wavelengths. The NIR window (in yellow) shows lower light absorption by the major tissue chromophores, specifically, water and hemoglobin, than other forms of non-ionizing radiation<sup>95</sup> ..... 45

Figure 19: Fluence maps for three different source locations on a compressed breast. ... 49

Figure 20: A volumetric breast mesh created from a stack of DBT images. The left side shows the nodes, connected to form tetrahedral elements. The right side shows a slice through the mesh, providing easy visualization of the preservation of spatial information about fibroglandular and tumor tissue structures..... 51

Figure 21: Reconstructions for a sample patient using the conjugate gradient method shows accurate recovery of tissue chromophores when compared to the simulated actual data. .... 60

Figure 22: DBT image (left) with segmented slice and the resulting FEM mesh (center) and the overlay of the sources and detector locations (right) on this template..... 61

Figure 23: No prior (left) vs. hard prior (right) reconstruction of a patient with both a benign lesion and an invasive ductal carcinoma. The higher hemoglobin content of the carcinoma is clearly visualized in the case on the right, but not visualized in

the no prior reconstruction on the left. Additionally, significant high and low values are seen in diffuse reconstruction across the length of the breast that are known to be artifact. ....	62
Figure 24: a. Parallel path geometry, b. Partial isocentric motion, c. Full isocentric motion <sup>126</sup> . ....	66
Figure 25: The shift and add technique for image reconstruction of five exposures. The images are added together with different shifts in order to focus on object A or B <sup>132</sup> . ....	68
Figure 26: DBT Image slice prior to (left) and after (right) detector artifact correction thresholding.....	70
Figure 27: Images of skin segmentation process. ....	71
Figure 28: a. An x-z plane image from the 3D DBT image stack for a clinical case. b. $23 \times 23$ Gaussian kernel used in the bilateral filter before modification. c. Modified Gaussian kernel with an angular constraint of $2\theta$ corresponding to the angular range during projection view acquisition. d. An x-z plane after application of the angular-constrained bilateral filter that shows a reduction in out-of-plane artifacts. Zoomed (1.5 $\times$ ) regions of interest before and after application of the filter are shown <sup>138</sup> . ....	72
Figure 29: (a) DBT slice prior to processing and (b) after angular bilateral filtering step <sup>138</sup> . ....	73
Figure 30: KFCM segmentation steps for CC images .....	75
Figure 31: KFCM segmentation steps for MLO images with geographically separated fibroglandular and chest wall tissues. First round KFCM separates adipose and	

non-adipose, a second KFCM on the non-adipose region separates fibroglandular and muscle. ....	76
Figure 32: KFCM segmentation steps for MLO images with continuous fibroglandular and chest wall tissues. First round KFCM separates adipose and non-adipose, a second KFCM on the non-adipose region separates fibroglandular and muscle but requires additional morphological operations for separation.....	77
Figure 33: Three slices (x-y plane) extracted from the volume of interest (VOI) encapsulating the lesion: a. top slice in contact with the compression paddle; b. slice that best represents the lesion; and c. bottom slice in contact with the breast support. (a–c) are prior to and (d–f) are after VOI normalization <sup>138</sup> .....	79
Figure 34: Flowchart depicting lesions segmentation process. ....	80
Figure 35: Flowchart depicting DBT image processing steps for CC segmentation of adipose, fibroglandular, and tumor regions, as part of the segmented volume and mesh creation process. ....	81
Figure 36: Flowchart depicting DBT image processing steps for MLO segmentation of adipose, fibroglandular, and tumor regions, as part of the segmenting and mesh creation process.....	82
Figure 37: Volumetric breast density comparison between mammography via Quantra analysis, and DBT for raw data (left) and normalized results (right). ....	85
Figure 38: The Nirfast mesh creation GUI allows users to load segmented images and source locations, specify node density, and create a 3D mesh. Single regions can be refined with smaller node spacing <sup>144</sup> .....	87

- Figure 39: The left image is the DBT segmentation at full resolution 1500 x 1948. The second image was reduced to 20% of the image on the left. The final image shows an interpolated slice at the same level as the prior two images, extracted from a mesh of 40,000 nodes. The overall tissue structures are recognizable but most of the finer details have been lost..... 88
- Figure 40: A photograph of the large homogeneous resin phantom (left). Data showing the log of the amplitude of the detector response vs. the source detector distance (right). A line was fit to this graph and corresponded to an absorption coefficient 12% off from the measured value on a time-domain system..... 97
- Figure 41: Amplitude data from a patient shown for all wavelengths. The natural log of source-detector distance times intensity is linearly decreasing with source detector distance with the slope being  $\mu_a$  at that wavelength. .... 98
- Figure 42: The main parts of the absolute calibration algorithm are illustrated schematically..... 99
- Figure 43: Absorption and reduced scattering coefficient vs. wavelength as derived for all wavelengths from the time domain system measurements (shown in blue) as well as from measurements on the broadband system (shown in red). .... 100
- Figure 44: Photograph of the spectral slice phantom and early results from two separate phantom experiments using a single inclusion. The absorption coefficient for a single wavelength (785 nm) for the background (blue) and the inclusion (red) are shown for (15, 30, 45, 60, 75, 90  $\mu\text{M}$ )..... 104
- Figure 45: Graph of all data points collected for a contrast phantom experiment for 785 nm laser source. The x-axis shows all source-detector pairs plotted by distance,

while the y-axis shows the difference between the homogeneous calibration phantom and the anomaly data set. The anomaly data sets were 90 (yellow), 75 (teal), 60 (magenta), 45 (black), 30 (green), 15 (red) $\mu\text{M}$ Hb, each of which was measured twice.....	105
Figure 46: Graph showing the dependence of inclusion size chromophore recovery on regularization. ....	106
Figure 47: Graphs depicting total hemoglobin recovery vs. actual hemoglobin concentration for the background using inclusions of different size at three different depths .....	107
Figure 48: The effects of inclusion volume mischaracterization are shown for the shallowest depth. On the left, overestimation in all inclusions of 50%, true volume in the center, and 50% of the true volume on the right hand side.....	110
Figure 49: The effects of z-depth mischaracterization on phantom results are shown with the actual inclusions measured between 2 and 3 cm from the top of the phantom and modeled as between 3 and 4 cm from the top of the phantom.....	111
Figure 50: A section of the resin material was marked as a separate region for reconstruction. As expected, the recovery of hemoglobin was very similar to that of the background. ....	112
Figure 51: x-y cross-sectional views of the reconstructed HbT images for the (a) 1:1, (b) 2:1, and (c) 3:1 contrast phantoms. (d) Cut-away view of the FEM mesh showing the background and inclusion regions. (e) Plot of recovered HbT contrast in the background (solid triangles) and inclusion region (solid circles) vs. actual HbT concentration in the background and inclusion. Linear fits show that the HbT	

concentration is nearly constant in the background and varies linearly in the inclusion as expected<sup>68</sup> ..... 115

Figure 52: Agar inclusion phantoms were made with dimensions (a) and imaged in the DBT system (b) as well as with the NIRST components. Hemoglobin levels were recovered in two region (lower right) and compared to actual (upper right). (c) Diffuse reconstructions for three different cross sectional views, x-y (left), x-z (upper right) and y-z (lower right). Top plot depicts inclusion location, second is the negative contrast (0.5:1) and on the bottom is positive (4:1) inclusion to background. (d) The recovered total hemoglobin levels for different inclusion to background contrasts. The blue dots show recovery in the background region while the red dots show recovery in the inclusion. .... 117

Figure 53: The phantom creation process for lard, blood, guar gum mixture. .... 120

Figure 54: (a) Several early phantom creations comprised of 70% lipid and 30% water. The fats were butter, olive oil, Crisco© and canola oil (left to right). The first and third phantoms included guar gum as the emulsifier while the second and fourth utilized soy lecithin. (b) The chemical formula for guar gum<sup>180</sup>. (c) Data from the DOSI imaging system for a mostly lipid (left) and mostly water (right) phantom. The top graph shows the scattering data and fits, while the bottom graph shows the absorption results. Specific peaks for lipids and water can be discerned above 900 nm. .... 125

Figure 55: Graphs of measured water (left) and lipid (right) fractions with (round) data points and standard deviations based on ten measurements from the top of the phantoms. The dotted line is a linear fit for the phantoms with the higher water

content before mixing, exhibiting good linearity. The X-shaped data points and corresponding dashed linear fit for the high lipid content phantoms were obtained after their materials were manually mixed. The solid line depicts the actual water or lipid content. .... 127

Figure 56: (a) Photograph showing visible differences between the top (left) and bottom (right) of the phantom. (b) Corresponding depth-dependent measurements confirming the greater presence of lipids at the top of the phantom and higher water at the bottom of the phantom. (c) Repeatability of the phantom creation process in three independently-constructed phantoms with the same water and lipid ratio, each measured five times. .... 128

Figure 57: (a) Schematic of a free-standing three-compartment phantom and the grid pattern used to assess its optical properties. A given phantom was evaluated at 36 locations on a 1 cm grid pattern as shown. Interpolated results across the 5 cm x 5 cm grid of individual measurements of optical properties are shown for water in (b) and lipids in (c) in the fibroglandular, tumor and adipose regions. In the top row, the fibroglandular-simulating phantom was measured alone. The middle row depicts results when a tumor-like inclusion of ~2 cm diameter was added near 20-40 mm in x and 60 mm in y directions. In the bottom row, measurement data are shown when a uniform adipose simulating layer was added on top of the fibroglandular and tumor phantom. (d) Photographs of the phantom regions.... 130

Figure 58: The workflow and patient positioning of a human subject NIRST-DBT exam. Photographs proceed in sequence from left to right, showing how the breast is positioned and the light shielding mechanisms are used during the exam. The

procedure on top describes exam workflow for a single view. Each exam consists of four views, the steps of which are described on the lower series. .... 140

Figure 59: (a) The instrumentation cart for the DOSI system. (b) A close up of the handheld probe. (c) The measurement locations used in the NIRST-DBT and DOSI study. (d) A photograph of a patient exam in progress. .... 144

Figure 60: LABVIEW screenshots during the equalization phase (left) and during the actual scan (right). Equalization shows the light output for a single detector with an unchanging source..... 145

Figure 61: The data calibration GUI (a) allows for nearly instantaneous feedback on phantom data collected. Results from the exam are shown as plots of the log of the detector output vs. SD distance in mm (c). Individual data points can be highlighted, with their corresponding source and detector information appearing to help localize bad data points. Sources and detectors are numbered as shown in (b)..... 149

Figure 62: Flowchart outlining the major steps in data dropping and restructuring before image reconstruction can take place. .... 151

Figure 63: The modeling of data along the boundaries does not correspond to the actual data. Data points within 0.5 cm of the boundaries of the phantom mesh are included in (a), while data points are that are less than 1.5 cm from the edge are dropped in (b). At 1.5 cm from the edge, the data appears quite linear; the data points near the edge greatly alter the modeled data output. When far edge data points are included in the reconstruction, there are differences in the recovered

hemoglobin concentration, (c) shows a 30% decrease in adipose HbT when boundary data is removed (d). ..... 153

Figure 64: Steps in the data dropping scheme. The top row depicts sequential steps for an excellent data set. The bottom row depicts issues that can arise in the data. (a) A linear fit of the log of the amplitude vs. source detector distance is derived for inner data points. (e) Including data points near the outside can skew the slope. Only the inner data is included because variation in data points near the outside can skew the slope, as shown in (e) for two different fitting algorithms. All data is plotted and those more than half a standard deviation below the lowest point in the slope fit are dropped (b, f) and are shown in red. Then cut based on variation from the slope fit is applied, with all points more than a certain distance away removed (c, g). Final data is shown, with colors corresponding to different regions (d), as well as data taken from the calibration phantom (h) to ensure that all detectors are working properly. .... 155

Figure 65: Color-coding the data as shown in (a) and (c). Sources and detectors are labeled as being primarily associated with adipose (red) or fibroglandular (yellow) tissue. In the top row, there is greater fibroglandular absorption in the data (a), manifests as higher HbT (b). The opposite is true in (c) and (d). .... 158

Figure 66: Pictorial flow chart representing a summary of the data reconstruction scheme. DBT images are obtained (a), segmented (b) and used as the basis for creating an FEM mesh (c). NIRST data is collected (e), dropped and reformatted (f) and reconstructed using the FEM mesh. The resulting output can be displayed as an overlay on the original DBT image (d) or more quantitatively (g)..... 161

Figure 67: First projection (a) and processed (b) DBT images taken during a NIRST-DBT exam show metal wire in place inside the detector shroud. Detector calibration artifacts (c) apparent in some patients. .... 165

Figure 68: Changes made to breast modeling and image reconstruction. First, slope-based calibration was adopted for all patients as a consistent data removal scheme (a). Based on the images of source positions at different heights (b), it was determined that pixel spacing corrections needed to be implemented based on slice height. These same corrections were applied to the detector panel (c). .... 167

Figure 69: Sample reconstructions for two early study subjects. NIRST results for adipose and fibroglandular tissues are overlaid on a DBT slice. Low signals in the higher wavelengths prevented reconstruction of water and lipids in one case. .... 170

Figure 70: Histograms of key demographic and clinical information for the 32 normal subjects imaged here. .... 170

Figure 71: Comparison of summary data on breast density and tissue chromophores for normal subjects. Black bars indicate statistical significance ( $p < 0.05$ ). .... 172

Figure 72: Comparison of tissue chromophores for normal subjects grouped together based upon bra cup size. .... 173

Figure 73: Comparison of breast thickness and tissue chromophores for these normal subjects, and trendlines shown in red for each. .... 175

Figure 74: Comparison of body mass index and tissue chromophores for normal subjects, with trendlines shown in red for each. .... 177

Figure 75: Comparison of fibroglandular percent and tissue chromophores for normal subjects with trendlines shown in read for each. ....	179
Figure 76: Comparison of adipose and fibroglandular tissues across chromophores for normal subjects. There were no significant differences between adipose and fibroglandular regions for these chromophores. ....	181
Figure 77: Comparison of CC and MLO views across chromophores for normal subjects. ....	183
Figure 78: Scatter plots of compressed and uncompressed data across all chromophores. Blue lines shown 1:1 correlation, and red dotted lines are offset from 1:1 by 20% ....	184
Figure 79: Comparison of uncompressed and compressed breasts across chromophores for normal subjects. ....	186
Figure 80: Scatter plots of compressed and uncompressed data across all chromophores. Blue lines shown 1:1 correlation, and red dotted lines are offset from 1:1 by 20%. ....	187
Figure 81: Comparison of NIRST and DOSI recovery of tissue chromophores. DOSI results are plotted on the x-axis with NIRST recovery on the y axis. Red lines show best fits of the data, while the black line depicts the 1:1 correlation between DOSI and NIRST results. ....	190
Figure 82: Workflow chart for patients entering breast cancer screening showing the anticipated clinical niche for NIRST-DBT. ....	196
Figure 83: Interactions with the research staff from the patient’s perspective. ....	198

Figure 84: Workflow chart of steps required by the research team for imaging a biopsy patient with NIRST-DBT..... 199

Figure 85: Histograms of summary statistics for the biopsy cohort including tumor volume (in mm<sup>3</sup>), thickness (in cm), percent fibroglandular tissue, density category, bra cup size, and age. .... 202

Figure 86: Comparison of average patient characteristics for normal subject and biopsy subject cohort. The breast thickness is in cm, density and bra cup size have been converted to an ordinal scale, height is in inches and breast volume is in cm<sup>3</sup>/10. .... 203

Figure 87: Graph showing the dependence of inclusion size chromophore recovery on regularization. Smaller lesions require lower regularization values; in this case 10<sup>-6</sup> is necessary to fully recover the smallest inclusion while 10<sup>-4</sup> could recover HbT in the largest inclusion..... 206

Figure 88: (a) Original processed DBT slice screenshot with circles drawn by the radiologist to indicate ROIs. (b) The segmented regions and (c) the resultant mesh with the right hand lesion enlarged to improve NIRST sensitivity while the left lesion was not enlarged. The resulting reconstruction for HbT (d) and oxygen saturation (e). The graphs depict the change in chromophore content vs. regularization for true-to-size lesions (f) and expanded lesions (g) for a different patient. Colors indicate different chromophores while line types represent different tissues regions. The solid lines represent the small lesion (f) and expanded lesion (g). .... 207

Figure 89: (a) DBT image slice with arrows pointing to a benign (left) and malignant lesion (right), as well as the DBT image segmentation (b) and visualization of the mesh before (c) and after (d) enlargement of the malignant lesion. (e) and (f) are the results of NIRST reconstruction for the smaller and larger lesion respectively. These results are displayed as DBT image overlays for total hemoglobin (g) and oxygen saturation (h). ..... 209

Figure 90: (a) Processed DBT slice with a cluster of tiny microcalcifications outlined with a yellow box. (b) The segmented image slice. (c) The mesh with the enlarged lesion. Overlays of total hemoglobin, oxygen saturation, water, and lipids are shown in (d, e, g, h) with a graphical summary in (f). ..... 212

Figure 91: (a) Processed DBT image slice containing a fibroadenoma (top arrow) and large fluid-filled cyst (bottom arrow). (b) Segmented DBT image. DBT with NIRST overlays for tissue HbT, oxygen saturation, water, and lipids (c, d, f, g) as well as a graphical display of the same data (e). ..... 213

Figure 92: Summary slide showing the tumor to fibroglandular total hemoglobin ration minus one for all the benign and malignant lesions present in the first six patients of the biopsy cohort. Lesions shown here are invasive ductal carcinoma (IDC), ductal carcinoma in-situ (DCIS), sclerosing adenosis (SA), fibrocystic disease (FCD), fibroadenoma (FA), and cysts. The malignancies are depicted in red while benign lesions are blue. Lesions directly adjacent to the tissue boundaries are indicated by an asterisk on the x-axis. Mean contrast for malignancies is shown in the red line, while the mean contrast for benign lesions is shown in blue.

When cysts and edge lesions are excluded from the benign lesion group, the mean contrast is shown in green..... 215

*Figure 93: Solid line shows the mean and the error bars show standard deviation of the average HbT, recovered in the image volumes from all patient cases as a function of error in optical scattering. Red data points show the same analysis from the phantom experiments. .... 221*

Figure 94: Boxplots showing the scattering amplitude (left) and scattering power (right) bulk tissue estimates for 15 patients as a function of BIRADS category. .... 224

Figure 95: Graphs comparing absolute chromophore recovery (left) and contrast ratios (right) for individual scattering estimate vs. uniform group scattering estimate as derived from DOSI. Each color in the graphs represents a different chromophore, with red representing total hemoglobin, magenta as oxygenated hemoglobin, green as deoxygenated hemoglobin, teal as water, yellow as fat, and dark blue as oxygen saturation. The black line in each graph represents 1:1 correlation. .... 225

Figure 96: Graph comparing absolute chromophore recovery (blue) and contrast ratio (red) correlation coefficients for individual scattering estimate vs. uniform group scattering estimate as derived from DOSI. The line shows the cutoff for statistical correlation, all cases are statistically correlated..... 226

Figure 97: The workflow for normal subject imaging and chromophore recovery. Current efforts are focused on comparing DBT pixel intensity to the optical scattering obtained from the DOSI system, encouraged by previously published work shown in the bottom right, indicating a correlation between breast density and optical scattering<sup>77</sup> ..... 228

Figure 98: (a) The step wedge phantom used to calibrate the patient images and a sample X-ray image of the phantom. (b) An example of the raw central projection image from a normal subject breast. (c) Calibrated X-ray transmission data for all subjects<sup>208</sup> ..... 229

*Figure 99: Graph showing the DOSI measured scattering power vs. the mean X-ray intensity after phantom calibration for all patients. Fit line was added after dropping patients with higher compression levels<sup>208</sup> ..... 230*

Figure 100: A normal subject reconstruction of total hemoglobin, oxygen saturation, water, and lipids for both adipose and fibroglandular regions for two cases: Scattering as determined from (top) the DOSI system and (bottom) the DBT-based estimate using the linear fit for scattering power and scattering coefficient at 850 nm.<sup>208</sup> ..... 231

Figure 101: These graphs show the relationship between calculated percent fibroglandular content and optical scattering amplitude (left) and power (right). Trend lines show a generally positive correlation between increasing fibroglandular content and optical scattering. Blue data points correspond to the log of the mean of the image, while red data points correspond to taking the average of the log of the image. .... 234

Figure 102: These graphs show the relationship between volumetric fibroglandular fraction as determined from segmented DBT images and scattering amplitude (left) and power (right)..... 236

Figure 103: Mock-up images of the new detector (a, b) and detector case (c, d)..... 250

Figure 104: Clinical Hologic Dimensions unit at Dartmouth (a) and unit with biopsy plate attachment (b). ..... 251

Figure 105: Signal from all detectors for a phantom scan imaged (a) with the shroud and (b) without the shroud. .... 253

## List of Abbreviations

Full Field Digital Mammography	FFDM
Digital Breast Tomosynthesis	DBT
Near-Infrared	NIR
Near-Infrared Spectral Tomography	NIRST
Screen Film Mammography	SFM
Three-Dimensional	3D
Human Epidermal Growth Factor Receptor 2	HER2
Vascular Permeability Factor	VPF
Vascular Endothelial Growth Factor	VEGF
Positive Predictive Value	PPV
Negative Predictive Value	NPV
Area Under the Curve	AUC
Receiver Operating Characteristic	ROC
Magnetic Resonance Imaging	MRI
Positron Emission Tomography	PET
Computed Tomography	CT
Continuous Wave	CW
Frequency Domain	FD
Time Domain	TD
Diffuse Optical Spectroscopic Imaging	DOSI
Dartmouth-Hitchcock Medical Center	DHMC
Printed Circuit Board	PCB

Institut National D'Optique	INO
Radiative Transport Equation	RTE
Finite Element Modeling	FEM
Filtered Back Projection	FBP
Matrix Inversion Tomosynthesis	MITTS
Kernal-Based Fuzzy C-Means	KFCM
Craniocaudal	CC
Mediolateral Oblique	MLO
Voxel of Interest	VOI
Volumetric Breast Density	VBD
Glandular Volume	GV
Total Breast Volume	TBV
Region of Interest	ROI
Phosphate Buffered Saline	PBS
Committee for the Protection of Human Subjects	CPHS
Body Mass Index	BMI
Breast Imaging-Reporting And Data System	BIRADS
Linear Attenuation Coefficient	LAC

# Chapter 1: Introduction

## *Project Overview*

Most women in the United States undergo breast cancer screening via mammography, aiming to detect cancer at an earlier and more treatable stage. However, there are some significant limitations to full-field digital mammography (FFDM) that lead to a sizeable percentage of women receiving a false positive result, which can lead to additional imaging and possibly, an invasive biopsy procedure. Since its FDA approval in 2011, digital breast tomosynthesis (DBT) is playing an increasingly important role in clinical breast cancer screening and diagnosis, as it has been shown to have lower false positive rates than mammography. The work presented in this thesis aims to develop and test a combined imaging platform that may further decrease the false positive rate through the addition of near-infrared (NIR) spectral tomography (NIRST)

NIR light (650-1000nm) is preferentially absorbed by hemoglobin, water, and lipids, tissue chromophores that can be altered in the presence of malignancy. Tumors often cause angiogenesis (the proliferation of blood vessels) and inflammation, which alters the metabolic markers measured by NIRST. One difficulty with this technique is the high likelihood of light scattering, which severely limits the spatial resolution of this modality in a stand-alone setting. Prior spatial information obtained from DBT imaging can synergistically improve NIRST results.

Successful implementation in clinical breast imaging requires that the near-infrared adjunct be fast, easy to operate, and inexpensive, with few potential side effects.

With these qualities in mind, this thesis presents work in simulation, hardware design, calibration, phantom testing, normal subject imaging, and assessment of lesion status in women who have been recommended for biopsy. The hypothesis was that a combined NIRST-DBT imaging platform can better distinguish between cancerous and benign lesions as compared to DBT alone. Breast imaging phantoms with small inclusions of physiologically relevant chromophore contrast were detected and a cohort of women with breast pathology showed greater contrast between cancerous and normal tissues than benign and normal tissues. Adding information about the metabolic status of the tissue along with the extensive anatomic information provided by DBT may decrease the false positive rate of breast cancer diagnosis, improving patient experience and decreasing health care costs ultimately by reducing the number of needed biopsies.

### ***Current State of Clinical Breast Imaging***

There were over 1 million cases of breast cancer diagnosed worldwide in 2013, with 230,000 in the United States alone<sup>1</sup>. One in 8 women will be diagnosed in the course of her lifetime, and it is the second leading cause of cancer mortality in women<sup>2,3</sup>. Early diagnosis and treatment improve patient outcomes. Hence, breast cancer screening using screen film mammography (SFM) has been a clinical standard for almost forty years, as it is effective at early detection of cancer and reduction in mortality<sup>4-7</sup>. Current clinical guidelines from the American Cancer Society recommend annual screening for women over 40; however, other groups such as the United States Preventative Services Task Force have recently recommended biannual screening starting at age 50, citing some of the limitations of SFM in its analysis.

SFM possesses several significant limitations including low specificity<sup>8-10</sup> and positive predictive value<sup>10</sup>. These limitations are especially pronounced in women with dense breasts<sup>11-13</sup>, a particularly important subset of women who experience higher incidence and mortality rates from the disease<sup>14</sup>. The extensive overlapping of functional structures, which are more prevalent in dense breasts, can obstruct visualization of malignancy. This leads to false negatives or inconclusive results and additional imaging; 25% of recalls may be due to tissue superposition<sup>15</sup>. FFDM has shown similar accuracy rates to SFM<sup>16-18</sup>.

Widespread screening with mammography has led to many false positive results; 30-70% of women who undergo ten years of breast cancer surveillance including mammography will have at least one false positive examination<sup>10,19-21</sup>. Furthermore, about one in ten women who is screened for breast cancer has inconclusive SFM/FFDM and is called back for additional imaging based on suspicious or inconclusive results. These women go on to diagnostic imaging where approximately one in six receives a recommendation for biopsy. Only one in five of the biopsies are pathologically confirmed cancers,<sup>20,21</sup> as shown in Figure 1. Each step of this process is more time consuming and expensive, and more likely to incur side effects than the previous step. Many women who undergo diagnostic imaging and biopsy procedures do not have cancer. Imaging techniques that reduce the level of tissue superposition while maintaining similar clinical workflow and reading procedures as SFM/FFDM have high potential for near-term improvements in clinical outcomes.

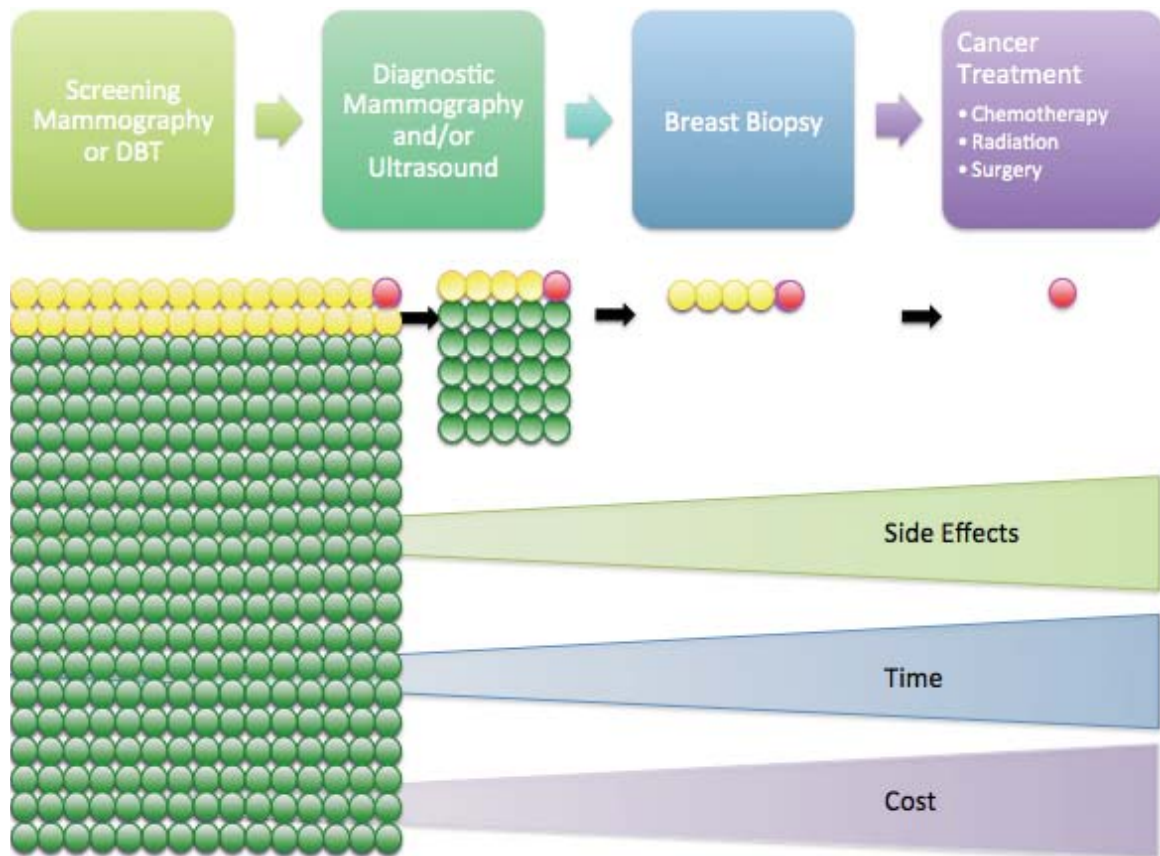


*Figure 1: Workflow diagram of breast cancer screening, diagnosis, and treatment. Each circle in the diagram represents one woman. If the results from the screening are suspicious or inconclusive, women go on to diagnostic mammography or ultrasound and may be recommended for a breast biopsy. Each step along the path is more time consuming and expensive, and more likely to incur side effects than the previous step.*

### ***Role of DBT in Breast Cancer Management and Detection***

DBT is a limited angle X-ray tomography system that eliminates some of the volume superposition apparent in SFM/FFDM. Initial clinical studies of DBT exhibit potential to decrease the false positive recall rate by 10-17%<sup>22-24</sup> and improve sensitivity<sup>23</sup>, accuracy<sup>25</sup>, and detection of invasive cancer<sup>26</sup>, with significant

improvements seen in women with denser breasts<sup>23,27</sup>. Based on proven performance in a clinical setting, a DBT system made by Hologic Inc. has been approved for clinical use by the FDA to perform breast cancer screening exams. It is poised for widespread adoption due to its similarity to existing SFM/FFDM systems in terms of image type and patient positioning. Dose estimates are similar to those of SFM/FFDM but can be higher or lower depending on patient characteristics<sup>28,29</sup>. Some differences and limitations to DBT remain, including the training of radiologists and technologists, and a greater number of images to be analyzed due to the 3-dimensional (3D) nature of this technique. Radiologist reading times for DBT are approximately double those of SFM/FFDM, but may decrease over time<sup>26</sup>.

### ***NIRST Imaging of the Breast***

NIRST uses non-ionizing electromagnetic radiation (between 650-1000nm) to image several important functional indicators in tissue, including hemoglobin concentration, oxygen saturation, water and lipid levels, as well as scatter particle size and number density<sup>30-32</sup>. Imaging is possible through up to about 10cm of tissue due to lower absorption levels in the NIR regime. The potential for non-invasive functional imaging has led to the development of both academic<sup>31,33-36</sup> and commercial<sup>37,38</sup> stand-alone<sup>32,39</sup>, X-ray<sup>40</sup>, ultrasound<sup>41</sup>, and MRI-guided<sup>42,43</sup> diffuse optical systems.

Contrast arises from structural differences between normal and malignant tissue. Hemoglobin levels are typically higher in tumors due to angiogenesis-induced hypervascularity and increased vessel permeability with upregulation of several pro-endothelial cell growth factors like HER2, VEGF/VPF<sup>44-48</sup>. Numerous studies using

diffuse imaging methods have found a contrast ratio of about 2:1 in breast cancer when compared to normal tissue<sup>49-51</sup>. Lower oxygen saturation and lipid levels are expected due to the increased metabolic demands and lower volume of adipose tissues, respectively. Higher water content from edema can also be present in malignancies. Cancer changes tissue stroma, leading to significantly higher scattering properties<sup>52-54</sup>. Characterization of NIR imaging accuracy shows promise for determination of the presence or absence of cancer. Sensitivity measurements have been reported between 91-96%, specificity between 93-95%, positive predictive value (PPV) between 89-95% and negative predictive value (NPV) between 89-97%<sup>33,55,56</sup>. Studies have also examined the benefit of adding stand-alone diffuse optical tomography to traditional mammographic screening. A significant improvement in the PPV has been shown, as well as increases in the area under the curve (AUC) of a receiver operating characteristic (ROC) analysis<sup>38,51</sup>.

### ***Combining NIRST and DBT***

NIR imaging combined with highly spatially resolved clinical modalities such as DBT can improve the inherently low spatial resolution of diffuse optics alone. Studies on MRI spatial priors have improved NIR resolution to nearly 1mm<sup>57</sup>. Spatial prior information also increases the accuracy in recovery of optical properties<sup>58-60</sup>. Hence, NIRST with spatial priors is a promising technique because it produces highly spatially resolved images of functional parameters strongly associated with cancer. The workflow for image-guided NIRST reconstruction is shown in Figure 2.

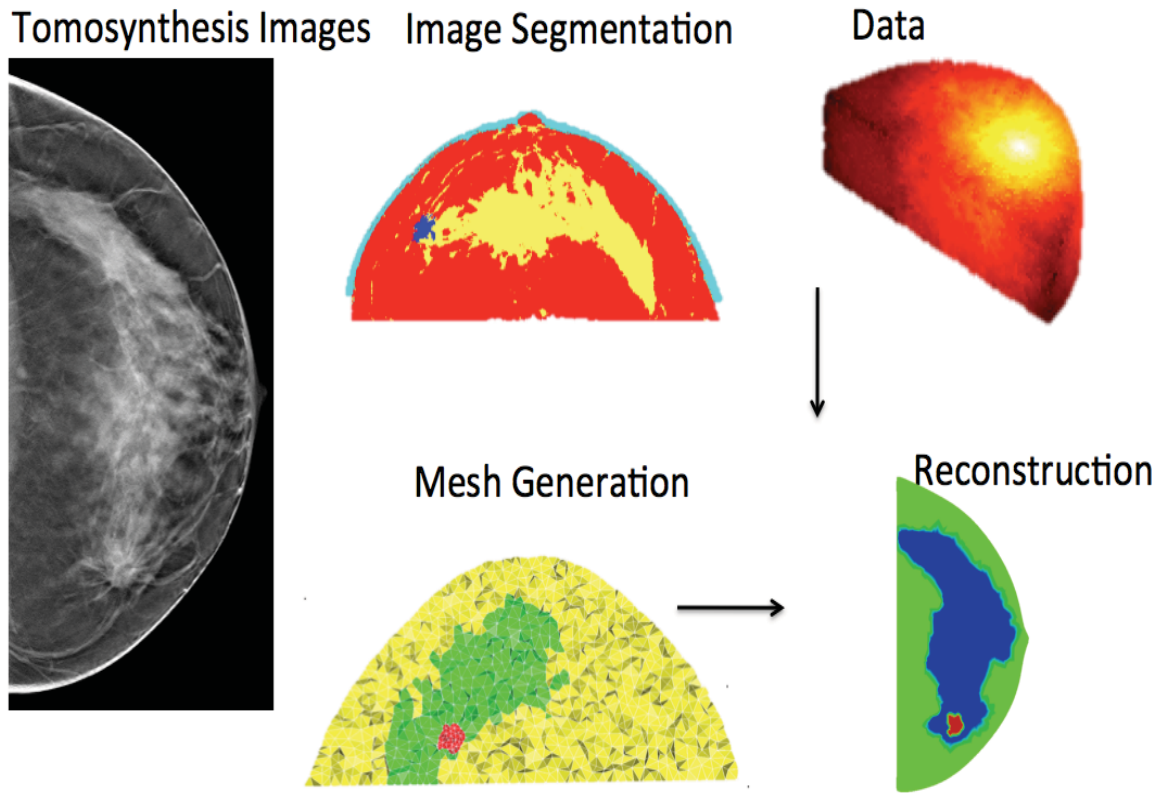


*Figure 2: Region-guided reconstruction of NIRST data involves segmentation of DBT slices creating images from which a volume mesh is generated. The prediction of the forward diffuse transport data is simulated on the finite element mesh and used in iteratively reconstructing a co-registered volume of the optical properties of the breast with the mesh regions as a template.*

An integrated NIRST-DBT system combines high spatial resolution to identify anatomic structures with functional imaging to evaluate the metabolic status of the breast. Such a combination has been previously adopted into clinical practice with the advent of combined PET-CT and PET-MRI systems. NIRST is non-ionizing, no contrast agents are required, and the hardware components are relatively inexpensive and can be easily integrated into existing DBT systems. DBT provides excellent 3D spatial resolution with fewer superposition artifacts than SFM/FFDM while maintaining similar clinical

workflow procedures. NIRST-DBT is a synergistic combination with the potential to decrease false biopsy rates during breast cancer screening. A combined NIRST-DBT system has already been developed and used at Massachusetts General Hospital (MGH) to image over 200 patients, as described in Zhang et al. and Fang et al.<sup>18,20</sup>. Early results are promising; a 2011 study showed significant differences in the optical properties of malignant and benign lesions. Different contrast levels for HbT and scattering properties between malignant and benign lesions were obtained, indicating that a multi-modal imaging system of this type may improve detection sensitivity and specificity over DBT alone<sup>12</sup>.

### ***Overview of this Thesis***

This thesis describes the simulation, hardware design, calibration, optimization, phantom and patient imaging of a new combined multi-wavelength NIRST-DBT imaging platform. Chapter 2 describes considerations for system development, simulations of the proposed system, and the selection of hardware components for light collection and delivery. Additionally, calibration procedures for the system are delineated. Chapter 3 describes the physics of light-tissue interaction for a better understanding of the image creation methods of NIRST, which are very different from X-ray imaging. Use of several wavelengths of light for reconstruction of water and lipids as well as hemoglobin is discussed, as well as the use of anatomical priors from DBT images. The phantom imaging work is described in Chapter 4, including calibration phantoms for system assessment, hemoglobin contrast phantoms, a resin-based phantom used for contrast, size,

and depth analysis, and the development of water and fat anthropomorphic breast phantoms for characterizing system recovery of tissue content.

Chapters 5-7 focus on imaging human subjects. Chapter 5 deals with patient imaging protocols and data analysis methods that are essential in the development of a new multi-modality imaging system. LABVIEW controls, MATLAB analysis, and data dropping procedures are discussed in detail. These building blocks facilitated normal subject imaging (Chapter 6) and imaging of women with breast pathology (Chapter 7). A cohort of 32 healthy volunteers was imaged using NIRST-DBT to ensure the detection of physiologically comprehensible tissue hemoglobin, water, and lipid concentrations across a wide range of breast sizes, shapes, and densities. Additionally, comparing optical recovery of different views and at different compression levels is described in Chapter 6. Thirteen women with breast lesions have been imaged using NIRST-DBT to date and preliminary results from these cases are detailed in Chapter 7. It discusses methods for recovering contrast in small regions and compares optical properties obtained in women with benign and malignant lesions.

Chapter 8 synthesizes information obtained from simulations, phantom experiments, and patient studies on the role of optical scattering and its effects on tissue absorption as manifested in recovered chromophore concentrations. The NIRST-DBT system cannot measure optical scattering in its current state and an understanding of the role of scattering mis-estimation was required to interpret the absorption-related results. Finally, Chapter 9 discusses conclusions that can be drawn from the work as well as areas for future investigation.

## Chapter 2: Imaging the Breast with Diffuse Light

### *Introduction*

Optical imaging is a term that is often used generically to imply the use of either visible wavelengths (400-650 nm) or NIR wavelengths (650-1000 nm) of light to image or measure transmittance or reflectance in order to characterize the absorption and scattering properties of the breast. NIR light can propagate to greater depths than visible light due to low tissue absorption. With detectable photons travelling up to approximately 10 cm, NIR is highly suitable for breast imaging. As a less energetic form of electromagnetic radiation, NIR light has the benefit of being non-ionizing, and thus poses less of a health risk to patients and medical personnel relative to traditional X-rays. NIR light undergoes multiple scattering events as it travels in tissue, whereas X-rays rarely scatter more than once. Differences in index of refraction in tissue components such as mitochondria and collagen fibrils contribute to Mie and Rayleigh scattering of NIR light. The transport mean free path describes the average distance between photon interactions and is usually on the order of 1 mm. Scattering is quantified by a scattering coefficient,  $m_s$ , where a modified version of this,  $m_s'$ , is more frequently used when considering multiple scattering where directionality is lost, which is known as the transport or reduced scattering coefficient and is relevant over long distances of measure relative to  $1/m_s$ . The scatter pattern is simplified by a single parameter, the average cosine of the scattering angle,  $g$ , which is close to 0.9 in most tissues, because multiple scattering can appear isotropic in the far field and  $m_s' = (1-g)m_s$ . Individual scattering

events are highly anisotropic and scattering angular patterns are a strong function of direction. But over large distances this is neither apparent nor useful in terms of interpreting transmission. This observation of multiple scattering significantly limits the ultimate spatial resolution of NIR imaging techniques.

Absorption of light can also attenuate the signal, both in the visible wavelengths as well as the NIR when light is transmitted through thick tissues. In the NIR regime, the absorption coefficient is about two orders of magnitude lower than its scattering counterpart. The absorption coefficient  $\mu_a$  represents the inverse of the mean free distance for exponential attenuation, estimated in the absence of scatter. This and several other important quantities are summarized in *Table 1*. Several molecular tissue components contribute significantly to light absorption in the NIR region, including oxy- and deoxy-hemoglobin, water, and lipids. At each wavelength, these individual chromophores contribute linearly to the total absorption coefficient, weighted by their respective concentrations and molar extinction coefficients.

Quantity	Symbol	Units	Quantity	Symbol	Units
Absorption coefficient	$\mu_a$	cm <sup>-1</sup>	Reduced scattering coefficient	$\mu'_s = \mu_s(1 - g)$	cm <sup>-1</sup>
Scattering coefficient	$\mu_s$	cm <sup>-1</sup>	Transport mean free path	$MFP' = 1 / (\mu_a + \mu'_s)$	cm
Anisotropy of scattering	$g$	dimensionless	Diffusion length	$D = MFP' / 3$	cm
Refractive index	$n$	dimensionless	Optical penetration depth	$\delta = \sqrt{D / \mu_a}$	cm

*Table 1: Important quantities, their symbols, units, and relationships in diffusion-based on NIR transport theory<sup>61</sup>.*

### ***Spectroscopic Imaging***

Tissue absorption and scattering coefficients vary as a function of wavelength. Spectroscopy is a technique that acquires measurements at multiple wavelengths to gain

additional information about tissue properties. Each of the major absorbers has a characteristic molar extinction spectrum in the NIR, which is its absorption coefficient normalized by the concentration at each wavelength. Thus, if measurements of the absorption coefficient are recorded at different wavelengths, concentrations of absorbers such as hemoglobin, water, and lipids can be determined based on the known extinction coefficients for each contributor at the different wavelengths, which are shown in Figure 3.

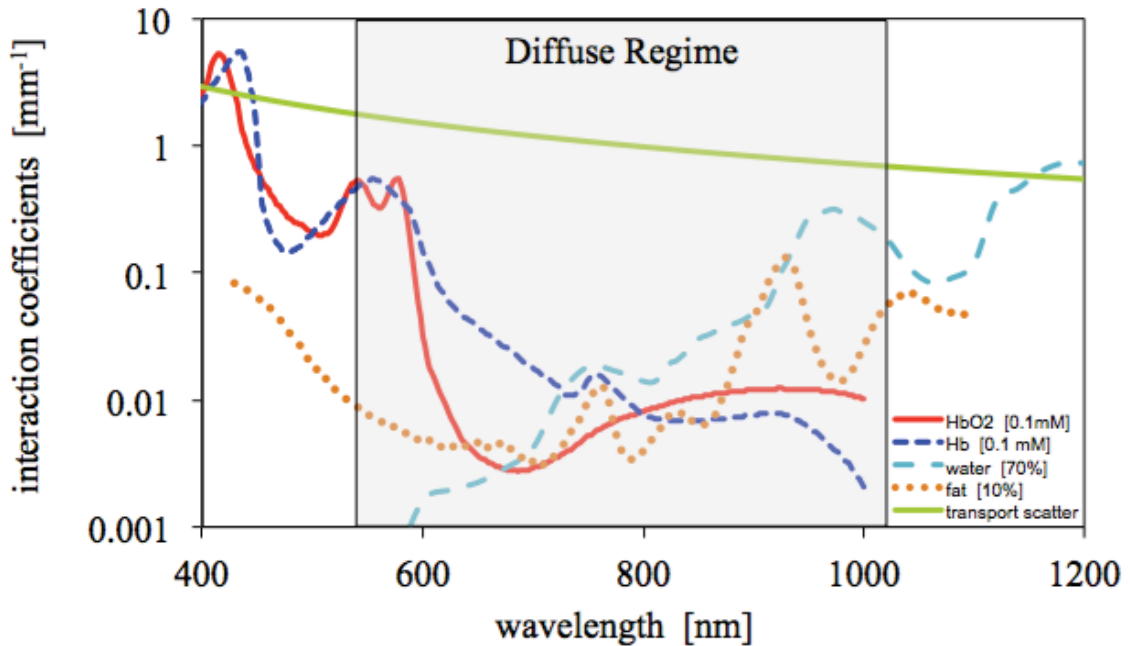


Figure 3: Absorption and scattering as a function of wavelength in the visible and NIR regime for major tissue chromophores in breast tissue<sup>62</sup>.

Spectroscopic techniques provide insight into the metabolic state of tissue. Knowledge of local oxy- and deoxy-hemoglobin, water, beta-carotene, bilirubin, and lipid concentrations along with scattering parameters is useful in distinguishing healthy from diseased tissue. Normal breast parenchyma is largely composed of two

constituents: fibroglandular and adipose tissue. Higher hemoglobin, water, and scattering are typically found in the fibroglandular component due to higher metabolic demands relative to fat<sup>59</sup>. Similarly, malignant tissue also possesses higher hemoglobin, water, and scattering levels, as well as a lower concentration of lipids when compared to healthy breast tissue<sup>49</sup>. These differences are likely due to the widespread angiogenic neovasculature that is characteristic of neoplasms.

When designing a spectral imaging system, more wavelengths improve accuracy, but at the cost of greater examination time and hardware complexity. Broadband imaging across the entire NIR (650-1200nm) would be the ideal, but detectors that operate across this broad regime have difficulty with low signal levels and phase measurements as well as longer scan time<sup>63,64</sup>. To avoid a lengthy examination time and high system costs, commonly available discrete wavelengths across the NIR regime can be used with a corresponding loss in spectral sensitivity as compared to broadband. This design is optimal for the combined NIRST-DBT system, as short examination time is one of the most important considerations.

### ***Imaging Types***

A number of NIR imaging systems have been developed with unique configurations of hardware technologies, source detector setups, and breast positioning geometries. Technical approaches have been used to determine absorption and scattering coefficients of breast tissue based on continuous wave (CW), time domain (TD) and frequency domain (FD) methods, as depicted in Figure 4.

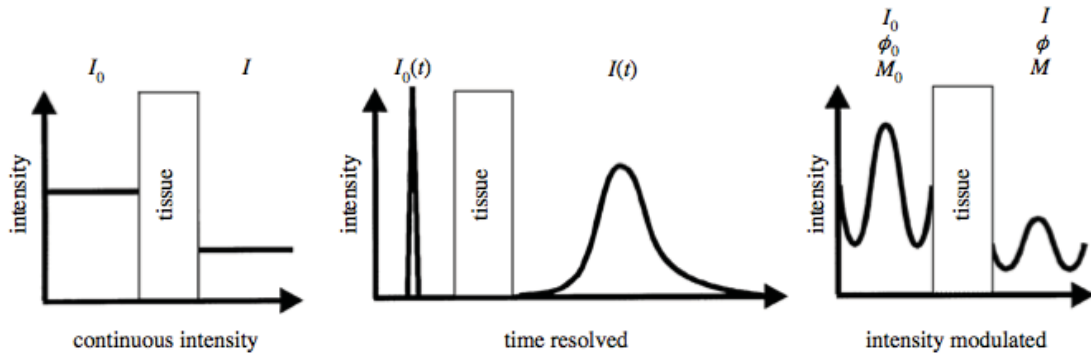


Figure 4: Different spectroscopy methods for probing tissue, to obtain absorption and scattering information used in diffuse optical imaging: continuous wave, time domain, and frequency domain<sup>65</sup>.

As previously mentioned, light interactions in tissue consist of absorption and scattering events. When detecting light from a time-invariant source at a position some distance from that source, a lower signal than the initial source strength can be attributed to some combination of light absorption and scattering away from the detector. Highly scattering tissues can appear similarly to highly absorbing tissues and vice versa. In continuous wave imaging, light is emitted into tissue at constant amplitude (or with very low frequency amplitude modulation) and detected at another position. It is the simplest, fastest, most compact, and least expensive technique. However, unlike the other approaches, it is unable to reliably distinguish between absorption and scattering in the tissue when measured over large distances. CW imaging has been used in many applications, because these systems are favored for their simplicity and low cost<sup>66-68</sup>.

Time domain imaging involves injection of a short light pulse with subsequent detection of the temporal distribution of photons that pass through the tissue. The detected distribution has a greater temporal spread than the initial light pulse due to

differences in the path lengths taken by the collected photons as they scatter between the source and detector. Absorption and scattering properties can be determined from the shape of this distribution. Time domain systems are most sensitive to low light levels because they can operate in single photon counting mode, but they are also the most expensive technology due to the cost of time-correlated photon counting devices and pulsed lasers<sup>69-72</sup>.

Intensity modulation of a laser source and measurement of the baseline amplitude and shift in phase are used in frequency domain imaging techniques. Measurements at many source and detector positions or at multiple frequencies are used in determining absorption and scattering. With frequency domain imaging, additional wavelengths can be added at relatively low cost and the instrumentation is typically more stable than time domain components, but with a bit less signal sensitivity<sup>73,74</sup>. There have been several breast imaging systems built that primarily emphasize FD data on account of its stability and discrimination of amplitude and phase<sup>75-78</sup>.

Two types of source detector arrangements are most often used in optical imaging. In reflectance geometry, the sources and detectors are on the same side of the tissue, typically attached to the same probe. In a transmission geometry light sources and detectors are on opposing sides of the breast. This configuration achieves greater penetration depth, however it also requires more sensitive detectors due to the high attenuation with longer pathlength. As we will see in this work, the CW transmission geometry was chosen for combination with DBT imaging, as this physically matched the available geometry and logistics of the project.

## *System Design*

### **2.1.1. Simulations of Proposed System and Optical Scattering Study**

Developing an imaging modality for recall screening presents unique challenges. In order to be clinically successful, it must be simple to operate and interpret, have low cost per exam, and pose minimal risks to the individual. In an effort to keep cost and complexity low, we have pursued a NIRST system which projects light onto the breast surface at discrete locations with a motor-driven mirror and measures the resulting light signals with a fixed rectangular array of silicon photodiodes integrated into a detection panel placed on the opposite side of the breast. The design relies extensively on CW measurements for rapid, low-cost quantification of tissue absorption. Measuring optical scattering in tissue is more difficult and adding FD elements would increase system cost, complexity and examination time. Minimizing exam time is important both to limit the time the breast is subjected to compression and to maintain efficiency of workflow in the mammography clinic. Estimation of optical scattering properties is necessary in breast imaging because of the wide variation in these values, which depend on breast composition and parenchymal density. Incorrect estimation of scattering greatly affects recovered absorption values. For spectral imaging, this is apparent in hemoglobin and other tissue chromophores. Accurate understanding of scattering is needed to quantify optical properties of the breast, as will be examined later in Chapter 8.

However one aspect of the design chosen here was the lack of data which would definitively separate scattering from absorption, and so through simulations and experimentation, we investigated whether a NIRST system with a limited number of FD

channels (to obtain minimal scattering information) could quantify hemoglobin and other chromophores in the presence and absence of tumor. This design is not the first to combine CW and FD information. Indeed, promising breast imaging results have been achieved with existing systems using a similar approach<sup>20,21</sup>.

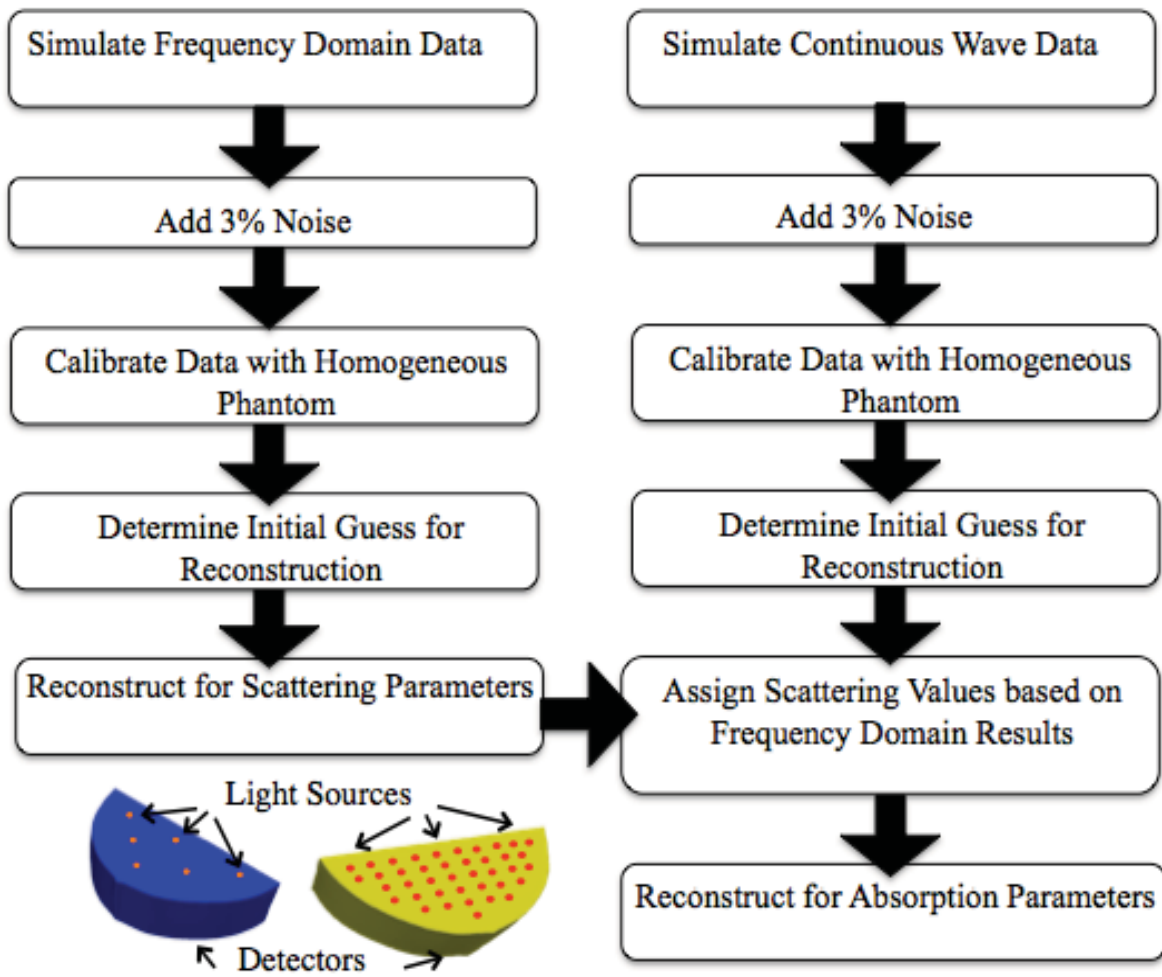
#### *2.1.1.1. Methodology*

Reconstructed DBT slices from eight patients with abnormal mammograms acquired during a previous study<sup>79</sup> provided anatomical information for the NIRST simulations. A radiologist specializing in breast imaging identified the lesions. DBT slices were segmented into three tissue types – adipose, fibroglandular, and malignant – based on grayscale intensity, location, and radiologist interpretation using the Mimics© software package.

The anatomic information from the DBT segmentation was incorporated in the finite element meshes used for NIRST image reconstruction through simple region classification. Specifically, nodes within the mesh were tagged as belonging to adipose, fibroglandular, or tumor regions depending on their correspondence with the co-registered DBT segmentation. Overall breast volume from the DBT image data also defined the mesh size and shape. Two 3D volumetric meshes were created for each patient image stack: a fine mesh with about 80,000 nodes for FD simulations and a coarse mesh with about 30,000 nodes for the CW case. Greater nodal density in the FD simulations is required to obtain accurate phase data. Fewer nodes in the CW problem simplified the simulations and minimized reconstruction time. In both cases, nodal density was increased in the tumor region to about 5% of the total nodes in the mesh.

Oxy- and deoxy-hemoglobin, water, lipid, and scattering values were assigned to each region for each patient based on prior near-infrared measurements in normal and diseased breasts<sup>37,80-83</sup>. Within each tissue region, values for a given chromophore were kept constant. Using these optical properties, both FD and CW data was simulated and then reconstructed as described in Figure 5.

Figure 5: Software procedures used in simulation are shown as a flow chart. Lower left shows source and detector configurations for the FD (left) and CW (right) data for a given patient study on the breast mesh/volume<sup>84</sup>.



Simulations were performed with the Nirfast software package ([www.nirfast.org](http://www.nirfast.org))<sup>85</sup>. For the FD data, wavelengths were selected from 660-850 nm and intensity modulated at 100 MHz. In the CW case, ten wavelengths were used between 660-980 nm. They were selected based on the availability of laser diodes and detectors with sufficient sensitivities over this spectral band. Additionally, the absorption spectra of oxygenated and deoxygenated hemoglobin as well as water and lipids were considered and wavelengths near absorption peaks were preferentially selected whenever possible.

The source-detector configurations were different for the simulated FD and CW measurements. The FD data came from six sources above the breast (cranial side) and six detectors below (caudal side). This geometry minimized the number of channels while providing sufficient sensitivity to most of the breast tissue volume<sup>86</sup>. It also accommodated a wide range of breast sizes, including all eight of the simulated DBT cases studied here. Preliminary results from a four source and four detector geometry yielded errors as high as 35% in scattering estimation, compared to 8% for the six source and detector case investigated in detail in this study. The CW acquisition consisted of a two-dimensional array of sources and detectors, each spaced 13 mm apart. The number of sources and detectors varied across patients depending on breast size. Source and detector positions that did not come in direct contact with the breast were not included. All measurements were recorded in transmission geometry. In the FD case, amplitude data five orders of magnitude below the highest intensity recorded for a given wavelength were not used in order to simulate the expected noise floor for measurements from a photomultiplier tube. In the CW case, amplitude measurements three orders of magnitude below the highest recorded value for a given wavelength were not used in

order to represent the uncorrupted data due to shot noise and the limited signal dynamic range from a photodiode. Three percent (3%) Gaussian noise was also added to each simulated data set, as a maximum noise level expected. Coupling errors at tissue surfaces due to skin texture and color were not included in the simulations, in part because the CW data probes the entire breast volume from multiple surface locations, reducing the effects from any single source-detector pair.

### 2.1.1.2. Sample Patient Simulations

Simulations of the NIRST-DBT design using patient-specific tomographic images were performed, and representative images are shown in Figure 6 and Figure 7. In both cases, six wavelengths of FD data were generated and scattering amplitude and power were recovered for two regions, one for adipose and one for both fibroglandular and malignant tissue. These scattering values were then used in the reconstruction of the other chromophores based on the CW measurements.

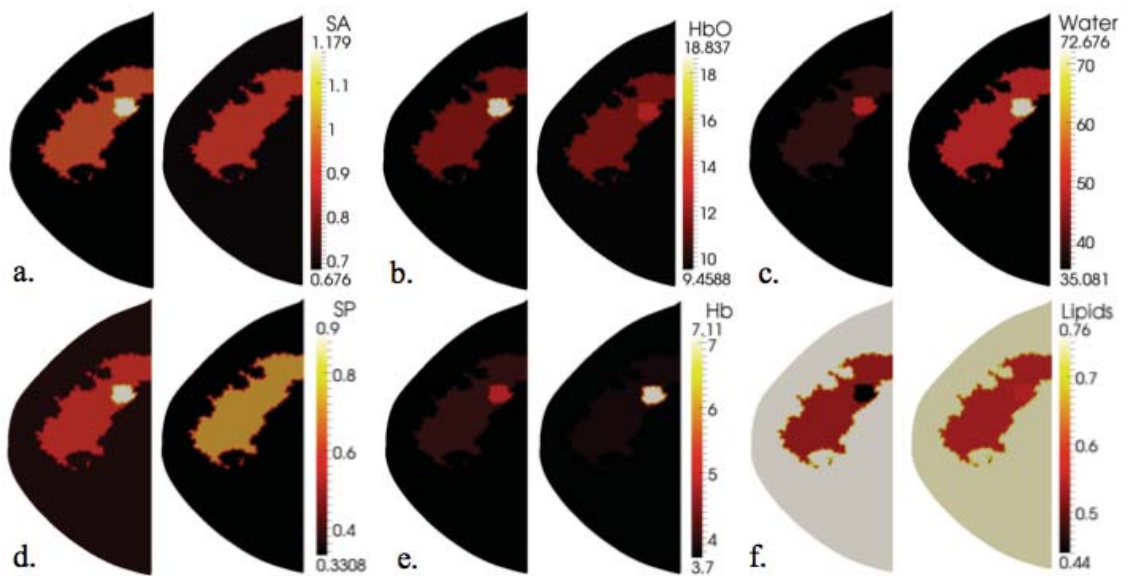


Figure 6: Illustrative example of a patient simulation with a malignant lesion is shown with (a) scattering amplitude, (b) oxy-hemoglobin ( $\mu\text{m}$ ), (c) water fraction (percent), (d) scattering power, (e) deoxy-hemoglobin ( $\mu\text{m}$ ), and (f) lipid content (percent). Exact (simulated) distributions are shown on the left while the corresponding recovered images are shown on the right for each quantity<sup>84</sup>.

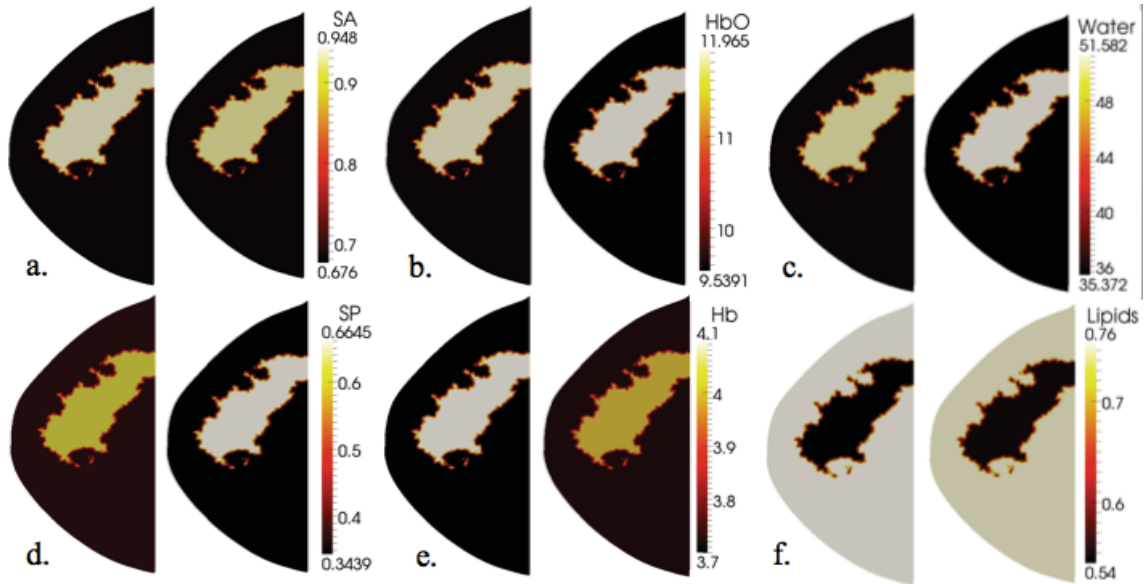


Figure 7: Illustrative example of a patient simulation with a benign lesion is shown, with (a) scattering amplitude, (b) oxy-hemoglobin ( $\mu\text{m}$ ), (c) water fraction (percent), (d) scattering power, (e) deoxy-hemoglobin ( $\mu\text{m}$ ), and (f) lipids content (percent). Exact (simulated) distributions are shown on the left while the corresponding recovered images are shown on the right for each quantity<sup>84</sup>.

The difference between Figure 6 and Figure 7 is the chromophore values assigned to the tumor region. In Figure 6, a malignancy was simulated with higher oxy- and deoxy-hemoglobin concentrations, water fraction, scattering amplitude, and power as well as lower adipose content than in the surrounding fat and fibroglandular regions.

Within the tumor, hemoglobin and deoxy-hemoglobin were recovered at 18.8 and 7.1  $\mu\text{M}$ , compared to 12.0 and 4.1  $\mu\text{M}$  in the fibroglandular region. In Figure 7, a benign mass was simulated. Here, the chromophore values were the same as those in the fibroglandular region. No enhancement occurred in the tumor region in the image formed from the synthetic system data.

#### *2.1.1.3. System Simulations*

Designing new multi-modal imaging systems typically presents tradeoffs, and prototype simulations can guide hardware selection and implementation. Minimizing the number of wavelengths as well as the number of sources and detectors in the FD imaging module decreases costs, complexity, and examination time in a multi-modality NIRST-DBT breast imaging platform. Simulations of NIRST data for eight subject-specific breast volumes based on DBT images highlighted differences in results from each system change.

Interestingly, no significant differences were found in HbT recovery between FD simulations performed with six versus three wavelengths of light. Comparing two region and single bulk tissue estimates of scattering had a large impact on the recovered HbT concentration. Mischaracterization of scattering led to errors in quantification of HbT.

These patient simulations have confirmed the importance of accurate scattering estimation for quantitative hemoglobin recovery, suggesting that accurate ( $\sim 10\%$  error) estimates of tissue scattering are important to the success of NIRST when combined with DBT. Based on the results shown, this can be achieved with a relatively modest number of wavelengths ( $\sim 3$ ) and signal channels ( $\sim 6$ ). Thus, successful NIRST-DBT imaging is

possible with a limited FD and robust CW data set. This conclusion has had a major impact on the design choices going forward with the NIRST system, where ultimately no FD channels were included in the first prototype, but whole breast scattering was measured independently with the diffuse optical spectroscopic imaging (DOSI) system, described later.

### **2.1.2. Development of a combined NIRST-DBT imaging system**

In building a system at Dartmouth, simulation results as well as system designs of other groups were carefully analyzed. A combined NIRST-DBT system at Massachusetts General Hospital has already been developed and used to image over 200 patients, as described in Zhang et al. and Fang et al.<sup>40,87-89</sup>. Early results are promising; a recent study showed significant differences in the optical properties of malignant and benign lesions. Different contrasts for HbT and scattering properties were obtained in each case, indicating that a multi-modal imaging system of this type might improve detection sensitivity and specificity over DBT alone<sup>87</sup>. At Dartmouth, we selected a different design for an integrated NIRST-DBT with the aim of improving tissue characterization with more spectral information. Four of the eight lasers emit light at over 830 nm, critical for accurate quantification of water and lipids. Additionally, the system has a flexible number and arrangement of sources and a greater number of detectors for more complete tissue analysis.

The DBT component is a Genesis Dimensions unit from Hologic. The NIRST instrumentation was developed at Dartmouth and is fully integrated with DBT, providing

sequentially-obtained completely co-registered NIRST and DBT data sets in less than one minute.

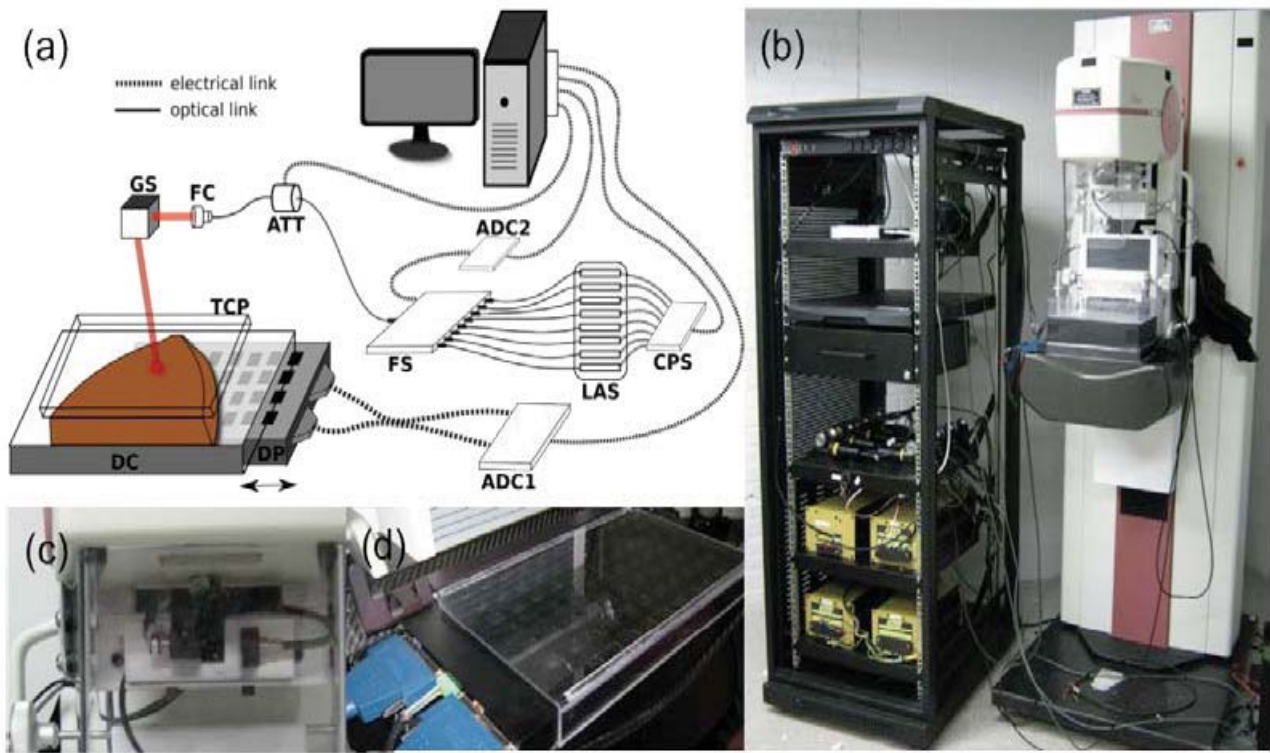


*Figure 8: (a) Schematic of the NIRST-DBT imaging system. (b) Photograph of the fully assembled NIRST-DBT system installed at the Dartmouth-Hitchcock Medical Center (DHMC). (c) Photograph of the 2-axis galvanometric scanning mirror assembly mounted adjacent to the X-ray emission port on the DBT scanner. The source unit allows arbitrary positioning and scanning of laser light beams onto the compressed breast surface without obstructing the X-ray field-of-view<sup>68</sup> (d) Photograph showing the silicon photodiode detector panel inserted into the custom designed cassette assembly to allow easy insertion and removal of the panel during sequential NIRST-DBT scans.*

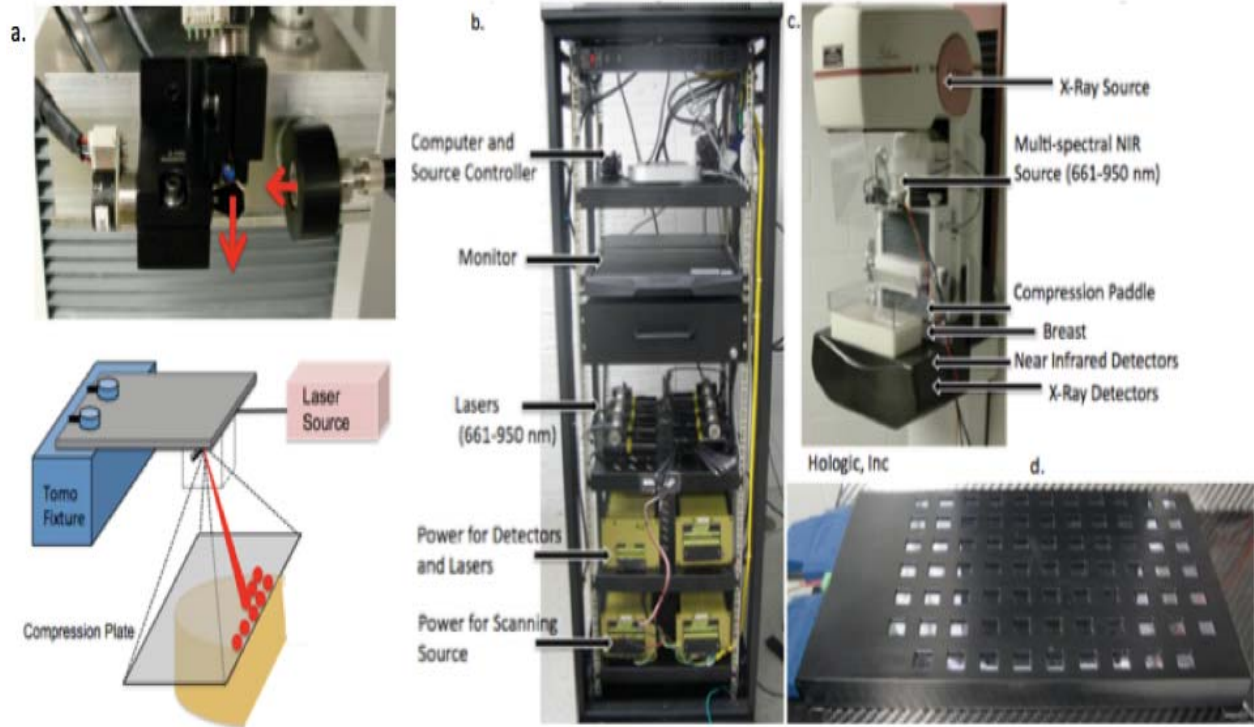


Figure 9: (a) Close up of the 2-axis galvanometric scanning mirror assembly mounted adjacent to the X-ray emission port on the DBT scanner; red arrows show how the light is reflected off mirrors and onto the tissue, depicted in the bottom schematic. (b) Photograph of the fully-assembled NIRST optical cart installed at the Dartmouth-Hitchcock Medical Center (DHMC). (c) Photograph showing the patient interface for the combined NIRST-DBT system (d) Photograph of NIRST detector panel without the cassette assembly.

### 2.1.3. Light Delivery

There are eight fiber coupled laser diode units (660, 785, 808, 830, 852, 905, 915 and 940 nm) selected for spectral characterization of oxy- and deoxy-hemoglobin, water and lipids. Each wavelength is sequentially applied to this tissue through a 9 x 1 piezoelectric fiber optic switch (FSM 9x1-200, OptoJena, MA) with a 200 micron

diameter output fiber. A software-controlled attenuator (DD-100 series, OzOptics, Canada) automatically attenuates the light output based on a single test measurement of the breast, which takes about ten seconds and is necessary due to the large variability in breast size and optical characteristics between patients. After collimation, a pair of galvanometric scanning mirrors (Cambridge Systems, MA) directs the light onto known locations on the tissue surface. These mirrors are attached to rails below and behind the X-ray source and do not interfere with the DBT imaging process. The spot diameter in the imaging plane is about 8 mm. This geometry offers arbitrary source location potential. For our phantom and breast imaging studies, we selected a pattern that roughly parallels the detector arrangement, specifically 77 measurements in 7 rows and 11 columns raster scanned across the tissue. The spacing between the sources varies between 1, 1.5, and 2 cm depending on breast size.

Co-registration of the optical scan with the DBT field is achieved by using the DBT compression paddle as a common frame of reference. The height of the compression paddle changes for every patient, so the scan angles of the mirror are adjusted in the control software via simple trigonometry calculations. This preserves the scan geometry at any given height of the compression paddle. The optical scan position accuracy was verified manually with a rectangular grid pattern printed on paper and placed in the compression paddle and is repeated after alterations to or movement of the light source.

#### **2.1.4. Light Collection**

The light is detected beneath the breast via a removable panel of 1 cm<sup>2</sup> active-area silicon photodiodes comprised of 75 individual detectors (S9270, Hamamatsu Corp., Japan) with built in amplifiers, shown in Figure 9 (d). An 80-channel analog-to-digital converter (ADC, USB-6255, National Instruments, TX) digitizes the 0-10 V signal output from the detectors through two small computer system interface cable attachments to the custom printed circuit board (PCB). The detectors and PCB are housed in a custom-made protective casing, shown in Figure 8 (d).

#### ***Integration of NIRST and DBT***

The NIRST light collection and delivery systems had to be attached to the DBT unit in a way that did not degrade the high quality of the DBT images. The light delivery system is affixed to the back side of the mammographic face shield, as shown in Figure 9(a). This is directly behind the X-ray source and attached to the highest possible position to limit the angular demands on the mirrors. At very thick breast heights (greater than 8.5 cm), there is a small delay in the movement of the mirrors at each position, adding an additional 30 seconds. No patient imaging to date has involved breasts so thick that the angular positions of the mirrors have been stretched beyond the limits.

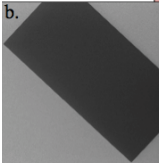
#### **2.1.5. Materials Characterization for NIRST-DBT Interface**

The light detectors are not transparent to X-rays and are located in between the DBT source and detector. Hence, the detector panel must be removed before DBT imaging can be performed. In order to maintain complete co-registration of DBT and NIRST data, the patient position must be the same in each case. Additionally, a layer of

material is needed to support the breast while under compression without excessive deformation or alteration of the X-ray or NIRST image quality. Several materials were studied to determine which would be most appropriate for the NIRST-DBT combined imaging system.

To develop the detector case, we analyzed seven different plastics along with a silica fiber plate and an NIR light-blocking material with openings over the detector locations. Comparisons of NIR light attenuation were performed with a resin phantom from Institut National D’Optique (INO)<sup>90</sup>. The phantom was placed directly on top of the detector panel during data acquisition, with each plastic material positioned between the phantom and the detector panel. Detector amplitudes from the five light source locations closest to the middle of the phantom and their nearest detectors were averaged across all wavelengths and compared for each plastic against the case without the material in place. For polycarbonate, several samples with different surface properties were examined. In addition, different materials were imaged with the DBT system to assess X-ray absorption. These studies were performed at 26 kVp and 35 mAs. Average pixel intensities from a region of interest for each material were compared to the background to calculate the linear attenuation coefficient.

a.	X-Ray Image Quality	NIR Transmission	Tensile Strength	Light Channeling	Cost
Fiber Plate	-	+	-	+	-
Clear Plastic	+	+	+	-	+
Black with Clear Plastic Windows	-	+	+	++	+
Carbon Fiber with Windows	-	++	++	++	+



b.



c.



d.

*Figure 10: (a) Attributes of possible detector case designs for the detector panel. (b) Single X-ray frame from a DBT scan showing attenuation from a thin fiber plate. (c) Depiction of a detector case model with windows over the locations of the detectors. (d) X-ray frame from DBT scan indicating attenuation of a panel with windows<sup>91</sup>.*

Figure 10 evaluates several potential detector case design options that would enable both DBT and NIRST imaging under the constraints imposed by this dual-modality system. Initial feasibility studies with DBT indicated a high level of X-ray attenuation with the silica fiber plates, and visible artifacts were generated by the light-blocking model with openings over the individual detector locations as shown in Figure 10 (b-d). Thus, a detector case constructed from fiber plates, a single material with openings, or a composite of two different types of plastics would all affect the DBT image.

The most important qualities in the optimal detector case include NIR attenuation, tensile strength, and flexural modulus. The tensile strength and flexural modulus of the various materials were found in the literature<sup>92</sup>, while the NIR and X-ray attenuation coefficients were experimentally derived (a picture of the materials is shown in Figure

11, and

	Tensile Strength (MPa)	Flexural Modulus (GPa)	NIR Attenuation Coefficient (cm <sup>-1</sup> )	X-Ray Attenuation Coefficient (cm <sup>-1</sup> )
Polycarbonate	62	2.4	0.66	0.35
Polypropylene	35	1.4	0.91	0.29
Acrylic	60	3.0	1.08	0.68
High Density Polyethylene	35	0.3	1.56	0.32
Acetal	61	2.5	2.18	0.89
Acetal Resin	69	2.8	2.00	1.05
Polytetrafluoroethylene	25	0.6	3.31	2.26

Table 2 exhibits comparisons). Polycarbonate plastic exhibited the highest level of NIR light penetration, second-lowest X-ray attenuation, and sufficiently high tensile strength to withstand full breast compression during a DBT examination.



*Figure 11: Photograph of the plastic materials tested in this study. Top row (from left to right) is polycarbonate, polypropylene, acrylic, high-density polyethylene, and*

polycarbonate with a diffusive sticker. Bottom row (from left to right) is acetal, acetal resin, polytetrafluoroethylene and sandblasted polycarbonate<sup>91</sup>.

	Tensile Strength (MPa)	Flexural Modulus (GPa)	NIR Attenuation Coefficient (cm <sup>-1</sup> )	X-Ray Attenuation Coefficient (cm <sup>-1</sup> )
Polycarbonate	62	2.4	0.66	0.35
Polypropylene	35	1.4	0.91	0.29
Acrylic	60	3.0	1.08	0.68
High Density Polyethylene	35	0.3	1.56	0.32
Acetal	61	2.5	2.18	0.89
Acetal Resin	69	2.8	2.00	1.05
Polytetrafluoroethylene	25	0.6	3.31	2.26

Table 2: Material qualities of plastics tested for detector case<sup>91,92</sup>

Polycarbonate appeared to be an ideal material. A prototype detector case was created from clear 1/8” polycarbonate integrated into the carbon fiber imaging platform as shown in Figure 12(a, b). Unfortunately, significant artifacts were present due to light channeling within the plastic (see homogeneous phantom data represented by blue dots in Figure 13(d)). Alternatives involving physical alteration of the plastic surface through sandblasting or addition of a thin superficial diffusive material (sticker) did not eliminate

the channeling effects. Placement of materials to block stray light entering from outside the phantom (or tissue) was needed.

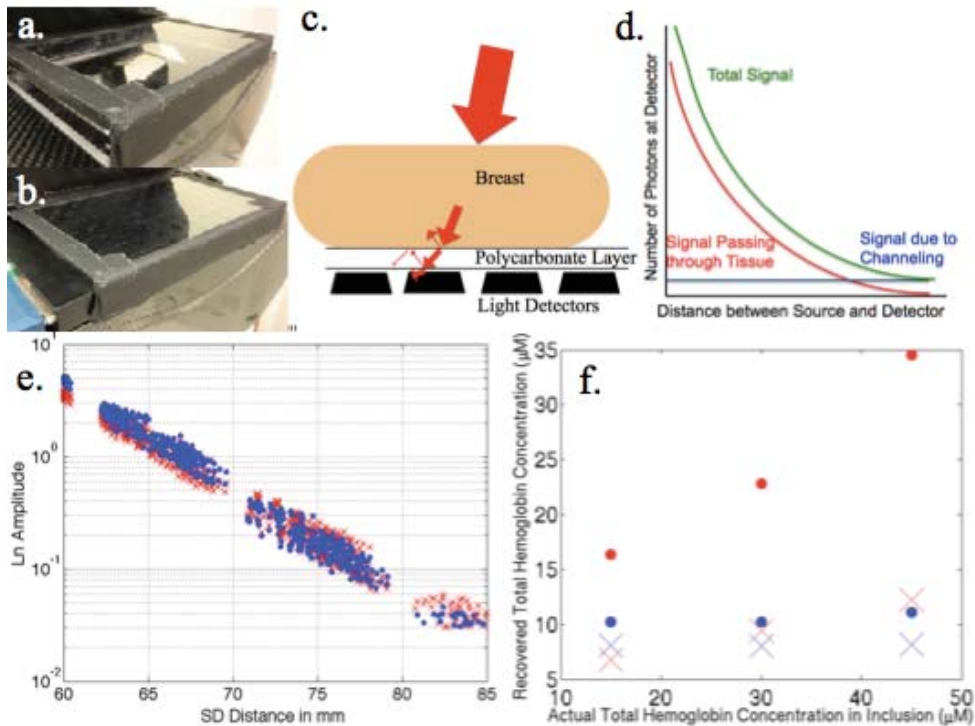


Figure 12: (a) Photograph of the detector case developed for the combined NIRST-DBT system. (b) Detector case with the detector panel inserted. (c) Depiction of light channeling in the detector case. (d) Graph illustrating the effects of light channeling on the acquired NIRST data. (e) Raw 660 nm data acquired from a homogeneous resin phantom when placed directly on top of the detectors (in blue) relative to when imaged with the detector enclosed in the case (red). (f) Agar inclusion phantoms with increasing hemoglobin contrast (background in blue, inclusion in red) when imaged on a thin plastic film above the detectors (dots) and when imaged on the detector case (Xs)<sup>91</sup>.

The data obtained from a homogeneous resin phantom in Figure 12(e) has a slight slope difference between the measurements acquired with and without the polycarbonate

detector panel in place. Reconstructed absorption coefficients at a wavelength with known scattering from these data resulted in a decrease in absorption of nearly 27% – dropping the value to  $0.0059 \text{ mm}^{-1}$  from  $0.0081 \text{ mm}^{-1}$  (which are 59% and 81% of the actual value, respectively) – when data was recorded through the detector case. Similar results were found in the more complicated inclusion phantom series shown in Figure 12(f). Reconstructed background and inclusion hemoglobin levels were much lower when the detector case was in place. The average total hemoglobin recovery for the background region was 70% of the expected value without the detector case, but only 54% with it in place, a 23% decrease due to the detector case. Contrast in the inclusion regions showed linearity in both instances with  $R^2$  values of 1.00 and 0.97, respectively without and with the case, respectively. Again, an average of 87% of the actual value was observed in the inclusion total hemoglobin without the detector cover (recovery was only 37% with it).

These results consistently undervalued absorption, likely due to light channeling within the detector cover. Differences in indices of refraction at the polycarbonate-tissue boundary caused approximately 9% of the light to be reflected back into the tissue<sup>93,94</sup>. Similar reflections can also occur at the polycarbonate-air boundary, leading to light channeling during which some photons travel far from where they exited the tissue as illustrated in Figure 12(c). This effect alters the signal recorded at the detectors, most significantly at farther source-detector distances where the light signal has been most attenuated as indicated in Figure 12(d). This changes the slope of the data, and hence, the absorption coefficient estimate. While the light channeling is similar for all source-detector positions, it most strongly influences data at far source-detector distances

because the number of photons traveling through the tissue and reaching these locations is relatively low. The effect decreases the magnitude of the overall slope of the linear relationship between logarithm of the detected signal and source-detector distance, as a larger than expected signal is measured at far source-detector distances leading to lower than expected absorption coefficient estimates in both the single wavelength resin phantom as well as the more complicated agar inclusion phantoms with variable contrast, as seen in Figure 12(e, f).

Specifically, the addition of the detector case led to a drop of 27% in the absorption coefficient estimate for a single wavelength in the resin phantom, and a 23% drop in total hemoglobin recovered in the background of the inclusion phantom, indicating that the accuracy of absorption quantification is significantly reduced when the case is present. Because most imaging systems based on diffuse light are unable to recover total hemoglobin values fully<sup>57</sup>, contrast between regions is often examined as a measure of image quality. Implementing calibration methods with homogenous phantom data can increase the overall accuracy of absorption property recovery<sup>51</sup>, as the decrease in absorption will affect all phantom and patient images similarly so although recovery values may be slightly lower with the polycarbonate plate than the true values, intra and inter patient comparisons will not be significantly affected.

### 2.1.6. Stray Light

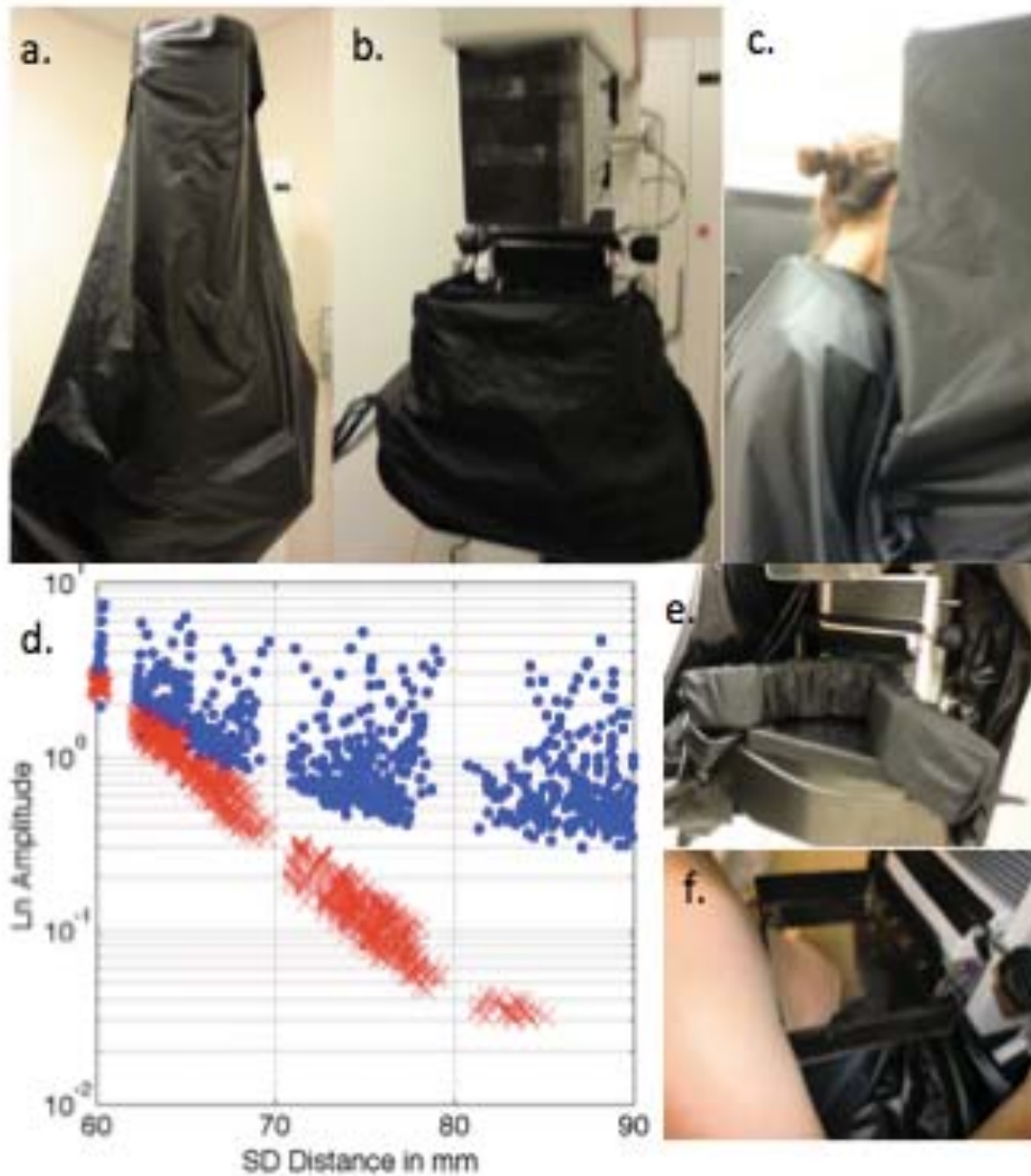


Figure 13: Light blocking materials used in patient exams. (a) Light blocking fabric draped over the DBT unit. (b) Light blocking skirt surrounding the breast compression paddle during phantom experiments. (c) Patient in position for NIRST-DBT exam (d) Raw data acquired from a homogeneous phantom imaged through the detector case with

*(in red) and without (in blue) the light blocking precautions. (e) Light blocking breast shroud used during patient exams (f) Patient positioning with the breast shroud.*

After the initial challenge of finding an acceptable material for the detector case which did not compromise DBT image quality, the most important task was to block any stray light in the imaging field. Light hitting the detector cover directly without traveling through the tissue is many orders of magnitude stronger than light attenuated by the tissue; hence, the blocking of this light was of utmost importance and critical to obtaining accurate measurements in the breast. Direct light can reflect internally within the plastic cover before being transmitted to a detector far from the light source and producing a falsely high signal, thereby increasing the amount of channeled light impinging on the detectors.

Unique challenges need to be overcome to eliminate stray light in a non-fiber-based NIRST imaging system. In the mirror-scanning source, most of the light reflects off the top compression paddle and disperses throughout the imaging cavity. As the DBT platform was not originally designed for optical imaging, many metallic and reflective surfaces exist that must be covered with blackout fabric and tape to reduce stray light propagation. These efforts are necessary because estimation of tissue optical properties relies on measurements at long source-detector distances, where channeling plays a large role.

The methods employed during patient exams are shown in Figure 13. They include two layers of blackout material, compressible foam shrouds of variable heights (depending on breast thickness) situated next to the breast, and blackout paper and tape covering surfaces of the DBT unit. These materials are necessary for successful patient

imaging but can make it difficult for breast positioning during the combined NIRST-DBT exam by limiting space available for technologists to adjust the tissue.

### System Calibration

In the process of building a new imaging system, calibration steps are necessary to understand and characterize sources of variability. Ideally, the light sources and detectors would consistently emit or detect the same quantity of light and all sources and detectors would behave identically. Of course, this is not the case, so experimentally-derived calibration factors were implemented when necessary to minimize differences between light sources and detectors.

#### 2.1.7. Source Calibration

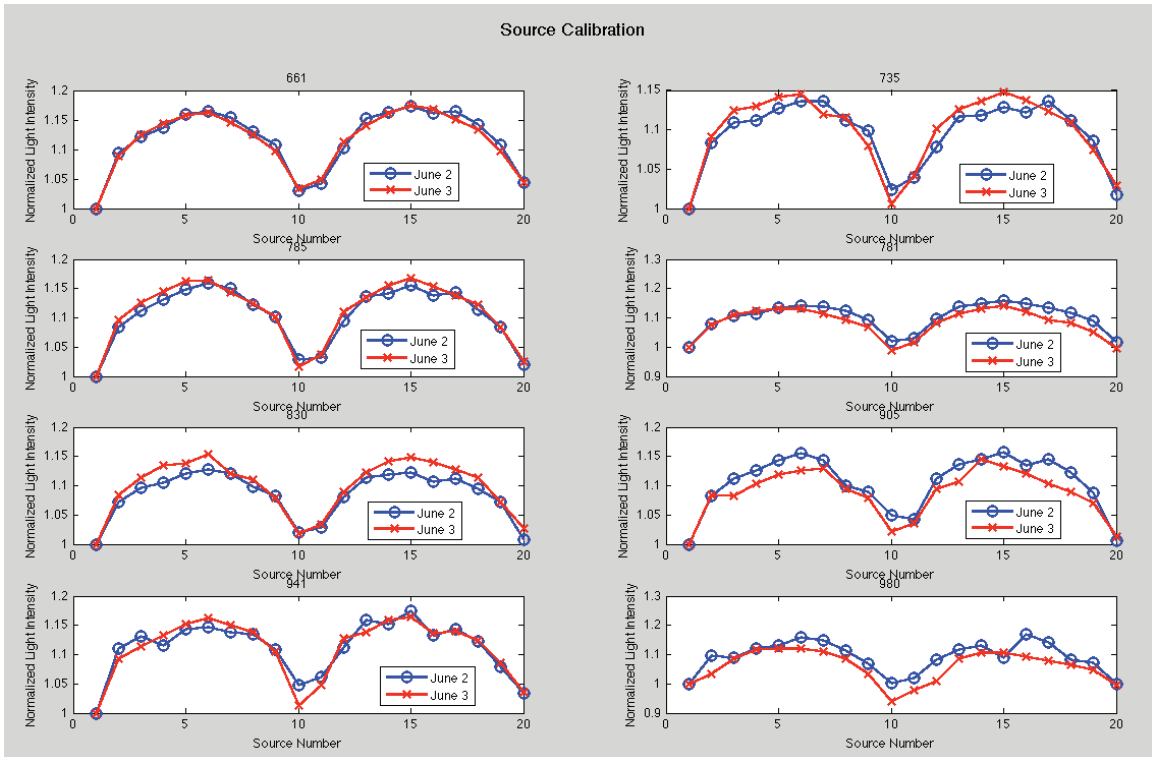


*Figure 14: Each graph shows a single wavelength of light coupled to an optical phantom and measured at 20 different detectors over two days. Significant variation in detector sensitivity is noted, but source strength measured on two different occasions showed variations ranging from less than 1% (for 660 nm) to nearly 5% (for 905 and 940 nm).*

The eight fiber coupled laser diode units were selected for the NIRST-DBT with careful consideration for their stability over time. To test this stability directly, a cylindrical piece of phantom was drilled to fit into a light-tight tube, opened on one side with square notches to fit snugly with the detector panel, and coupled to a fiber directly from the laser on the other side. This was centered over 20 different light detectors, and measurements were taken on two days as shown in Figure 14. Detectors had not been calibrated at this stage and showed inter-photodiode differences of up to 17% between two individual measurements. Source variability over the two days was much lower, less than 1% for some diodes, but still nearly 5% for the worst-performing cases (generally the higher wavelengths). Comparisons across the two days did not show a consistent trend for a given wavelength; some measurements were higher on day two, while others were lower. These differences are likely due to spontaneous fluctuations in current and temperature in the laser diodes. As this variation was much smaller than the inter-detector variation, no further efforts to characterize the source were made.

#### **2.1.8. Detector Calibration**

Differences in sensitivities between detectors must be accounted for to ensure the most accurate data. This was achieved using a uniform field of light supplied through a specifically-designed calibration puck. It was comprised of resin with similar optical

properties to tissue, with a square notch that fit precisely into the hole in the detector panel protective case as mentioned previously in the source calibration section. A voltage was measured for each of the 75 photodiodes to characterize the differences in sensitivity.

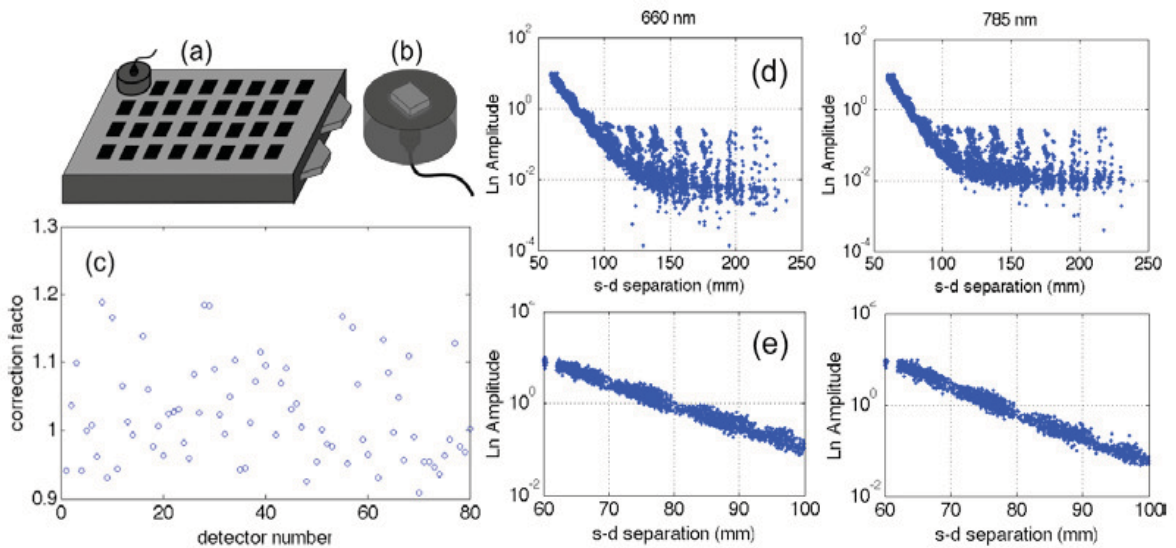


Figure 15: (a) Schematic showing the calibration puck positioned over an individual detector element in the detector panel. (b) Schematic drawing of the calibration puck showing a square notch on top that allows repeatable positioning over each detector element. (c) Correction factor for each of the 75 detector elements showing variations in individual detector response (certain detector channel numbers are unused). (d) Raw tomographic projection data plotted as a function of source-detector separation acquired from a homogeneous test phantom at 660 nm and 785 nm wavelengths. (e) Processed data showing the removal of known signal artifacts and noisy data<sup>68</sup>.

### 2.1.9. Attenuator Calibration

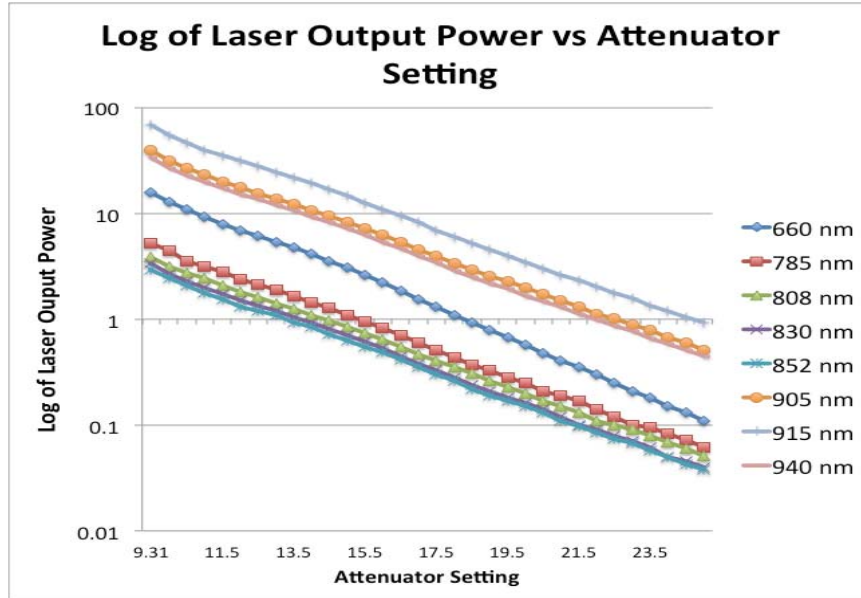


Figure 16: Graph of attenuator calibration showing the log of the laser's output power vs. attenuator setting in the LABVIEW control software for all the wavelengths of the system.

Due to the limited dynamic range of the photodiode detectors, it is important to adjust the incident light signals on the tissue so that the detected light will fall within the useful dynamic range, which is between the noise floor and saturation levels of the detectors. This has been accomplished through the inclusion of an attenuator between the fiber switch and the galvo scanning mirrors. Characterization of the light signals at each possible attenuator setting is needed to compare measurements of the calibration phantom and the patient data, which often require different signal strengths for maximal data collection. This was accomplished by measuring the laser output power via a power meter for all wavelengths for a wide range of attenuator settings, spanning the anticipated needs for all breast sizes and densities. Attenuator settings are determined and saved for

each patient and phantom and data set and are then adjusted using the calibration chart shown in Figure 16.

### 2.1.10. Source/Detector Localization

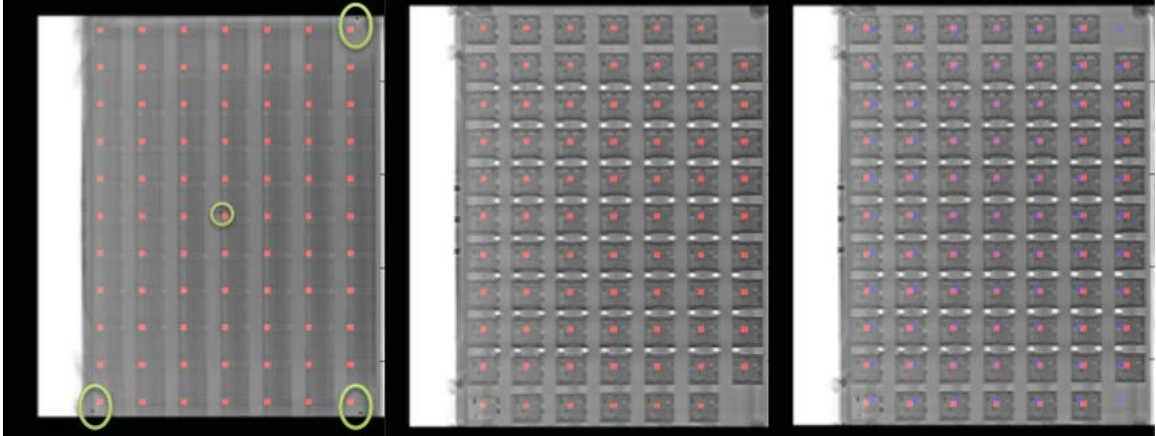


Figure 17: (a) DBT processed image slice from the source plane with several metal BB's located at the four corner source positions and central position, all shown in a darker color, with green circles highlighting the source and corresponding BB location. The red pixels indicate the locations of the point sources applied to the mesh for the NIRST reconstructions and the dark points are the BB locations. (b) DBT-processed image slice from the plane of the detector panel. The red pixels indicate the locations of the point detectors applied to the mesh for the NIRST reconstructions. (c) DBT-processed image slice from the plane including the photodiode detectors with red pixels indicating the locations of point detectors and blue pixels indicating the location of point sources.

With a large number of sources and detectors in a non-contact geometry, determining the exact location of each was particularly challenging. This was especially true for the light source positioning, which can vary from patient to patient. Initial positioning was determined using a 2cm x 2cm paper grid cut to fit inside the

compression paddle. Mirror coordinates for several source positions indicated by the chart were determined at a range of compression paddle heights, leading to an experimentally-derived formula to set the mirror coordinates based on the anticipated real-space coordinates on the surface of the breast. This was incorporated into the LABVIEW software.

Spatial prior information for the breast is derived from DBT images, so it is important to ensure that source and detector locations correspond with the DBT images. As laser light does not produce a detectable X-ray signal, an alternative, more complicated process is needed to localize the source positions. Source positions are placed on the breast mesh using real world coordinates. Confirmation of the sources was performed periodically to ensure that each position was spaced 2 cm apart and located as expected using a paper chart placed in the compression paddle. A single comparison between the most central source and detector assisted in placement of the sources relative to the detectors, along with the known real-space coordinates during the tissue modeling process. However, this was a multi-step process and could easily lead to errors in source placement of up to half a centimeter.

An alternative method for source placement ensures more accuracy via a similar method for the light detectors. Using the experimentally-derived formula for source positioning, light is shown at the four extreme corners for the largest scan pattern, and a metal BB is placed at each position inside the compression paddle. The central source was located with a metal BB as well. The processed DBT slice corresponding to the location of the compression paddle is used to assess the localization of the source positions. This is shown in Figure 17(b), with the sources shown as red pixels and the

four visible dark spots showing the corresponding BBs (one BB in the top left did not reconstruct, presumably due to its location on the edge of the tissue). The dark spot and corresponding source position are circled in green. The source placement does not completely correlate with the source locations as indicated by the BBs; this may be due to slightly inaccurate pixel spacing in the DBT images, and/or inaccuracies in the mirror scanning formula resulting in source offsets of a few millimeters.

For the detector panel, the geometry is fixed for all exams. To determine the detector locations, a DBT scan of the detector panel is obtained and the processed slice corresponding to the height of the detectors is used to set the detector locations as points in the center of each detector; this process is shown in Figure 17(b).

To better understand the relationship of the source positions to the detectors, the source positions were plotted on the DBT slice that shows the detectors the most clearly, as seen in Figure 17(c). As desired the sources and detectors are nearly on top of one another for the largest pixel spacing, with the detectors in red and the sources in blue. This is an intuitive geometry for phantom imaging and troubleshooting.

### ***Conclusions***

This chapter focused on the instrumentation of the NIRST-DBT imaging system, including considerations for system design and simulations of a proposed imaging platform followed by detailed descriptions of the actual hardware components added and the interface between NIRST and DBT imaging, and lastly characterizing the system through calibration. The rationale behind a CW-based imaging system with limited FD data was discussed and simulated, showing that it would be possible to obtain accurate

results for patient chromophore recovery and separation of benign and malignant lesions. The system that was built performs CW imaging exclusively, and more details on this decision will be discussed in Chapter 8.

There are several unique design challenges posed by the NIRST-DBT system. Complete co-registration of the images necessitates a detector panel cover that permits transmission of both NIR light and X-rays. Testing of many materials showed polycarbonate to be the best choice, but still was only feasible for imaging through in this geometry with extensive light blocking around the breast and detector shielding mechanisms to avoid stray light at the detectors.

As a new imaging system, many calibration tests were necessary to understand sources of data variation, specifically examination of the laser diodes for stability, light detectors for differences in sensitivity, and the effects of the attenuator on output power. Additionally, the system was designed with an easy-to-use non-contact geometry for light sources and detectors, which presented some new challenges in source and detector localization. This was accomplished through a combination of real-space calibration of the scanning mirrors and X-ray imaging of the detector panel and source position markers.

## Chapter 3: Image Formation Methods

### *Image Formation*

Optical imaging involves use of either visible wavelengths (400-650 nm) or near infrared (NIR) wavelengths (650-1000 nm) of light to image or measure transmittance or reflectance in order to characterize the absorption and scattering properties of tissue. NIR light is especially well suited to tissue imaging due to its lower level of absorption when compared to visible light, as shown in Figure 18.

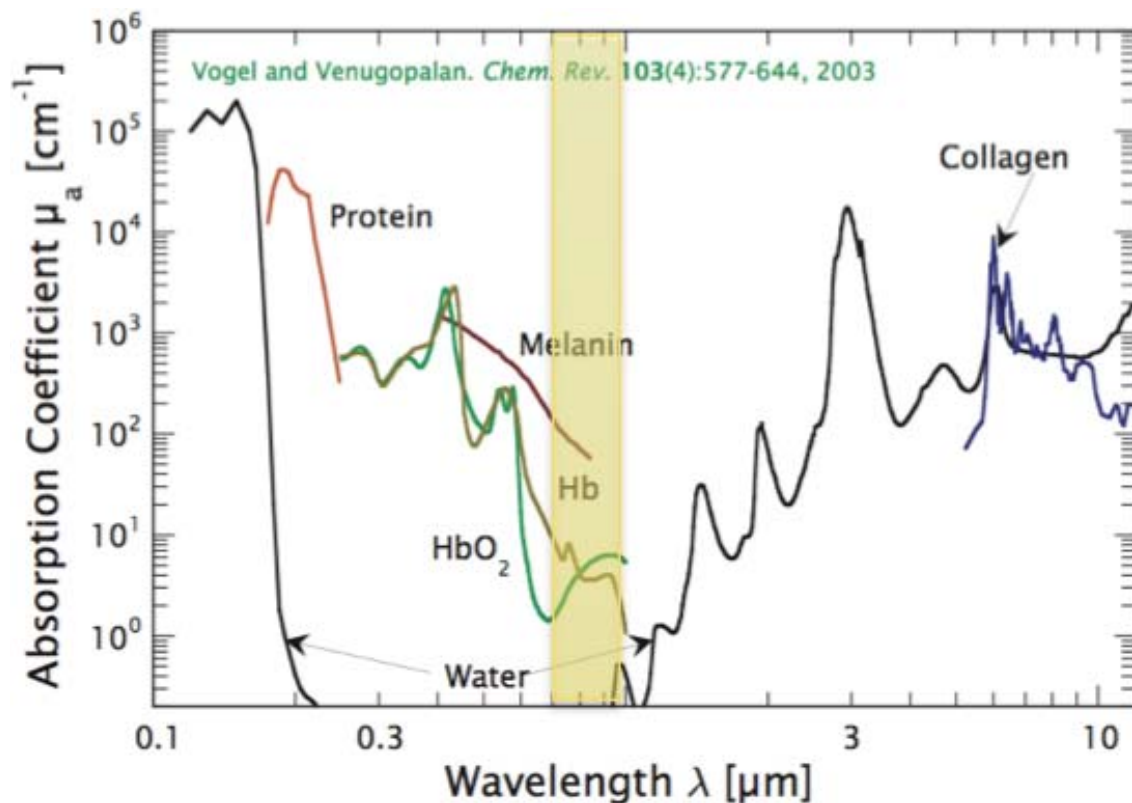


Figure 18: Absorption coefficient of different components of tissues at different wavelengths. The NIR window (in yellow) shows lower light absorption by the major tissue chromophores, specifically, water and hemoglobin, than other forms of non-ionizing radiation<sup>95</sup>.

Hence, NIR light can be used for imaging through thicker tissue such as the breast because total attenuation is reduced, but absorption is sufficiently high to prevent full body transmission imaging. NIR photons also possess less energy than X-ray photons and which is insufficient to break molecular bonds, and so the use of NIR in imaging has the benefit of being non-ionizing, and thus poses less of a health risk to patients and medical personnel relative to traditional X-rays. After obtaining data from an NIR imaging system, image reconstruction methods are important for mapping tissue functional parameters. The movement of light through tissue is more complex than that of X-rays. X-rays are weakly scattered; they pass nearly straight through tissue, and collimators can ensure that the measured attenuation is almost independent of scatter. Scattering is the dominant effect with optical photons and occurs 100 times more frequently than absorption. Individual photons follow a torturous path through tissue. On account of pervasive scattering process in NIR imaging, it is more complicated to model the transmission, propagation, and tissue interactions when compared to X-ray imaging. This chapter focuses on the physics of NIR light transport in tissue, methods for image reconstruction including finite element analysis, inclusion of DBT spatial prior information, and X-ray image segmentation techniques.

### **3.1.1. Optical Properties**

Innate tissue properties affect how light is propagated, and changes in these properties can provide important information about tissue metabolic status. Absorption and scattering are two such properties, and they are described by the absorption and scattering coefficients respectively ( $\mu_a$  and  $\mu_s$ ). These coefficients describe the

likelihood of a photon undergoing an absorption or scattering event over a certain depth of tissue. The inverse of the absorption or scattering coefficient is the mean free path, which describes the average distance that a photon will travel without experiencing an absorption or scattering event, typically around 1 mm in tissue. In terms of scattering, a photon can scatter in one of many directions; however, most photons are scattered in the forward direction within tissue. The reduced scattering coefficient ( $\mu_{s'}$ ) is typically used to incorporate some information on photon directionality after a collision. The reduced scattering coefficient,  $\mu_{s'} = \mu_s(1 - g)$ , where  $g$  is the average cosine of the scattering angle, is around 0.9 in tissue. This pervasive scattering severely limits the spatial resolution of stand-alone optical imaging.

Although the likelihood of an absorption event in tissue is two orders of magnitude lower than a scattering event, it can significantly attenuate the detected signal and is essential in determining the chromophore composition of the tissue. The absorption coefficient  $\mu_a$  represents the inverse of the mean free distance for exponential attenuation, precluding scattering. Tissue absorption and scattering coefficients vary as a function of wavelength; measurements at multiple wavelengths can be used to gain additional information about tissue properties.

Each of the major absorbers has a characteristic molar extinction spectrum in the NIR, which is its absorption coefficient per unit concentration at each wavelength. If measurements of the absorption coefficient are recorded at different wavelengths, concentrations of absorbers such as hemoglobin, water, beta-carotene, bilirubin, and lipids can be determined based on the known extinction coefficients for each contributor

at the different wavelengths. At each wavelength, these individual chromophores contribute linearly to the total absorption coefficient, weighted by their respective concentrations and molar extinction coefficients.

Clinical implementation of diffuse optical spectroscopy takes advantage of tissue optical properties to estimate absorption and scatter from transmission measurements at different wavelengths, ultimately describing physiological properties in tissue through the concentration of these chromophores.

### **3.1.2. Diffusion Modeling and Other Methods**

Modeling is essential to account for scatter and correctly quantify the non-linear relationship between the measured light signals and the optical properties of the traversed tissue.

Due to the pervasive scattering, light transport modeling can be simplified using the diffusion approximations to the radiative transfer equation (RTE). The RTE is highly complex and can be simplified with a few assumptions. They are:

1. Optical radiance is only linearly anisotropic; all higher-order terms are ignored.
2. The rate of change of the flux is much lower than the collision frequency.

The latter assumption hold true for NIR imaging of tissue because scattering occurs much more frequently than absorption. The former assumption holds true for regions far from light sources and tissue boundaries. In the case of breast imaging, most of the tissue is greater than one scattering distance from the sources and boundaries and

thus satisfies this assumption. The simplification that results is known as the diffusion approximation and is represented mathematically as follows:

$$\frac{1}{c} \frac{\delta \Phi(r,t)}{\delta t} - \nabla \cdot D \nabla \Phi(r,t) = -\mu_a \Phi(r,t) + S(r,t) \quad 1$$

which describes the fluence of light,  $\Phi$ , and where  $D = \frac{1}{3(\mu_a + \mu_s')}$ , is the diffusion

coefficient at a time,  $t$ , at a certain position,  $r$ , in tissue due to a source,  $S$ . The four terms in the equation represent changes in flux, diffusion, loss due to absorption, and gain due to a light source. A complete derivation can be found in the literature.<sup>96</sup> The diffusion approximation is not valid near boundaries and sources, but this region is very small compared to the total in breast imaging.<sup>96</sup>

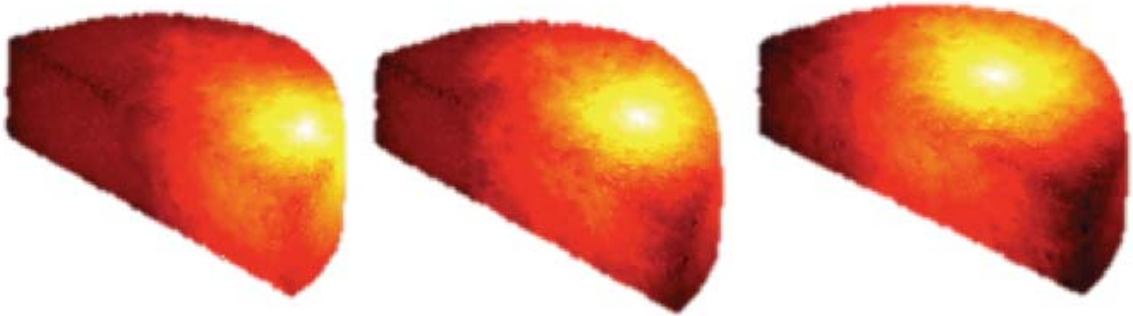


*Figure 19: Fluence maps for three different source locations on a compressed breast.*

In addition to modeling the light as it travels through the tissue, it is necessary to model whether the light is reflected back inside or exits at a tissue interface. This is accomplished through the use of appropriate boundary conditions.

Light reaching a tissue boundary can either leave the domain or be reflected back into the domain at the air-tissue interface. This is a type III boundary condition where

photons at the edge can leave but do not return<sup>97,98</sup>. The probability of a photon leaving is equal to the flux in that direction weighted by a factor that accounts for the internal reflection off of the boundary back into the medium. This is described by the equation

$$\Phi(\xi, \omega) + 2A\hat{n} \cdot \kappa(\xi)\nabla\Phi(\xi, \omega) = 0 \quad 2$$

where  $\xi$  is a point on the boundary and  $\hat{n}$  is a vector pointing outwards, normal to the surface.  $A$  is the probability of internal reflection at point  $\xi$  determined from Fresnel's law,

$$A = \frac{2/(1-R_0) - 1 + |\cos\theta_c|^3}{1 - |\cos\theta_c|^2} \quad 3$$

where  $\theta_c$  is the angle at which internal reflection occurs and  $R_0 = (n/n_a - 1)^2 / (n/n_a + 1)^2$ . Typically,  $n_a$  is assumed to be the index of refraction of free space, equal to 1.<sup>99</sup>

Analytic solutions to the RTE are available<sup>100</sup>, and can be easy to implement in a computationally inexpensive way, however only for simple geometries such as spheres and semi-infinite domains. Hence, they are impractical for many clinical applications. Monte Carlo methods are another class of solutions to the RTE. In Monte Carlo, individual photons are simulated stochastically through the tissue until they are absorbed or exit an external tissue boundary<sup>101,102</sup>. This method is highly accurate for all aspects of the imaging domain of any arbitrarily-designed shape, provided enough photons are simulated; however, it requires a lot of time and computational resources<sup>61</sup>. It is most useful in examining cases with short source detector distances and for validation of other methods. Finite element modeling (FEM) is another alternative. It can be used for complicated tissue shapes and is less computationally demanding than Monte Carlo

methods. On account of these advantages, FEM is currently the gold standard for modeling light propagation for NIR systems<sup>85</sup>.

### 3.1.3. Finite Element Modeling

FEM is an ideal modeling technique for optical breast imaging because of its reasonable computation time and complexity, and its ability to preserve both breast shape and internal structures with accurate results for most aspects of the tissue volume. It can be used to solve the diffusion approximation at discrete points across the tissue domain. These points are known as nodes and are interconnected to form a surface representative of the breast or other imaged area. The tissue fluence calculated at each node is linearly interpolated to create a smooth solution over the tissue. In FEM, the imaging domain is discretized into a two-dimensional grid or three-dimensional mesh, as shown in Figure 20.



*Figure 20: A volumetric breast mesh created from a stack of DBT images. The left side shows the nodes, connected to form tetrahedral elements. The right side shows a slice through the mesh, providing easy visualization of the preservation of spatial information about fibroglandular and tumor tissue structures.*

The nodes are mathematically linked to neighboring nodes, forming an element. In 2D, these elements are typically square or triangular, while they are tetrahedral or

cubic in 3D cases. Tetrahedral meshes are used in the NIRST-DBT imaging case to model the irregularly shaped breast tissues. Extensive analysis of finite element modeling can be found in the literature<sup>103,104</sup>. Discretization of the diffuse equation onto the finite elements necessitates a weighting function at each node, leading to the following equation.

$$\langle -\nabla \cdot D \nabla \Phi \phi_i \rangle + \left\langle \left( \mu_a + \frac{i\omega}{c} \right) \Phi \phi_i \right\rangle = \langle S \phi_i \rangle \quad 4$$

$\langle x \rangle$  refers to the integration over the solution domain.  $\phi_i$  is the linear weighting function at the  $i^{\text{th}}$  node ( $\phi_i = \sum_{j=1}^N \Phi_j \phi_j$ ) and is solved numerically along with the fluence.

The number of nodes included in a mesh can vary but generally, the more nodes, the more accurate the solution will be as the solution is calculated for more points within the fixed volume. However, increasing the number of nodes also increases the computational costs. The mesh can be made finer by increasing the number of nodes and decreasing the average space between nodes. Simulation studies of compressed DBT image stacks show that 30,000 node meshes with CW data obtain the same chromophore recovery as 80,000 node meshes with significantly lower computation time. In this thesis, reconstructions were performed in 3D using meshes between 30,000 and 45,000 nodes, corresponding to desired node spacing between 2 and 3 mm for the meshing software, depending on breast volume and presence or absence of a tumor. The average breast volume examined was 58,000 mm<sup>3</sup>, for a typical mesh of 35,000 nodes, and 200,000 elements, the volume of each element would be roughly 0.25mm<sup>3</sup> with each node

covering less than  $1.7 \text{ mm}^3$ , or 1.2mm in each dimension, slightly less than the average distance between scattering events of 1.3mm.

### ***Image Reconstruction***

#### **3.1.4. Forward Problem**

Simulation of light fluence at external boundaries is necessary for accurate modeling of light in tissues of known optical properties. This is known as the forward problem and, as previously discussed, uses FEM to solve the diffusion approximation on the discretized mesh domain. A smooth solution for the entire breast tissue domain included in the mesh is calculated through piecewise linear basis functions.

In the forward problem, the optical properties of the domain are considered known quantities. Light is emitted from sources on the surface of the tissue, and absorption and scattering are simulated through the volume according to the diffusion equation, providing results for the boundary data at the light detectors. The forward problem alone can be useful to compare expected data with actual data from a new NIR system when actual properties are known, for example, in the case of optical phantoms. However, in many cases, particularly human imaging, the actual optical properties are impossible to know a priori. In these cases, the forward model is an important component of image reconstruction, allowing for comparison of expected and actual data for an estimated set of optical properties.

#### **3.1.5. Inverse Problem**

In clinical implementation, NIRST is carried out with measurements recorded at detectors external to the tissue volume of interest. Using measurements recorded at

detectors near the tissue boundaries,  $\mu_a$  and  $\mu_s$ , can be estimated from this data at every node in the mesh by solving the inverse problem. This is challenging because it is non-linear, ill-conditioned, and underdetermined. It is underdetermined because there are many more unknowns (the tissue properties at each location) than there are knowns (detector measurements). In an ill-posed problem, small changes in the signal or noise can have large effects on the solution due to large variations in magnitude along the normalized diagonal of the inversion matrix. The general solution scheme involves an initial educated guess about the optical properties of the tissue, typically coming from a calibration procedure involving a phantom of known optical properties. Using these estimates, the forward problem is solved on an FEM mesh and compared to the experimentally measured data. Differences between the model and the data update the approximation of the optical properties based on the sensitivity of the detector measurements to the internal optical properties. This sensitivity matrix is known as the Jacobian,  $J$ , and is structured as:

$$J = \begin{bmatrix} \frac{d \ln I_1}{d \mu_1} & \frac{d \ln I_1}{d \mu_2} & \dots & \frac{d \ln I_1}{d \mu_{NN}} \\ \frac{d \ln I_2}{d \mu_1} & \frac{d \ln I_2}{d \mu_2} & \dots & \frac{d \ln I_2}{d \mu_{NN}} \\ \vdots & \vdots & & \vdots \\ \vdots & \vdots & & \vdots \\ \frac{d \ln I_{NM}}{d \mu_1} & \frac{d \ln I_{NM}}{d \mu_2} & \dots & \frac{d \ln I_{NM}}{d \mu_{NN}} \end{bmatrix} \quad 5$$

Here,  $NM$  is the number of source-detector measurements, and  $NN$  is the number of nodes. In the single-wavelength continuous wave case, only  $\mu_a$ , the absorption

coefficient is considered variable with respect of intensity measurements;  $\mu_s$  is assumed to be known. The Jacobian is calculated at each iteration of the reconstruction using the adjoint method, which is computationally efficient because it takes advantage of reciprocity<sup>105</sup>. This process is repeated until a stopping criterion is reached. Many methods are available for solving inverse problems. Each have advantages and disadvantages in NIRST image reconstruction, and a number of research groups are working on optimizing these techniques<sup>106-109</sup>.

Nirfast software<sup>99,110</sup> ([www.nirfast.org](http://www.nirfast.org)) was used to reconstruct all the images presented herein. This involves minimization of the objective function  $\chi^2$  until a user-defined stopping criteria is reached. Using the Tikhonov formulation, the objective function is:

$$\chi^2 = \sum_{i=1}^{NM} (\phi_i^M - \phi_i^C)^2 . \quad 6$$

Where  $\phi^C$  is the calculated data from the forward model for a specific estimation of absorption and scattering and the measured data,  $\phi^M$  is the data collected from the imaging system. The first derivative of the objective function  $\frac{d\chi^2}{d\mu}$  can be Taylor-expanded about a nearby point to form a relationship between the data  $\phi$  and the optical properties  $\mu$ :

$$\frac{d\chi^2}{d\mu} = \frac{d\chi^2}{d\mu}(\mu_i) + (\mu_{i+1} - \mu_i) \frac{d}{d\mu} \left( \frac{d\chi^2}{d\mu}(\mu_i) \right) + \dots \quad 7$$

To minimize  $\chi^2$ ,  $\frac{d\chi^2}{d\mu} = 0$ . Ignoring higher order terms and solving for  $\mu_{i+1}$ ,

$$\mu_{i+1} = \mu_i - \left( \frac{d}{d\mu} \left( \frac{d\chi^2}{d\mu}(\mu_i) \right) \right)^{-1} \frac{d\chi^2}{d\mu}(\mu_i). \quad 8$$

This yields an iterative update for the optical properties. Solving for  $\frac{d\chi^2}{d\mu}$  and  $\frac{d^2\chi^2}{d\mu^2}$

from equation 6, we obtain

$$\frac{d\chi^2}{d\mu}(\mu_i) = 2 \left( \frac{d\phi^C}{d\mu} \right)^T (\phi^C - \phi^M) \quad 9$$

and

$$\frac{d}{d\mu} \left( \frac{d\chi^2}{d\mu}(\mu_i) \right) = 2 \left( \frac{d\phi^C}{d\mu} \right)^T \frac{d\phi^C}{d\mu} + 2 \frac{d^2\phi^C}{d\mu^2} (\phi^C - \phi^M). \quad 10$$

Ignoring the small second derivative term gives us

$$\frac{d}{d\mu} \left( \frac{d\chi^2}{d\mu}(\mu_i) \right) = 2 \left( \frac{d\phi^C}{d\mu} \right)^T \frac{d\phi^C}{d\mu}. \quad 11$$

Substituting in equations 9 and 11, equation 8 becomes

$$\mu_{i+1} = \mu_i - \left[ \left( \frac{d\phi^C}{d\mu} \right)^T \left( \frac{d\phi^C}{d\mu} \right) \right]^{-1} \left( \frac{d\phi^C}{d\mu} \right)^T (\phi^C - \phi^M). \quad 12$$

Knowing that  $\frac{d\phi^C}{d\mu}$  is the Jacobian Matrix  $J$ , the update equation is

$$\mu_{i+1} = \mu_i - [J^T J]^{-1} J^T (\phi^C - \phi^M). \quad 13$$

Since  $J^T J$  is always ill-conditioned, the inversion is stabilized using Levenberg-Marquardt regularization by adding a term,  $\lambda$ , to make it more diagonally dominant, resulting in:

$$\Delta\mu = [J^T J + \lambda I]^{-1} J^T (\phi^C - \phi^M). \quad 14$$

This equation is iterated on until the change in  $\mu$  from one iteration to the next is less than 2%, which is an empirically derived factor in the Nirfast software. The inversion process is computationally intense because the forward problem must be solved at every iteration.

In performing CW imaging only, it is not possible to distinguish between signal loss due to absorption vs. scattering without additional information. Frequency or time domain imaging provides added information beyond signal amplitude at the detector, which can be used to determine scattering and absorption independently. In the reconstructions performed herein, scattering values are assumed and remain unchanged throughout the process, while iterative updates are made exclusively to the absorption parameters and data model mismatch is minimized for absorption alone. Hence, any mischaracterization of scatter can affect the recovered absorption coefficients.

### 3.1.6. Spectral Reconstructions

Each chromophore in the NIR regime has a specific molar extinction spectra and after calculating absorption at each wavelength, a best fit can be performed for hemoglobin, water, and lipids. Alternatively, this information can be embedded in the inverse problem. Rather than reconstruct each wavelength separately and then solving for chromophore concentrations, it is possible to restructure the problem in terms of the chromophores and solve for them directly, providing a solution that is faster, more accurate, and more robust to noise<sup>111,112</sup>. The absorption coefficient at each wavelength is comprised of a linear combination of the absorbers at that wavelength. Hence, chromophore concentration C can be determined by:

$$C = \sum_{i=1}^{\#wv} \frac{\mu_a(\lambda_i)}{\varepsilon_c(\lambda_i)}. \quad 15$$

Here,  $\mu_a$  is the absorption coefficient at the chosen wavelength, and  $\varepsilon_i$  is the molar extinction coefficient as a function of wavelength of  $i^{\text{th}}$  chromophore. Absorption is measured at several wavelengths (at least as many as the number of chromophores) and  $\varepsilon_i$  has been well established<sup>113,114</sup>. In Nirfast, a least squares fit is used to calculate chromophore concentrations from absorption coefficients. Similarly, scattering coefficients can be spectrally combined to scattering amplitude A and scattering power b and then fit to an empirically derived power law approximation to Mie Theory, shown to be a good approximation<sup>115,116</sup>.

$$\mu_s' = a\lambda^{-b} \quad 16$$

To reconstruct directly for tissue chromophores, the Jacobian is modified to incorporate the sensitivity of the tissue chromophores on the boundary data and arranged in blocks by wavelength:

$$J(\lambda_i) = \begin{bmatrix} J_{c1}(\lambda_1) & J_{c2}(\lambda_1) & \cdots & J_{cM}(\lambda_1) \\ J_{c1}(\lambda_2) & J_{c2}(\lambda_2) & \cdots & J_{cM}(\lambda_2) \\ \vdots & \vdots & \ddots & \vdots \\ J_{c1}(\lambda_N) & J_{c2}(\lambda_N) & \cdots & J_{cM}(\lambda_N) \end{bmatrix} \quad 17$$

The update equation is similarly modified:

$$\begin{bmatrix} \Delta c_1 \\ \vdots \\ \Delta c_{NC} \end{bmatrix} = [J^T J + \lambda I]^{-1} J^T \begin{bmatrix} \phi^{C_1} - \phi^{M_1} \\ \vdots \\ \phi^{C_N} - \phi^{M_N} \end{bmatrix} \quad 18$$

to account for the fact that  $c$  is a vector and there is a  $\phi^C - \phi^M$  term for each wavelength. Including multiple wavelengths makes the reconstruction less ill-posed since all data is used to estimate all parameters simultaneously, and is favorable because spectral constraints can be introduced during the reconstruction. Previous work has shown improvement in chromophore concentration using this method<sup>117</sup>. However, this technique is especially memory intensive, as the Jacobian matrix is larger by a factor of number of wavelengths, initially impossible on standard cluster computing. On a mesh using 30,000 nodes, 2,500 measurements, 8 wavelengths, and 4 chromophores, the size of the full spectral Jacobian becomes  $(30,000nodes \cdot 4chrom) \times (2,500measurements \cdot 8wvs)$ , which, for double type storage, is 18 GB. For phantom measurements using all source and detector combinations, the requirements can exceed 80GB simply for storing the Jacobian.

A forward model calculation of this size can take 30-60 minutes on a powerful cluster computer, depending on the number of light sources and detectors on the breast. Typical reconstructions involve about five iterations and thus can take between three and five hours. An alternative conjugate gradient method with lower memory demands was tested; a sample patient reconstruction is shown in Figure 21.

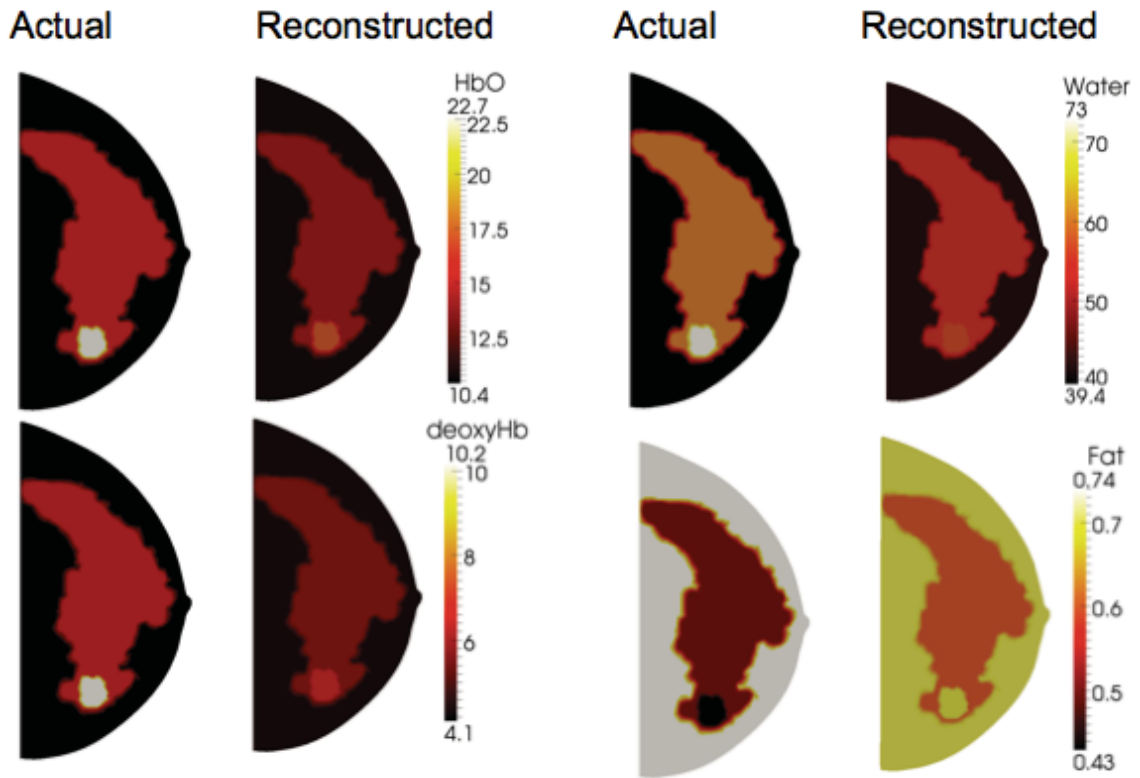


*Figure 21: Reconstructions for a sample patient using the conjugate gradient method shows accurate recovery of tissue chromophores when compared to the simulated actual data.*

This technique was successful but required a very large number of iterations, leading to longer reconstruction times. Its use was discontinued after an upgrade in computing power permitted spectral reconstructions of the NIRST-DBT data sets.

### **3.1.7. Inclusion of Anatomic Spatial Priors**

Stand-alone NIRST has low spatial resolution, on the order of one centimeter<sup>33,57,59</sup>. Spatial information from the DBT image stack can be used to guide the NIRST reconstruction, improving resolution up to an order of magnitude<sup>57,118,107,119</sup>. DBT

images can be segmented into different types (typically fibroglandular, adipose, and malignant) based on pixel intensity, location, and architecture, as shown in Figure 22.

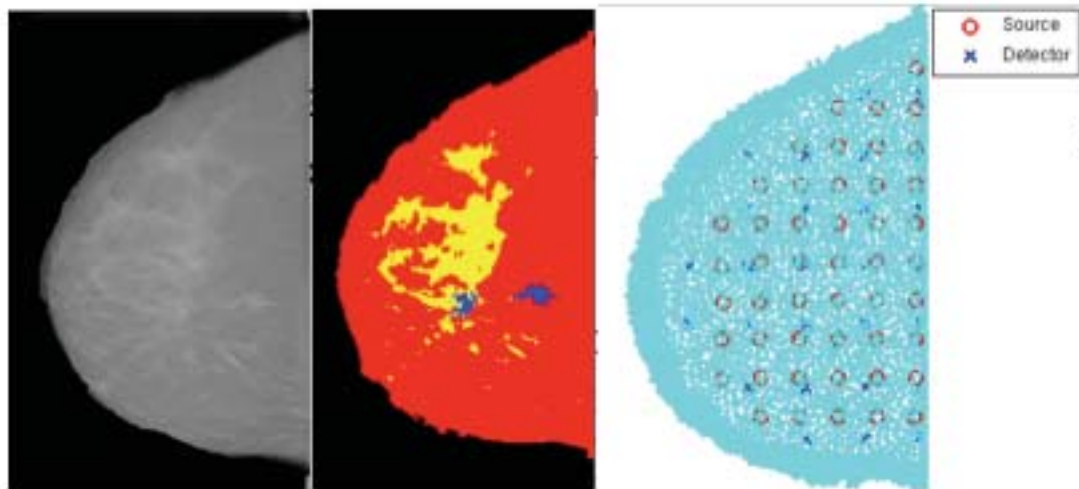


*Figure 22: DBT image (left) with segmented slice and the resulting FEM mesh (center) and the overlay of the sources and detector locations (right) on this template.*

In the FEM mesh, each node is tagged as a single tissue type. During the reconstruction, chromophore concentration estimates are subjected to spatial prior constraints whereby all nodes within a given region are constrained to the same value during the iterative updating process. This technique is referred to as hard priors. Alternatively, in soft prior reconstruction, the values can vary in all regions, but variations within a single region are dampened. All the work discussed in this thesis show either hard prior or no prior images, those in which no spatial information is included.

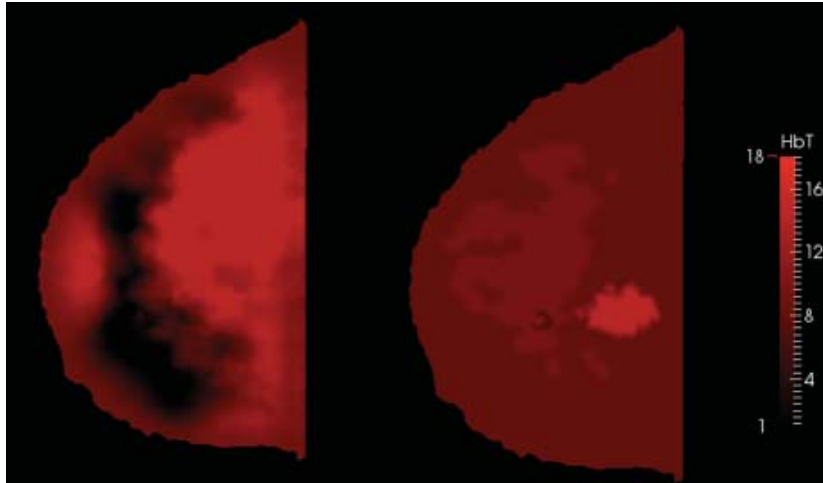


*Figure 23: No prior (left) vs. hard prior (right) reconstruction of a patient with both a benign lesion and an invasive ductal carcinoma. The higher hemoglobin content of the carcinoma is clearly visualized in the case on the right, but not visualized in the no prior reconstruction on the left. Additionally, significant high and low values are seen in diffuse reconstruction across the length of the breast that are known to be artifact.*

In addition to improvements in accuracy and resolution, the use of spatial prior information decreases the number of unknowns to be updated and converts the inversion from being underdetermined to overdetermined, while also decreasing its size and associated computation time. Optical properties vary only across regions, so the Jacobian matrix can be mapped for particular regions to assess region-specific sensitivity. In this process, the Jacobian is reduced to a number of columns equal to the number of regions rather than the number of nodes, typically a much smaller matrix, as shown below.

$$J = \begin{bmatrix} \frac{d \ln I_1}{dC_1} & \frac{d \ln I_1}{dC_2} & \dots & \frac{d \ln I_1}{dC_{NR}} \\ \frac{d \ln I_2}{dC_1} & \frac{d \ln I_2}{dC_2} & \dots & \frac{d \ln I_2}{dC_{NR}} \\ \vdots & \vdots & & \vdots \\ \frac{d \ln I_{NM}}{dC_1} & \frac{d \ln I_{NM}}{dC_2} & \dots & \frac{d \ln I_{NM}}{dC_{NR}} \end{bmatrix} \quad 19$$

It imposes tissue homogeneity within segmented zones, and when used appropriately improves lesion detectability assessed by receiver operating characteristic (ROC) analysis compared to no prior information<sup>120</sup>. Homogeneous sub-region constraints can cause inaccurate reconstructions if region localization is not accurate<sup>121</sup>. Since optical imaging alone is unable to detect lesions smaller than about 1cm, it is advantageous to use a highly resolved imaging modality to complement the optical imaging. Hard priors algorithms and DBT spatial information can enable detection of smaller lesions with lower contrasts on a spatial scale, possibly approaching 3mm<sup>122</sup>. Alternatively if a lesion is unidentifiable in DBT, it will most likely not appear in the optical image as any contrast will be averaged with the rest of the defined region, unless the contrast is very high or the region is very large. Hence, NIRST will not increase the sensitivity of DBT in detecting cancer, but may improve the specificity. While DBT provides highly resolved 3D anatomical detail in the breast, NIRST produces complementary metabolic information including hemoglobin concentration, oxygen saturation, water content, lipid fraction, and scattering properties. Synergistically combining the two information streams by using the DBT spatial information to guide the

NIRST chromophore recovery may improve the specificity of recall screening for breast cancer.

### ***Image Segmentation Methods***

A patient-specific mesh is required to use spatial prior information. DBT image volumes localize the tissue boundaries and internal structures, highlighting any regions of interest. While DBT images are highly resolved in the x and y plane, there is very limited resolution on the z plane, leading to some challenges. The reasons behind this are described below, along with several steps to improve the images, work done with collaborators at the University of Massachusetts Medical School. The prior information from DBT is used to create a stack of segmented images that is then converted into a mesh for NIRST image reconstruction. Prior information can be used to refine mesh resolution within regions of interest, and synergistic combining of the DBT and NIRST information streams yields the most accurate final results.

#### **3.1.8. DBT Image Formation**

The theoretical framework for tomosynthesis began in the early 1900s. However, a lack of technology prevented experimental work until the 1970s. The initial systems took multiple images in parallel path geometry. In this type of system, the detector moved in one direction while the image receptor moved the opposite way.<sup>123</sup> In order to create images in this manner, a technician had to manually change the films between each projection, a process that would be too time consuming to be practical in a clinical setting. In addition, there was blurring of images outside the plane of interest that made the images difficult to read.

These problems would be solved later with the development of digital detectors and faster computers that could perform image reconstruction and eliminate the blurring effects<sup>124</sup>. In the 1980s, before the advent of a flat panel detector, interest in tomosynthesis waned as CT scanning was refined and brought into the clinic. Finally, in the late 1990s, appropriate flat panel detector technology was developed, to the point where now the current designs use detectors made with selenium. These detectors have a high detective quantum efficiency, absorbing over 95% of incoming X-rays, making low dose detection a possibility<sup>125</sup>. Interest in tomosynthesis for clinical applications has been restored on account of this new development<sup>126</sup>.

Tomosynthesis is a unique medical imaging technique because of the method by which the images are taken. There are several geometric configurations used, including parallel path, full isocentric motion, and partial isocentric motion<sup>126</sup>. In parallel path imaging, the tube moves parallel to the detector. This was the earliest type of detection system. In full isocentric motion, the detector and tube are fixed with respect to each other but move around in a circular pattern. In partial isocentric motion, the tube moves in an arc but the detector remains fixed. This geometry is currently used in virtually all breast tomosynthesis machines.

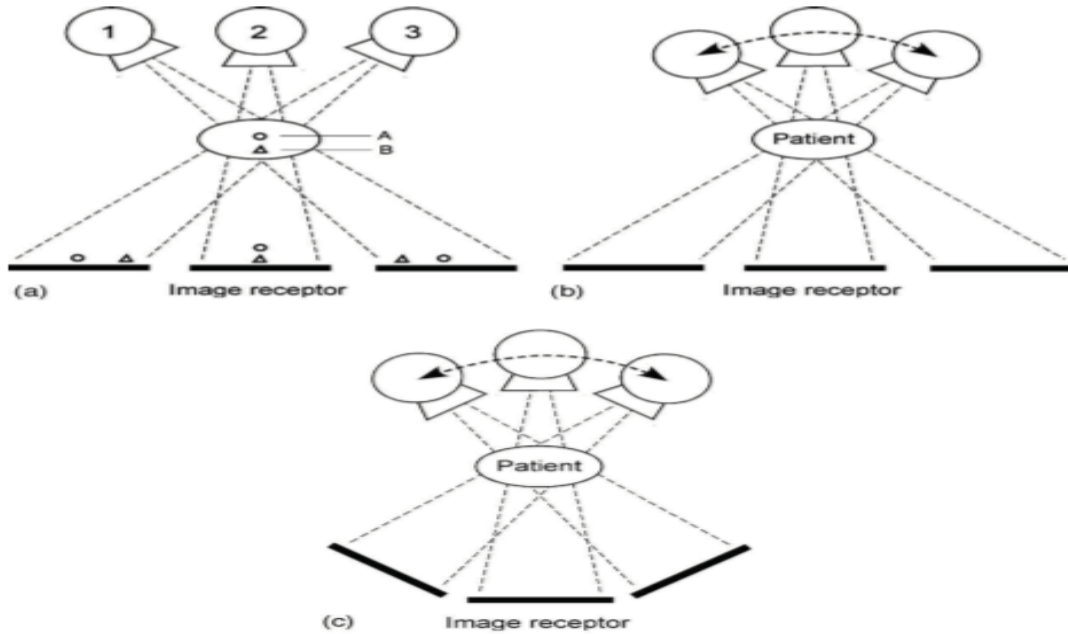


Figure 24: a. Parallel path geometry, b. Partial isocentric motion, c. Full isocentric motion<sup>126</sup>.

There are other factors beyond system geometry that affect the overall image quality. The number of images taken can be changed for a given dose. Increasing the number of images decreases the signal-to-noise ratio and lengthens the reconstruction time. Another variable that can be altered is the angular range of imaging. Smaller angles allow more structures in a given slice to be in focus, while using larger angles leads to greater slice separation. The latter can increase the image resolution and help to sort out clusters of microcalcifications and other small structures<sup>125</sup>. One study found that 13 images taken over 60 degrees gives optimum in-plane clarity and vertical resolution<sup>127</sup>. Another study showed that somewhere between 11 and 17 projections over 45 degrees is best in detecting a 3 mm mass<sup>128</sup>. Clearly, more research in this area is needed.

In addition to considering projection angles, there are also different methods of acquiring images. Images can be taken continuously or at discrete locations. With

continuous imaging, the detection time must be kept short to avoid image blurring due to motion at the point of focus. If the imaging occurs at discrete locations, the gantry must completely stop before the image is taken to avoid blurring.<sup>124</sup>

After the images are taken, they must be reconstructed. The most important issue when dealing with reconstruction is the blurring effect of out-of-plane objects, which can obscure details in the plane of interest. Many different techniques have been developed for this task. They fall into four main types: backprojection, algebraic, iterative and statistical<sup>129</sup>.

The most basic and earliest method is a backprojection technique known as shift and add. As the name indicates, each projection is shifted and then added together. Changing the amount of shift will determine which plane is in focus<sup>126</sup>. As is true with all types of reconstruction, it is important to take into account the slight movement of the patient during the exposure. One method that has been used in the past involves fiducial markers<sup>130</sup>. However, this is less of a concern as the breast is compressed in breast tomosynthesis, preventing significant movement of the patient. Filtered backprojection (FBP) is a transform technique that uses line integrals at various angles to reconstruct the values at each voxel. Simple backprojection is unstable when noise is included. More involved techniques include an inversion filter, a spectral filter, and a slice thickness filter to increase stability during the reconstruction<sup>131</sup>.

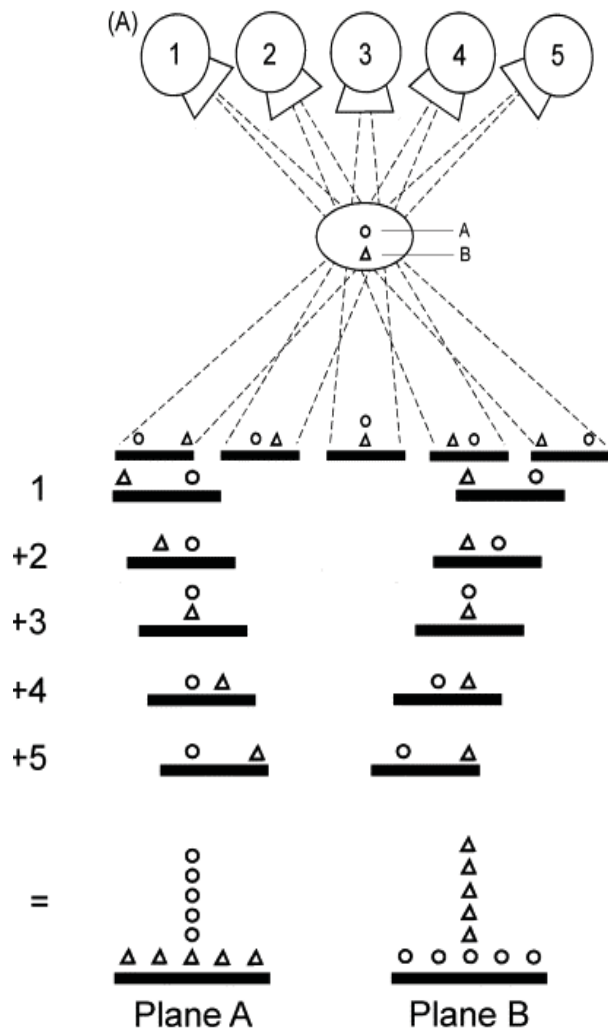


Figure 25: The shift and add technique for image reconstruction of five exposures. The images are added together with different shifts in order to focus on object A or B<sup>132</sup>.

Matrix inversion tomosynthesis (MITS) is an algebraic technique in which linear algebra can be used to solve for blurring in each plane. This technique is very good at reconstructing high-frequency image components, but the matrices are not well conditioned for inversion at lower frequencies<sup>124</sup>. A similar approach involves iterative reconstruction, which uses all elements of the data set (including those taken at wide

angles, which are not included in MITS). However, it is more computationally intensive and can take longer to run<sup>126</sup>.

Statistical methods can also be used to reconstruct tomosynthesis images. The maximum likelihood expectation maximization technique uses data to determine the most probable linear attenuation coefficients for each voxel<sup>131</sup>.

Several studies measure the performance of the various reconstruction techniques in different phantom and patient scenarios. These studies often compare signal-to-noise ratios as well as artifact spread functions. FBP is the most commonly-used algorithm. It has been shown to more accurately reconstruct lower frequencies, while MITS is more accurate at high frequencies<sup>126</sup>. Other studies that have compared FBP methods with the statistical maximum likelihood expectation maximization technique have shown better results for the statistical method when studying masses and microcalcifications<sup>133</sup>. FBP has also been compared to the shift and add method for breast tomosynthesis imaging of microcalcifications, and was shown to be superior in clarity<sup>134</sup>. Also, the acquisition methods can affect the success of the reconstruction algorithm. For example, the MITS technique works better at smaller angles than the FBP; these parameters should be considered when determining which reconstruction method to use<sup>134</sup>. In the case of our DBT system, the reconstruction algorithms used are proprietary information. However, no matter what reconstruction method was selected, there are significant challenges to image segmentation, including partial volume averaging artifacts and low z plane resolution.

### 3.1.9. DBT Image Post Processing

After DBT image reconstruction is performed from the initial 11 projection frames, post-processing steps are necessary before tissue type segmentation is possible. First, the lowest 34 reconstructed slices are removed. These slices correspond to the 3.4 cm of additional height above the traditional breast tray occupied by the NIRST detector cover and do not contain any breast tissue. Some of the DBT images possess detector artifacts, and these are removed via thresholding, removing pixel values outside of one standard deviation from the mean, as shown in Figure 26. Next, the posterior edge of the NIRST detector is identified by the user via a single mouse click for future assignment as adipose tissue. If this is not performed, the image artifacts from this edge may be incorrectly segmented as fibroglandular tissue. Skin thickness can be estimated next, as shown in Figure 27. However, the skin is not segmented as a separate tissue in the work described here because along the tissue edge, reconstruction is known to be inaccurate.

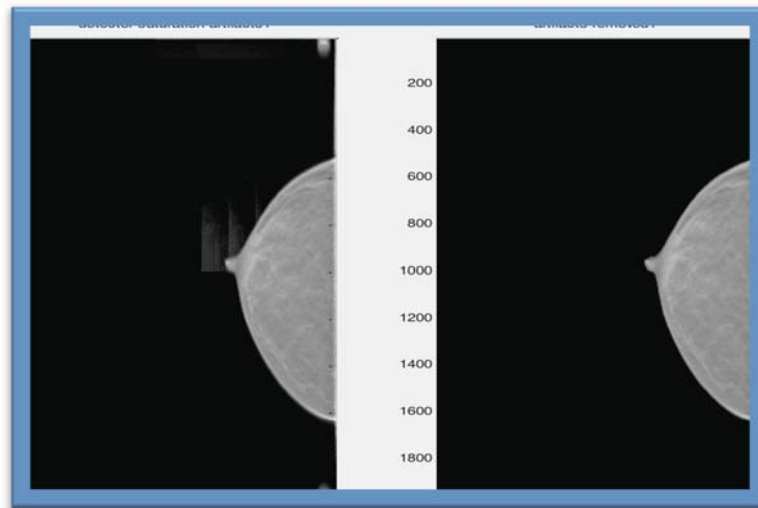


*Figure 26: DBT Image slice prior to (left) and after (right) detector artifact correction thresholding.*

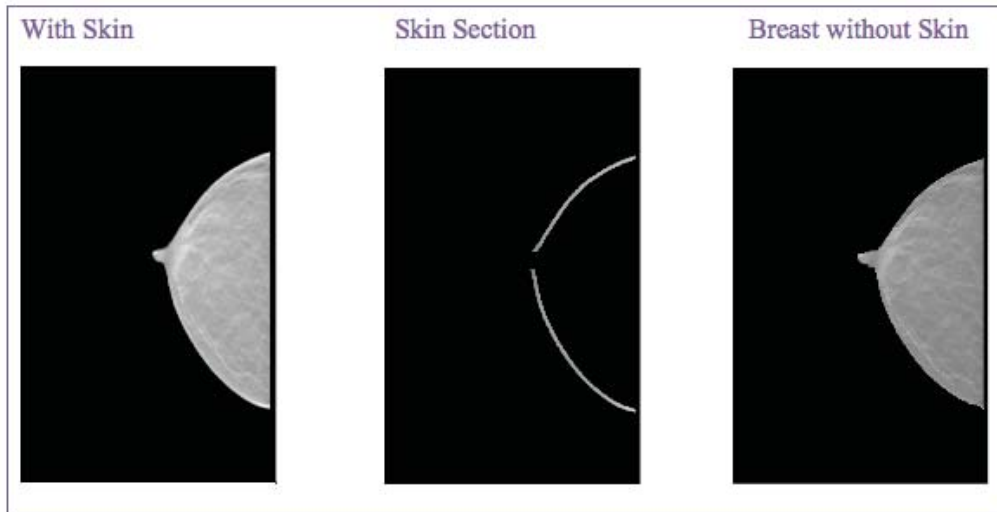


*Figure 27: Images of skin segmentation process.*

After eliminating slices and artifacts due to the unique geometry of the NIRST-DBT system, an out-of-slice artifact suppression step is performed using an angular constrained bilateral filter. Out-of-slice artifacts in DBT reconstruction are due to the limited angular range of this imaging modality. They appear as increasingly laterally shifted, with decreasing intensity in slices farther from the slice containing the original object, as shown in Figure 28. Viewed in the  $x$ - $z$  plane, they appear as X's. An edge-preserving bilateral filter was applied along this plane, including an angular constraint accounting for the angular range of the DBT imaging system<sup>135-137</sup>. This step decreases the out-of-plane artifacts, readying the images for adipose and fibroglandular segmentation.

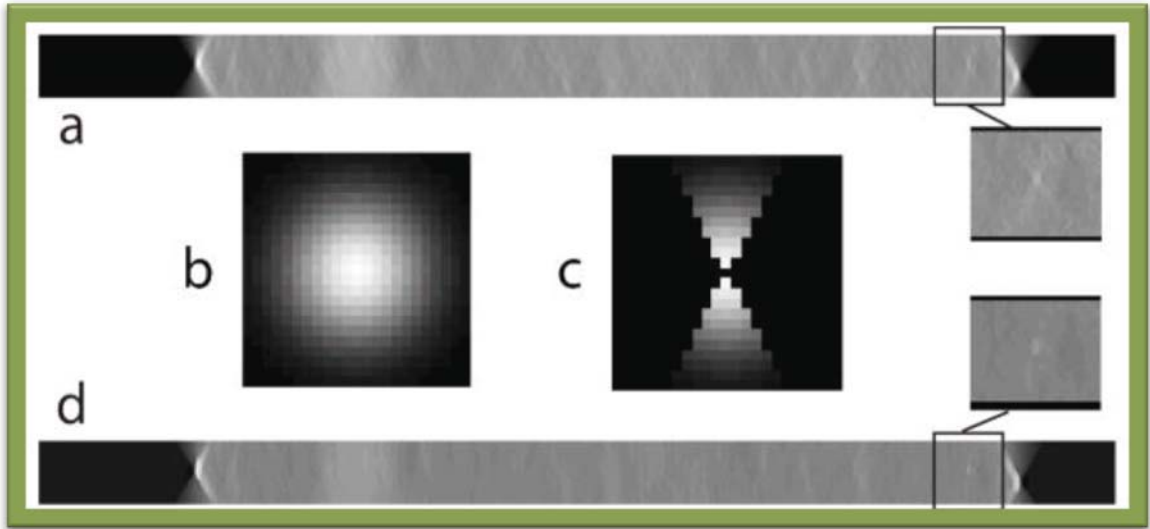
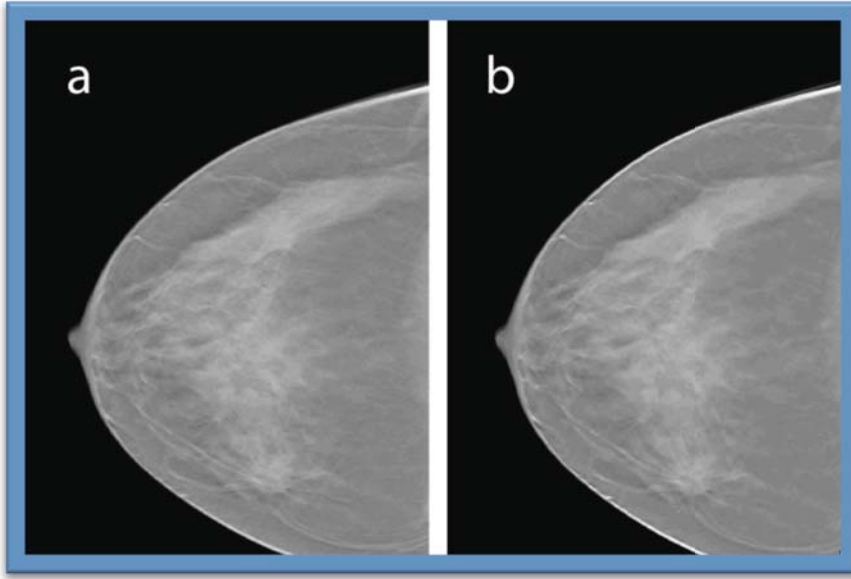


Figure 28: *a. An x-z plane image from the 3D DBT image stack for a clinical case. b.  $23 \times 23$  Gaussian kernel used in the bilateral filter before modification. c. Modified Gaussian kernel with an angular constraint of  $2\theta$  corresponding to the angular range during projection view acquisition. d. An x-z plane after application of the angular-constrained bilateral filter that shows a reduction in out-of-plane artifacts. Zoomed ( $1.5\times$ ) regions of interest before and after application of the filter are shown<sup>138</sup>.*



*Figure 29: (a) DBT slice prior to processing and (b) after angular bilateral filtering step<sup>138</sup>.*

### **3.1.10. Adipose and Fibroglandular Segmentation**

Tissue type segmentation is performed using a kernel-based fuzzy c-means (KFCM) clustering algorithm. This broadly-applied technique for medical image segmentation has been previously used in MRI and digital mammography<sup>139–142</sup>. The whole breast is selected for clustering into distinct regions, either two or three in craniocaudal (CC) (three if muscle is present), and two in mediolateral oblique (MLO) initially due to similarity between fibroglandular and chest wall pixel intensities. This process is shown in Figure 30-Figure 32 for three cases, CC images, MLO images with disjointed fibroglandular tissue and chest wall, and MLO images with chest wall and fibroglandular tissue connected, respectively. KFCM classifies pixels that are geographically and intensity similar into a cluster. It is an iterative method that

minimizes an objective function that depends on the Euclidean distance of the gray levels to the center of the cluster, which has been arbitrarily defined. The KFCM classification is performed on the 3D volume stack, producing classifications of 2 or 3 regions in every slice. This step is repeated for the MLO case to separate fibroglandular and muscle tissue and followed by morphological operations when both are present in a connected cluster, as shown in Figure 32. When muscle and fibroglandular tissue present as two separate clusters, it is possible to separate them based on the known location of the chest wall, anterior and either superior or inferior depending on the breast imaged, however when they are the continuous, additional morphological operations are necessary for separation. At this point, the tissue has been segmented into adipose and fibroglandular tissue, with muscle as well when applicable. The segmentation process is complete for normal breasts, but an additional step is needed for lesion segmentation in cases from the biopsy cohort.

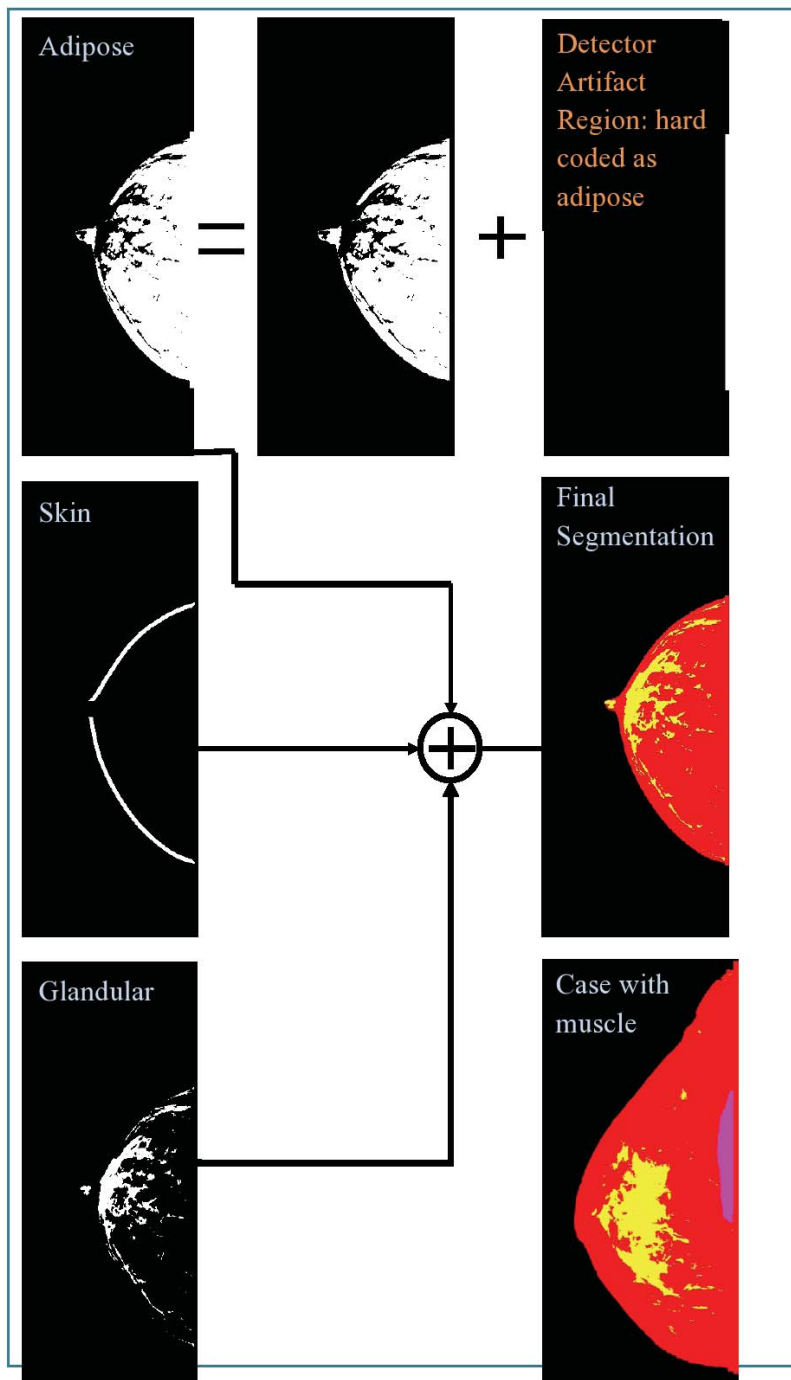
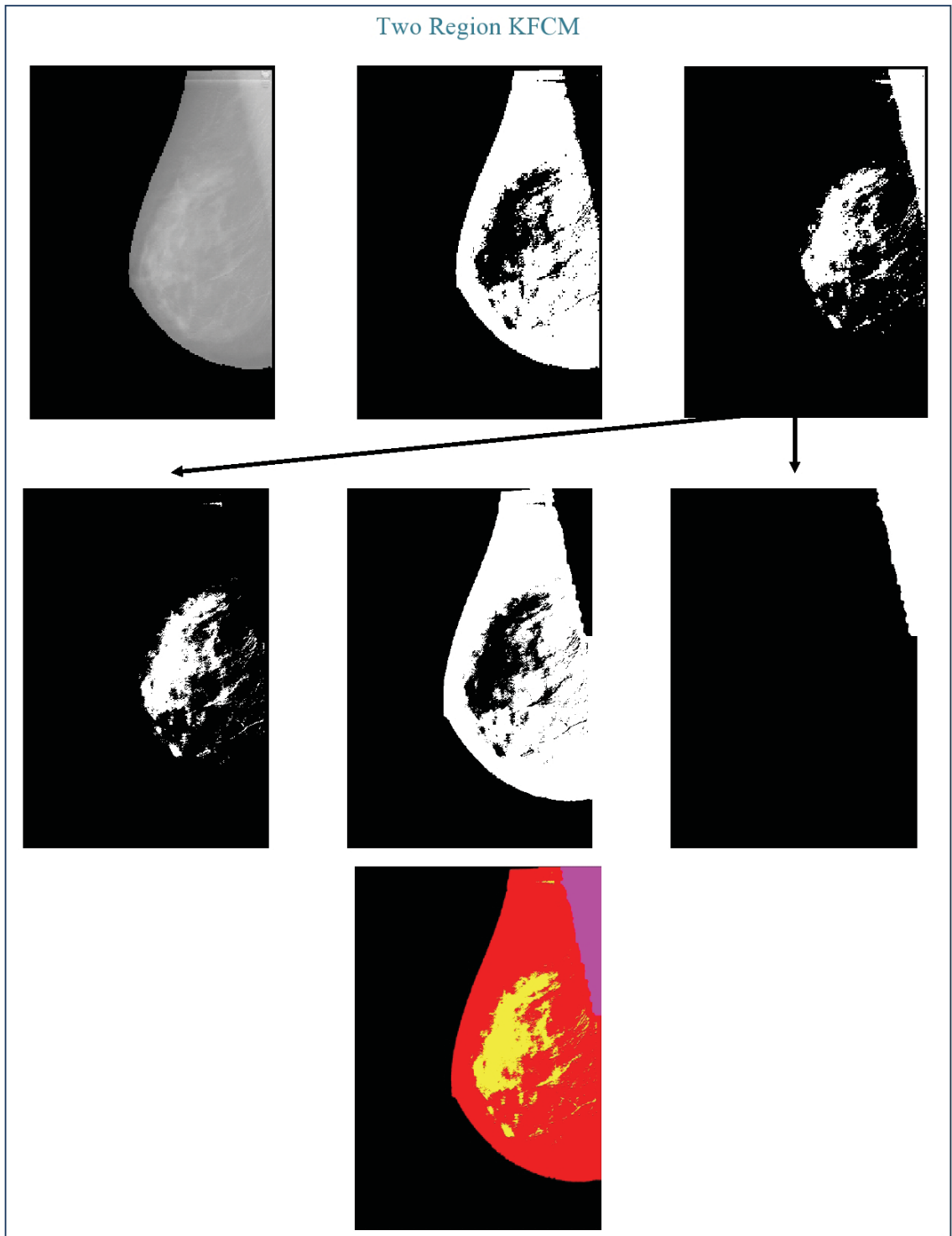
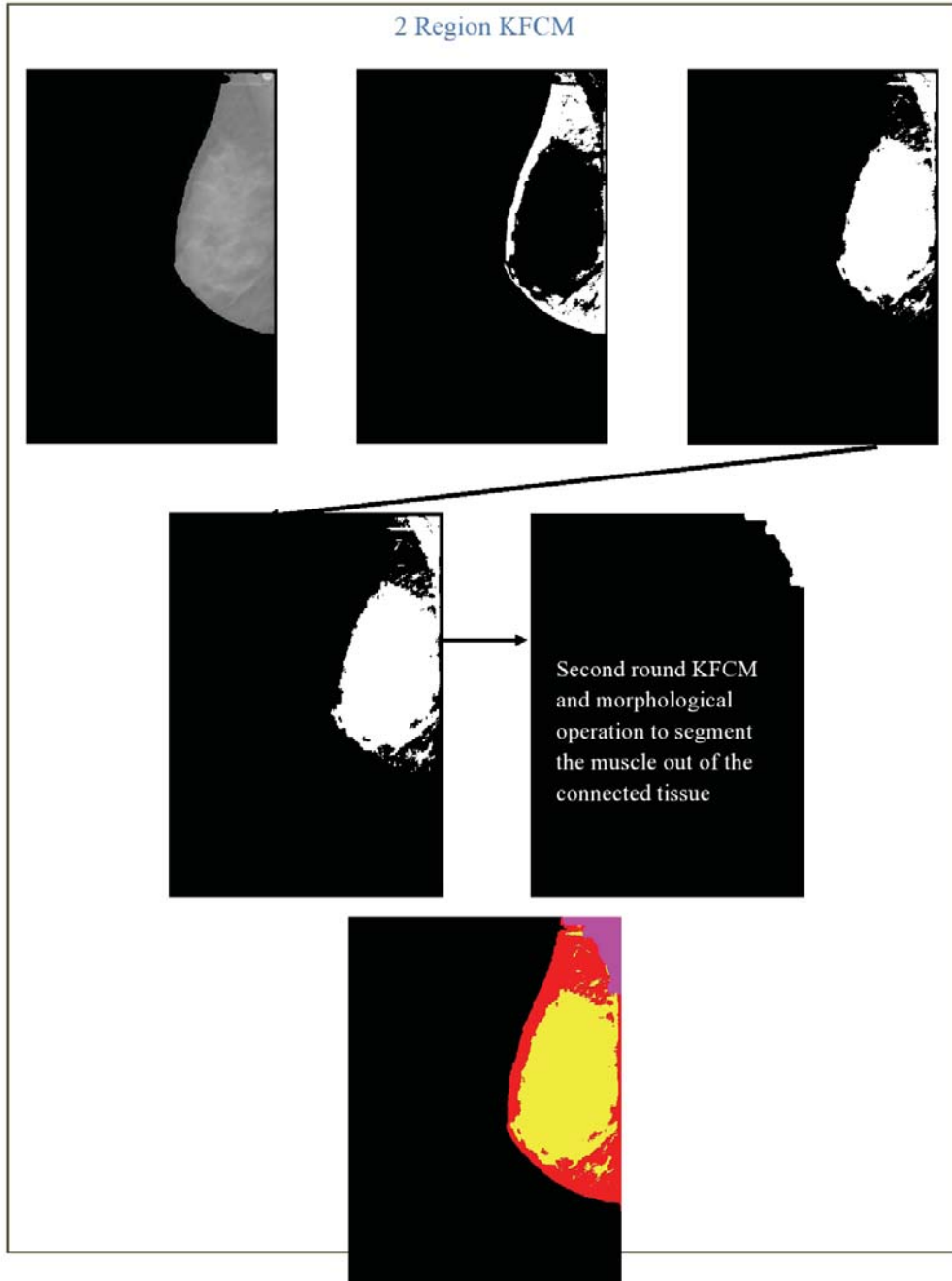


Figure 30: KFCM segmentation steps for CC images



*Figure 31: KFCM segmentation steps for MLO images with geographically separated fibroglandular and chest wall tissues. First round KFCM separates adipose and non-*

*adipose, a second KFCM on the non-adipose region separates fibroglandular and muscle.*



*Figure 32: KFCM segmentation steps for MLO images with continuous fibroglandular and chest wall tissues. First round KFCM separates adipose and non-adipose, a second*

*KFCM on the non-adipose region separates fibroglandular and muscle but requires additional morphological operations for separation.*

### **3.1.11. Lesion Segmentation**

All images have been carefully reviewed by a breast radiologist, Dr. Steven Poplack. For women with abnormalities, he determines the slice where the lesion is most clearly visualized as well as the extent of the lesion in the z-direction. Additionally, he circles the lesion in the clearest slice. For segmentation, the process is semi-automated, requiring three user inputs. Identification of the center of the region of interest, as well as the lesion periphery along the axis of largest diameter (2 points) are obtained in the plane of best lesion visualization. Using these measurements, a cubic voxel of interest is developed, centered at the lesion center and extending to the largest diameter points in all three dimensions. Within the bounds of this region, background correction, KFCM, and additional morphological operations are performed to obtain the tumor segmentation.

There are differences in pixel intensity in slices of DBT image volumes, with images near the breast periphery having greater intensity than more centrally-located images. This is due to the lack of an X-ray scattering grid for DBT images; a greater scatter-to-primary ratio as well as beam hardening effects lead to lower intensity in central breast slices. A background correction is applied whereby the average intensity value for all slices in the voxel of interest (VOI) is determined and used to normalize each individual slice, as shown in Figure 33. KFCM is applied to the VOI after background correction, separating the volume into two clusters: background and lesion.

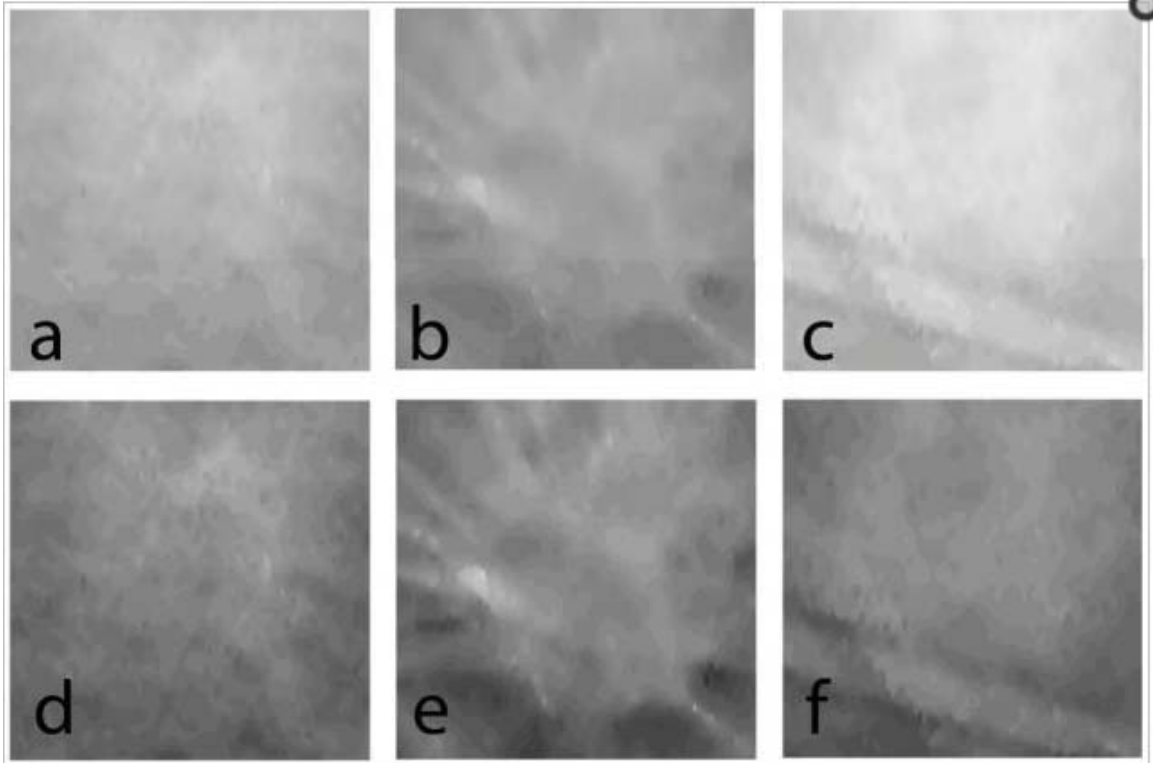


Figure 33: Three slices ( $x$ - $y$  plane) extracted from the volume of interest (VOI) encapsulating the lesion: a. top slice in contact with the compression paddle; b. slice that best represents the lesion; and c. bottom slice in contact with the breast support. (a–c) are prior to and (d–f) are after VOI normalization<sup>138</sup>.

Lastly, morphological operations are performed on the lesion to obtain a single region of interest within the VOI. This includes hole filling algorithms to remove voids as well as region growing to connect different aspects of the lesion in 3D space as a single contiguous tumor. After all of these steps have been performed, the lesion is overlaid on existing fibroglandular and adipose segmentations as a different color. This

process is demonstrated in Figure 34.

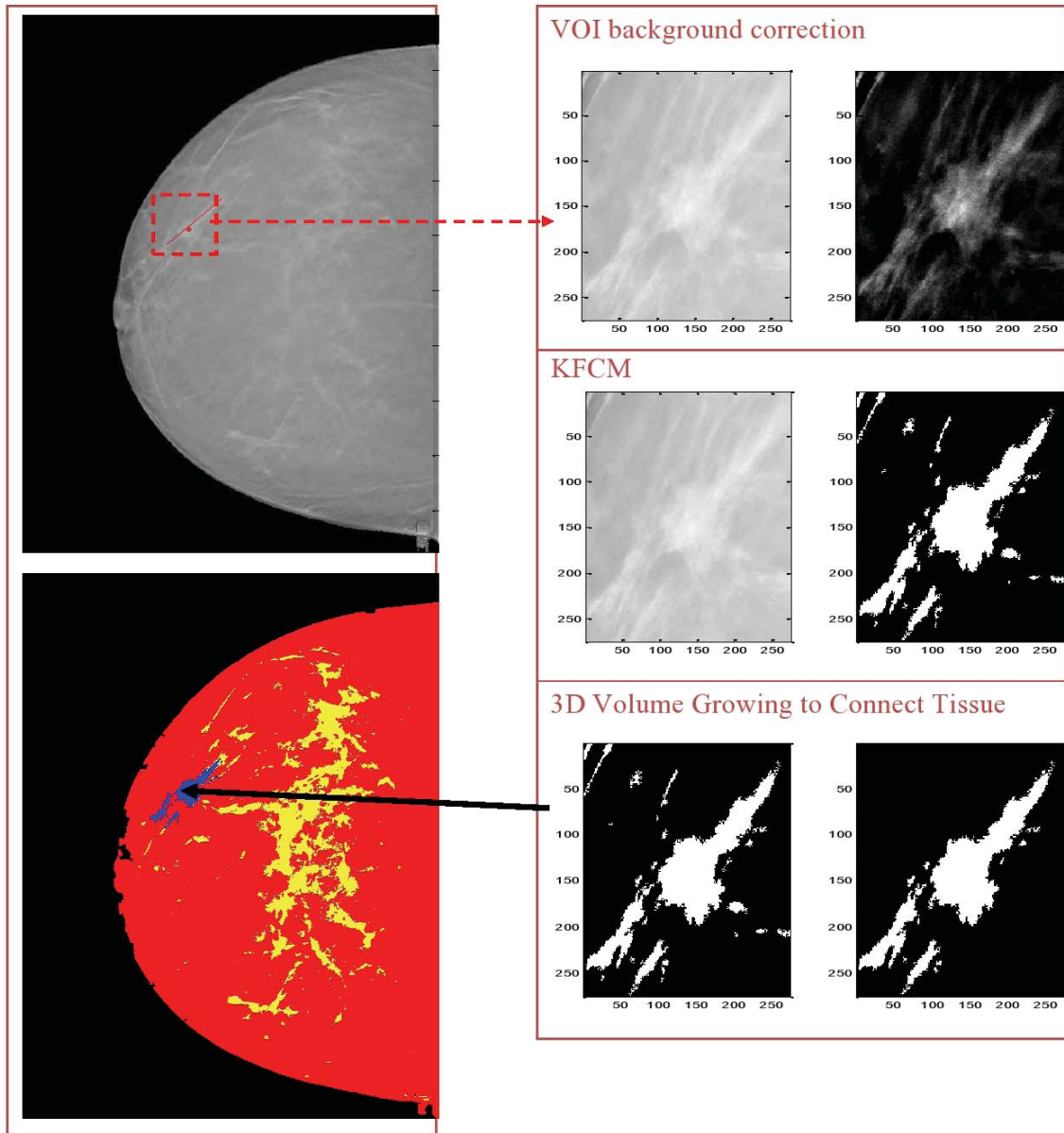


Figure 34: Flowchart depicting lesions segmentation process.

An overview of the entire process for both CC and MLO can be seen in Figure 35 and Figure 36. In these flowcharts, the color coding of the text corresponds to the bounding boxes on the previous figures for improved comprehension of the many steps involved in segmentation.

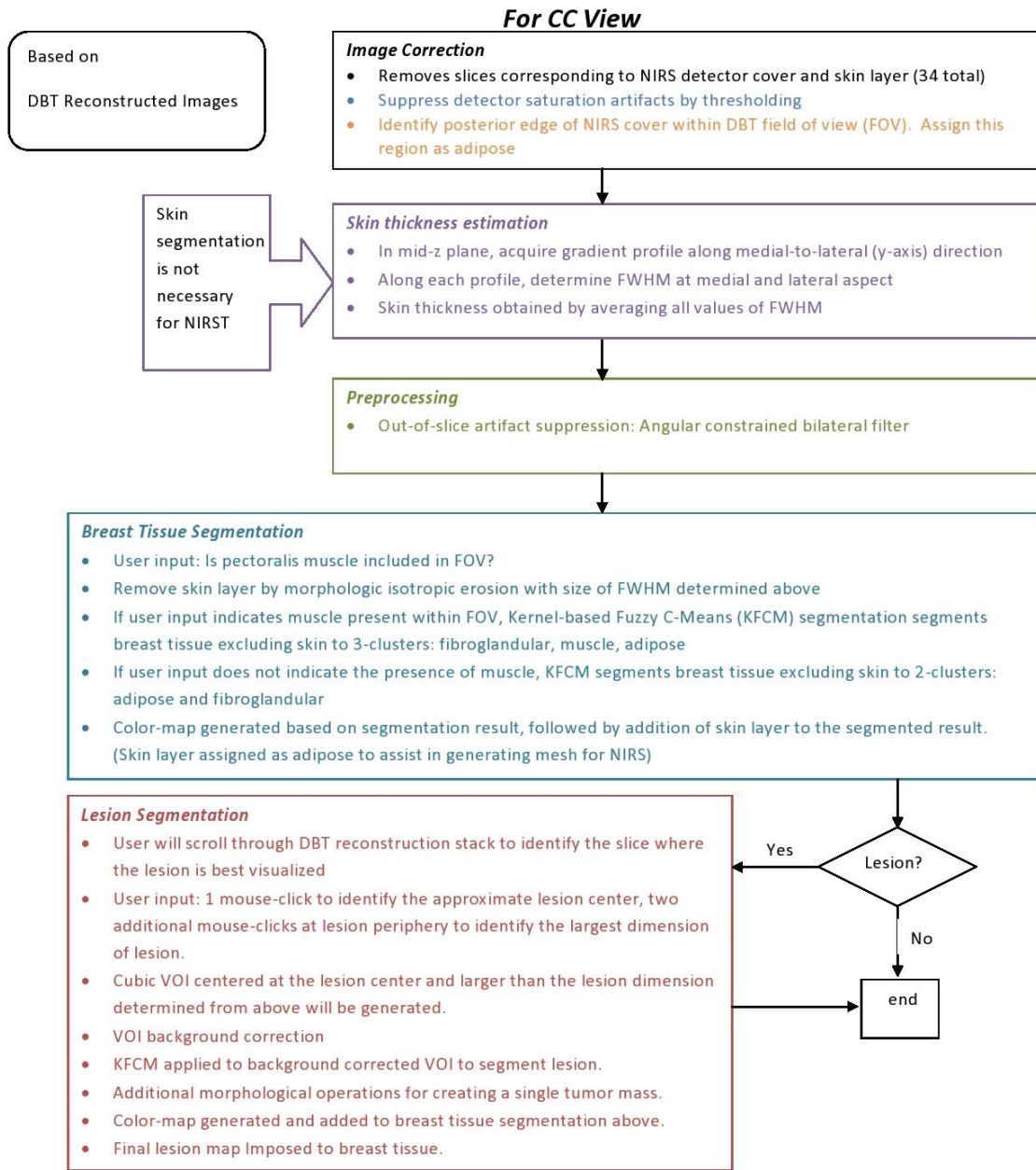


Figure 35: Flowchart depicting DBT image processing steps for CC segmentation of adipose, fibroglandular, and tumor regions, as part of the segmented volume and mesh creation process.

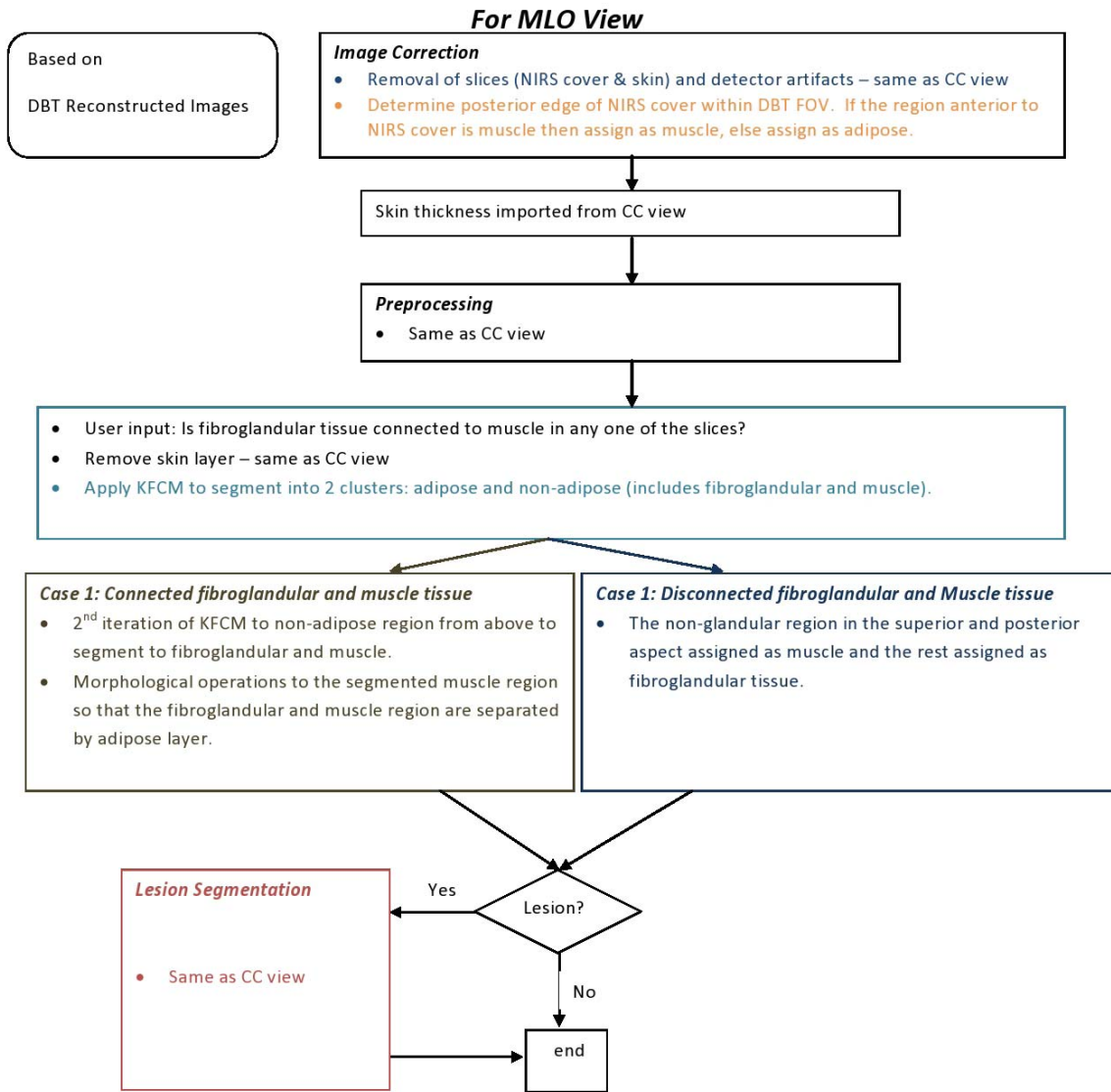


Figure 36: Flowchart depicting DBT image processing steps for MLO segmentation of adipose, fibroglandular, and tumor regions, as part of the segmenting and mesh creation process.

### **3.1.12. DBT Segmentation Assessment**

After development of the semi-automated segmentation algorithm, comparisons with existing segmentation tools confirmed the accuracy of the chosen technique. The comparison metric was an FDA approved tool for breast density analysis of mammographic images, (Quantra™, Hologic Inc.), which assesses breast volume as well as percent fibroglandular (or dense) tissue,

In order to compare the DBT segmentation with the assessment from Quantra, it was necessary to obtain raw mammographic images from a clinical Hologic unit. These raw images are not normally save to a patient's medical file but can be obtained from the unit itself. However, there is limited hard drive space on these machines, so scans are automatically removed after a certain amount of time, usually four weeks. For this study, it was necessary to wait until normal subjects completed their next annual screening mammogram, at which point the raw images could be retrieved. Only screening exams completed at DHMC could be included in the study, so many subjects that participated in the DBT research scans were not included a part of this analysis. Additional scans at the time of the DBT research study would increase radiation exposure and were not included in the CPHS study plan.

In this analysis, 17 DBT reconstructions of women from the NIRST-DBT study were compared with estimates from mammography using Quantra. Percent fibroglandular tissue, alternatively, volumetric breast density (VBD) was calculated from the segmented DBT image slices as well as through the Quantra software package (performed by collaborators at Hologic, Inc) as a percent glandular volume (GV) out of the total breast volume (TBV). As the images were taken on two different machines, at

time points up to one year apart, the compressed breast thickness (T) differed between mammography and DBT as did the TBV. This may be due to changes in patient positioning, system geometry and weight gain or loss over the interval between imaging exams. To account for these differences, a normalized breast density (nVBD) was introduced.

$$nVBD = VBD/T$$

The results are summarized below Table 3. There were statistically significant differences between breast thickness on the DBT system and the clinical units with DBT images typically obtained smaller thicknesses. nVBD took the thickness differences into account showing statistically significant correlation between DBT segmentation and Quantra, which was not the case for VBD without normalization. Scatter graphs showing comparisons between DBT segmentation and Quantra for both VBD and nVBD are shown in Figure 37.

T <sup>§</sup> [mm]	Mean difference (MQ-DBT): 6.7; p=0.013*
TBV <sup>§</sup> (cc)	Mean difference (MQ-DBT): 183; p<0.001*
GV <sup>§</sup> (cc)	Mean difference (MQ-DBT): 9.6; p=0.211
VBD	Pearson's r: 0.471; p=0.056
nVBD	Pearson's r: 0.658; p=0.004*

Table 3: Prototype DBT vs. Mammography–Quantra (MQ) <sup>§</sup> indicates paired t-test; \* indicates statistical significance<sup>143</sup>.

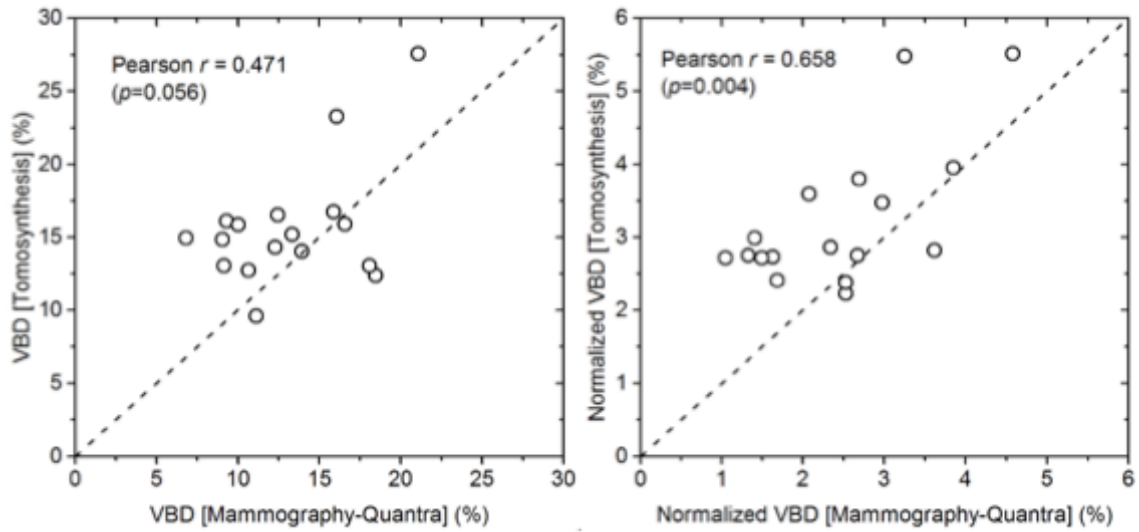


Figure 37: Volumetric breast density comparison between mammography via Quantra analysis, and DBT for raw data (left) and normalized results (right).

After confirmation that the segmentation algorithm worked as well as Quantra for determination of fibroglandular dense tissue, it was important to compare the calculations for two views of the same breast as a secondary test of segmentation accuracy. Correlation between two views was surprisingly low for mammographic methods, and for both VBD and nVBD, DBT had a higher correlation. As MLO images are often obtained at different breast thicknesses than CC images, normalization improves the correlation between views for both Quantra and DBT. For DBT only, the correlation between views was statistically significant, as summarized in Table 4.

Metric	Mammo-Quantra	DBT- current algorithm
VBD	r=0.309; p=0.552	r=0.394; p=0.439
nVBD	r=0.572; p=0.236	r=0.860; p=0.028*

*Table 4: Comparison of two views of the same breast, \* indicates statistical significance<sup>143</sup>.*

Testing this new DBT segmentation method via comparison with existing, well-documented software for breast density analysis as well as via comparison of different views of the same breast both demonstrated statistically significant correlation. This evidence strongly supports the assertion that the new DBT segmentation algorithms will accurately represent breast spatial prior information for NIRST reconstruction algorithms.

### ***Mesh Creation***

Meshing converts the spatial information contained in the DBT image stack into a precise model of the breast for NIRST image reconstruction. The results shown here rely on the meshing toolkit included in Nirfast to create phantom and breast meshes. There is a meshing GUI in Nirfast, shown in Figure 38.

This is an incredibly useful tool for creating single meshes for optical phantoms. However, for analysis of patient images, a script-based meshing tool was written to increase speed of patient image reconstruction creating meshes automatically in a repeatable, reliable way.

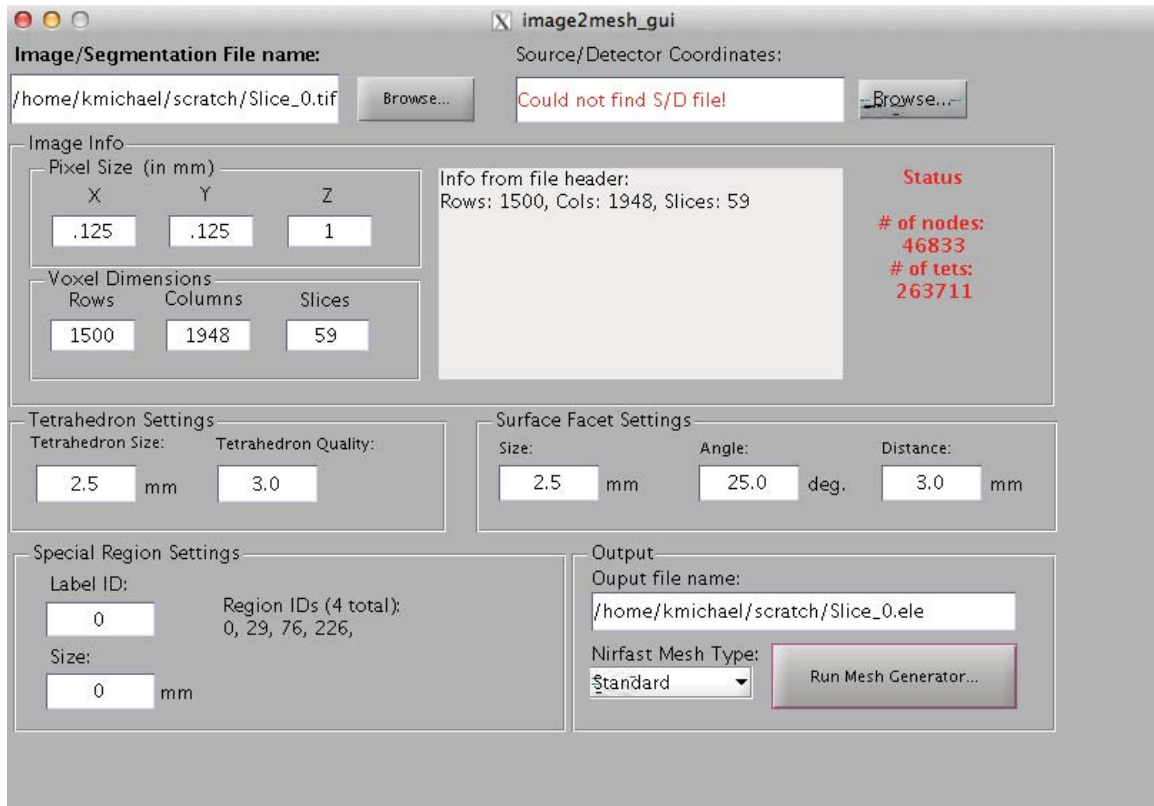
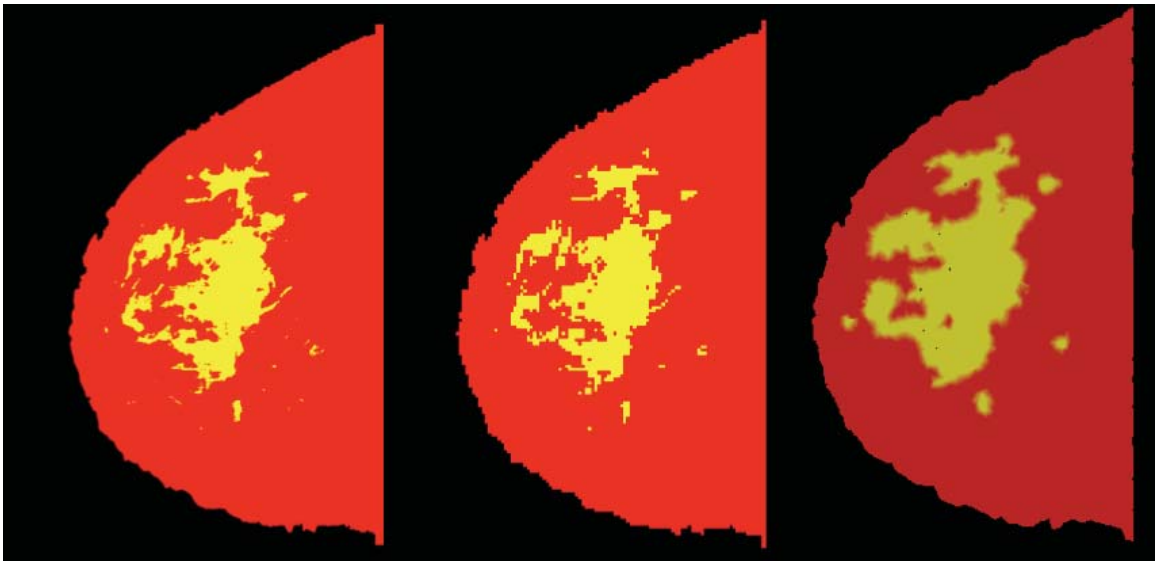


Figure 38: The Nirfast mesh creation GUI allows users to load segmented images and source locations, specify node density, and create a 3D mesh. Single regions can be refined with smaller node spacing<sup>144</sup>.

### 3.1.13. DBT Segmented Image Post Processing

Images obtained from the DBT segmentation require post processing before meshing can be completed. The DBT image stack is typically reconstructed with 1 mm spacing in the z-plane. The stack includes 34 slices corresponding to the 3.4 cm breast detector panel that must be removed. This can be done prior to segmentation to decrease segmentation time, but it is important to note that the first slice of image stack in this case actually corresponds to an image 3.4 cm above the original breast tray, prior to NIRST modifications.

The pixel spacing in the x and y planes of the DBT images are quite small (0.125 mm) owing to their high resolution; they are nearly ten times smaller than the z resolution (1 mm). This is challenging for the meshing software, which aims to preserve the spatial information of the images while creating a high-fidelity tetrahedral mesh (those with similar angles at all junctions). Meshes made with the full DBT images take a very long time and, if they are even possible, are often of poor quality due to extended tetrahedral with extreme angles attempting to preserve small variations in the segmented images. Instead, segmented images are reduced to 20% of their original size, producing high-quality meshes in a reasonable amount of time but with the loss of some of the finer segmentation details. These are likely unimportant due to the low spatial sensitivity of NIRST; note that the images are not extremely distorted in Figure 39.



*Figure 39: The left image is the DBT segmentation at full resolution 1500 x 1948. The second image was reduced to 20% of the image on the left. The final image shows an interpolated slice at the same level as the prior two images, extracted from a mesh of*

*40,000 nodes. The overall tissue structures are recognizable but most of the finer details have been lost.*

Setting an equal pixel spacing for all DBT images is another important post-processing step. Although the DBT header files indicate the same pixel spacing for all images, this is not the case as confirmed by Hologic engineers. Inferior slices are taken with a larger X-ray field than superior slices. The superior slices appear magnified and have larger spacing between the nodes than the inferior slices. For this particular system, the following linear interpolation formula can be used to determine the true pixel spacing for a given slice:

$$\text{Pixel Spacing} = (K - k_i)/K \quad 20$$

Here,  $K=584$  is the fixed source-to-detector separation for the DBT unit, and  $k_i$  is the slice height above the breast tray, in centimeters. For all images, the center pixel on the right hand side is in the same location, and the images are expanded about that point. Additional code was written to normalize the pixel spacing for all images according to the formula. While the true pixel spacing does not matter for radiologists viewing the images, it is vital when trying to model a breast volume for NIRST reconstructions, which require correctly sized breast volumes and correct source and detector separation distances to accurately model light absorption through the volume.

#### **3.1.14. Meshing**

When making a mesh, the number of nodes desired will change depending on the tissue volume and imaging system being used. In our case, 30,000-45,000 nodes were sufficient to reconstruct the tissue volume in a normal breast. This resolution is lower

than other imaging systems; however, as this system relies exclusively on CW data, simulations showed reasonable reconstructions at a lower resolution than for FD data sets. Additionally, with an exceptionally rich data set (over 5,700 measurements per scan), computation time was quite high so meshes were made as small as possible to reduce this time.

In the automated mesh script, a desired number of nodes (32,500 for normal breasts) is input, as well as a threshold value off from the desired number of nodes that would be acceptable (in this case, 2,500), so that the mesh is guaranteed to possess between 30 and 35,000 nodes. Starting with a tetrahedron size of 2.5 mm, experimentally tested to produce optimal results across cases, the script creates meshes, increasing or decreasing this size according to the number of nodes produced, until the desired number of nodes is achieved. This streamlines the meshing process, produces uniform and comparable meshes for all patients, and can be performed by anyone without any advanced knowledge of meshing techniques. Typical final tetrahedron sizes range from 2-3 mm depending on the breast size.

The meshing tools in Nirfast possess additional capabilities to refine a specific region of interest. It is possible to increase the number of nodes in a subsection of tissue by using smaller node spacing, typically between 0.5 and 1 mm depending on the size of the region of interest (ROI). If this spacing was used on the whole breast, the number of nodes would be very large and require lengthy computation times. For any cases with small ROI, spacing is selected such that 5% of the total number of nodes are labeled as being part of the ROI, or the smallest node spacing possible. These meshes were

reconstructed with around 40,000 nodes so as not to decrease the overall mesh resolution while creating a highly resolved ROI.

After the volume has been meshed, sources and detectors are placed along the tissue boundaries. The detector locations remain fixed for all imaging, and are saved in a text file. Source locations vary depending on which source spacing pattern is used. The small pattern has the sources spaced at 1.0 cm intervals, the medium at 1.5, and the large at 2.0. Most patients need either small or medium spacing, but there are some cases requiring the largest spacing. Information about the source configuration is contained in the header file for the patient, including the number of rows and columns, the starting source position, and the spacing between positions. The origin of the coordinates for the sources is the center detector location. This method of positioning sources allows for greater versatility in source numbers and positions without requiring extensive software changes.

### ***Conclusion***

This chapter describes how NIR light propagates through tissue, and the methods of image reconstruction, image segmentation, processing, and mesh creation. Clinically relevant tissue chromophores such as hemoglobin, oxygen saturation, water, and fat content can be derived from absorption properties, although the reconstruction process is considerably more complex due to the pervasive light scattering. Using the diffusion approximation to the radiative transport equation, it is possible to generate boundary data based on the optical properties of an FEM mesh. Minimization of the error between simulated data from forward models and actual data allows for iterative solutions of the

inverse problem, generating optical properties from boundary data. This chapter also extensively describes DBT image formation and segmentation methods. DBT image processing is more challenging than CT due to the limited angle rotation of the X-ray gantry, making tissue segmentations particularly difficult. Post processing DBT images can remove some artifacts and improve segmentation. Segmentation methods for distinguishing adipose and fibroglandular and chest wall muscle, as well as separating lesions from the background have all been successfully adopted for DBT imaging. Using such techniques, it has been shown that DBT segmentation performs as well as FDA-approved Quantra software for mammography in calculating fibroglandular volume percentages, although it does not have the same fidelity as CT- or MRI-based segmentation in localizing the different tissue types.

Finally, this chapter discussed mesh creation from DBT segmented images. They require post-processing changes to convert to real space coordinates and facilitate the meshing process. These steps, as well as meshing and source detector placement, are all semi-automatic to decrease sources of error from user variation and to decrease the time between data collection and image reconstruction.

## **Chapter 4: Phantom Experiments**

Phantoms play a vital role in the development, validation, and quality control of imaging systems. Clinically, they are recommended for quality management or mandated for technical surveillance to avoid system malfunction and possible adverse effects on patients undergoing examination. In research and development, phantoms are used for early-stage feasibility testing and performance evaluation, diagnosing errors and detecting underperforming instrumentation, and enabling comparisons of data acquired on different imaging systems.

### ***Introduction***

Breast mimicking phantoms are an important component for data quality assurance for both X-ray and optical imaging modalities. Phantoms possess known qualities that can be correlated with imaging results to ensure minimum performance standards (as required by law for clinical X-ray imaging) as well as provide feedback on the capabilities and limitations of a developing imaging system. Four main types of phantoms have been used in order to probe the size, contrast, and depth resolution as well as chromophore recovery in the combined NIRST-DBT imaging system. The first phantom experiments involve a homogeneous resin phantom, helpful in testing the system while designing and optimizing hardware as well as for calibration during phantom and patient exams. The second phantom study involves using a spectrally varying resin phantom comprised of several slices and containing three different-sized inclusions in order to characterize size, contrast, and depth resolution of the NIRST-DBT platform. Next, phantom experiment uses agar-based hemoglobin phantoms to

demonstrate the ability of the NIRST system to quantify linear recovery of hemoglobin levels in tumor-sized inclusions in a background similar to the average breast. Lastly, development of an anthropomorphic breast phantom with lipid and water composition similar to that of tissue is useful in quantifying system sensitivity to these chromophores.

#### **4.1.1. Calibration Phantoms**

Phantoms are typically used in validation studies of system accuracy and repeatability, and can be constructed from resins or plastics. They should be long lasting, homogeneous, and durable, possessing optical properties similar to tissue. Extensive work has been reported on the development of these types of phantoms, and several papers review the different materials and scattering agents that are available<sup>145,146</sup>. Measurements from these phantoms should be highly repeatable so that any changes in the data can be attributed to changes in the system. At present, commercial companies exist that produce customized homogeneous phantoms with tissue-like optical properties in a wide range of sizes and materials<sup>90</sup>. Two such phantoms have been purchased and tested on the NIRST-DBT system. One is a hard rectangular resin homogeneous phantom used for initial calibration and testing of the system. The second is made up of spectrally varying resin cut into slices so that the thickness of the phantom can be changed. In addition to five solid slices, an additional slice was drilled to create three different cylindrical inclusions of varying heights and diameters. This phantom is important in understanding the depth- and size-dependent effects on recovered hemoglobin concentration.

#### 4.1.2. Anthropomorphic Phantoms

A second type of optical phantom, referred to as an anthropomorphic phantom, is intended to mimic the breast more closely both in physical shape and tissue composition. It is important to recover tissue chromophores in different concentrations, locations and sizes within a heterogeneous volume of material of similar scale to the breast when investigating a NIRST system's ability. These phantoms assist in the optimization of data collection and image reconstruction for a given system. They are additionally helpful in determining which patient populations are most likely to benefit from the technique. As in system validation phantoms, durability and repeatability are important. However, maintaining a spectral absorption profile and absorber concentrations similar to those in the tissue of interest is paramount to success in developing an anthropomorphic phantom. To mimic the breast closely, the phantom should be composed of hemoglobin, water, and lipids in varying physiological concentrations, with central zones more similar to fibroglandular tissue and outer areas more representative of adipose tissue in concordance with the typical breast parenchymal pattern<sup>147</sup>.

Early experiments describe breast-simulating phantoms constructed from hemoglobin, water, and intralipid<sup>148</sup>. The intralipid is added not to mimic breast lipid content, but to create optical scattering. Thus, it is used in low concentrations by volume (~1%). These phantoms effectively emulate the tissue optical properties of oxy-hemoglobin, but they do not represent physiologically relevant water or lipid contents due to their low intralipid percentage<sup>149-151</sup>. The final section of this chapter discusses a

novel phantom technique that incorporates water and lipids in physiologically relevant concentrations.

### ***Phantom Calibration***

#### **4.1.3. Characterization of Reference Phantom**

The earliest reconstructions involved the simplest possible case, a large homogeneous resin phantom. This involved matching slope of the log of the detector output versus the source detector distances to an expected absorption coefficient. In this case, an analytical fitting method was needed as there was no additional calibration phantom available. This phantom had been previously measured at the factory where it was made using a time-domain imaging system at a single wavelength that was also used in the NIRST-DBT system. The scattering coefficient was taken directly from the factory's measurements. The calculated absorption on the NIRST-DBT system was  $0.0094 \text{ mm}^{-1}$ , while the measured absorption was  $0.0107 \text{ mm}^{-1}$ , a 12% error in the measurement. This phantom was used for initial characterization studies, but the absorption coefficients were quite high relative to actual breast tissue, so a second phantom with optical properties more similar to the breast was purchased for the reference calibrations and is described below.

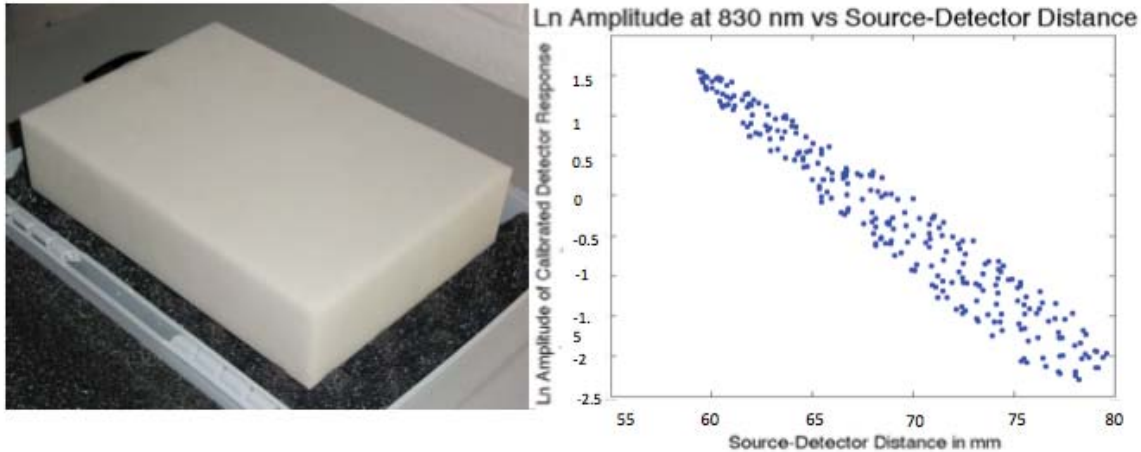


*Figure 40: A photograph of the large homogeneous resin phantom (left). Data showing the log of the amplitude of the detector response vs. the source detector distance (right). A line was fit to this graph and corresponded to an absorption coefficient 12% off from the measured value on a time-domain system.*

#### **4.1.4. Prior Calibration Methods**

After early phantom measurements showed reasonable accuracy using analytical fitting methods, methods for calibrating phantom and human subject measurements were developed to minimize system artifacts in image reconstruction. After data is collected, it is calibrated in two steps. Data is first calibrated to adjust for the difference in detector sensitivities as described in Chapter 2. The second calibration step must fit the data to the model, and generate an initial guess. We account for small errors such as slight mischaracterization of source and detector positions, scratches in polycarbonate plates, and source strength by imaging a homogeneous reference phantom prior to patient imaging as described for other systems<sup>152,153</sup>. Essentially, these methods fit a first-order approximation to the log of the intensity times the source detector distance vs. the source

detector distance, as shown for a phantom in Figure 41. According to both model and experiment, data presented this way are linear<sup>154</sup>. This is an intuitive way to present data from a system with many sources and detectors, such as the NIRST-DBT system. The slopes of these lines are equal to the attenuation coefficient at a particular wavelength. This is a reasonable approach to calibrate data to the model. Unfortunately, it also smoothens the data, reducing image contrast, and tends to break down when the number of data points is severely limited<sup>155</sup>. Therefore, a new method was made to calibrate each individual data point to improve data fidelity and preserve contrast.

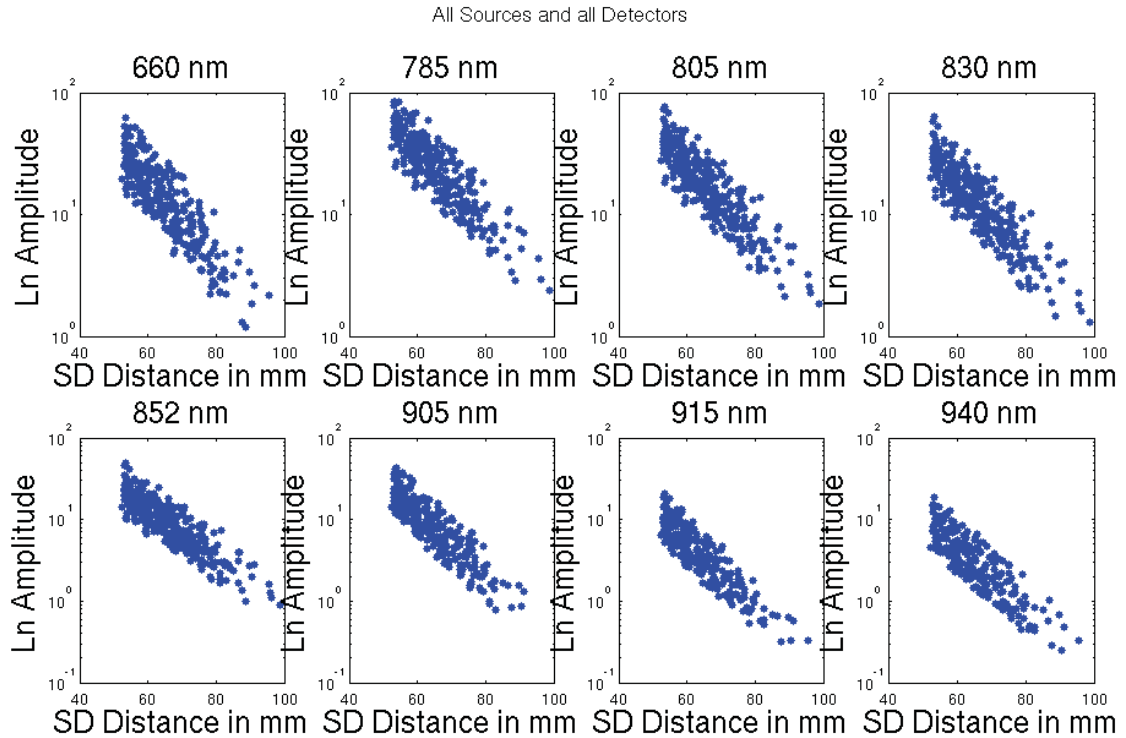


*Figure 41: Amplitude data from a patient shown for all wavelengths. The natural log of source-detector distance times intensity is linearly decreasing with source detector distance with the slope being  $\mu_a$  at that wavelength.*

#### 4.1.5. Direct Data Calibration Techniques

Early calibration techniques relied on analytical photon fluence for cylindrical geometries<sup>13, 14</sup>. However, the breast volume represented in the images in NIRST-DBT do not fit into such a simple model. Rather than calculate photon fluence directly, an alternative technique using the difference between the diffusion model and measured data on a known reference phantom is used in calibration.

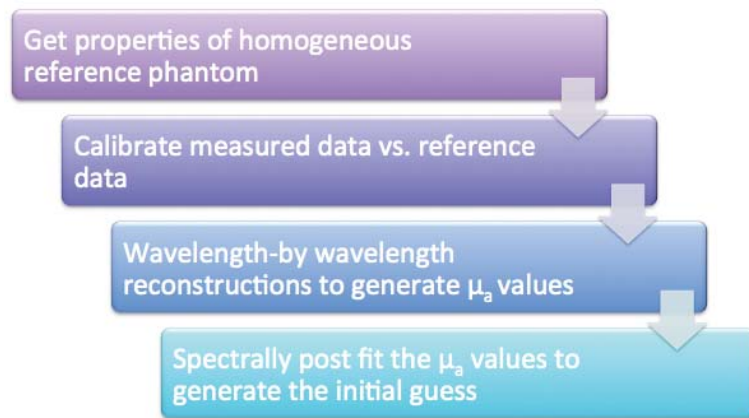


*Figure 42: The main parts of the absolute calibration algorithm are illustrated schematically.*

This method is shown in Figure 42 with four steps: assigning the optical properties of the homogeneous reference phantom, calibrating the measured data, wavelength by wavelength reconstructions and generating the initial guess for reconstruction. The properties of the reference phantom must be measured or supplied, and once they are assigned, they can be used in future experiments. The phantom used here was purchased from a company and ordered to be similar to another smaller spectrally varying phantom that had previously been characterized on a broadband system. The phantom had been tested at two different wavelengths for absorption and

scattering coefficients. Using this information as well as the spectral measurements of the smaller phantom, expected absorption and scattering coefficients for all wavelengths measured on the NIRST-DBT system were calculated and written to a text file that is referenced during the calibration process. In addition, this calibration phantom was measured on a broadband system, yielding significantly different results for the scattering coefficient as shown in Figure 43. At some wavelengths, the two have very similar absorption profiles, but at others there is up to a 40% differences between the two. The measured scattering using the broadband system is roughly half of the time domain measurements. Absolute measurements on the broadband system were known to vary depending on calibration procedures, so we opted to use the time domain measured and fit absorption and scattering coefficients as the ‘truth’ for the calibration for our system.

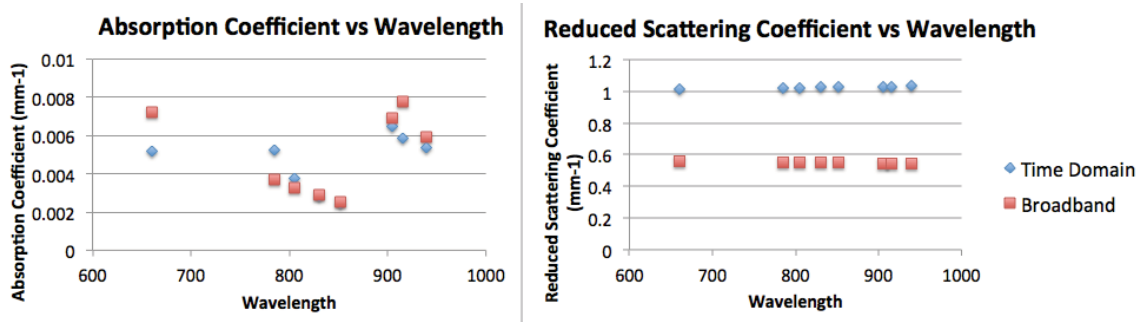


Figure 43: Absorption and reduced scattering coefficient vs. wavelength as derived for all wavelengths from the time domain system measurements (shown in blue) as well as from measurements on the broadband system (shown in red).

Patient data ( $d_p$ ) is calibrated absolutely with respect to measured data on the homogeneous reference phantom ( $d_r$ ) and simulated data from a tetrahedral finite element mesh of the phantom with correct optical properties ( $f_r$ ). Data ( $d_c$ ) are calibrated by

$$d_c = \frac{\log(f_r)}{\log(d_r)} \log(d_p) \quad 21$$

This corrects for errors that in the data acquired from the reference phantom and patient as well as fitting all the data to the model in one step. Maximum image contrast is preserved because there is no averaging for difference over sources; each data point is calibrated absolutely versus the difference between the reference and the model.

Additionally, the absolute method is effective when the number of data points is limited.

#### 4.1.6. Single Wavelength Reconstructions

The initial guess for reconstruction must be generated. Wavelength-by-wavelength calibration methods have been shown to be more robust for calibration than multi-wavelength methods<sup>158</sup>. Similarly to the slope-calibration method, we obtain  $\mu_a$  and  $\mu_s$  at each wavelength and post fit them to the main absorbers' extinction coefficients. Rather than using the slope of the data, we elect to use single-region reconstructions at each wavelength. This method fits the data to the model iteratively and can be used with only a handful of data points. The drawback is that these reconstructions also require an initial guess. However, since they are only calculating  $\mu_a$  in a single region, they are much less sensitive than the initial guess of multi-region spectral problems<sup>159</sup>. Initial guesses for absorption at each wavelength are calculated from an average breast case consisting of 10 $\mu$ M of both oxy- and deoxy-hemoglobin and 0.4 volume fractions of water and lipids. This initial guess works for the vast majority of cases, but is too far off from the actual value for convergence in some cases. In all of these cases, the initial

guess was too high; simply halving the initial guess led to convergence for all wavelengths in all patients.

Lastly, the data is post fitted to recover tissue chromophore concentrations for the initial guess of the spectral fit. An alternative method involving an additional single-region, multi-wavelength spectral reconstruction that applies the spectral constraints present in the full image reconstruction may be desirable, but adds additional time to the reconstruction. Obtaining an initial guess in this fashion means that the initial guess will be closer to the final values and minimizes the chances of the reconstruction falling into a local minimum<sup>160</sup>.

### ***Spectral Slice Phantom***

In order to successfully image breasts with suspected masses, it is necessary to know the capabilities of our NIRST-DBT system in terms of size, depth, and contrast resolution. Efforts to characterize these limits were performed using a custom-designed rectangular resin based phantom with a spectrally varying absorption profile.

#### **4.1.7. Phantom Design**

This phantom is comprised of four 1 cm slices as well as two 2 cm slices. One of the 2 cm slices has several cylindrical holes of different sizes machined into it, including a 1.5 cm diameter and 1.5 cm height for the largest hole, 1 cm x 1 cm for the medium-sized inclusion, and 0.7 cm x 0.7 cm for the smallest one. These slices can be arranged in any order, mimicking a lesion at four different depths and two different locations by rotating the asymmetrical hole layer. This phantom is comprised of a spectrally varying resin; the absorption and scattering coefficients have been quantified using both time

domain and broadband imaging as described in the prior section, Characterization of Reference Phantom. When only the homogeneous slices are included, the phantom is used as the reference calibration for patient exams. The experiments described below discuss the use of this phantom with the inclusion slice.

#### **4.1.8. Procedure**

Spectral slice phantom imaging closely mirrors procedures used in patient imaging in order to accurately assess the system's capability to detect small tumors in large breasts. In the experiments described below, the phantom was measured using the NIRST-DBT system with a carefully fixed liquid volume pipetted in each small hole in the phantom, starting with the lowest hemoglobin concentration and sequentially testing up to the maximum. The phantom is shown in Figure 44. By fixing the volumes and position of the phantom, it was possible to minimize errors due to slight differences in volume and position so that the only source of variation was inter-depth position changes and source and detector hardware differences in strength and sensitivity respectively. The liquid in each inclusion was comprised of 1.15% intralipid to roughly match the scattering of the resin phantom, as well as carefully measured concentrations of porcine blood and water. The phantom slice containing the inclusions was not moved in between each contrast level but was of necessity moved between each depth level after all concentrations for a given level were measured, as prior experimentation without fixed volume and altered positions showed some data that were inconsistent with the contrast linearity trends as shown in Figure 44. The overall trends are linear with a single data point in each case appearing off the expected trend. In these experiments, the inclusions

were filled with a volume until they appeared full, and instead of keeping the depth constant while changing the contrast, the contrast was fixed while the phantom position was changed. Slight differences in positioning and volume may have caused inaccurate reconstructions. These graphs show the same experiment repeated twice for consistency. Only four of the most stable wavelengths were used in the reconstruction, corresponding to wavelengths 660, 808, 830 and 852 nms, as other wavelengths were unstable, as shown in Figure 45. There are large variations in detector output between homogeneous and anomaly data sets, with up to 0.2 V difference near inclusions for the highest contrast levels. However, there is a pervasive +/-0.05 V difference for all data points at all contrast levels; this range was larger for 785 nm than the wavelengths selected for this experiment.

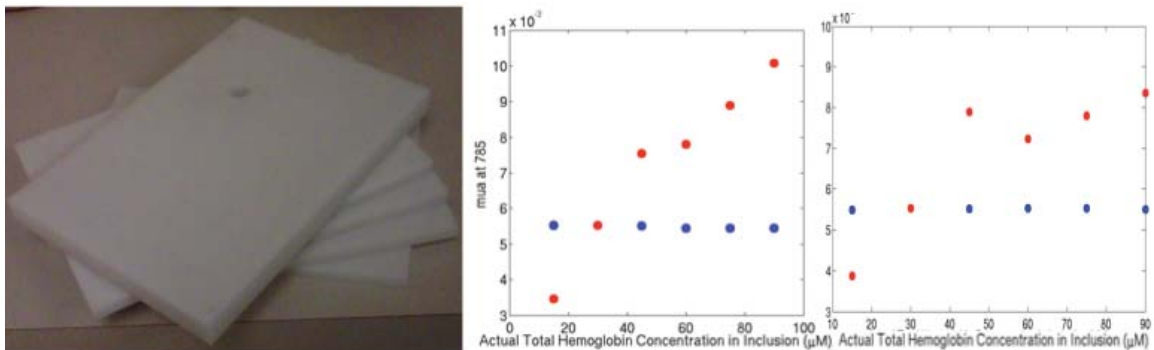


Figure 44: Photograph of the spectral slice phantom and early results from two separate phantom experiments using a single inclusion. The absorption coefficient for a single wavelength (785 nm) for the background (blue) and the inclusion (red) are shown for (15, 30, 45, 60, 75, 90 μM).

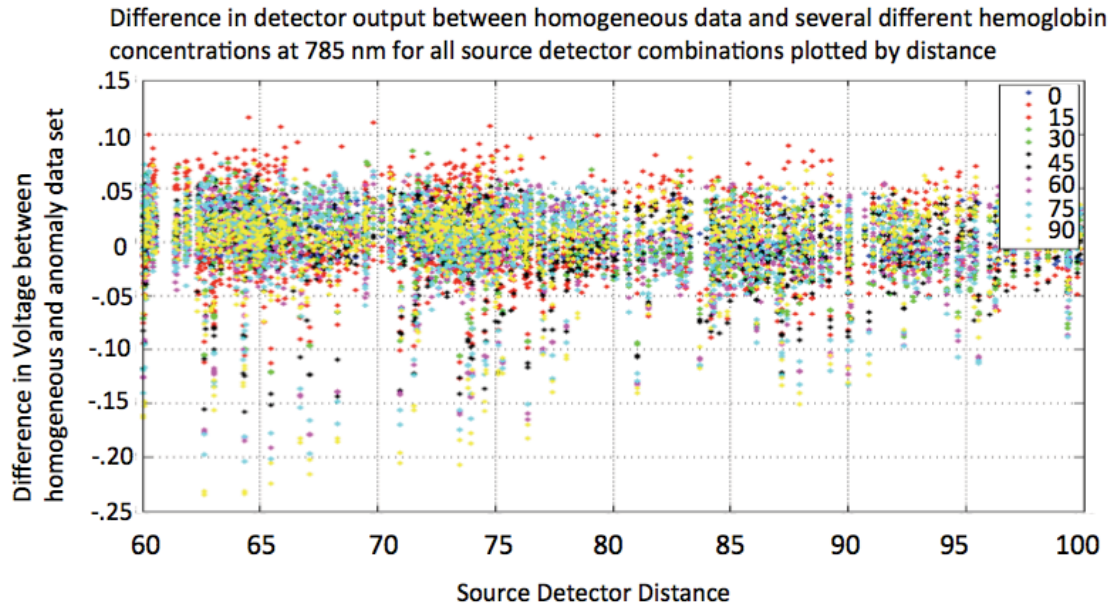


Figure 45: Graph of all data points collected for a contrast phantom experiment for 785 nm laser source. The x-axis shows all source-detector pairs plotted by distance, while the y-axis shows the difference between the homogeneous calibration phantom and the anomaly data set. The anomaly data sets were 90 (yellow), 75 (teal), 60 (magenta), 45 (black), 30 (green), 15 (red)  $\mu\text{M}$  Hb, each of which was measured twice.

Reconstructions were performed on a wavelength-by-wavelength basis because the resin phantom was not made up of tissue chromophores. The phantom meshes were highly refined in the inclusion regions, with a spacing of 0.8 mm for all inclusions and 2.5 mm for the remainder of the volume. The reference phantom in this case had a hemoglobin concentration of  $15\mu\text{M}$  in the inclusions, as that most closely matched the absorption of the background. Hard priors reconstructions of four regions was performed: one for the background and one for each inclusion. Small regularization values were used to recover HbT for all the inclusions, as shown in Figure 46. This was possible

because noise levels were extremely low since the reference phantom was very similar to the anomaly phantom, varying only in the area of the inclusion. At low regularizations, noise can dominate and reduce the stability of the reconstruction. That did not happen in these phantoms; chromophore recovery was quite stable even at very low regularization. Smaller lesions require lower regularization values; in this case,  $10^{-6}$  was necessary to fully recover the smallest inclusion, while  $10^{-4}$  could recover HbT in the largest inclusion. Post fitting of the inclusion results was performed to obtain total hemoglobin levels. Water and lipid content was not assessed due to non-physiological levels in the inclusions and elimination of higher wavelengths due to lower stability.

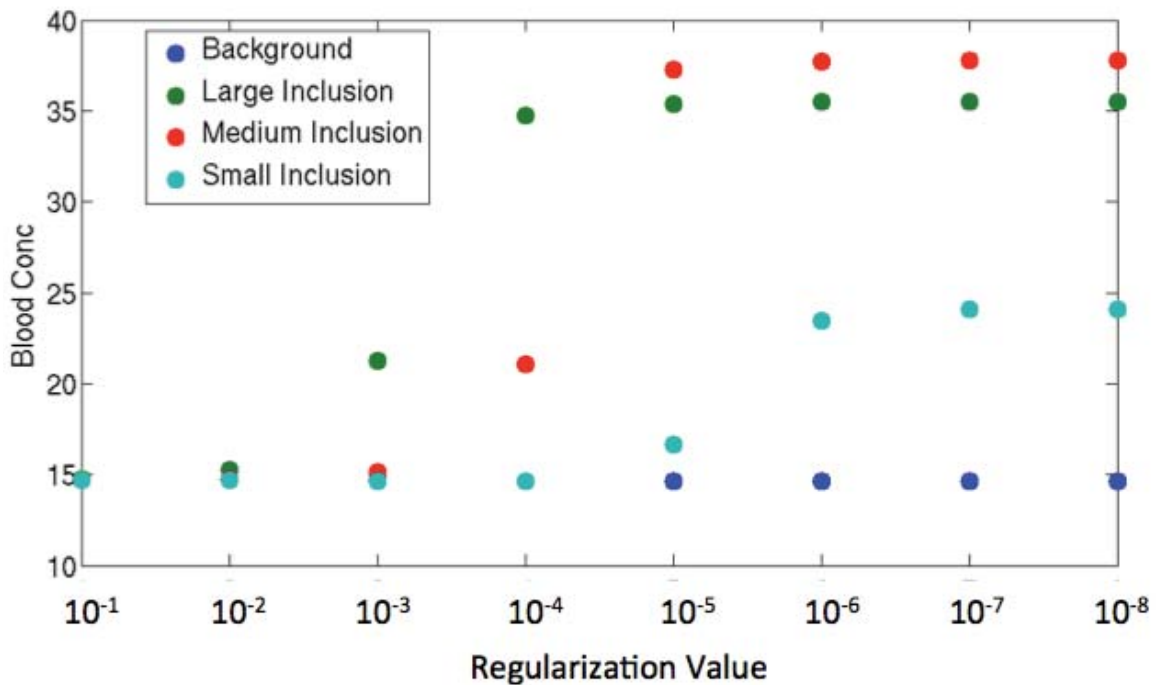


Figure 46: Graph showing the dependence of inclusion size chromophore recovery on regularization.

#### 4.1.9. Depth-Dependent Contrast Recovery

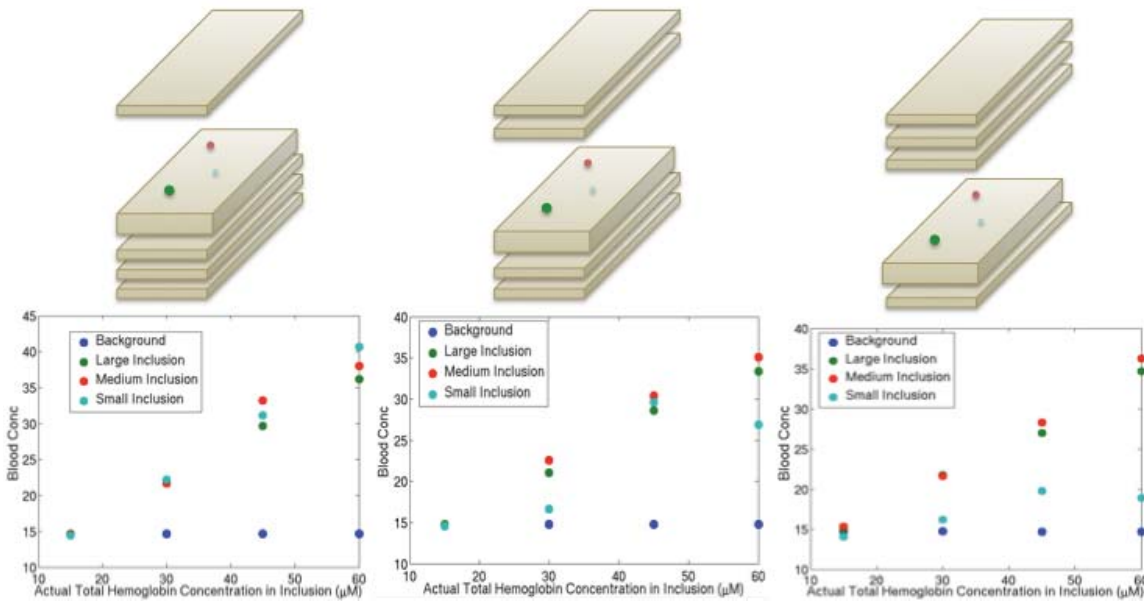


Figure 47: Graphs depicting total hemoglobin recovery vs. actual hemoglobin concentration for the background using inclusions of different size at three different depths

Measurements of the slice phantom at several different depths showed linear contrast recovery of about 66% of the actual value on average. . Linear recovery of hemoglobin concentration is noted for all levels with similar recovery at each concentration for all depths. The largest and medium-sized inclusions were consistently recovered in a linear fashion regardless of depth with similar HbT levels. There was slightly lower recovery of hemoglobin at the two deeper depths (38 uM vs. 34 uM) for the largest two inclusions. The smallest inclusion was recovered as well as the larger lesions for the shallowest depth. At the middle depth, recovery was variable and in the deepest depth, the overall recovery of the smallest inclusion was lower than for the middle and larger inclusion sizes. There are several potential causes for this. The

smallest inclusion is the most susceptible to recovery changes due to slight position shifts, as may have been the case for the consistent lower recovery seen in the deepest case. Additionally, as signal disturbances for an inclusion of this size are quite small, random fluctuations in source strength could easily augment or diminish the recovery in the smallest inclusion.

#### **4.1.10. Inclusion Volume Mischaracterization**

This phantom model is a reasonable surrogate for a tumor-bearing breast. As the NIRST imaging is coupled to DBT, it is important to understand the strengths and limitations of DBT in localizing tissue regions and the effects of spatial mischaracterization on the NIRST results. For example, DBT is a highly spatially resolved imaging technique, but the limited angle of rotation leads to poor z-resolution and partial volume averaging. Thus, it can be difficult to determine the extent of a lesion in the z-plane direction. To simulate this potential error in the model of the inclusion phantom, inclusions were extended by 50% of their volume in the z-direction, and also shrunk by 50% in the z-direction. In all cases, the average depth was the same. For a single depth, there were marked changes in the recovered contrast as a result of volume mischaracterization as shown in Figure 48. Average hemoglobin recovery for the highest concentration, 60 $\mu$ M, were 32, 38 and 53 $\mu$ M for the overestimated, true, and underestimated tissue volumes, respectively. With the exception of the smallest inclusion in the underestimated case, the three graphs are remarkably similar, except in their actual recovery of HbT. This is due to the constraints of hard priors, in which all nodes marked as part of a specific region will recover the same chromophore properties.

In the overestimation case, the inclusion included some of the background tissue, so the average content in the inclusion was a lower HbT, as the background possessed lower HbT. For the underestimation case, a tiny portion of the inclusions were mischaracterized as background. However, due to the large volume of background tissue, this small addition did not alter the recovered HbT in that region; instead, a larger amount of signal attenuation was attributed to a smaller inclusion region, leading to higher HbT recovery. As shown in the small inclusion, there are limitations to this. As inclusions become too small, their measurement sensitivity and importance during image reconstruction decreases and they may not recover a higher concentration when the size is underestimated.

Another potential segmentation scenario was tested involving mischaracterization of z-position. For this test, the correct volumes of the inclusions were used; however, the phantom model predicted that the lesions were 1cm deeper in the tissue than they actually were, as shown in Figure 49. The results for the correct model are found in Figure 47 and comparing the two, there is a decrease in recovered hemoglobin for two of the three lesions, with a 20% decrease in recovered HbT for the smallest lesion and a 10% decrease for the largest lesion. With the exception of the smallest inclusion in the shrunken case, which had fewer than 300 nodes in the mesh and was only 0.7 mm x 0.35 mm, there were no changes in the linearity or shape of the graphs. However, the actual recovered blood concentrations were altered by the changes in volume for the three cases. Thus, it appears that depth mischaracterization can decrease the recovered contrast, especially in small lesions.

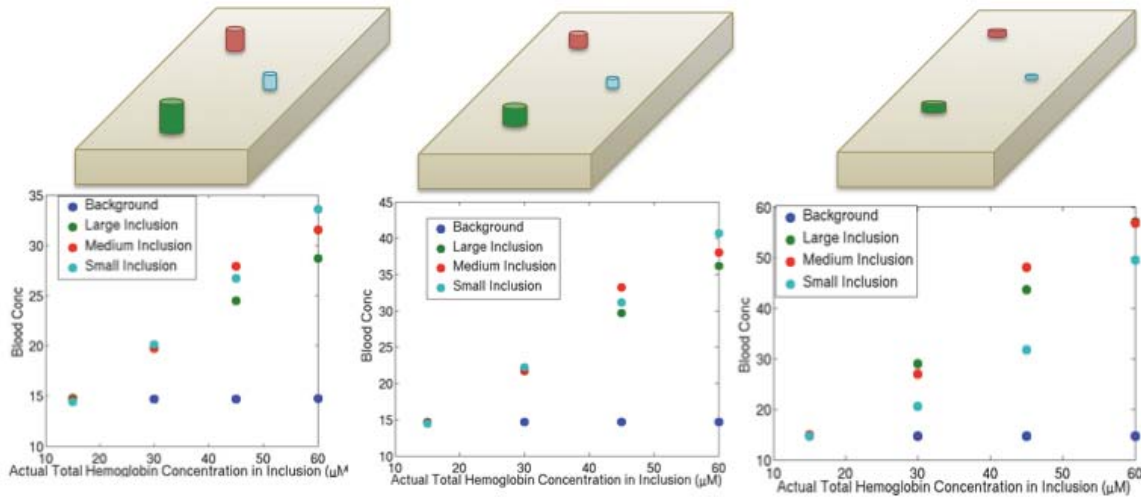


Figure 48: The effects of inclusion volume mischaracterization are shown for the shallowest depth. On the left, overestimation in all inclusions of 50%, true volume in the center, and 50% of the true volume on the right hand side

Breast DBT segmentation for NIRST will benefit from these results, as accurate segmentation of tissue structures is vital to recovering the correct HbT. However, it is important to note that a phantom has distinct boundaries, whereas malignancies and benign tissue can have much more fluid boundaries. In DBT segmentation, the radiologist defines the boundaries of the ROI and past studies have shown that estimates based on mammography of tumor size are underestimated by 1 mm average when compared to pathological estimates along the largest diameter, with up to an 11 mm 95 % confidence interval. Additionally, the composition of the surrounding tissue can effect the volume of can affect the estimated voulme<sup>161-163</sup>. The radiologist's measurements are solely along the longest axis of the tumor, so total volume estimates are likely off by a considerably larger margin. It is particularly challenging to determine the extent of the tumor in the z direction when partial volume averaging can make the lesion appear

throughout nearly the entire thickness of the breast. However, Doppler ultrasound has shown that there are often regions of increased vascularity outside of the defined tumor area<sup>164</sup>, so overestimation of the tumor boundaries may not lead to an overall decrease in hemoglobin recovery. Hence, although segmentation errors will occur in deciding the boundaries of an ROI, it is expected that in breast tissues the effects of such errors will be less than in phantoms due to the lack of rigid boundaries found in phantoms. Any volume overestimation error will result in an averaging of tissue that can lower contrast recovery if the surrounding region is not highly vascularized. Tumor volume underestimations can result in higher-than-expected tumor contrast if the region surrounding the tumor is large and not absorbing.

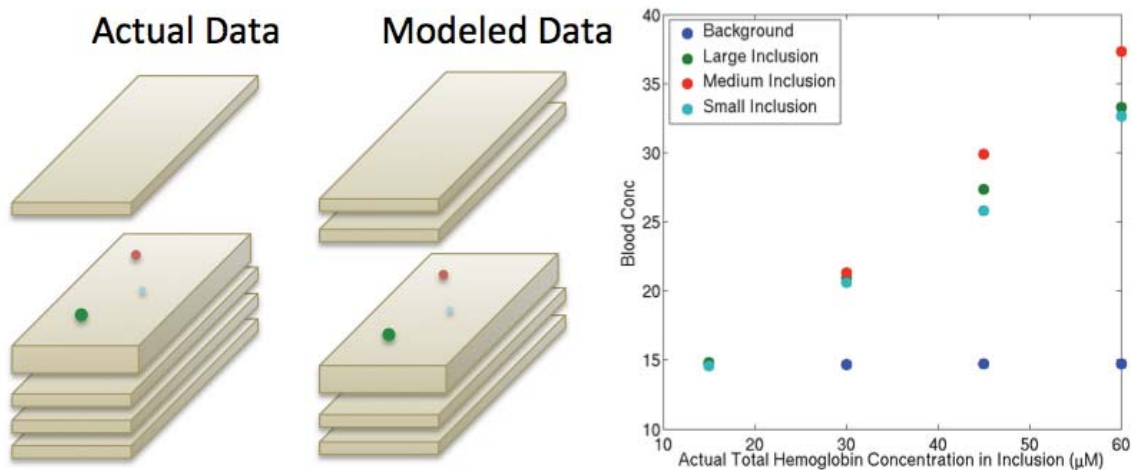
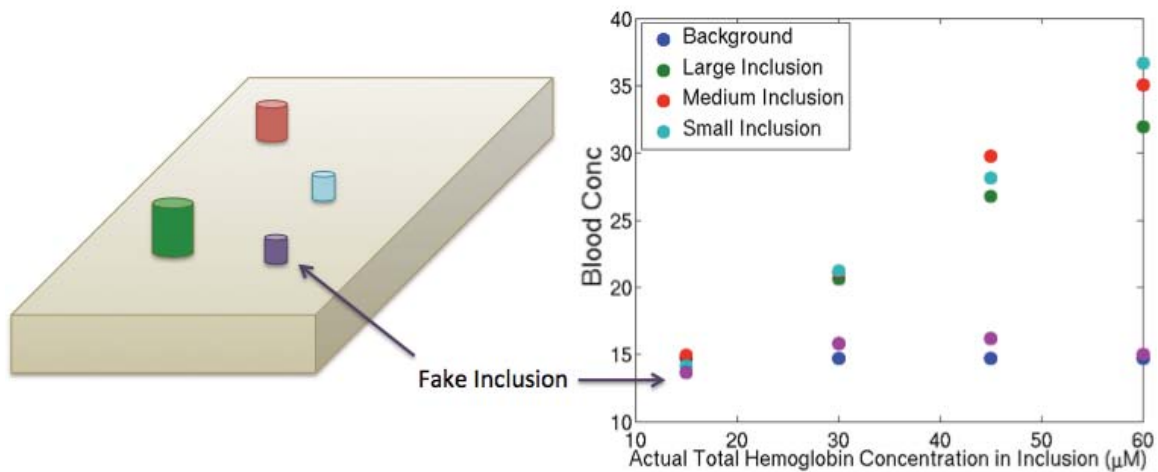


Figure 49: The effects of z-depth mischaracterization on phantom results are shown with the actual inclusions measured between 2 and 3 cm from the top of the phantom and modeled as between 3 and 4 cm from the top of the phantom.

The inclusions were highly refined in the mesh process and their volumes were much smaller than the background area. In order to be sure that no contrast was due to

the specialized meshing or small size of the inclusions, an additional inclusion was added to the model that did not exist during the experimental process. As expected, this region recovered hemoglobin levels very close to those of the background and did not vary with different hemoglobin concentrations. This indicates that it is unlikely that a false positive result would occur, i.e., that a region in a DBT image was labeled by a radiologist as benign and actually had no greater hemoglobin content would appear to have higher hemoglobin than the background.



*Figure 50: A section of the resin material was marked as a separate region for reconstruction. As expected, the recovery of hemoglobin was very similar to that of the background.*

#### 4.1.11. Discussion

Imaging small inclusions only minimally alters signal levels at a few detectors. Reduction or elimination of noise sources are important in order to detect such signals. This type of experiment assists in diagnosing minor issues with system hardware and

reconstruction algorithms. Two particular issues were brought to light during the course of this experiment, one involving the pixel spacing in the DBT images and a second involving the source strength variation. As noted in Chapter 2, pixel spacing in the DBT images is not uniform. This was uncovered and fixed during extensive source and detector localization studies to ensure the phantom inclusions were correctly located in the imaging field. Keeping the phantom stable throughout the imaging process mitigated errors due to phantom positioning.

Earlier calibration showed source strength variation on the order of 0.5-4% depending on the laser diode. Unfortunately, when measuring small inclusions in a large phantom, changes in signal attenuation for the smallest inclusion at source and detector pairs near the inclusion can cause signal attenuation of only a few percent as well. For example, in case of the smallest inclusion measured here, a 3% difference in signal attenuation for the largest contrast level and the closest source detector pair between the measured and homogeneous case was detected. Thus, although source calibration seemed unimportant during initial system development, these phantom experiments highlight the importance of this step. In a repeatability experiment, the same inclusion phantom was measured seven times, without movement. Variation in the background, large, medium, and small inclusion were calculated to be 0.3, 4.7, 13.3 and 5.6% respectively. Thanks to the highly controlled nature of this phantom experiment, all sources of error are attributable to short-term shifts in source strength and detector sensitivity. In the large background region, there wasn't a lot of change as small shifts are averaged over a large number of data points so random fluctuations can be smoothed out. However, for the inclusions, there was a much greater variation in the recovered

concentration because their measurement sensitivity is limited to a small number of sources and detectors. Hence, small shifts in source strength correspond to variation in recovered chromophore concentration, especially for smaller regions of interest.

Unfortunately, it is not possible to retroactively obtain this information; instead, multiple scans of each phantom were taken to ensure measurement fidelity, a luxury not possible during patient scans. Future work will involve hardware improvements allowing real-time referencing of the source strength, facilitating an improved signal-to-noise ratio.

### ***Hemoglobin Phantoms***

Phantoms comprised of water, type 1 agarose, 20% intralipid (to recreate physiologically relevant scattering), and whole porcine blood were the earliest tests of chromophore and contrast recovery of the new NIRST-DBT system. These phantoms focused on recovery of oxy-hemoglobin, as inclusions created in the phantom had variable oxy-hemoglobin while the rest of the chromophores were unchanged across the study.

#### **4.1.12. Phantom Design**

Agarose-based phantoms were created using water, type 1 agarose, dilutions of 20% intralipid, and whole porcine blood. Two phantoms were created, both with 15  $\mu\text{M}$  blood concentration mixed with 1% intralipid solution to mimic typical breast optical properties<sup>22</sup>. Each phantom was 6 cm in height, comparable to average compressed breast thickness during mammography<sup>29</sup>. The phantoms were comprised of two sections – the first being a 5 cm lower slab, and the second being a 1 cm thick upper slab (placed on top of the lower section). The two-section design facilitated the addition of internal

inclusions with different contrasts created by mixing intralipid with varying amounts of blood. System calibration was performed with a homogeneous phantom (i.e., upper and lower slabs with the same concentrations of blood and intralipid and no inclusions). Contrast detection was evaluated by embedding a localized region of heterogeneity in the lower section through the filling of a cylindrical hole 3 cm in diameter and 2 cm in height with solutions of 15, 30, and 45  $\mu\text{M}$  blood mixed with 2% intralipid. A 1 cm thick homogeneous slab was placed on top of this lower section to complete the internal inclusion structure. True scattering values were extrapolated from prior optical property characterization studies<sup>165</sup> and were used in the CW reconstruction algorithm.

#### 4.1.13. Results

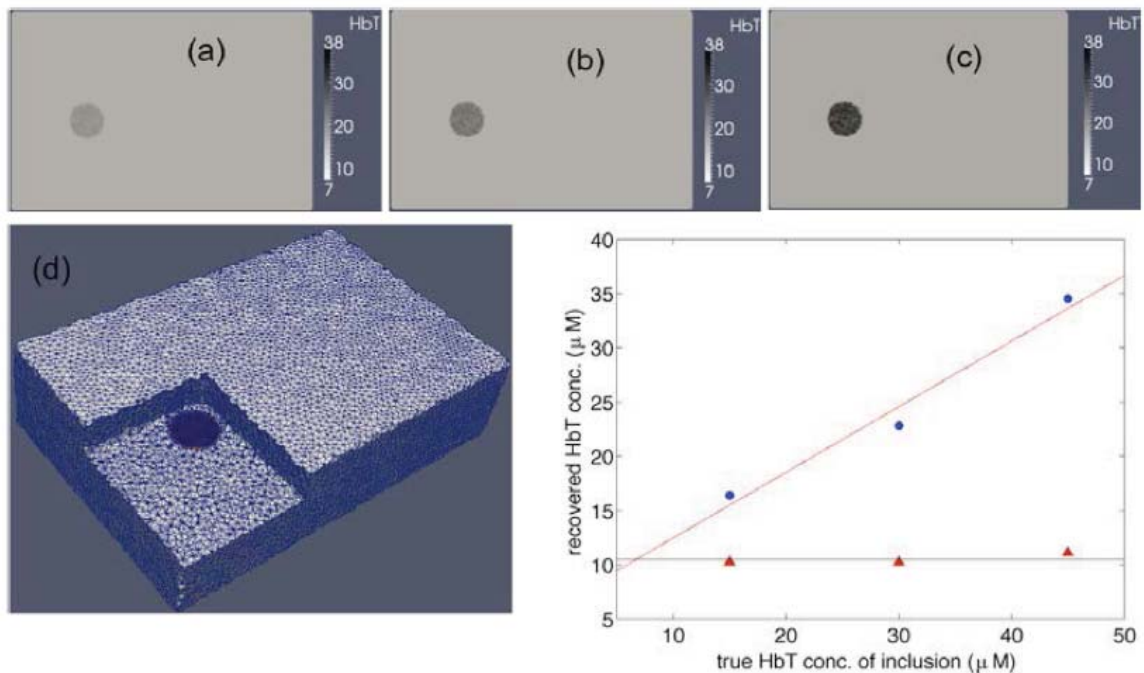
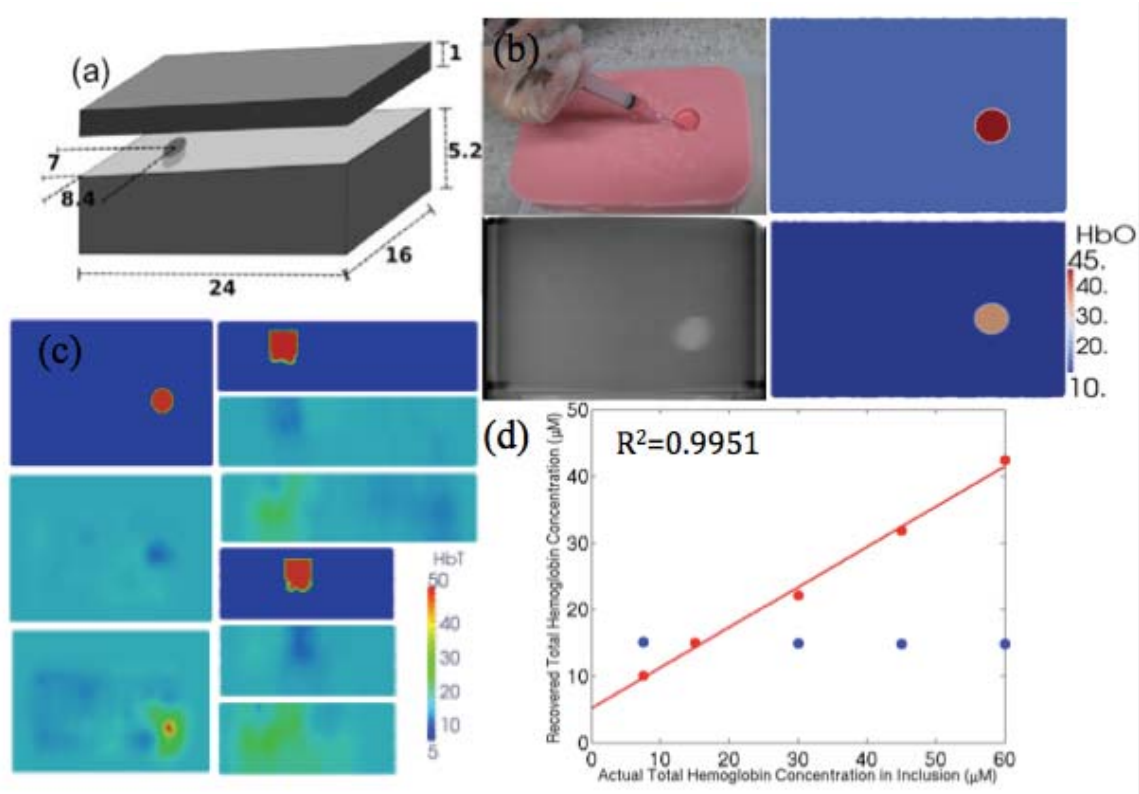


Figure 51: x-y cross-sectional views of the reconstructed HbT images for the (a) 1:1, (b) 2:1, and (c) 3:1 contrast phantoms. (d) Cut-away view of the FEM mesh showing the

background and inclusion regions. (e) Plot of recovered HbT contrast in the background (solid triangles) and inclusion region (solid circles) vs. actual HbT concentration in the background and inclusion. Linear fits show that the HbT concentration is nearly constant in the background and varies linearly in the inclusion as expected<sup>68</sup>.

Hemoglobin recovery in the background was 70% of the actual 15  $\mu\text{M}$  blood concentration as shown in Figure 51. This level is consistent with prior measurements of a resin optical phantom from INO and previously conducted research<sup>167</sup>. Background values were similar across the three cases and had a standard deviation of 4.8% of the actual value. Recovered HbT values from the inclusion showed a linear relationship ( $R^2=0.973$ ) with the actual hemoglobin concentration incorporated into the phantom. Average recovery in these cases was 87% of the true blood concentration.



*Figure 52: Agar inclusion phantoms were made with dimensions (a) and imaged in the DBT system (b) as well as with the NIRST components. Hemoglobin levels were recovered in two region (lower right) and compared to actual (upper right). (c) Diffuse reconstructions for three different cross sectional views, x-y (left), x-z (upper right) and y-z (lower right). Top plot depicts inclusion location, second is the negative contrast (0.5:1) and on the bottom is positive (4:1) inclusion to background. (d) The recovered total hemoglobin levels for different inclusion to background contrasts. The blue dots show recovery in the background region while the red dots show recovery in the inclusion.*

Additional studies using a larger number of concentrations (7.5, 15, 30, 45, 60  $\mu\text{M}$ ) of blood have obtained similar linearity results and good localization of the inclusion for diffuse reconstructions, indicating that source and detector locations as determined from the DBT image and NIRST calibration are reasonably accurate. They are shown in Figure 52. Also, localization of the inclusion to the upper half in the z-plane for the lowest concentration indicates some sensitivity to depth; this did not hold for the high concentration, likely due to liquid penetration of the agar-based phantom towards the end of the imaging session. This z-resolution was examined extensively in the resin-based phantom experiments.

### ***Water and Lipid Anthropomorphic Phantoms***

Development of physiologically relevant water and lipid phantoms is especially important for evaluating NIR imaging systems that incorporate wavelengths above 900 nm<sup>36,68,168</sup>, where absorption by these chromophores is more significant than at lower

wavelengths where the hemoglobin absorption dominates. Water and lipids are not only the main absorbers at longer optical wavelengths; they also comprise the bulk of breast tissue volume. Accordingly, several groups have described the development of water and lipid phantoms. For example, Merritt et al.<sup>169</sup> correlated a series of water and lipid fractions with MRI and diffuse optical tomography. Nachabé et al.<sup>170</sup> analyzed water and lipid contents at higher wavelengths. Most recently, Quarto et al.<sup>171</sup> characterized several recipes for phantoms comprised of water and lipids with three different emulsification agents.

Here, a robust method is reported for creating semi-solid phantoms with physiologically relevant water and lipid volume fractions that have sufficient structural integrity to stand alone. The free-standing character of these phantoms eliminates the confounding effects of light channeling from a housing container<sup>145</sup>, and allows anthropomorphic breast shapes and sizes to be created. The breast is typically comprised of about 81% adipose tissue on average<sup>172</sup>, and although adipose tissue is not 100% lipids, it does have a lipid fraction up to 85%<sup>173</sup>; hence, the most accurate breast phantoms should have high lipid content. Here, we investigate the creation of phantoms with lipid contents over 70% in a free-form geometry. A major focus is the systematic examination of emulsifiers to provide the physical scaffolding necessary to create anthropomorphic freestanding phantom structures. Combining water and lipid-based phantoms with hemoglobin is also important. Thus, ease of creation, durability, reproducibility, cost, and accessibility of materials are additional factors that serve as driving forces for the development of this new optical breast tissue phantom.

#### **4.1.14. Composition**

The most effective phantom recipe was found by testing different combinations of lipid, emulsifier, and water. Water was mixed with butter, margarine, olive oil, canola (rapeseed) oil, Crisco© (vegetable oil), and lard. For each of these combinations, a different emulsifier was used: guar gum, soy lecithin, and borax (sodium borate). These emulsification agents were selected because they are ubiquitous, inexpensive, and non-toxic. The components were mixed using a common blender. The liquid mixture was then poured into a small plastic container and refrigerated overnight. Different ratios of fat-to-water phantoms were created: 30:70; 40:60; 50:50; 60:40 and 70:30, and tested with different concentrations of emulsifiers. These phantoms were then inspected for their malleability and homogeneity. The purpose of this was to ensure that semi-solid models could be constructed from a wide range of water and lipid combinations that simulate actual breast tissue.

To determine how the different emulsification agents altered the optical absorption characteristics of the water and lipid combinations, they were mixed separately with liquid (heated) Crisco© and water, and imaged in a spectrophotometer from 600-1000 nm.

#### **4.1.15. Procedure**

After experimenting with a number of lipids and emulsifying agents, lard and guar gum were selected and used in all of the following studies. Combinations of 15:85, 25:75, 30:70, 65:35, 60:40, 50:50 by volume of water:lipids (and vice versa) were measured. Initial work (not shown) involved mixtures closer to 50:50 in content. After

satisfactory results were obtained in these cases, phantoms were created that had more extreme water and lipid fractions. Additionally, several identical phantoms were constructed using the same procedure to test the repeatability of the procedure, and some phantoms were imaged longitudinally to assess their longevity at time points separated by two weeks, during which the phantom was stored in a dark refrigerator between imaging sessions. The procedure for creating these phantoms is illustrated in Figure 53.

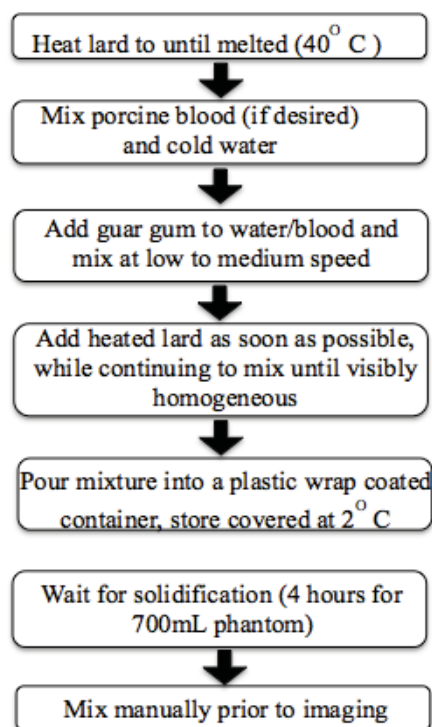


*Figure 53: The phantom creation process for lard, blood, guar gum mixture.*

First, lard was heated until melted ( $38^{\circ}\text{C} \pm 2^{\circ}\text{C}$ ), and then it was added to a mixture of water and 3% guar gum by weight. A handheld automated mixer was immediately used to stir the ingredients at low and then medium speed settings. This mixture was then poured into containers that were covered in plastic wrap. The phantoms were refrigerated overnight to solidify before being tested with a diffuse optical

spectroscopic imaging (DOSI) system<sup>22</sup>. In many cases, these phantoms were imaged the following day with no additional modifications; however, for thicker and larger phantoms, manual mixing using a handheld potato masher was required. Each measurement takes approximately two seconds, and the phantoms were measured multiple times at different locations to assess heterogeneity. All scans were performed at room temperature.

#### *4.1.15.1. Fully Anthropomorphic Phantoms*

To create a more anthropomorphic phantom, different components were designed to represent fat, fibroglandular tissue, and tumor, with the first two layers incorporated into a breast shape mold. Porcine blood was added to phosphate buffered saline (PBS) to introduce hemoglobin content. Once the lard was melted, guar gum was added to the blood mixture, and immediately afterwards, lard was added while mixing with handheld beaters. The tumor inclusion was formed in a 115 mL container with 80:20 water:lipid ratio and 3% by weight guar gum with 30 uM Hb. To construct the layer representing fibroglandular tissue, a 70:30 water:lipid phantom with 3% by weight guar gum and 20uM Hb was made, with a total volume of 1400 mL. The thickness of this layer was approximately 4.5 cm. To form the layer that represented fat, a 30:70 water:lipid 1.3 cm thick phantom of 360 mL total volume was made with 3% by weight guar gum and 10uM Hb. All of the phantoms were refrigerated after mixing. In the case of an anthropomorphic phantom, the remixing step was not necessary because the layers of different compositions were thinner than in the water and lipid-only phantoms. Some mixing was performed in the process of adding the tumor inclusion to the fibroglandular

layer as some of the fibroglandular material was removed so that the tumor region could be added.

An anthropomorphic breast-shaped phantom with three distinct tissue regions was imaged in a grid pattern similar to the one used for patient imaging with the DOSI system<sup>174</sup>. The grid pattern consisted of 36 measurement points, each separated by 1 cm in x and y directions and spanning 5 cm x 5 cm across the phantom. First, just the fibroglandular-like tissue layer was imaged, then a section 2 cm in depth and diameter was removed from the phantom and replaced with the tumor-like material. The entire phantom was reimaged with measurements acquired from the same positions. Lastly, a layer of adipose simulating tissue was placed on top of the fibroglandular/tumor layer and the grid pattern of images was repeated.

#### *4.1.15.2. The Imaging System*

Measurements were obtained on a diffuse optical spectroscopic imaging (DOSI) system, currently on loan from the University of California at Irvine as part of a multi-center clinical trial<sup>49,175</sup>. This system possesses both frequency domain and continuous imaging capabilities, which characterize reduced scattering coefficient and absorption across the NIR spectral bandwidth (650 nm-1000 nm). The frequency domain components use six distinct wavelengths from 650-850 nm, sweeping through modulation frequencies from 50-600 MHz with light detected via avalanche photodiodes. The continuous wave portion of the DOSI data samples the tissue at 1024 wavelengths between 580 nm and 1020 nm spaced about 0.5 nm apart using a broadband white light source and a CCD spectrophotometer. Measurements obtained with this system are

reported to be accurate to  $0.0006 \text{ mm}^{-1}$  for the absorption coefficient and  $0.03 \text{ mm}^{-1}$  for the reduced scattering coefficient<sup>64</sup>. For the absorption and scattering properties of the phantoms studied here, this accuracy is equal to an error of about 5% in these parameters.

The sample interface is a handheld probe with a fixed-source detector separation of 28 mm. A series of phantom measurements were recorded for calibration prior to sample measurements<sup>176</sup>. For initial experiments, the measurement probe was placed directly on the phantom surface and cleaned after each measurement. Later phantoms were wrapped in a very thin layer of plastic to prevent direct contact with the handheld imaging probe. Comparisons of measurements in phantoms with direct contact versus plastic covering showed negligible differences.

#### *4.1.15.3. Data Reconstruction*

A power law fit of the data for the reduced scattering coefficients measured at selected wavelengths defines the scattering properties across the measured range. Chromophore concentrations were calculated using the Beer-Lambert law for the measured absorption coefficients. Molar extinction values for hemoglobin, deoxy-hemoglobin, water, and lipids<sup>177-179</sup> were used in this process. Water and lipid fractions were constrained to 100%, and hemoglobin absorption was not considered for the phantoms composed exclusively of water, lard, and emulsifier, but was included for the anthropomorphic phantoms containing porcine blood.

## 4.1.16. Results

### 4.1.16.1. Creation of Optimal Phantoms

In creating semi-solid phantoms consisting of water and lipids, lipid and emulsifying agents were tested across a range of physiologically relevant water-to-lipid ratios (30:70-70:30) as shown in Figure 54(a). The amount of emulsifying agent was kept constant for a given volume of phantom to ensure that its effect on optical properties would not vary across different phantom concentrations. As expected, phantoms comprised mostly of water were more gelatinous than phantoms comprised mostly of lipids.

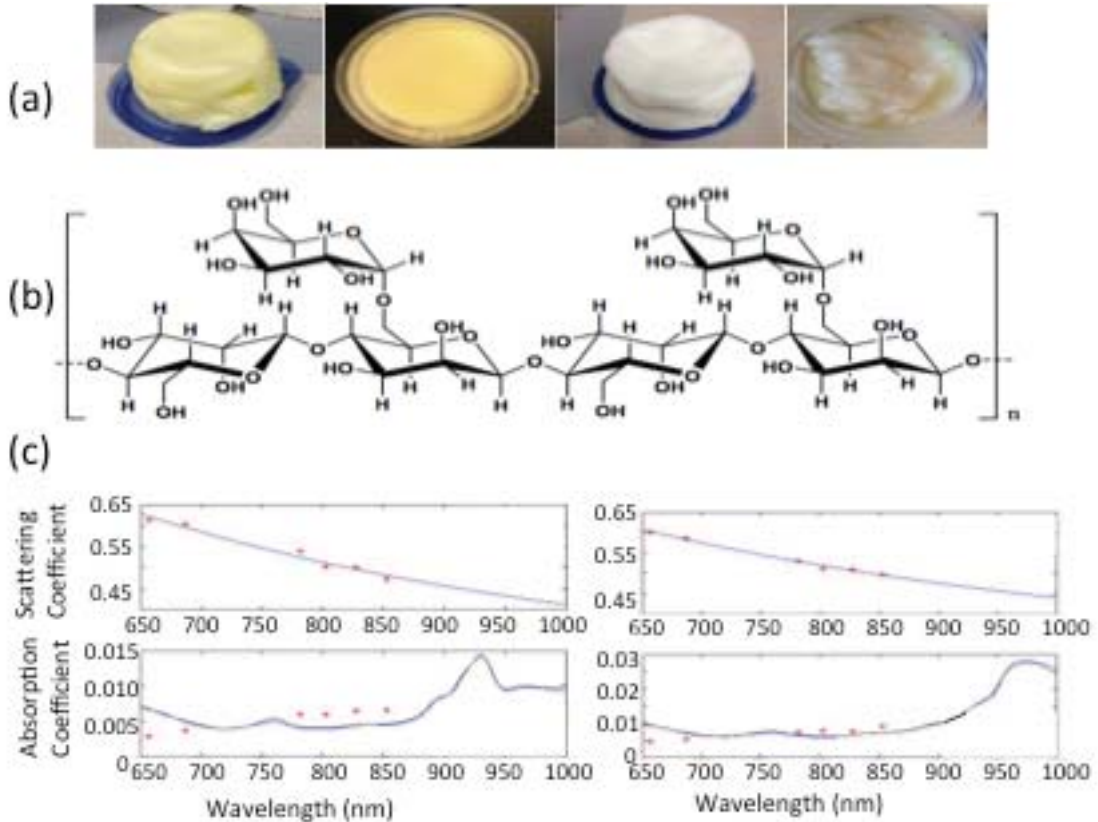


*Figure 54: (a) Several early phantom creations comprised of 70% lipid and 30% water. The fats were butter, olive oil, Crisco© and canola oil (left to right). The first and third phantoms included guar gum as the emulsifier while the second and fourth utilized soy lecithin. (b) The chemical formula for guar gum<sup>180</sup>. (c) Data from the DOSI imaging system for a mostly lipid (left) and mostly water (right) phantom. The top graph shows the scattering data and fits, while the bottom graph shows the absorption results. Specific peaks for lipids and water can be discerned above 900 nm.*

When guar gum was used, all phantoms were semi-solid and visually homogeneous. Additionally, guar gum had the lowest signal attenuation in spectrophotometry measurements in the NIR regime of any of the emulsifying agents presented here. Thus, it appeared to be the most viable emulsifier for water and lipid phantoms. Several lipid-dominant materials underwent spectrophotometry analysis in the near infrared range and Crisco© (vegetable oil) and lard (porcine fat) matched published absorption spectra<sup>178,181</sup>. Ultimately, lard was selected for the phantoms as the types and percentages of fatty acid were more similar to the breast in the animal fat than the vegetable oil<sup>182</sup>. Despite the addition of an emulsification agent to these phantoms, water and lipid peaks were clearly discernable as shown in Figure 54(c). The lipid absorption peak is evident in the left graph as a sharp rise around 930 nm, while the water absorption, highlighted in the right graph, has a broad peak above 950 nm that extends to almost 1000 nm. The average scattering amplitude of  $0.66 \cdot 10^{-3} \lambda \text{ m}^{\text{b-1}}$  and average scattering power of 0.42 of the lard-based phantom are on the low end of values found in human subjects<sup>59</sup>.

#### 4.1.16.2. Contrast Sensitivity

Linear contrast recovery of water and lipids was found when measuring several water: lipid ratios from 15:85 to 85:15, roughly the physiologic limits for the macroscopic tissues probed by diffuse optical techniques<sup>173</sup>. These results are shown in Figure 55 with an  $R^2$  of 0.998 for the linear fit. Each phantom was measured at ten distinct locations and the mean standard deviation of these measurements was 3.5%. However, as noted by other groups,<sup>169,171</sup> lipid content is overestimated, especially for high lipid ratios. Visual inspection of these phantoms showed a color gradient as observed in the photograph in Figure 56, and measurements along the side of this phantom demonstrate a decrease in lipid content from the top to the bottom. These phantoms were subsequently remixed manually, and then re-measured. The recovered water and lipid content were again linear with an  $R^2$  of 0.96, but with recovered values within 2.5% of their actual values on average as shown by the dashed line in Figure 56. They maintained homogeneity as well with an average standard deviation of 4.1%. The phantom constituents do not separate after manual remixing as long as the phantoms, once fully formed, are maintained at room temperature or colder, so only a single remixing step is required.

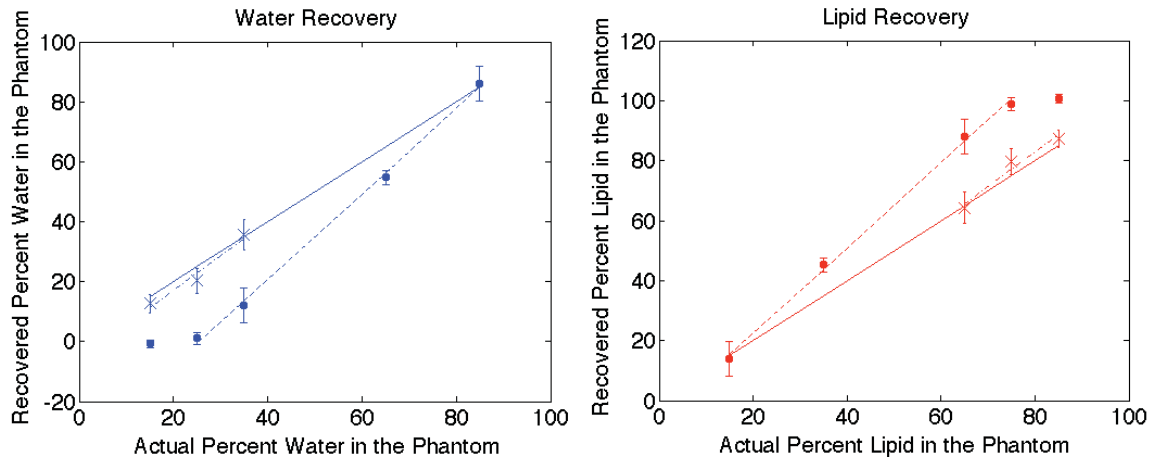


Figure 55: Graphs of measured water (left) and lipid (right) fractions with (round) data points and standard deviations based on ten measurements from the top of the phantoms. The dotted line is a linear fit for the phantoms with the higher water content before mixing, exhibiting good linearity. The X-shaped data points and corresponding dashed linear fit for the high lipid content phantoms were obtained after their materials were manually mixed. The solid line depicts the actual water or lipid content.

#### 4.1.16.3. Reproducibility

In order to test the reproducibility of the phantom creation process, three phantoms comprised of the same volume of water, lard, and guar gum were fabricated. Each phantom was created by independently following the steps shown in Figure 53, but all three used ingredients from the same containers and were made by the same individual. The results of this study are shown in Figure 56(c). The recovered lipid contents were 60.7%, 59.7%, and 65.0% for the three samples, and had intra-phantom standard deviations of 1.97%, 1.60% and 4.72%, respectively, and an inter-phantom standard deviation of 3.81%.

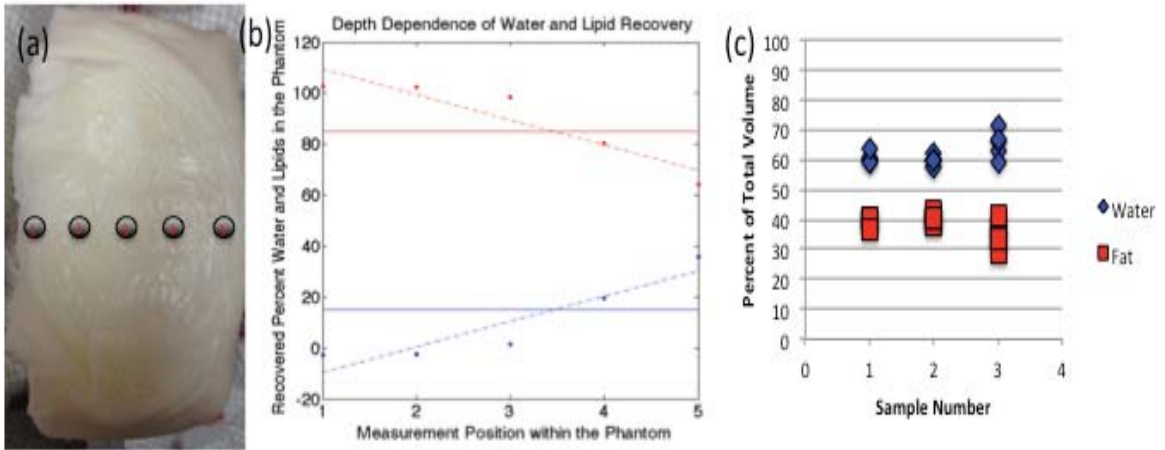


Figure 56: (a) Photograph showing visible differences between the top (left) and bottom (right) of the phantom. (b) Corresponding depth-dependent measurements confirming the greater presence of lipids at the top of the phantom and higher water at the bottom of the phantom. (c) Repeatability of the phantom creation process in three independently-constructed phantoms with the same water and lipid ratio, each measured five times.

#### 4.1.16.4. Durability

Phantoms were evaluated at several time points after initial creation. Because of the need for cooling, no phantoms were tested without at least four hours of refrigeration. Three phantoms with 15:85, 25:75, and 35:65 water: lipid contents were tested after two weeks of refrigeration. At the time of creation, the recovered lipid content was 87.9%, 72.1%, and 65.8%, respectively. Two weeks later the values were 87.3%, 79.7%, and 64.3%, respectively. After an additional week of refrigeration, some phantoms developed mold, indicating that with proper refrigeration these phantoms may last for several weeks.

#### *4.1.16.5. Anthropomorphic Test Case*

The average water content of the fibroglandular simulating layer was measured as 54.9%, 72.8% for the tumor layer prior to insertion in the multi-layer phantom, and 29.5% for the adipose layer. As shown in Figure 57, the tumor inclusion was recovered with 16% greater water content when compared to the fibroglandular region. The actual tumor water content was 10% greater than its fibroglandular counterpart. The adipose region was recovered with a water content within 0.5% of the actual amount. After the tumor region was included in the phantom, measurements in that area showed higher water content and lower lipid content than the surrounding measurement points. Additionally, after the adipose layer was placed on top of the other two, measured water content decreased and lipid content increased as expected. Hemoglobin recovery was 33.2 $\mu$ M, 25.5 $\mu$ M and 8.2 $\mu$ M for the tumor, fibroglandular, and adipose regions, respectively, relative to the actual amount of hemoglobin added of 30 $\mu$ M, 20 $\mu$ M and 10 $\mu$ M Hb in each of the three tissue types.

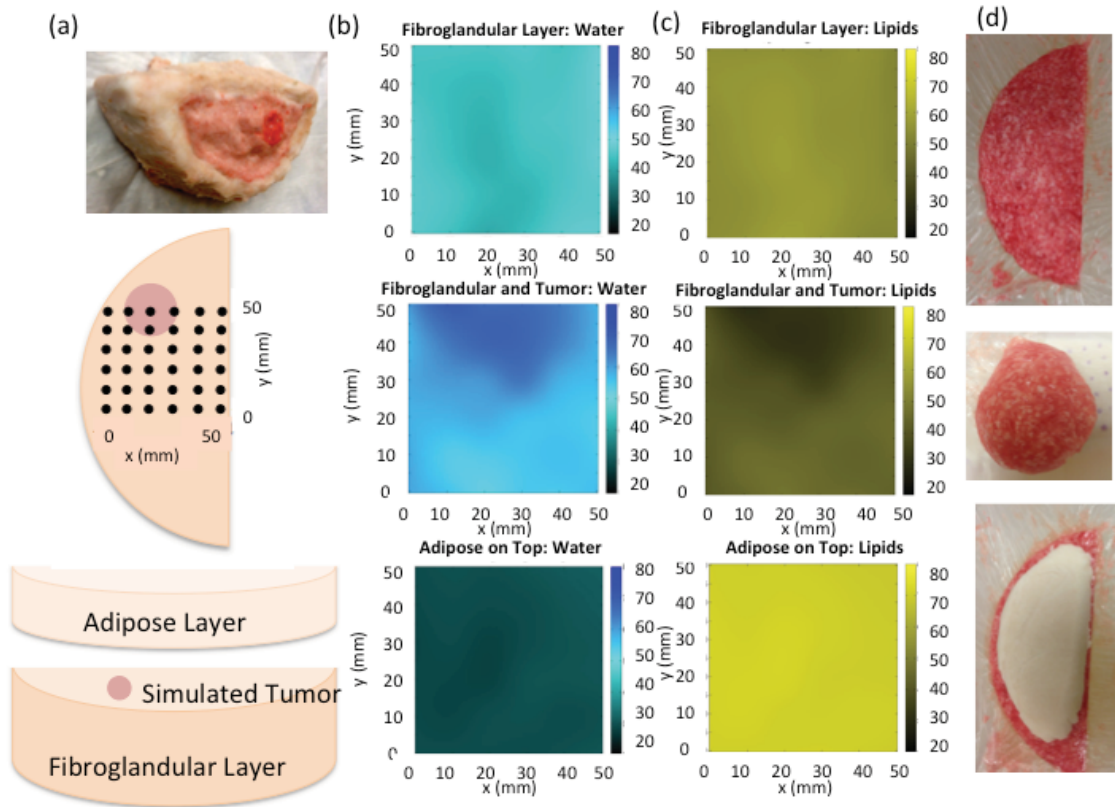


Figure 57: (a) Schematic of a free-standing three-compartment phantom and the grid pattern used to assess its optical properties. A given phantom was evaluated at 36 locations on a 1 cm grid pattern as shown. Interpolated results across the 5 cm x 5 cm grid of individual measurements of optical properties are shown for water in (b) and lipids in (c) in the fibroglandular, tumor and adipose regions. In the top row, the fibroglandular-simulating phantom was measured alone. The middle row depicts results when a tumor-like inclusion of ~2 cm diameter was added near 20-40 mm in x and 60 mm in y directions. In the bottom row, measurement data are shown when a uniform adipose simulating layer was added on top of the fibroglandular and tumor phantom. (d) Photographs of the phantom regions

#### 4.1.17. Discussion

After testing several types of emulsification agents and lipids, guar gum and lard were selected as the ideal constituents for creating breast-mimicking phantoms. Lard was preferable as animal fat is more similar to the adipose content in human tissue than vegetable oil-based products. However, the percent of different types of fatty acids contained in the lard can change depending on the animal's diet and the part of the animal from which the fat was contributed<sup>183</sup>. Regardless, changes in the near-infrared absorption due to different fatty acid composition are very small<sup>182</sup>, indicating that both Crisco© and lard could be used depending on their availability. To minimize the effects of impurities, all samples produced on a given day were constructed from the same batch of melted lard.

Guar gum showed the lowest absorption in spectrophotometry studies and had the greatest thickening power and homogeneity in phantom formation – characteristics which can be understood from its molecular structure. Guar gum is a high molecular weight polysaccharide comprised of highly branched galactose and mannose units<sup>180</sup>. The chemical formula for guar gum is shown in Figure 54(b). Additionally, examinations of the absorption spectra of phantoms composed of water, lipids, and emulsifier exhibited easily discernable peaks for their water and lipid constituents as shown in Figure 54(c), and accurate chromophore recovery occurred as demonstrated in Figure 56.

Water and lipids do not mix spontaneously, but vigorous mixing can create an emulsion, although the two will separate shortly thereafter. The large size and abundance of branches and hydroxyl groups on the guar gum creates bonds that decrease molecular movement after mixing, thus creating a stable emulsion that is thickened and more solid

than the liquid components. Lastly, cooling after mixing further inhibits separation of water and lipids and enhances the solidity of the phantom. The final product is moldable, and retains its shape after application of minimal pressure.

This process is not infallible as some separation of lipid and water may occur as the phantom begins to solidify, causing the linear concentration gradients shown in Figure 56. The effect is a result of the time delay between the mixing and solidification of the phantom. Procedures exist to mitigate these effects. One method is post-refrigeration manual mixing, which was very successful as shown in the data and dashed line in Figure 55, and significantly improved the accuracy of the water and lipid quantification of the mixed material when compared to the same measurements of the unmixed material. Mixing techniques can have an impact on the final phantom outcome. Manual mixing involves slow, gentle compression of the materials at room temperature by hand for a few minutes (the amount of time can vary depending on the size of the phantom). It should not be mixed at high speed as blending the solid phantom may introduce air bubbles that would alter the desired optical properties. When different individuals mixed the same phantom, average differences in measured water and lipid content were less than 5%.

Other potential steps include minimizing the height of the phantom, mixing the heated lipids with cold water to decrease the time to solidification, or cooling the mixture more quickly. The first strategy was successful when making the thin adipose layer; the other approaches were not investigated in this study, but would likely improve results in future phantom experiments.

These phantoms possess intrinsic scattering properties resulting from their water and lipid interfaces, which change with concentration. Specifically, higher fat content leads to greater scattering. This behavior is opposite from the scattering found in breast tissue, possibly because tissue water is mostly found within cells that also possess a number of light scattering organelles, whereas these phantoms are comprised of pure water with no additional scatterers. Differences in scattering and absorption are accounted for in the frequency domain instrumentation.

Despite this water-lipid separation issue, creating durable, homogeneous, repeatable semi-solid phantoms across a broad range of water-to-lipid ratios with easily accessible ingredients and tools was demonstrated. Inter- and intra-phantom variability was less than 5%. The phantoms do not break and can be remolded into different shapes as needed, unlike agar or gelatin materials that often crack. They can be compressed with manual force (more easily for higher water content but possible at all compositions), unlike hard resin phantoms. Phantoms measured two weeks after creation exhibited water and lipid contents within 5% of their originally-measured concentrations. The semi-solid consistency eliminates the complexities of imaging phantoms within containers where light channeling may occur. These phantoms were inexpensive to construct, costing less than \$5.00 per 700mL of phantom material, and all of the ingredients and equipment could be purchased at a local grocery store.

An anthropomorphic breast-shaped phantom with three distinct tissue regions was studied as a test case. It contains the three main light absorbers in the NIR – hemoglobin, water, and lipid – and possesses intrinsic scattering properties, albeit on the lower end of what is expected for a human breast because its materials do not contain human cells or

organelles. Because the melting point of lard is well below the temperature of hemoglobin denaturation, blood can easily be incorporated into this phantom<sup>184</sup>. Adding hemoglobin to the water and lipid phantoms did not substantially alter the water and lipid fractions. Fat content was overestimated in the fibroglandular and tumor phantom sections by about 15 % and 8%, respectively, likely due to the thickness of these compartments (post-refrigeration mixing was not performed in this case), but was less than 1% in error in the adipose layer. The tumor can be localized when added to the fibroglandular background as shown in Figure 57. This example demonstrates the feasibility of producing physiologically relevant NIR phantoms comprised mainly of water, lipid, and blood which have sufficient structural integrity to be used without any other supporting containers or fixtures.

Given the positive characteristics of these phantoms, several areas of research could benefit from their construction. For example, these phantoms can be used for evaluating imaging systems that obtain limited spectral information above 900 nm in order to understand their sensitivity to water and lipid contrast. Alternatively, a multi-compartment phantom model of different tissue types can be used to test region-based reconstructions for tomographic imaging systems as well as to assess signal-to-noise characteristics in an optically heterogeneous environment. The semi-solid character of these phantoms is useful for testing the effects of different breast shapes and sizes on patient interfaces and at tissue boundaries. Use of these phantoms, which closely mimic tissue optical properties, can provide information to help optimize imaging system development and determine which patients can be successfully imaged on those systems.

These phantoms should be used to assess the capabilities of the NIRST-DBT system to characterize water and lipid content in the near future.

### ***Conclusions***

Calibration phantoms are essential for clinical imaging. Reference phantom measurements and calibration procedures can correct for variations in source strengths, detector sensitivities, and positioning for every data point measured. This chapter focuses on a new method to calibrate NIRST data with respect to a known, absolute reference phantom, takes advantage of DBT spatial prior information, and generates an initial guess that works for both phantom and patient imaging. This chapter described results from three different phantom experiments in addition to the earliest system tests to examine the ability to accurately recover hemoglobin, water, and lipids as well as test the limits of recovery in terms of size, depth, and contrast. Using a spectrally varying phantom, with small inclusions positioned at different depths and varying concentrations of hemoglobin, it was possible to detect increases in hemoglobin in the smallest inclusion, 7 mm in size. Additionally, tests on the effects of volume mischaracterization improve understanding of the possible effects of similar mischaracterization of DBT ROIs, which is likely given the limitations of DBT image segmentation. Lastly, examination of a fake inclusion in phantoms is similar to benign ROIs during patient studies.

Phantom tests to assess chromophore recovery were performed to determine if hemoglobin changes could be detected. This experiment involved a larger inclusion and showed excellent linear recovery of HbT, with an  $r^2$  value greater than 0.99. This is strong

evidence that hemoglobin recovery in the NIRST-DBT will be possible for patients. However, these phantoms did not possess physiologically relevant water and lipid concentrations so the ability to quantify these qualities was not tested. We set out to develop a fully anthropomorphic phantom, with appropriate water and lipid content, that could be varied along the range expected for breast tissues in order to assess NIRST-DBT water and lipid recovery. Breast-mimicking tissue optical phantoms with sufficient structural integrity to be deployed as stand-alone imaging targets were developed and successfully constructed with biologically relevant concentrations of water, lipid, and blood. The results show excellent material homogeneity and reproducibility with inter- and intra-phantom variability of 3.5% and 3.8%, respectively, for water and lipid concentrations ranging from 15% to 85%. The phantoms were long lasting, and exhibited water and lipid fractions that were consistent to within 5% of their original content when measured two weeks after creation. A breast-shaped three-compartment model of adipose, fibroglandular, and malignant tissues was created with water content ranging from 30% for the adipose simulant to 80% for the tumor. Mean measured water content ranged from 30% in simulated adipose to 73% in simulated tumor, with the higher water localized to the tumor-like material. This novel heterogeneous phantom design is comprised of physiologically relevant concentrations of the major optical absorbers in the breast in the near infrared wavelengths that should significantly improve imaging system characterization and optimization because the materials have stand-alone structural integrity and can be readily molded into the sizes and shapes of tissues needed for clinical breast imaging.

Phantoms are crucial to understanding the potential as well as the limitations of the new NIRST-DBT system. The small inclusion phantoms demonstrate that the source strength variation is an important factor that should be taken into consideration to improve recovery of small breast lesions. Hardware improvements will be included in the next generation prototype to address this issue. Specifically, a continuous, real-time detection of the source strength will be added. This can be accomplished by redirecting a fraction of the source light via a fiber delivered to a single isolated photodiode for simultaneous measurements with each source-detector measurement. This can be used to normalize the detector outputs and reduce system noise. Additionally, although the water and fat phantoms have not yet been tested on the NIRST-DBT system, it would be easy to do, now that the procedure has been developed and tested; this would improve the understanding of the quantification of these tissue chromophores and should be performed as soon as possible, as well as after any major changes to the system geometry or components.

## **Chapter 5: Methods for Combined NIRST-DBT**

### ***Introduction***

In this section, the exact methods for image acquisition and combining of the NIRST-DBT data sets is outlined. The approach to this is complicated by a lack of established methods for doing this type of hybrid imaging, but the process has required an iterative approach to validation with phantoms, people and simulations with a careful study of signal quality and how this impacts the images. When calibrating and testing the system, phantoms can provide an approximate representation of the optical and material properties of living tissue, and can be imaged repeatedly, making them ideal for testing algorithms and optimizing system performance. Also though, for emerging imaging techniques, a complete understanding of performance characteristics and assessment of clinical utility requires imaging healthy volunteers and women with breast lesions. Imaging healthy volunteers is the first step and can be used to test imaging systems and algorithms and gain an understanding of normal tissue properties before imaging abnormal or malignant tissue or women recommended for biopsy. The calibration phantom is not especially similar to the actual human tissue data; in human tissue, there can be some low-quality data points due to poor shielding or breast coverage. Additionally, tissue heterogeneity and edge effects near the breast boundaries are present and may not be accounted for accurately in phantom imaging. The major drawback of imaging healthy volunteers is that the true optical properties are unknown and results can only be compared against the literature. However, coupling healthy volunteer studies with phantom imaging studies can give a complete assessment of an imaging technique.

While building this new NIRST-DBT imaging platform, extensive software developments were necessary to obtain data from the hardware components, visualize the data, and drop data points that do not adequately represent tissue light transmission. This chapter describes human subject exam imaging procedures, data collection, and real-time monitoring during the examination procedure. Additionally, as this system possesses an unusually large number of light sources and detectors, novel methods for data visualization are developed to better understand and troubleshoot hardware issues. Lastly, this chapter discusses useful techniques for automatic data dropping with uniform data selection steps for all patients.

### ***Exam Workflow***

Each patient exam flows in a different way, but there are procedures in place to guide the exam to ensure a smooth and fast process for the patient and imaging team. Committee for Protection of Human Subjects (CPHS) approval has been obtained for all exam procedures involving NIRST-DBT and DOSI imaging systems. Currently, these are two separate studies and patients have been enrolled in NIRST-DBT alone as well as NIRST-DBT and DOSI exams. The first step in all exams is to obtain patient informed consent; this is always achieved prior to the date of imaging or at the start of the exam itself. This process typically takes ten to twenty minutes depending on the patient's familiarity level with the consent form and comfort with the proposed study plan.

### 5.1.1. NIRST-DBT

NIRST-DBT examinations run between twenty and forty minutes depending on the ease of patient positioning, and are comprised of four NIRST scans as well as two or four DBT scans depending on the study arm.

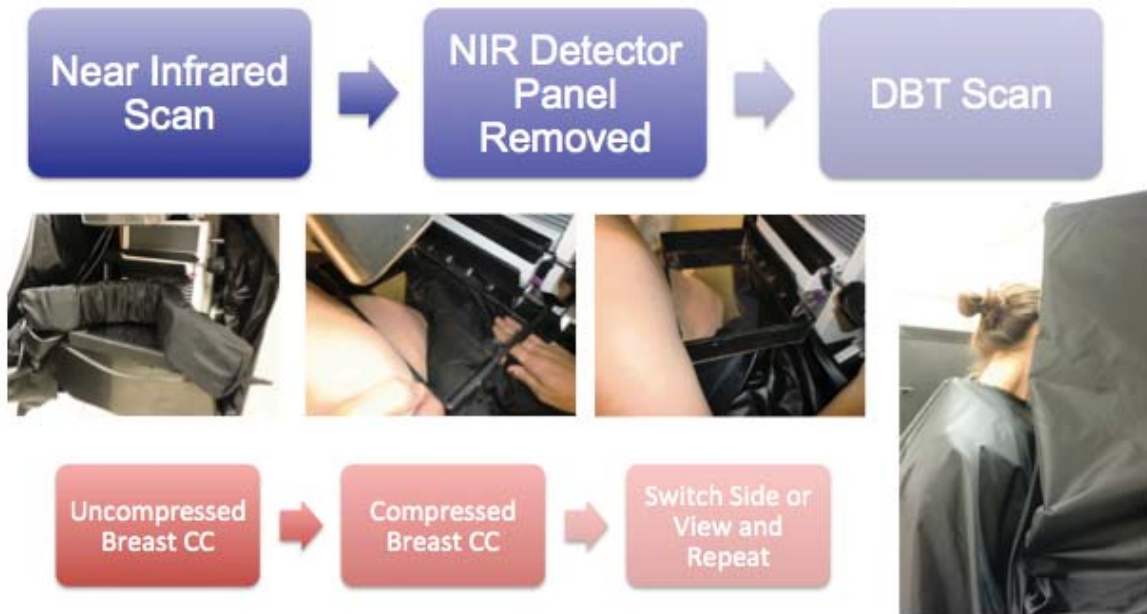


*Figure 58: The workflow and patient positioning of a human subject NIRST-DBT exam.*

*Photographs proceed in sequence from left to right, showing how the breast is positioned and the light shielding mechanisms are used during the exam. The procedure on top describes exam workflow for a single view. Each exam consists of four views, the steps of which are described on the lower series.*

After obtaining consent, the patient is positioned for NIRST imaging. The first set of images is taken in the craniocaudal (CC) position, while the second set is taken in mediolateral oblique (MLO) of the same breast or CC of the contralateral breast for some women in the biopsy cohort. The breast technologist positions the patient at an appropriate low-compression level based on patient feedback. Next, the light blocking

breast shroud is brought into contact with the breast to block light from unexposed detectors. A black cape is affixed at the nape of the subject's neck to protect the patient's eyes from laser light and to prevent ambient light from hitting the detectors. After the NIRST scan is completed, the cape and shroud are removed, followed by the detector panel itself. Then, a DBT scan is obtained. For healthy subjects, NIRST scans are taken at two compression levels prior to the DBT scan. For biopsy patients, there are two DBT scans obtained for each view, one at uncompressed and one at compressed breast thickness. For such cases, the detector panel, shroud, and cape are replaced after the first DBT scan while the patient is maintained in the same position by the breast technologist. Then, compression is increased and another set of NIRST and DBT images are collected.

After NIRST and DBT images are obtained for a single view in both the compressed and uncompressed cases, the patient is released from the machine. During this break, several health-related inquiries are made including the patient's height, age, weight, bra cup size, and menopause status. When two NIRST examiners are present, one can replace the NIRST panel, shroud, and cape while a second speaks with the patient. For healthy subjects, the right breast was imaged in most cases, with three women imaged bilaterally. Then, a second set of compressed NIRST and DBT images are obtained in the second view. As the detector panel can only be removed to the left of the patient, it could be challenging to remove the panel during left MLO imaging; thus, for some women of the biopsy cohort with left-sided lesions, CC images of the contralateral breast were obtained instead of left MLO.

DBT imaging protocols used a look up table technique chart to determine the correct kVp and mAs settings for patients. This look up table was developed for the

specific Hologic DBT research unit used in the study prior to modification for NIRST imaging and is included in the appendix. However, in many patients, detector saturation artifacts were apparent in the images, necessitating modifications to the original technique chart. These bar artifacts are due to differences in preamplification gains among the different blocks of pixels in the detector<sup>185</sup>. Pixels are grouped together in blocks for readout, and differences in gains among the blocks can appear as bars on the image, particularly in areas of very low or high exposure. Normally, differences in gains are small and are normalized with respect to each other in a well-calibrated system to yield a uniform image. However, when these differences are significant, the blocks of pixels appear inhomogeneous. Ongoing efforts to modify the technique chart to account for the inclusion of an additional polycarbonate layer in the X-ray path are hampered by the inability to reconstruct the patient images on the acquisition console. Reconstructions take place after all DBT images have been obtained for a given patient.

### **5.1.2. DOSI**

The NIRST-DBT system possesses CW imaging capabilities only. It can be a successful imaging modality on its own, but it is important to estimate scattering properties in normal and diseased breasts for a number of cases in order to compare the effects of using the true, measured scattering with some other estimation of optical scattering. Measurements were obtained on a diffuse optical spectroscopic imaging (DOSI) system, currently on loan from the University of California at Irvine as part of a multi-center clinical trial<sup>49,175</sup> (shown in Figure 59). This system possesses both frequency domain and continuous imaging capabilities, which characterize reduced

scattering coefficient and absorption across the NIR spectral bandwidth (650 nm-1000 nm). The frequency domain components use six distinct wavelengths from 650-850 nm, sweeping through modulation frequencies from 50-600 MHz with light detected via avalanche photodiodes. The continuous wave portion of the DOSI data samples the tissue at 1024 wavelengths between 580 nm and 1020 nm spaced about 0.5 nm apart using a broadband white light source and a CCD spectrophotometer. Measurements obtained with this system are reported to be accurate to  $0.0006 \text{ mm}^{-1}$  for the absorption coefficient and  $0.03 \text{ mm}^{-1}$  for the reduced scattering coefficient<sup>64</sup>. For the absorption and scattering properties of the phantoms studied here, this accuracy is equal to an error of about 5% in these parameters.

A power law fit of the data for the reduced scattering coefficients measured at selected wavelengths defines the scattering properties across the measured range. Chromophore concentrations are calculated using the Beer-Lambert law for the measured absorption coefficients. Molar extinction values for hemoglobin, deoxy-hemoglobin, water, and lipids<sup>177-179</sup> are used in this process.

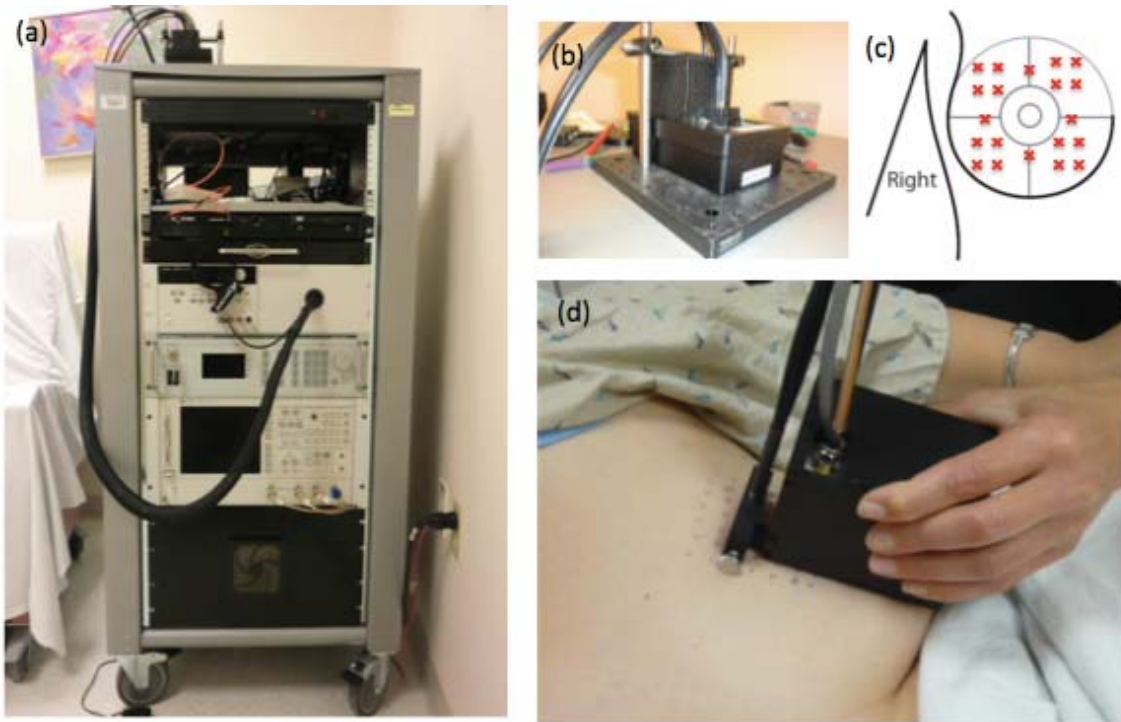


*Figure 59: (a) The instrumentation cart for the DOSI system. (b) A close up of the handheld probe. (c) The measurement locations used in the NIRST-DBT and DOSI study. (d) A photograph of a patient exam in progress.*

The sample interface is a handheld probe with a fixed-source detector separation of 28 mm. A series of phantom measurements were recorded for calibration prior to sample measurements<sup>176</sup>. For this exam, the patient sits or reclines in a chair while the reflectance probe is gently placed on the breast surface. Instead of measuring at 1 cm intervals over a large grid as is performed in neoadjuvant chemotherapy studies, twenty measurements are taken as shown in Figure 59(c); four measurements are taken in a square pattern in each quadrant, as well as four interquadrant measurements. This process takes about ten minutes and all data points are analyzed and averaged to obtain a bulk tissue scattering estimate that can be used during NIRST-DBT reconstruction.

Region-based estimations of optical scattering are not possible due to the large differences in patient positioning and geometry between the two imaging modalities.

### ***LABVIEW Interface***

Exam options and real-time monitoring tools are integrated into the hardware controlling LABVIEW software, as shown in Figure 60. The user interacts with two tabs, one for equalization and one for the scan itself. The equalization procedures set the attenuator for the breast scan. The breast scan can be performed in different geometries depending on breast size. Ultimately, the user must read the compression paddle height off the system, provide a filename, and select the source geometry while every other aspect of the scan is automated by the LABVIEW software. This makes it possible for new system operators to perform NIRST-DBT scans with limited engineering knowledge and short training time.

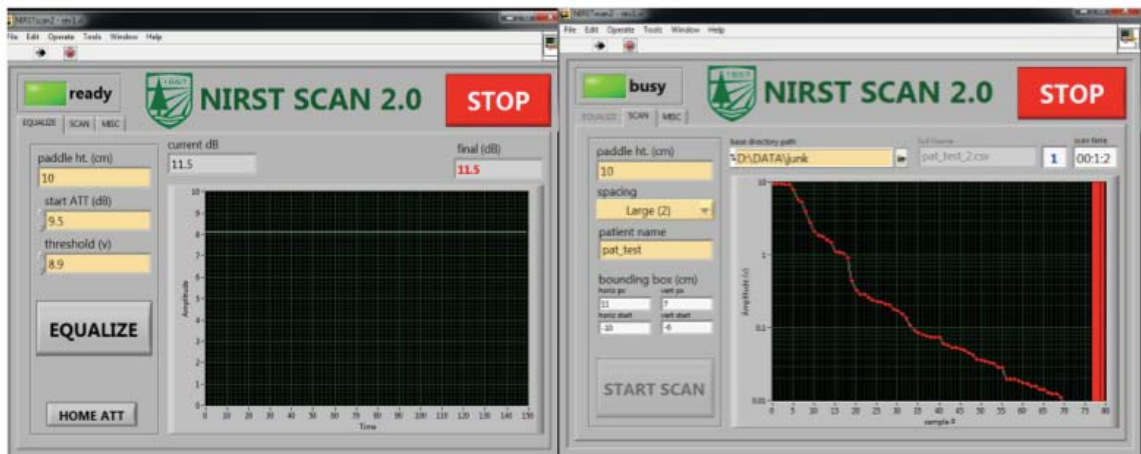


*Figure 60: LABVIEW screenshots during the equalization phase (left) and during the actual scan (right). Equalization shows the light output for a single detector with an unchanging source.*

### **5.1.3. Setting Source Strength**

For patient imaging, attenuator settings must be determined such that optimal light levels are incident upon the detectors. After the patient is positioned and the compression paddle height is obtained from the system, a single laser shines at a central point near the chest wall and the output from the nearest detector is recorded. The light level is attenuated at small intervals until the detector output is below a certain level (3V was the experimentally-derived optimal output for most patients). This attenuator setting is maintained and saved to a header file during the full light scan. After the equalization step, the scan is taken. The user can select from three different source scanning patterns, depending on breast size. The entire scan typically takes 45 seconds.

### **5.1.4. Real Time Exam Monitoring**

During the scan, the LABVIEW graphically displays the output from all the detectors, allowing real-time monitoring of the data collection process. This is useful for cases where breast shielding is suboptimal. A large number of detector output signals will be visible at the saturation level; in Figure 60, these are the 6 detectors displayed on the left hand side of the scan graph at the saturation level. During the scan, the detector outputs are graphed in order of decreasing value, with saturated detectors appearing on the left and red bands on the right indicating no signal at some detectors. The shielding can be adjusted for the next exam to prevent or mitigate this issue. Additionally, if the source scanner is not working properly, there will be no change in the output signals at different positions. The graphical display makes it easy to diagnose and fix this issue.

### 5.1.5. Output

The LABVIEW code saves two .csv files with names indicated by the user prior to obtaining a scan. The first file contains the data in a 49280 x 150 matrix. Each row of the matrix corresponds to a detector output, with 150 measurements sampled. Each row corresponds to the output for a specific AI channel (there are 80 for our DAQ, only 75 of which are populated by detectors) for a specific wavelength. Each wavelength is recorded sequentially.

An additional header file containing specific information about the source geometry, breast thickness, and attenuator settings is created for each scan. It possesses the same filename as the original file with a ‘\_sd’ extension. It consists of a single row of data, specifically the starting x and y coordinates for the leftmost source position closest to the chest wall, measured relative to the center detector as the origin. The next two columns indicate the number of rows and columns in the raster scanning pattern, followed by the spacing between source positions (equal in both x and y). The last two columns contain information on the compression paddle height and attenuator setting. All of these values are needed to position the sources on the mesh, calculate breast thickness, and adjust the source strength for the exam.

### *MATLAB Analysis Tools*

Developed MATLAB software tools serve two major purposes: immediate feedback on experimental phantom scans, and LABVIEW data restructuring in preparation for image reconstruction. New tools for data visualization are instrumental in understanding and diagnosing hardware problems and distinguishing reconstruction

irregularities from raw data differences. This is especially important as the NIRST-DBT system possesses a larger number of sources and detectors than any prior system in the laboratory at Dartmouth and it would have been impossible to make any conclusions about the data with the existing visualization tools.

#### **5.1.6. Phantom GUI**

Early phantom measurements were performed to assess the system hardware. As all images were taken on phantoms of the same size, covering all source and detector positions, it was possible to create a fast data calibration GUI to examine the data seconds after it had been taken. This is possible because no mesh creation or spatial prior information is needed and all sources and detectors possess useful data due to the large size of the phantom. This GUI model was important in determining the most basic data calibration steps, such as distance and voltage thresholding and is shown in Figure 61. Its fast speed and ease of use make it particularly helpful in ensuring data quality whenever changes to the LABVIEW code or system hardware are being performed.

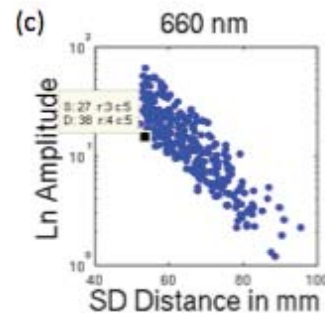
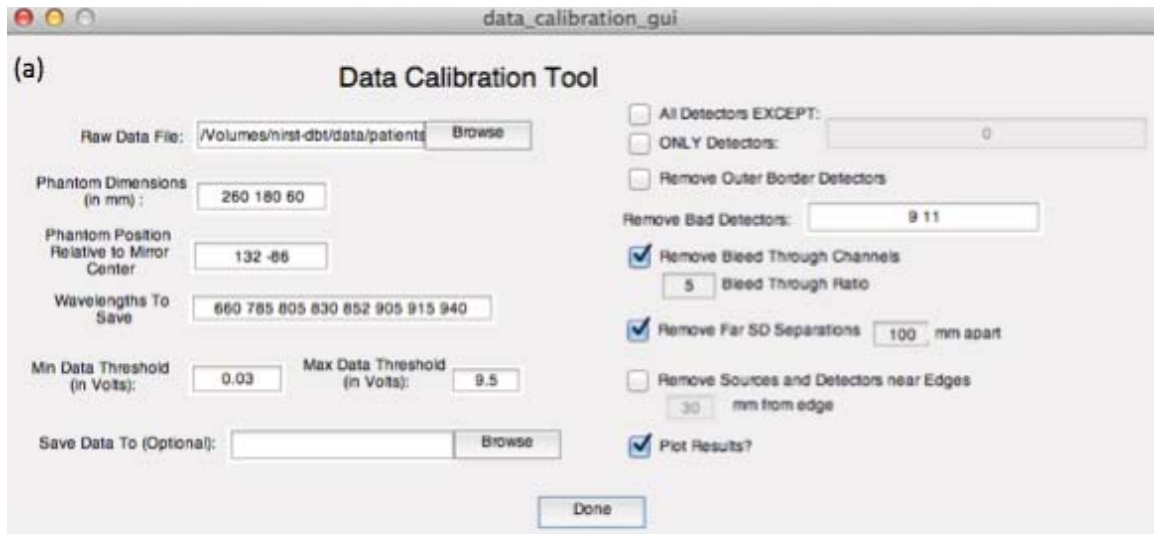


Figure 61: The data calibration GUI (a) allows for nearly instantaneous feedback on phantom data collected. Results from the exam are shown as plots of the log of the detector output vs. SD distance in mm (c). Individual data points can be highlighted, with their corresponding source and detector information appearing to help localize bad data points. Sources and detectors are numbered as shown in (b).

### 5.1.7. Source/Detector Pair Identification

It is important to distinguish sources and detectors from one another to pinpoint specific issues that may arise from a single bad detector or blocked source. Although the detectors are mapped to AI channels, this numbering system is not sequential or intuitive. Hence, we decided to implement a numbering scheme for sources and detectors that

works in roughly the same way. Detector and source number one is located on the back left of the panel, moving left to right as one would read, with numbers increasing towards the patient's chest wall as shown in Figure 61(b). For the largest source spacing, the sources are nearly centered over the detector of the same number. Data plotting tools such as those used in the GUI plot the log of the detector output vs. SD distance, allowing for selection of an individual data point. When the user does this, a text box will appear stating the corresponding source and detector, as well as their row and column on the panel as shown in Figure 61(c). Rows and columns are labeled from right to left and top to bottom in the same manner as the individual sources and detectors themselves. This has been very useful when troubleshooting both hardware and software issues.

### ***Data Dropping and Adjustments***

Unlike in phantom imaging, where the entire detector panel is typically covered and nearly all data points provide useful results, breast imaging can cover a variable number of sources and detectors and consistent, experimentally-derived schemes for removing data points are needed for robust and consistent chromophore recovery. There are three main steps to data dropping (shown in Figure 62): the first involves assessment of detector output, the second is tissue geometry-based cuts, and lastly, slope-based data elimination tools were developed to deal with some of the challenges of patient imaging. The first step does not require any knowledge of the breast geometry; these cuts were developed based on hardware tests using phantom GUI results. The second two sets cuts are necessary for breasts and phantoms that do not cover the entire expanse of the breast,

while the third group are exclusive to human subject imaging due to poor contact between the breast and the light shielding shroud.

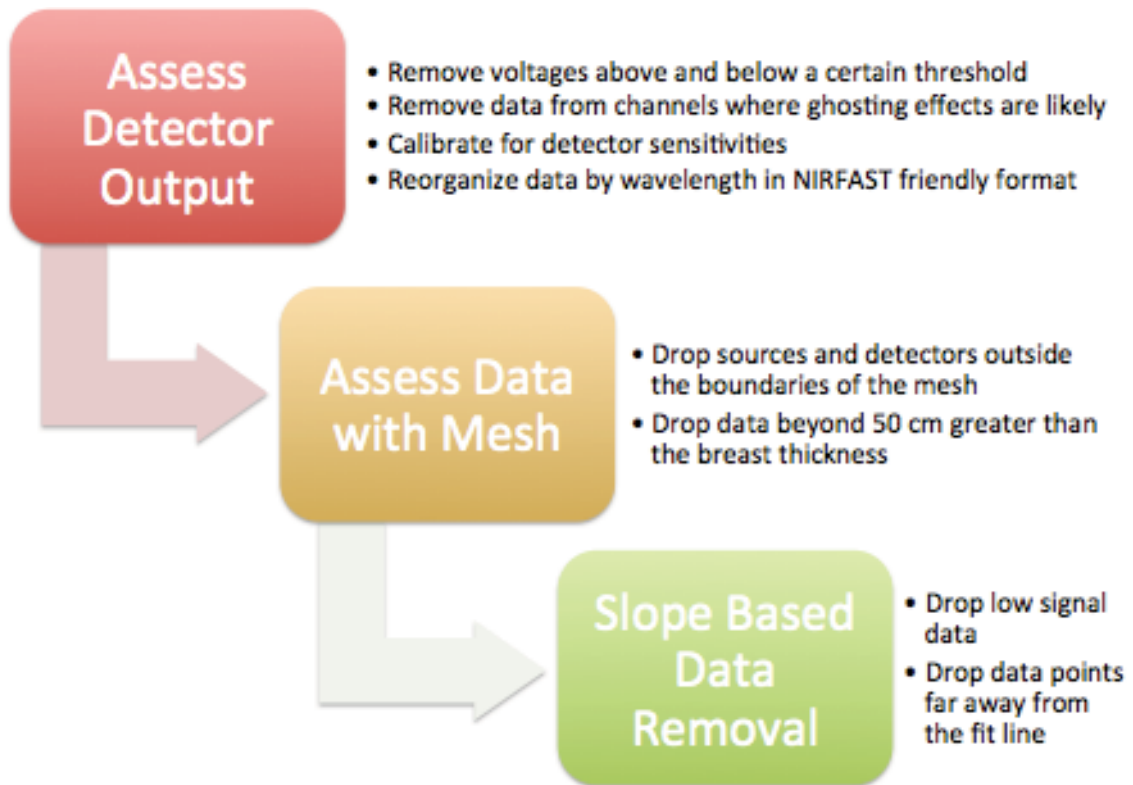


*Figure 62: Flowchart outlining the major steps in data dropping and restructuring before image reconstruction can take place.*

### **5.1.8. Detector Output Thresholding**

Noise floor and saturation thresholds are easily determined by examining the detector output through homogeneous phantom measurements. These are set at 0.02 and 10V, respectively. The ghosting effects within the DAQ are more difficult to discern; high signals at one AI significantly increase the signal at a neighboring AI. This was confirmed by covering all detectors but one with optical blackout material and investigating the signal detected at neighboring AI channels. This signal was noticeably

increased, up to 50% for very low light levels, as compared to the signal detected when the channel was completely covered. Based on these experiments, any detector signals with greater than five times the output of a directly adjacent AI are eliminated as a large portion of the signal likely stems from ghosting effects, not tissue light transmission. These data removal steps are performed on the raw data output from the LABVIEW code after the last 100 samples are averaged (to remove any instability in early signals). Data points are listed in order of AI channel so ghosting effects can be effectively detected by simply comparing adjacent data points in the file. After these steps, the data is reorganized by detector number, calibrated for differing detector sensitivities, and reorganized by wavelength. Some detectors are known to be non-functional, and all data from such detectors is removed.

#### **5.1.9. Tissue Geometry Data Dropping**

After mesh creation, every source and detector position is placed on the mesh. Sources and detectors that are not in contact with the tissue are consequently removed and their corresponding data points dropped. Detector positions are removed based on the coordinates of the detector corner that is farthest from the breast. Additional data within the edges of tissue are dropped as well. Points that are 1.5 cm or less from the edge are removed for two reasons. First, as depicted in Figure 63(a), data modeling near the edges (at 5 cm from the chest wall) is poor and doesn't correlate with the experimental data. The chest wall side of the mesh depicts a false boundary. The mesh is ended on this side because this is the edge of the DBT image; of course, tissue extends beyond this region in patients. Hence, a non-existent boundary is modeled, and the data

points near the edges can cause differences in recovered hemoglobin, as shown in Figure 63(b and c). 1.5 cm edge boundaries were selected because artifacts were no longer present, as shown in Figure 63(d). The second reason that data near the edges is removed is because partial volume averaging of DBT images prevents accurate modeling of external breast boundaries. Specifically, breast curvature cannot be adequately determined from the DBT images and is likely overestimated, especially near the top of the breast. Hence, dropping data 1.5 cm from the edges will get rid of most of the data points along the curvature.

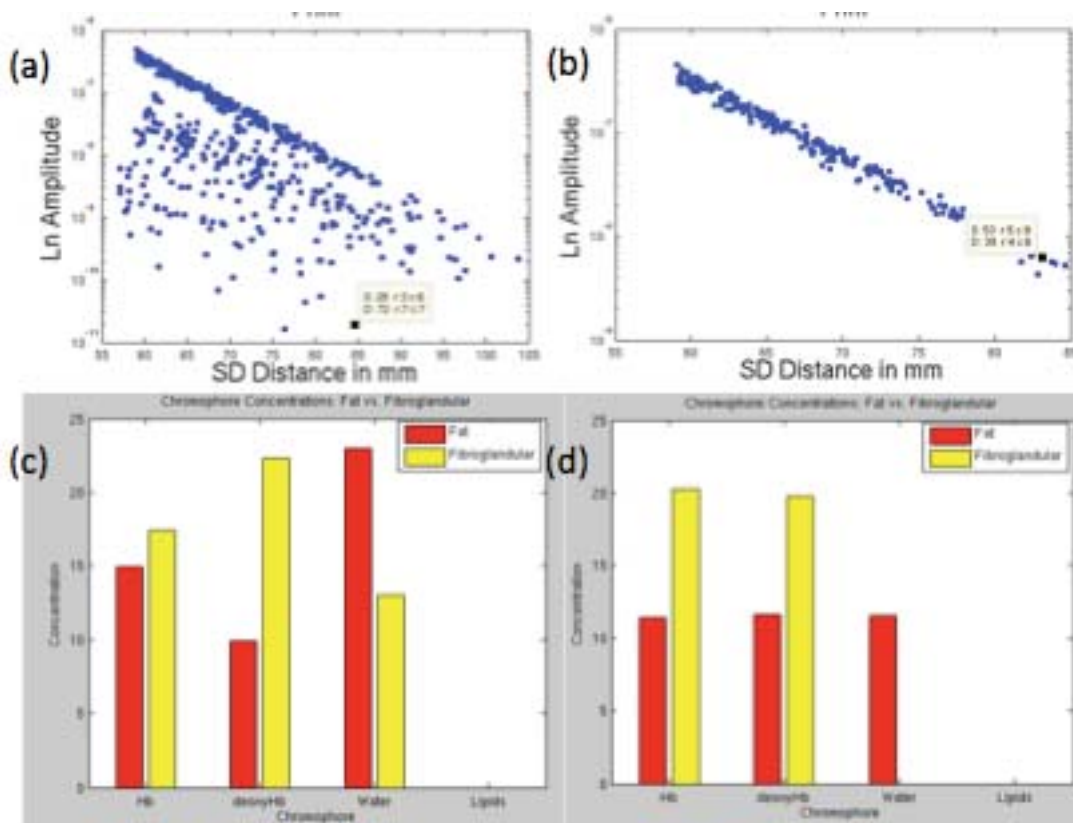
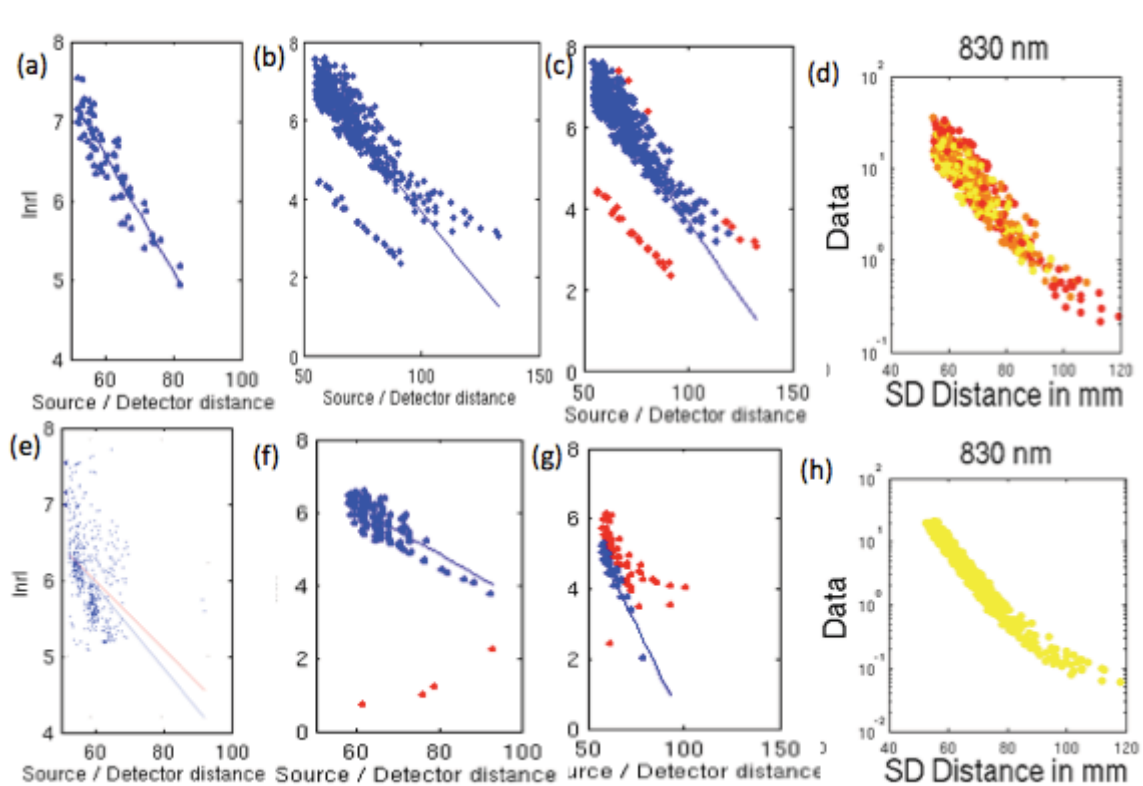


Figure 63: The modeling of data along the boundaries does not correspond to the actual data. Data points within 0.5 cm of the boundaries of the phantom mesh are included in (a), while data points are that are less than 1.5 cm from the edge are dropped in (b). At

1.5 cm from the edge, the data appears quite linear; the data points near the edge greatly alter the modeled data output. When far edge data points are included in the reconstruction, there are differences in the recovered hemoglobin concentration, (c) shows a 30% decrease in adipose HbT when boundary data is removed (d).

### 5.1.10. Slope-Based Data Removal

There is a wide variation in data quality depending on the patient breast positioning and shroud movement during the scan. In some cases, many data points beyond those described in the two preceding steps will need to be removed. In other cases, very few will need removal. The following method, shown in Figure 64, is used as a way to automatically and uniformly remove poor data from the NIRST-DBT system.



*Figure 64: Steps in the data dropping scheme. The top row depicts sequential steps for an excellent data set. The bottom row depicts issues that can arise in the data. (a) A linear fit of the log of the amplitude vs. source detector distance is derived for inner data points. (e) Including data points near the outside can skew the slope. Only the inner data is included because variation in data points near the outside can skew the slope, as shown in (e) for two different fitting algorithms. All data is plotted and those more than half a standard deviation below the lowest point in the slope fit are dropped (b, f) and are shown in red. Then cut based on variation from the slope fit is applied, with all points more than a certain distance away removed (c, g). Final data is shown, with colors corresponding to different regions (d), as well as data taken from the calibration phantom (h) to ensure that all detectors are working properly.*

As shown in Figure 64(e), a cluster of data points with a linear slope is visually apparent in the log output vs. SD distance. However, two different fitting approaches were originally attempted but for both, the data are skewed by many poor data points. Most of the poor data points are localized near the breast edges, as the shroud may not cover all the detectors outside the breast and the polycarbonate panel may channel some light to detectors near the edge of the breast. Excluding data up to 5 cm from the edge experimentally showed excellent slope fits (shown in Figure 64(b, f)) for both poor and excellent data sets. 5 cm is the default, but may be lowered or raised in the case of particularly small or large breasts.

Reconstructing only the most central detectors would limit sensitivity and detectability of lesions near the edges. Instead, after fitting the innermost breast data, the same slope is applied to all the data. Any data points with detector output more than half

a standard deviation below the slope fit value for the farthest source detector distance is removed, dropping particularly low data points. Generally, although they are above the 0.02 V threshold, signals at these locations are due to channeling through the polycarbonate detector cover. This cut is shown in Figure 64(b, f).

After a lower threshold cut, a second cut is made to eliminate data points far from the fit line. The amount of data removed depends on the strength of the fit; for data that closely fits the slope, only points more than two standard deviations away are removed, while for data with a lot of variation, points one standard deviation away are removed. This results in the final data, as shown in Figure 64(c, g). This technique consistently yields usable data, although further refinements to more fully automate and assess the effects of slight changes in the technique could be implemented.

### ***Data Analysis Tools***

When performing the first patient scans on the new NIRST-DBT system, many important decisions about hardware settings, data dropping, and reconstruction parameters were tested and assessed. The reconstruction time for this system is particularly long, taking several hours to a day depending on patient breast size. A visualization tool for the data was developed for quick understanding of whether or not the data matched the expected outcome. This tool is shown in Figure 8. In a normal breast, there are two region: adipose and fibroglandular. This tool uses the region assignments of nearby nodes in the x-y plane for the entirety of the breast thickness to determine the sensitivity of a source or detector to adipose vs. fibroglandular tissue. The sensitivities for each source and detector are combined for all the data and then

thresholded so that source and detector pairs with greater sensitivity are colored yellow for fibroglandular tissue, or red for adipose as shown in Figure 65(a,c). Using these plots, one can determine the expected outcome of reconstruction and lower detector signal in fibroglandular should it correspond to higher hemoglobin, and vice versa. If the resulting reconstruction does not show the expected outcome, there is likely a problem with the reconstruction parameters. If the data itself does not show the expected outcome, the problem may be related to source and detector positioning, inaccurate segmentation, or something inherent in the system design. In Figure 65(b,d), the results from the data were consistent with reconstruction, so the unexpected results in Figure 65(d) were likely due to the data itself.

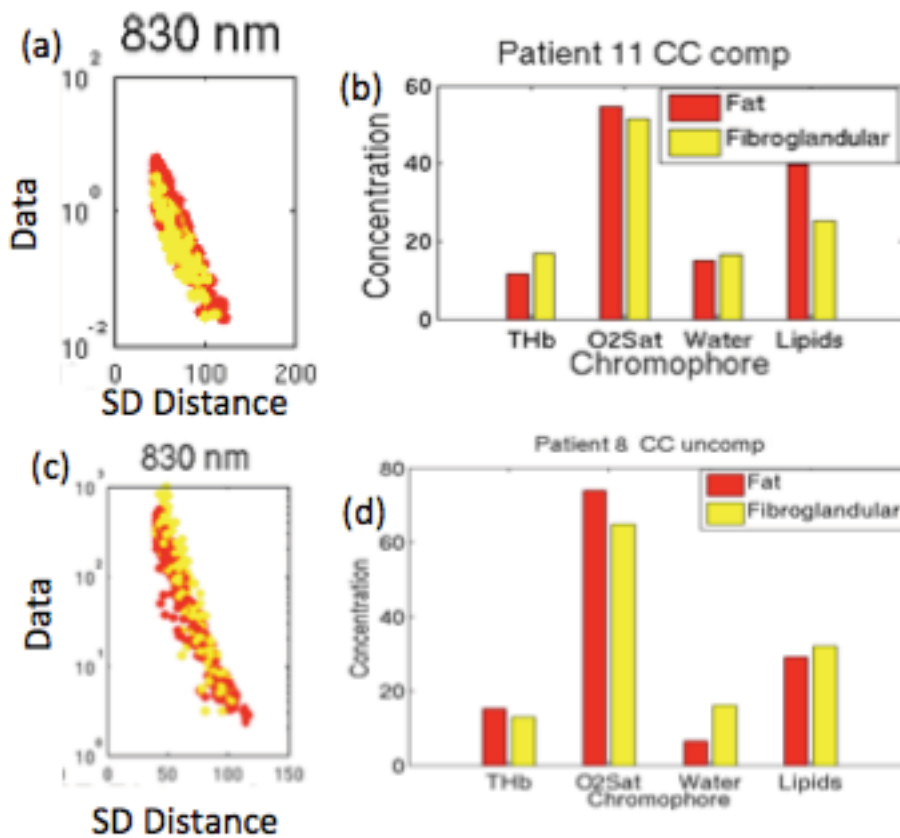


*Figure 65: Color-coding the data as shown in (a) and (c). Sources and detectors are labeled as being primarily associated with adipose (red) or fibroglandular (yellow) tissue. In the top row, there is greater fibroglandular absorption in the data (a), manifests as higher HbT (b). The opposite is true in (c) and (d).*

### ***Image Formation***

After mesh and data creation, the final step in the process is image reconstruction. Calibration procedures are described extensively in Chapter 4. Regularization values were 0.01 for standard calibration and 0.1 for spectral reconstruction for all iterations for normal subjects, with lower values used for spectral reconstructions of phantoms and higher for biopsy patients. Stopping criteria for the standard reconstruction required at least five iterations as well as projection error changes of less than 0.01%, typically taking seven iterations. If the initial guess chromophore concentrations of HbO and deoxyHb are less than 0.01  $\mu\text{M}$ , they are set at 5  $\mu\text{M}$ . If the initial guess chromophore concentrations of water and lipids are less than 0%, they are set to 20%. If they are over 100%, they are set to 80%. During the spectral reconstruction, water and lipids are constrained to be between 0 and 100%, at every iteration. Stopping criteria for the spectral reconstruction requires at least five iterations as well as projection error changes of less than 2%.

### ***Conclusions***

Developing a new imaging platform necessitates careful understanding and experimentation to successfully recover expected chromophore values in human breast tissue. An acceptable patient workflow has been designed to allow full NIRST-DBT

imaging in a half an hour after patient consent has been obtained, and the patient's time from door to door is kept under an hour, even when including the DOSI exam. Software tools using LABVIEW have been developed to control the hardware components. They are highly dependable and easy to use, facilitating fast training of new imagers. Additionally, they are optimized to minimize examination time, and real-time graphs provide feedback to the imaging team.

The MATLAB software developments assist in diagnosing problems as caused by hardware, software, segmentation, data, or reconstruction efforts. A data calibration GUI can quickly address issues when imaging homogeneous phantoms during hardware improvements. Data can be visualized graphically, allowing the user to select individual problematic points and know which source and detector obtained that data to diagnose problems with specific sources or detectors. Assigning data points to tissue types can help to identify and address problems with reconstruction algorithms and data quality without waiting for complete reconstruction. Additionally, code has been written to convert the output files from the LABVIEW software into Nirfast-friendly formats for reconstruction with bad data points removed based on experimentally derived results. The data dropping procedures are robust and semi-automatic, providing inter-patient consistency.

Several important developments described in this chapter improved NIRST recovery and optimized workflow. Without some of these processes, analysis would be significantly slower and variable between patients. For example, development of easy data visualization tools assisted in discriminating data problems from recovery issues.

Without them, it would have been much more challenging to figure out problems, requiring full blown reconstructions which can take up to one day.

These visualization tools were essential in figuring out a solution to a second problem, why adipose regions were consistently reconstructing higher hemoglobin levels than fibroglandular regions. Through examination of the data with these tools, it seemed that they should have lower hemoglobin, however visualization of the calibrated data showed the opposite, indicating an issue during the calibration phase. Simulations determined that this was caused by data close to the boundaries, where the model and actual data are vastly different. It was solved by removal of data at least 1.5 cm from any edges. Future work should focus on improving the model to allow for inclusion of these data points and increase edge sensitivity of NIRST-DBT.

Another challenge poised by patient imaging was large differences in data quality between different patients. There were some data sets with lots of noisy data and erroneous data points and some with very little. By examination of the data visually, it was possible to see where the 'good' data was located, but at the time, there were only manually assisted tools for removing the poor points. This process would induce human error and decrease repeatability. Early systematic evaluations of edge data removal (typically the location of the most poor noisy data points) showed that the effects of removing more and more boundary data differed on a case-by-case basis depending on breast volume and data quality (data not shown). Additionally, exclusive removal of all data from the external boundaries led to very poor sensitivity in those regions. The slope based calibration method was introduced which preserves the best data near the outside

of the tissue and can be applied to all patients automatically improving repeatability and consistency across all reconstructions.

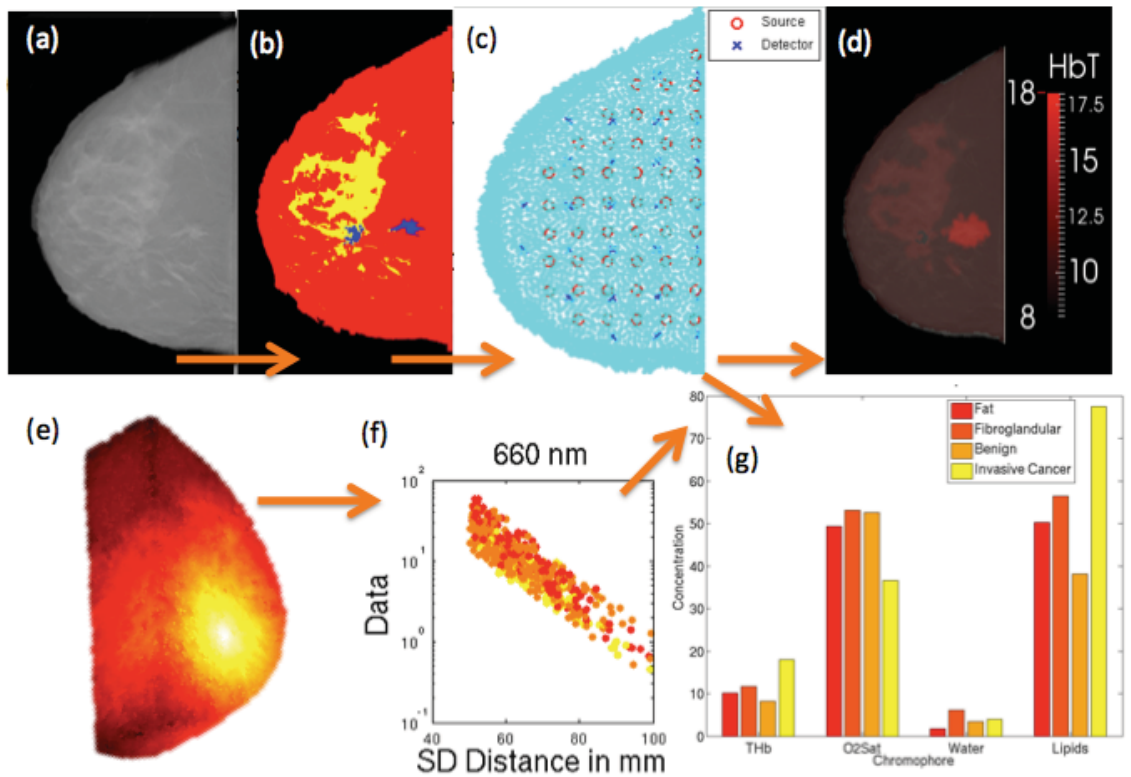


Figure 66: Pictorial flow chart representing a summary of the data reconstruction scheme. DBT images are obtained (a), segmented (b) and used as the basis for creating an FEM mesh (c). NIRST data is collected (e), dropped and reformatted (f) and reconstructed using the FEM mesh. The resulting output can be displayed as an overlay on the original DBT image (d) or more quantitatively (g).

Development of software tools for data visualization, analysis and removal improved the NIRST recovery for patients with variable data quality. The entire process from DBT and NIRST data collection to image reconstruction for patients is outlined in Figure 66. Careful development of the patient imaging steps made it possible to obtain results from most of the women who participated in studies of the NIRST-DBT system.

## Chapter 6: Healthy Volunteers

### *Introduction*

It is important to test novel imaging techniques through healthy volunteers studies to clearly understanding normal tissue property range of variation, assess patient comfort, perfect patient workflow, and test reconstruction algorithms. This is an important step prior to imaging abnormal or malignant tissue. The strengths and weaknesses of a novel imaging system critically depends upon its performance on imaging subjects without lesions, to characterize healthy breast tissue in vivo. The major drawback of imaging healthy volunteers is that the true optical properties before reconstruction are unknown. Instead, results must simply be compared against the literature. By combining extensive phantom and healthy subject studies, both chromophore recovery and patient workflow can be studied in a novel imaging system.

Data from healthy volunteers for the NIRST-DBT system served different purposes. The earliest patient imaging studies addressed a simple hypothesis: adequate NIRST and DBT data can be obtained in a completely co-registered fashion such that optical chromophore content of the breast can be determined and DBT slices are of clinical quality. After addressing this most basic question, women across a large range of breast sizes, shapes, and densities were imaged to test the limitations of the imaging platform and determine if any types of patients should be excluded in future studies of a biopsy cohort on account of such limitations. Additionally, enrollment of healthy subjects continued after imaging of a biopsy group was initiated in order to test small

changes in system software, hardware, X-ray protocols, etc. Specific details on patient exam procedures and reconstructions are detailed in the preceding chapter.

The focus of this chapter is on analyzing the results from 32 normal women, each of whom was imaged with four NIRST and two DBT scans, providing over 120 sets of NIRST-DBT data. With so much information, it is possible to examine the data in great depth and do more than just a simple comparison of healthy subject results and literature values. For example, NIRST results of CC and MLO views of the same breast are compared, as well as the effects of compression on NIRST chromophore recovery. The first region-based analysis of a NIRST-DBT multimodal system is presented here. In addition, NIRST results are compared with patient characteristics like breast density, bra cup size, body mass index (BMI), and age. Also, NIRST and DOSI chromophore recovery are compared for a small cohort that underwent both imaging procedures. By imaging each woman several times, the data is much more valuable than for a singular comparison to literature results, as it can assess effects of mechanical compression, repeatability, and effects of positioning variation.

### ***Normal Subject Imaging Summary***

A total of 32 women were imaged over one and a half years. Many system improvements were initiated based on patient, examiner, and researcher feedback during this time. Of all of the data collected, only the first five exams were unusable. The first examination had poor DBT quality, while exams 2-4 were obtained at different and unrecorded laser power settings. The fifth exam was unusable due to examiner error after a new code adjustment. One additional patient has only CC views due to software

malfunction prior to MLO imaging. Three patients were imaged on both the right and left side for a total of eight NIRST scans and four DBT scans. All other patients were imaged on the right side only. Detectable signal was obtained through all breast sizes and shapes. Exams of the thickest breasts (8.5-9.5cm during uncompressed images) were considerably slower, taking roughly twice as long to complete as it took more time for the mirror position adjustments at their extreme angular limits; however, good signal quality was obtained. The following sections highlight the improvements made to the hardware, software, and image reconstruction process on account of these negative exams, as well as through discussion with the healthy subjects, technologists, and examiners.

#### **6.1.1. System Improvements**

Areas for system improvement were identified during the very first exam and continue through to the most recent patient examinations. The DBT images obtained during the first exam were unacceptable, appearing quite blurry with little contrast in the breast, as shown in Figure 67(a,b). Further testing determined that the cause of this issue was leaving the black breast shroud in place during the DBT exam. The shroud contained a wire to help to keep the foam in a semicircular pattern around the breast without exposing any of the plastic detector panel cover. This wire itself was not in direct contact with the breast, so it was not expected to cause issues, but it did impact the reconstructed image. For all future exams, the breast shroud is removed along with the detector panel so the DBT images remain unaffected.

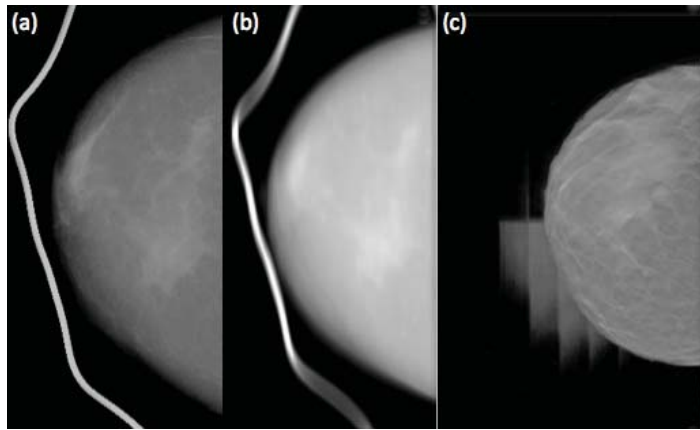


*Figure 67: First projection (a) and processed (b) DBT images taken during a NIRST-DBT exam show metal wire in place inside the detector shroud. Detector calibration artifacts (c) apparent in some patients.*

In early patient imaging (subjects 1-4), estimations of expected relative source strengths for each wavelength were determined through literature absorption profiles and phantom experimentation in hopes that light incident on the detector would be roughly equal for all wavelengths. This is important because the photodiode detectors have limited dynamic range. Additionally, there was not enough time to adjust each wavelength individually, so a single wavelength was altered, with all the other wavelengths correspondingly adjusted. In these early patients, there was limited detector signal for the highest wavelengths, so the output of these lasers was increased relative to the others, leading to a reliable data output for all wavelengths with correct patient positioning during future exams. Additional improvements included a LABVIEW tab to adjust source strength with a single click, increasing speed and usability.

Another difficult issue has been detector artifacts and subclinical quality in some of the DBT images as shown in Figure 67. Such artifacts are typically removed during

image processing, but as this system was the third ever built, it does not possess such capabilities. These artifacts must be removed manually and this process is described in the preceding chapter. Accounting for the fact that this is a research system lacking automatic exposer and that we have added an additional piece of polycarbonate to the breast platform, adjustments in the look up table for kVp and mAs for different breast thicknesses were made with the help of DHMC medical physicist John Weaver. These adjustments have largely eliminated detector artifacts, both the old and new look up tables can be found in appendix A.

One final issue has been the detector panel cables. The cables are short and this fact along with room constraints means it is only possible to remove the panel from the patient's left side. This prevents left-sided MLO imaging of women with larger arms as the cables may come loose during the exam or the panel may be impossible to remove for DBT imaging. Also, screws do not line up between the cables and panel and they must be manually reattached prior to each phase of the exam as they have a tendency to come loose during exams if a patient's arms weigh down on them. When loose, they may emit spurious signals, leading to an infinite loop in the LABVIEW program. This was the cause of the only biopsy patient exam failure performed by an inexperienced research assistant. This issue has been fixed in the LABVIEW code

### **6.1.2. Reconstruction Algorithm Adjustments**

Over the one and a half years of normal subject imaging, improvements have been made to the DBT image pixel spacing and source and detector placement. The earliest reconstructions were performed using the DBT header file pixel spacings, constant for all

slices, which are actually inaccurate. This was determined while measuring the light source positions at various heights and noting differences in the DBT reconstruction slices. Information on the correct pixel spacing was obtained from Hologic and implemented in future reconstructions. As the detector positions were measured from a reconstructed DBT image, it was also necessary to change their positions once the pixel spacing for the corresponding DBT image slice were in place. This change has decreased variability in homogeneous phantom data and should improve fidelity of patient reconstructions, even though changes in detector position are less than 5 mm.

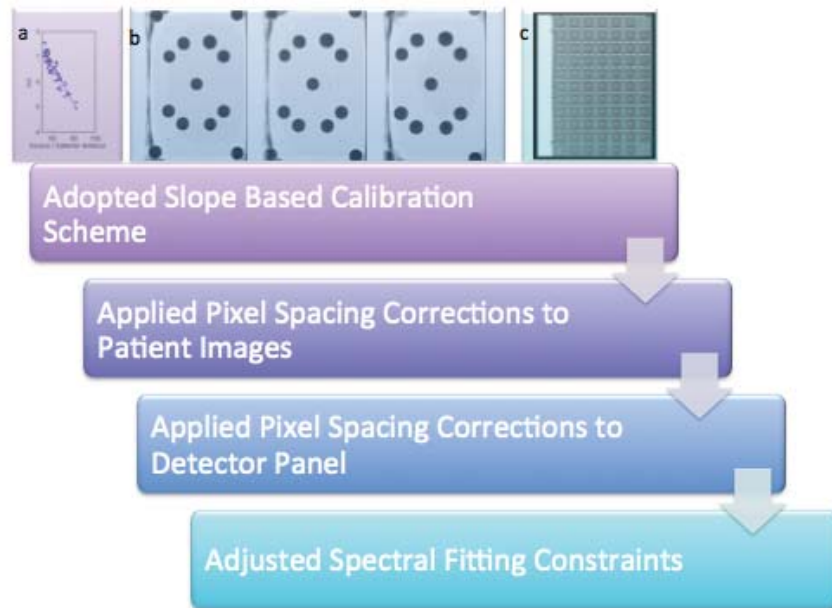


*Figure 68: Changes made to breast modeling and image reconstruction. First, slope-based calibration was adopted for all patients as a consistent data removal scheme (a). Based on the images of source positions at different heights (b), it was determined that pixel spacing corrections needed to be implemented based on slice height. These same corrections were applied to the detector panel (c).*

Lastly, based on the normal subject cohort data, the spectral constraints on water were adjusted to account for the lower-than-expected water recovery. Early reconstructions for water, in which the concentration was less than 0, were set to 20%. This is higher than the recovery for most patients and was adjusted down to 5%. All of these changes have evolved over the past year and a half, each incrementally improving the fidelity of the data model match. The reconstructions shown in this chapter have not all been performed with all these changes due to time constraints, but will be performed prior to publication. Additionally, some of the latest normal subjects have yet to be reconstructed for MLO views, but additional data should bolster existing correlations.

### **6.1.3. Patient Considerations**

Early reports from normal subjects described neck pain due to the plastic face shield attached to the DBT gantry that keeps the patient's head and hair out of the X-ray path. This particular face shield was designed to be used exclusively for mammographic imaging, so it moves and can make contact with the head of the subject during a tomosynthesis scan. Unfortunately, the face shield is also used to hold the light source in place. An existing Hologic shield was modified to fit with the NIRST source and a new independent placement for the source was also developed for a more comfortable fit. However, these changes have not been implemented yet due to the significant downtime required for the system to undergo such a transformation.

### ***NIRST Results***

Looking at aggregate values for all chromophores, mean HbT is 16  $\mu\text{m}$ , oxygen saturation is 54%, water is 11%, and lipids are 31%. When compared to results from

studies of other healthy volunteers in DBT, MRI, and stand-alone NIRST systems, the chromophore quantification is physiologically reasonable and comparable<sup>186-190</sup>.

Hemoglobin and lipid quantities fall well within the expected ranges, while water and oxygen saturation are somewhat lower than previously published results. With many of the exams performed under compression, it is understandable that the breast hemoglobin would possess fewer oxygen molecules if blood flow is impeded. However, it seems unlikely that water is squeezed out of the tissue simultaneously. Possible causes for the lower-than-expected water include cross talk with lipids, the other main absorber at higher wavelengths and cause of overestimation of scattering at the highest wavelengths. Overall, absolute values of our tissue components occur within physiological limits and can be aggregately studied.

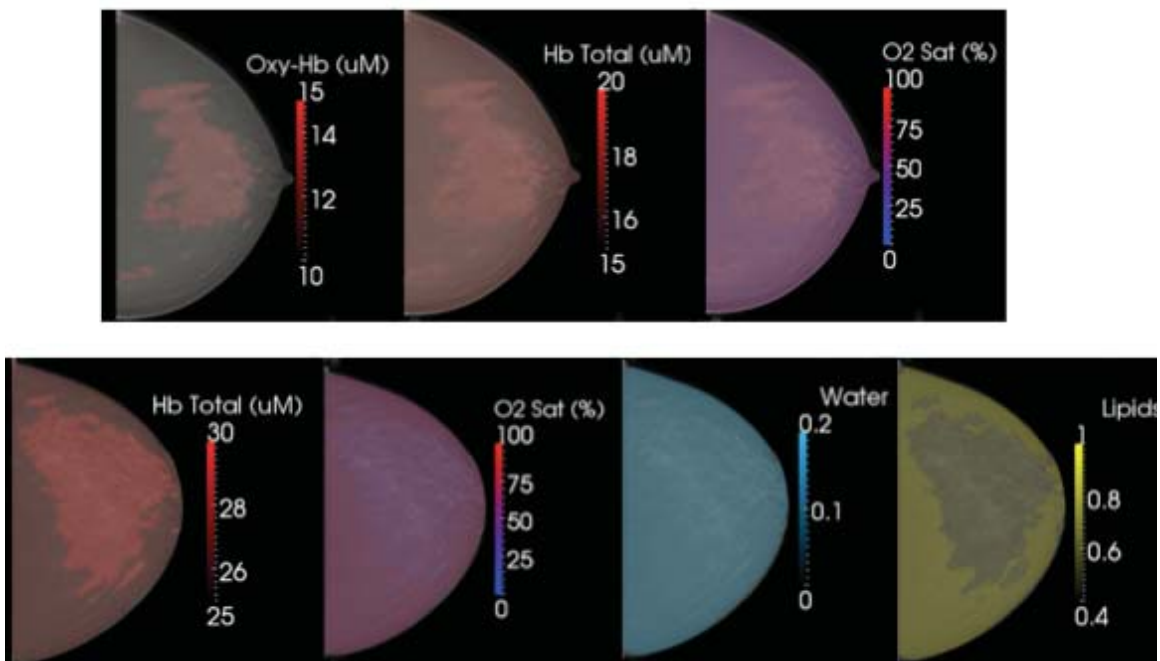


Figure 69: Sample reconstructions for two early study subjects. NIRST results for adipose and fibroglandular tissues are overlaid on a DBT slice. Low signals in the higher wavelengths prevented reconstruction of water and lipids in one case.

### Patient Characteristics and NIRST Results

Looking at the NIRST results in the context of different patient characteristics such as breast density, thickness, FG percentage, and BMI may provide some insight into the metabolic status of healthy breast tissue, which can be compared to results of prior studies<sup>77,188,189,191</sup> but are unique in that this system uses X-ray based spatial prior information and is exclusively CW.

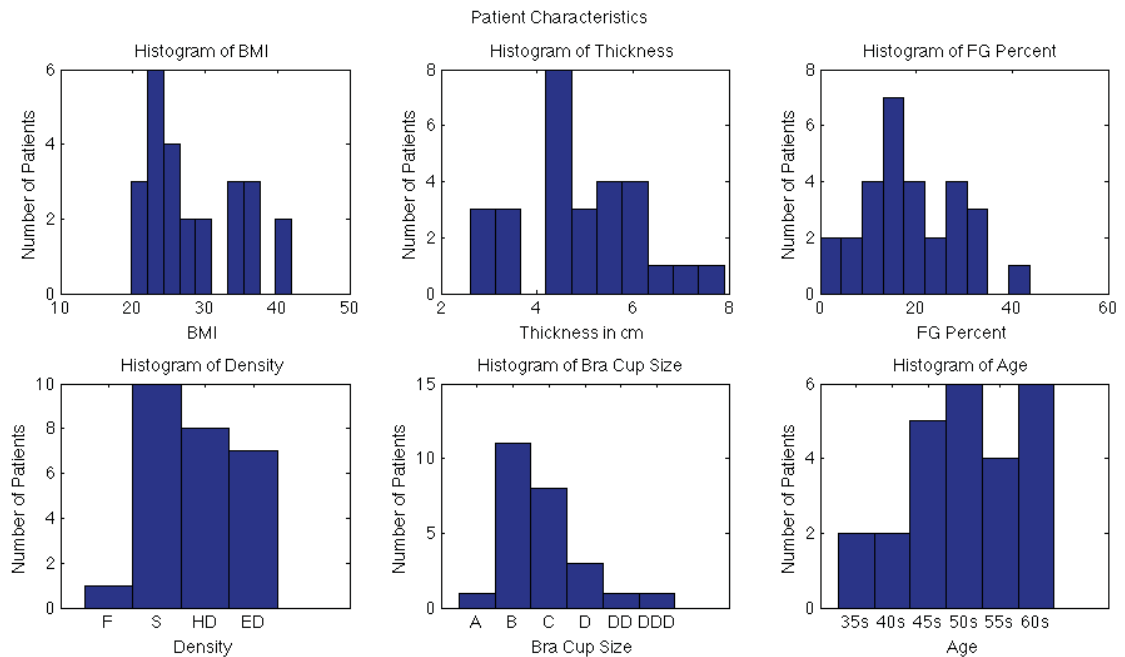


Figure 70: Histograms of key demographic and clinical information for the 32 normal subjects imaged here.

Figure 70 shows several properties of the women imaged, including BMI, breast thickness, percent fibroglandular tissue, density, bra cup size, and age. The average BMI

was 28.5, similar to 29<sup>192</sup>, the US average for older women. The average age was 51 years. The average bra cup size was slightly below C with a density closer to heterogeneously dense but between heterogeneously dense and scattered. Note that there is a single patient in the fatty density category. The average breast compressed to a thickness of 4.9 cm, and average fibroglandular content was 19%. These values are comparable to averages obtained in larger studies. The fibroglandular content was higher than in the average population, where the mean is 12-14%; however, this technology specifically targets denser breasts, so it is important to image more women with denser breasts<sup>193</sup>. The compressed breast thickness is similar to other studies (4.4-4.8 cm), with the thickness during NIRST-DBT possibly slightly higher due to the increased length of the examination<sup>29,194,195</sup>. Overall, this group is composed of a variety of breast sizes, shapes, and densities and is similar to the average woman in the United States who is recommended for breast cancer screening. It is an excellent representative sample group to understand and assess the NIRST-DBT imaging platform.

NIRST recovery of chromophores was performed for a wide range of situations, different views, and compression levels, and in different tissue types. In order to compare patient characteristics and chromophore recovery, all data was included. However, for each exam, a single weighted average of each chromophore was calculated using the fibroglandular volume determined by the segmented images, rather than including both fibroglandular and adipose or only one tissue type. This volume-weighted average per exam contains information about both fibroglandular and adipose chromophores.

### 6.1.4. Breast Density

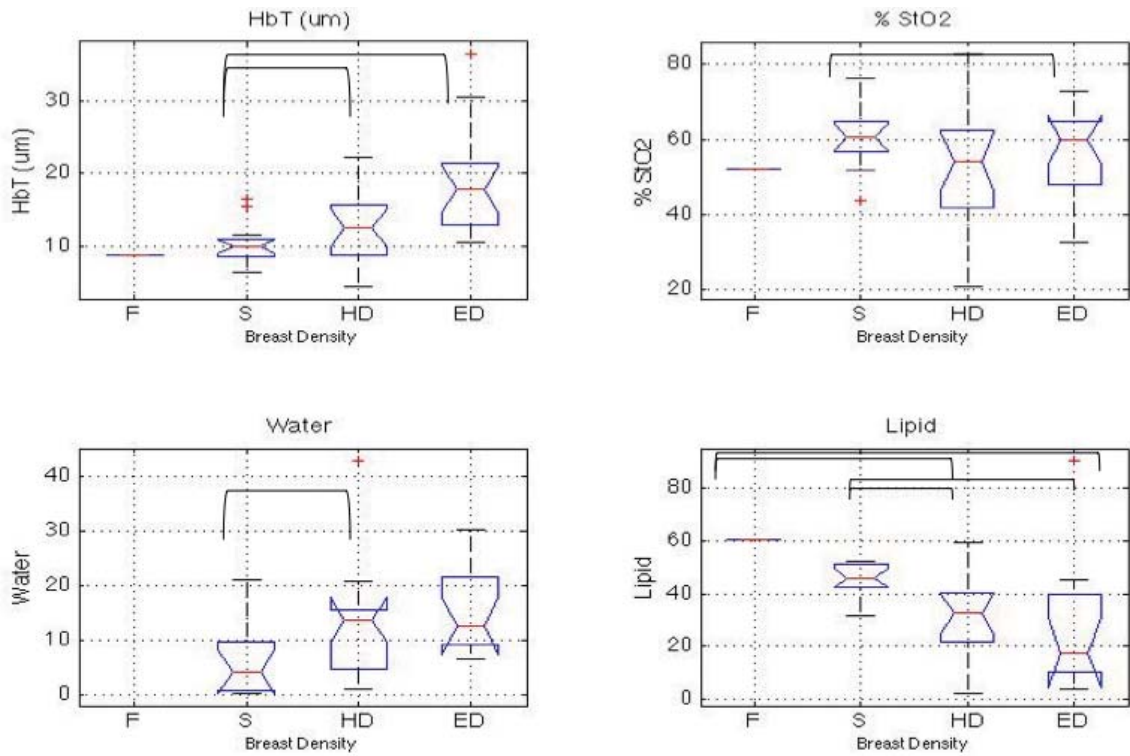


Figure 71: Comparison of summary data on breast density and tissue chromophores for normal subjects. Black bars indicate statistical significance ( $p < 0.05$ ).

<i>Breast Density</i>	<i>Correlation</i>	<i>p value</i>
HbT	<b>0.643</b>	<b>0.001</b>
O2 Sat	-0.100	0.658
Water	<b>0.616</b>	<b>0.003</b>
Lipids	<b>-0.737</b>	<b>0.000</b>

Table 5: Correlation between breast density and hemoglobin, oxygen saturation, water and lipids. Bold values indicate statistical significance ( $p < 0.05$ )

As expected from prior literature, there are significant correlations between tissue chromophores and breast density<sup>77,191</sup>. Increases in HbT and water are positively

correlated with increasing breast density, while lipid content and oxygen saturation are inversely correlated. The correlation for HbT, water and lipids are all statistically significant, as 

Bra Cup Size	Correlation	p value
A		
B		
C		
D		
DD		
DDD		

 shown in Table 5. This makes sense as denser breasts are comprised of less fat and thus should have lower lipid content and higher water content. Hemoglobin concentration increases correspond to greater metabolic demands of active fibroglandular tissue.

### 6.1.5. Bra Cup Size

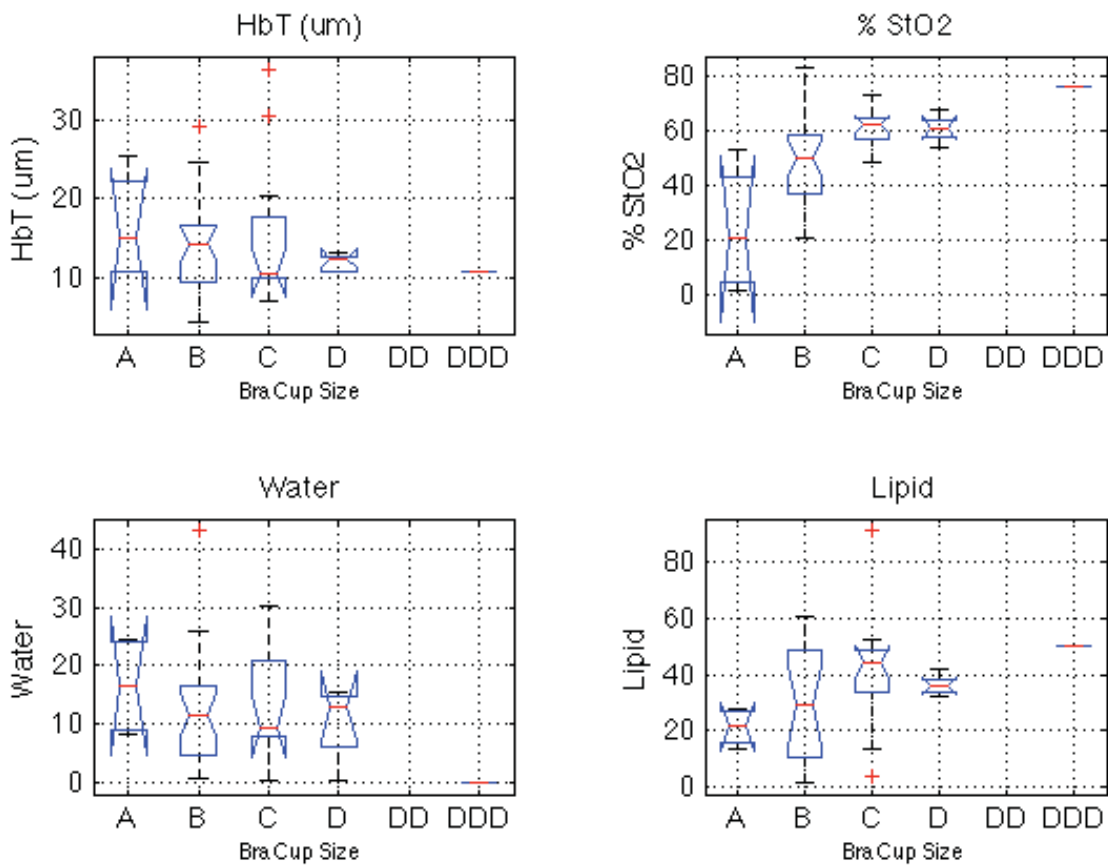


Figure 72: Comparison of tissue chromophores for normal subjects grouped together based upon bra cup size.

HbT	-0.183	0.416
O2 Sat	<b>0.538</b>	<b>0.010</b>
Water	-0.278	0.222
Lipids	0.269	0.239

*Table 6: Correlation between bra cup size and hemoglobin, oxygen saturation, water and lipids. Bold values indicate statistical significance ( $p < 0.05$ )*

Correlations between metabolic properties and bra cup size alone are unexpected as bulk tissue volume differences without changes in functional status should be accounted for in the NIRST model. However, changes in volume alter patient positioning, as well as the number of data points collected during the NIRST scan. Negative controls such as bra size can help to ensure that differences in hardware or software do not lead to systemic alterations in the data. In this case, the results do not show statistically significant correlation with any factor other than oxygen saturation. This may actually be a result of a confounding effect of breast thickness on oxygen saturation, shown in the next section, breast thickness and bra cup size are highly correlated ( $r=0.70$ ,  $p < 0.0001$ ), and breast thickness shows a much stronger correlation with oxygen saturation than bra cup size ( $p=0.0001$  vs.  $p=0.01$ ). Hence, it is unlikely that bra cup size alone significantly affects any of the chromophores when the effects of confounding variables are removed, as will be performed in a future multi-variable analysis.

### 6.1.6. Thickness

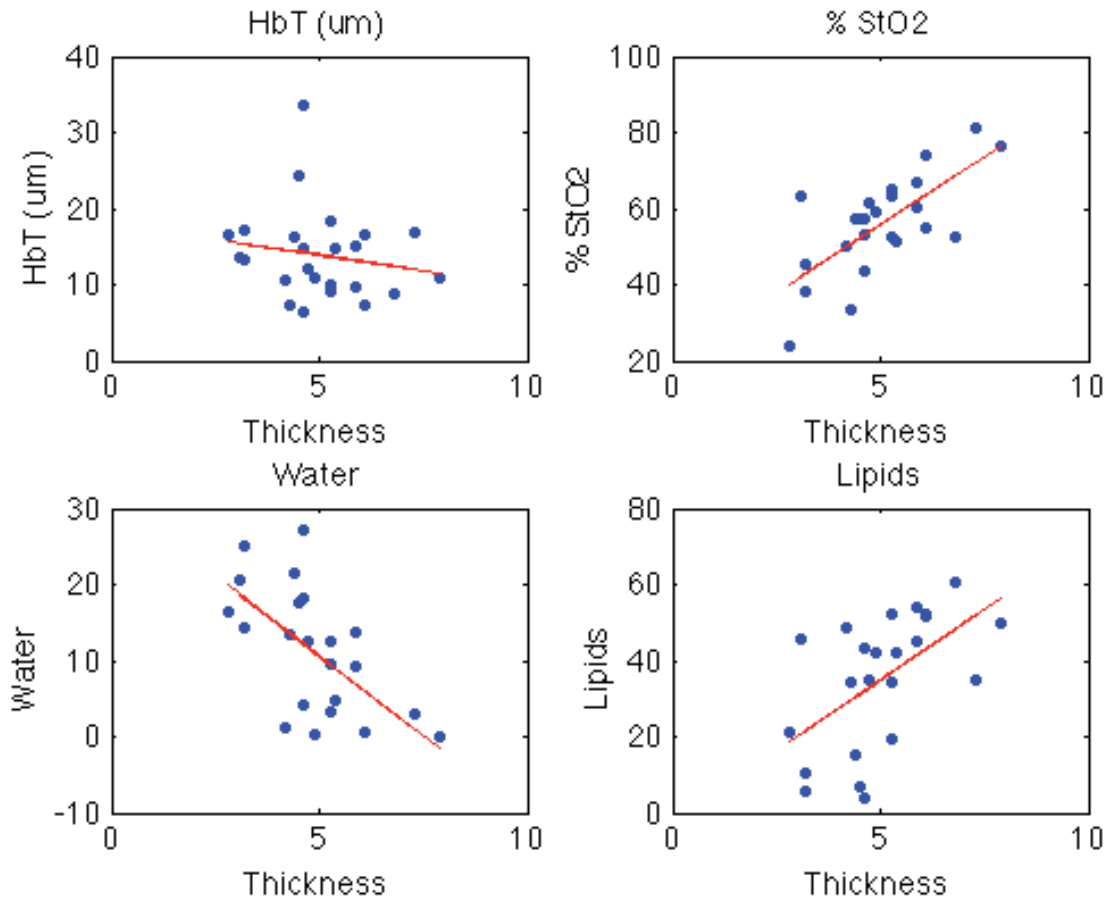


Figure 73: Comparison of breast thickness and tissue chromophores for these normal subjects, and trendlines shown in red for each.

Thickness	Correlation	p value
HbT	-0.183	0.391
O2 Sat	<b>0.706</b>	<b>0.000</b>
Water	<b>-0.628</b>	<b>0.001</b>
Lipids	<b>0.563</b>	<b>0.005</b>

Table 7: Correlation between breast thickness and hemoglobin, oxygen saturation, water and lipids. Bold values indicate statistical significance ( $p < 0.05$ )

Breast thickness is highly correlated with oxygen saturation, as well as with water and lipids as shown in Table 7 but is not correlated with hemoglobin. Breast compression decreases breast thickness while simultaneously restricting blood flow into or out of the tissue. The larger the decrease in thickness, the less blood can move into or out of the tissue, necessitating further deoxygenation of existing hemoglobin to meet metabolic demands. Unfortunately, the research system was not equipped with a compression force measurement and measurements of the undeformed breast thickness were not performed, so breast thickness is the best measurement of compression available. It is likely that these other metrics could show greater correlation than thickness but this is the only option for this initial study. In terms of the lipid and water changes, this may again be a result of confounding with other variables such as BMI, which is highly correlated with thickness ( $r=0.79$ ,  $p<0.000001$ ), and as demonstrated in the next section, and shows the same correlation for water and lipids as is present for thickness.

### 6.1.7. Body Mass Index

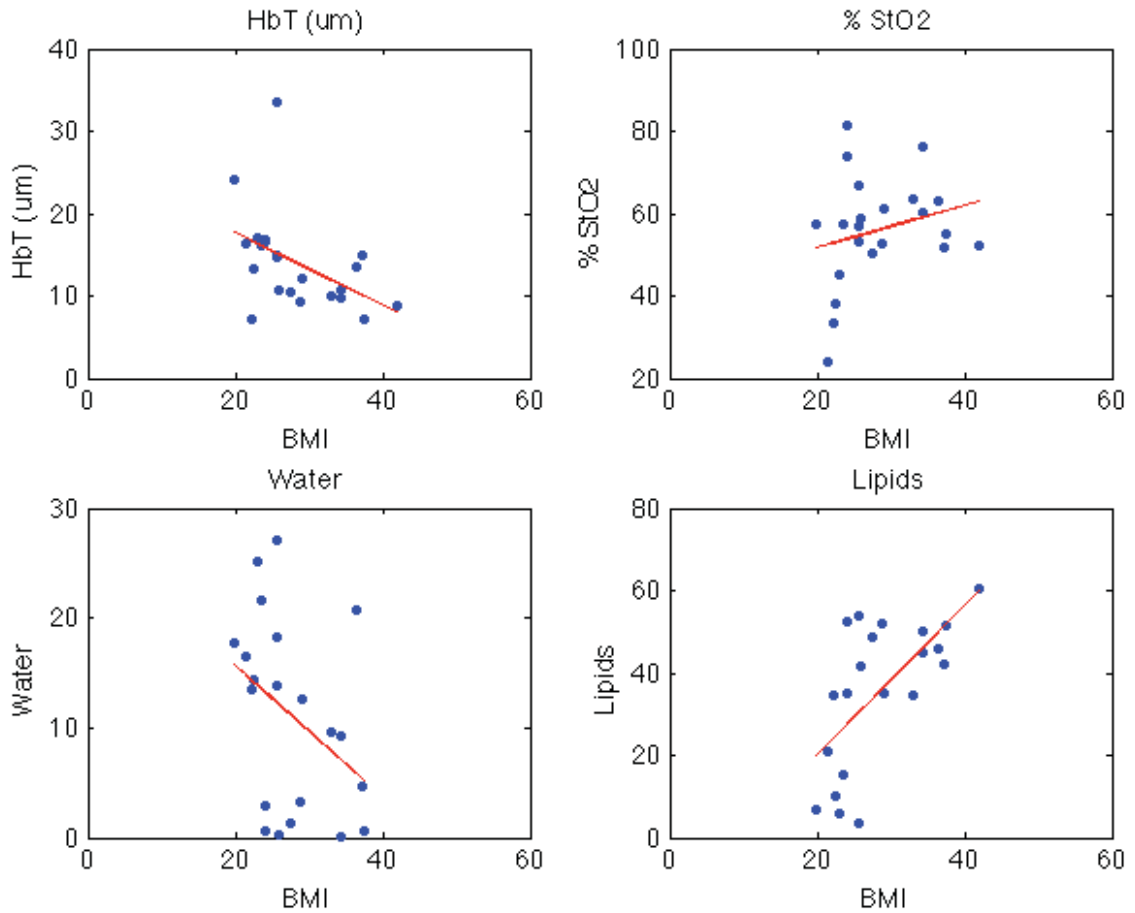


Figure 74: Comparison of body mass index and tissue chromophores for normal subjects, with trendlines shown in red for each.

BMI	Correlation	p value
HbT	<b>-0.454</b>	<b>0.034</b>
O2 Sat	0.247	0.268
Water	-0.381	0.088
Lipids	<b>0.646</b>	<b>0.002</b>

Table 8: Correlation between BMI and hemoglobin, oxygen saturation, water and lipids.

Bold values indicate statistical significance ( $p < 0.05$ )

*Increases in body mass index typically correspond with a larger percentage of body fat. In the breast, this corresponds to a larger subdermal adipose tissue deposit, increasing the percentage of the breast comprised of adipose tissue and skewing the tissue chromophore recovery towards values associated with fat. This includes higher lipids and lower water and hemoglobin as demonstrated in Figure 74, as well as in the highly significant correlation between BMI and lipids ( $p < 0.002$ ) shown in*

Table 8. With higher lipid concentrations, statistically significant lower total hemoglobin makes intuitive sense as adipose tissue has lower metabolic demands than more dense tissues.

### 6.1.8. Fibroglandular Percent

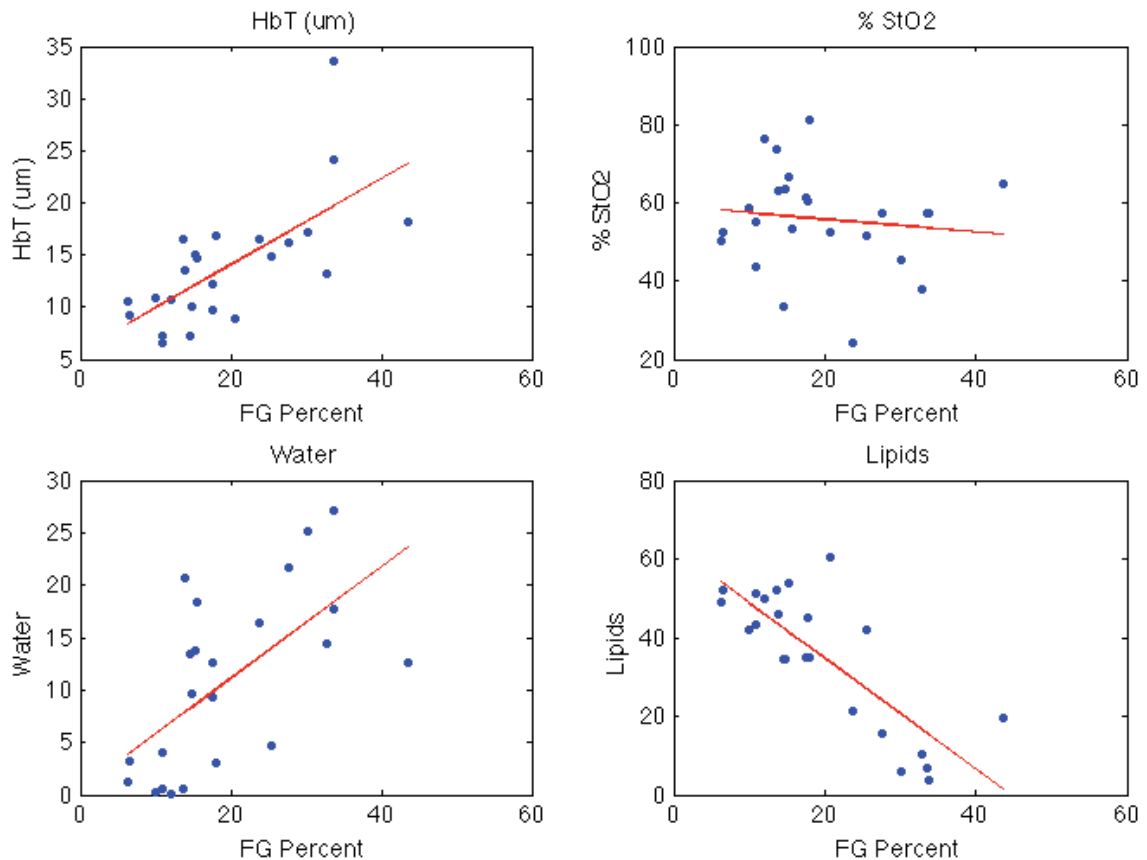


Figure 75: Comparison of fibroglandular percent and tissue chromophores for normal subjects with trendlines shown in read for each.

Fibroglandular Content	Correlation	p value
HbT	<b>0.677</b>	<b>0.000</b>
O2 Sat	-0.120	0.578
Water	<b>0.624</b>	<b>0.001</b>
Lipids	<b>-0.800</b>	<b>0.000</b>

Table 9: Correlation between fibroglandular content and hemoglobin, oxygen saturation, water and lipids. Bold values indicate statistical significance ( $p < 0.05$ )

Fibroglandular percent was assessed from segmented DBT images and shows the opposite results of BMI studies. Fibroglandular content is statistically correlated with total hemoglobin, water and lipids. Based on the previous discussion of the higher metabolic demands of fibroglandular tissue, these correlations make intuitive sense. All of the above results are promising, following expected literature trends and additional investigation using multivariable analysis can determine the patient characteristics that have the greatest impact on the NIRST results. Additionally, these studies lend credence to the possibility of using exclusively CW breast imaging with a scattering estimate.

### *Assessing NIRST Data*

With multiple NIRST datasets of the same breast under different compression levels in different views and completely co-registered with DBT information, there are many ways to compare and analyze the data. These analyses serve two purposes: first, it is possible to understand the metabolic effect of different conditions, such as compressed vs. uncompressed via the recovered NIRST quantities. Secondly, these studies confirm

that the novel NIRST-DBT system is functioning in the expected manner in all aspects from hardware to image reconstruction. For example, when studying a negative control case, such as CC vs. MLO views of the same breast, they are expected to have the same optical properties; any deviation from this expectation must be explained or attributed to some aspect of NIRST data collection or reconstruction. Taking multiple data sets greatly enhances the analytical value of healthy subject studies.

#### **6.1.9. Comparing Adipose and Fibroglandular Regions**

As the NIRST and DBT images are completely co-registered, it is possible to separately calculate chromophore quantities in the segmented adipose and fibroglandular regions. No prior work on NIRST-DBT has used spatial prior formation, so this is the first of its kind for this multi-modal combination<sup>12,13</sup>. Adipose and fibroglandular tissue regions are assigned after DBT image segmentation, a process described in detail in Chapter 3. All views and compression levels are included in the analysis.

### 6.1.9.1. Results

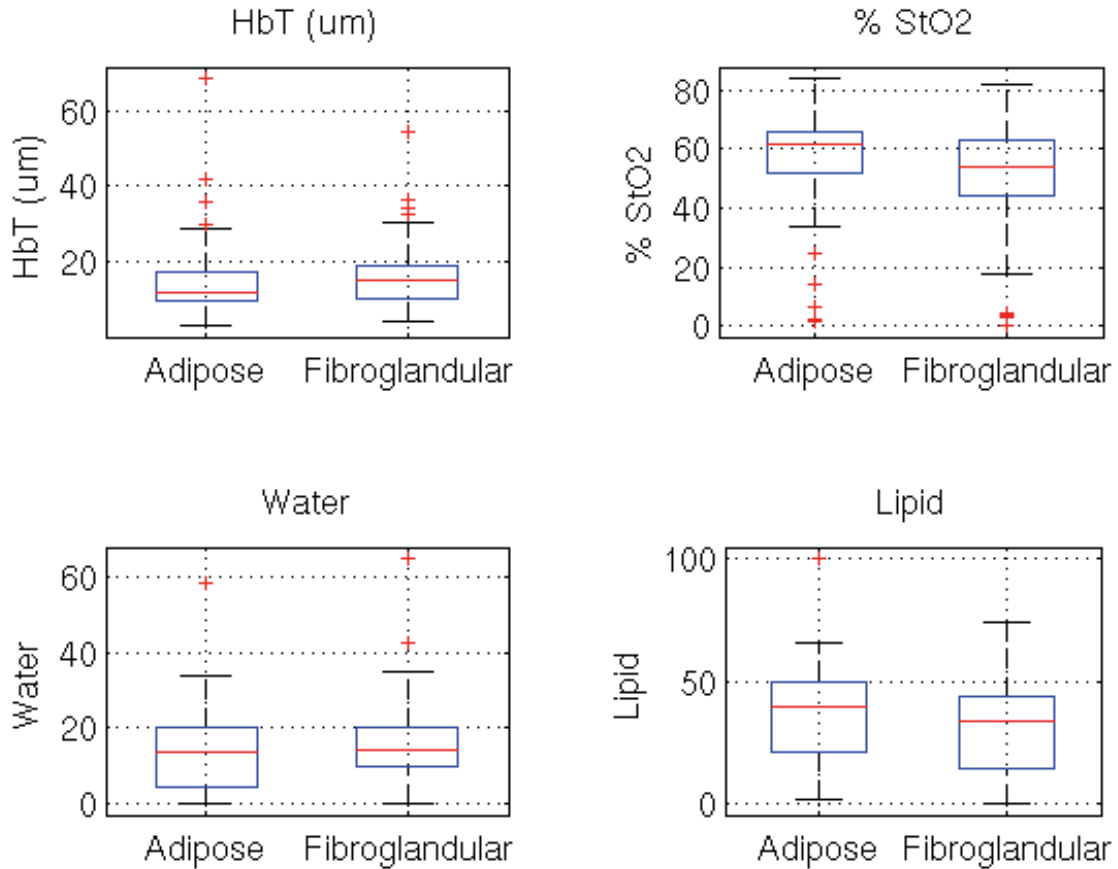


*Figure 76: Comparison of adipose and fibroglandular tissues across chromophores for normal subjects. There were no significant differences between adipose and fibroglandular regions for these chromophores.*

The results are shown in Figure 76. There were no statistically significant differences between any of the chromophore properties in the two regions.

### 6.1.9.2. Discussion

Fibroglandular tissue is comprised of more hemoglobin and water, but with less oxygen saturation and lipids. Each of these trends makes physiologic sense when

metabolic demands of these tissue types are considered. However, none of the differences are statistically significant. This may be due to the large variation within the data sets, as all views and compression levels are included. Additionally, effects from partial volume averaging are likely to occur in these healthy volunteers, because even with anatomical priors, pure separation of absorption and scattering is difficult due to the blended sensitivity profiles across tissue types. This is especially pertinent to DBT images, as our z-plane segmentation is known to be inaccurate. In the current segmentation algorithm, nearly all nodes along the same z-axis are declared part of the same region, regardless of height. Clearly, this is not physiological but rather is an artifact of DBT-based segmentation. These partial volume averaging effects may make quite subtle and non significant differences in tissue compartments, as demonstrated here

#### **6.1.10. Comparing CC and MLO Views**

When imaging two views the same breast, one must compare them to ensure similar results. We compared all CC and MLO images for all normal subjects.

##### *6.1.10.1. Results*

The results are shown in Figure 77 for all subjects, while scatter plots comparing individual CC and MLO chromophore recovery are found in Figure 78. As expected, there is little variation in average tissue chromophore for CC and MLO cases, no statistically significant difference is present. There is statistically significant correlation between CC and MLO views comparing each individual patient of the graphs shown in Figure 78 except for water.

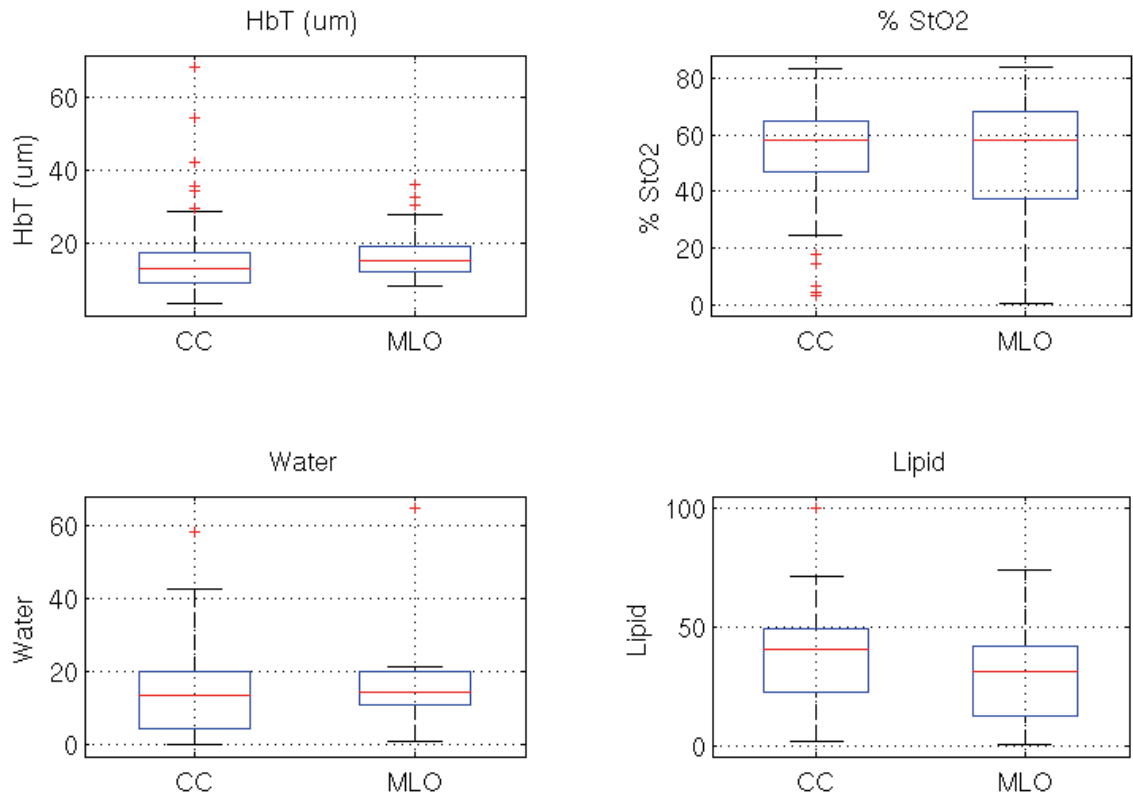


Figure 77: Comparison of CC and MLO views across chromophores for normal subjects.

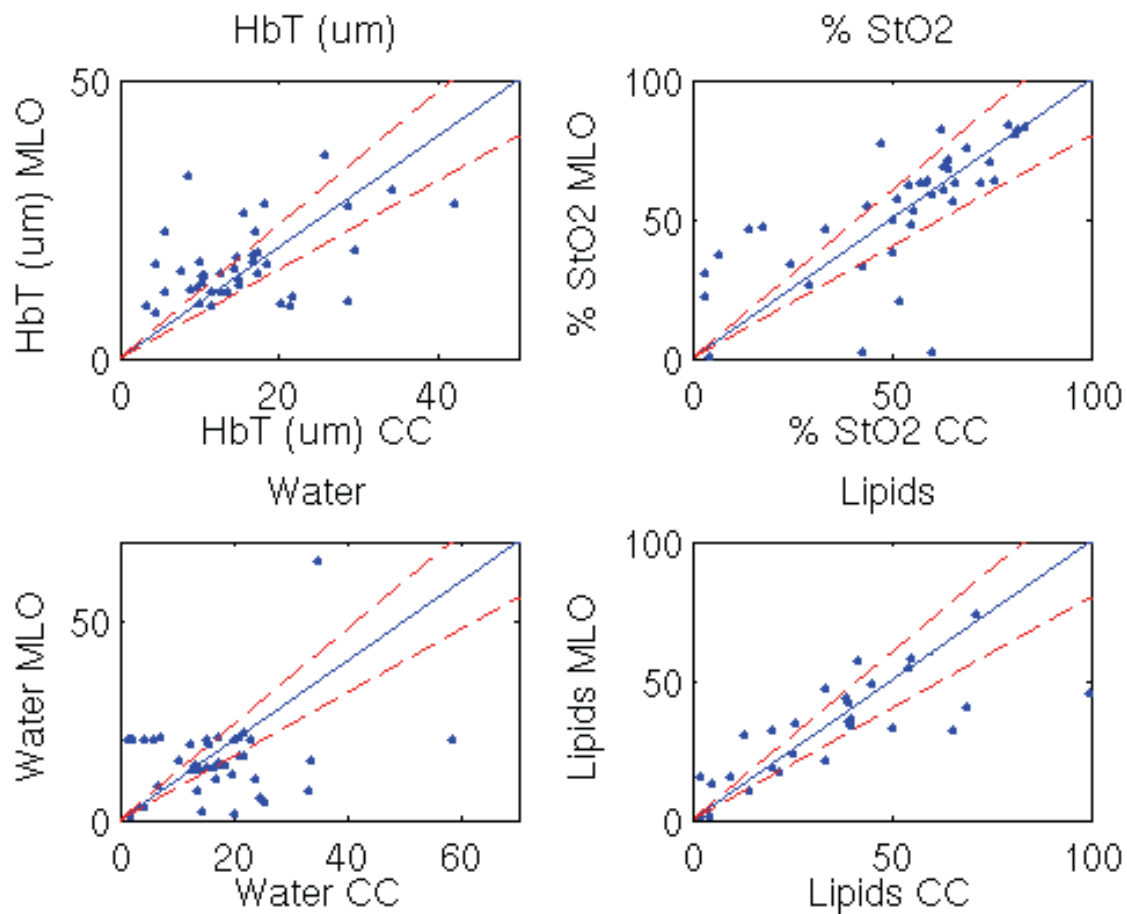


Figure 78: Scatter plots of compressed and uncompressed data across all chromophores.

Blue lines shown 1:1 correlation, and red dotted lines are offset from 1:1 by 20%

#### 6.1.10.2. Discussion

As expected, when comparing CC and MLO results through boxplots, the results were remarkably similar on average for the two cases. There was a non significant lower lipid content in MLO imaging that is likely due to poorer breast light shielding. The greater curvature of the breast in MLO makes it incredibly difficult to cover all unused light detectors, so generally some of the plastic panel cover is exposed during the exam. This is problematic because this plastic transmits light to nearby detectors, especially at

higher wavelengths (where lipid sensitivity is greatest). Data dropping methods described in Chapter 5 have been performed to eliminate such data points, but there may be some residual effects of poor shroud placement. Since we are comparing all CC and all MLO cases here, and several patients are missing either CC or MLO data, there is some chance that a larger percentage of dense breasts were reconstructed in CC and more fatty breasts in MLO. Excluding such cases and/or performing phantom studies with poor shroud placement would effectively clarify this issue. There was no statistical significance to this difference in any case.

Scatter plots for individuals show statistically correlation between the CC and MLO views of the same compression level for a single person for all chromophores except for water. Water results appear more scattered, partially due to a number of reconstructions reaching the minimum water value allowable (0) and adjusted back to 20%, specifically in the MLO case. This may be due to poor breast shroud positioning as described above. Differences in segmentation and patient positioning likely contribute to the variability between CC and MLO images. Improvements to or elimination of the breast shroud as well as fine-tuning the segmentation algorithm may decrease this variability.

#### **6.1.11. Comparing Compressed and Uncompressed NIRST**

DBT imaging is performed under high levels of breast compression; however, there are relatively few studies of NIRST imaging under high compression<sup>88,89,196</sup>.

Examining the effects of compression on tissue chromophores is essential to determine if

NIRST imaging could be performed at a lower compression level than the DBT imaging, for patient comfort, while still recovering co-registered high fidelity results.

6.1.11.1. Results

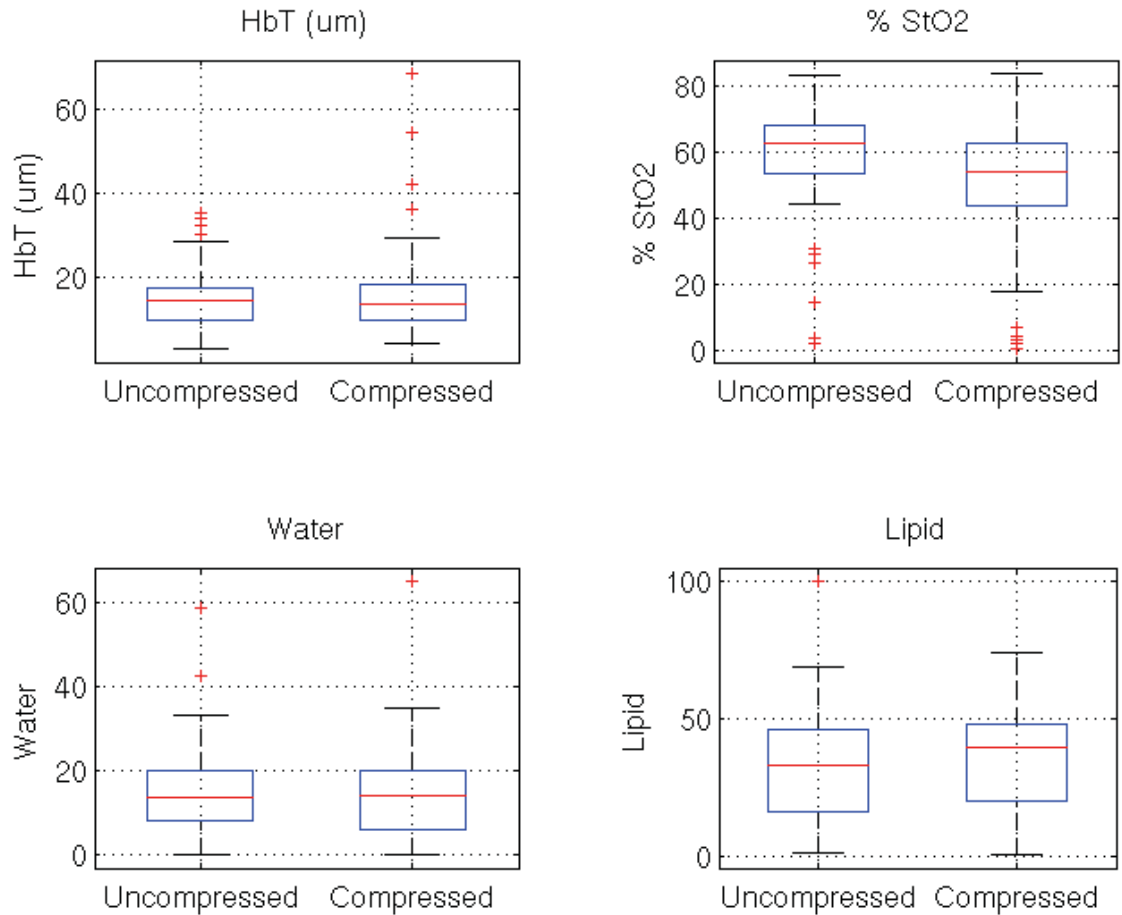
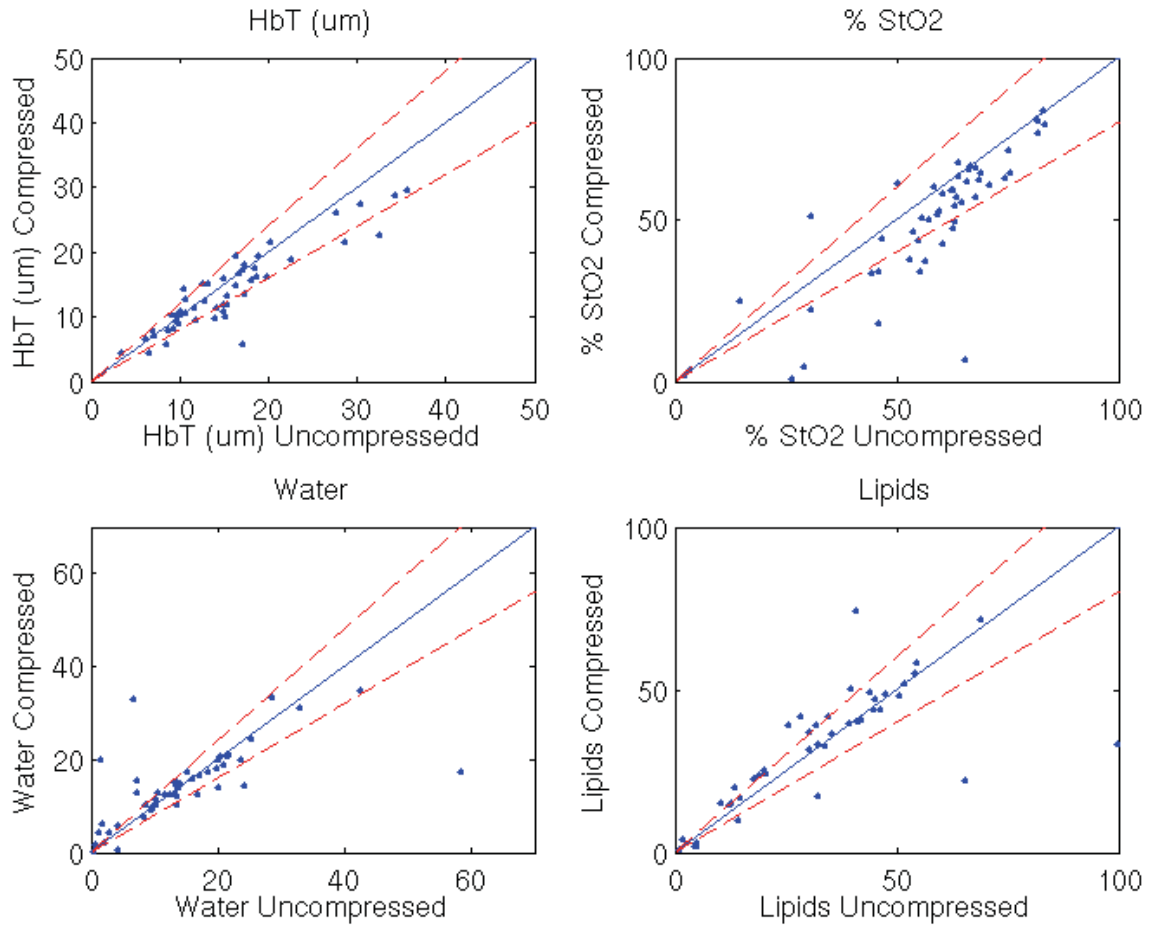


Figure 79: Comparison of uncompressed and compressed breasts across chromophores for normal subjects.

As shown in Figure 79, recovery of tissue chromophores is similar for compressed and uncompressed cases, with no significant differences except for oxygen saturation ( $p=0.0427$ ), with an average of 58% oxygen saturation for the uncompressed case and 50% for the compressed case.



*Figure 80: Scatter plots of compressed and uncompressed data across all chromophores.*

*Blue lines shown 1:1 correlation, and red dotted lines are offset from 1:1 by 20%.*

Scatter plots for individuals show very high statistical correlation between the uncompressed and compressed cases of the same view for a single person for all chromophores, with an average  $r$  of 0.79.

#### *6.1.11.2. Discussion*

Outside of oxygen saturation, there is no statistically significant difference either within the whole group or in individual patients for differences in chromophore content in compressed and uncompressed imaging scenarios. Reduction in oxygen saturation is expected during compression, assuming blood flow is restricted, as tissues use up remaining oxygen in the static blood for ongoing metabolic processes.

Given the limited variation between compressed and uncompressed cases, it may be possible to perform NIRST imaging at a lower compression level. However, as the DBT image stack is used for prior information, this can reduce the sensitivity of NIRST if tissue regions are mislabeled. This is of particular importance for small regions of interest, where slight movement can greatly alter the percentage of that lesion correctly characterized by an ROI in a segmented image stack. Additional studies in the biopsy cohort are required to confirm that DOSI imaging may be performed at a lower compression level than NIRST.

Overall variation in the scattering plots is much lower in the compression study than in the view study comparing CC and MLO. There are two possible reasons for this: patient positioning differences and segmentation differences. Slight changes in position are made between compression levels, only increasing the compression and making small adjustments to the shroud. Additionally, the same segmentation is used for both NIRST image sets so as to limit the dose to healthy volunteers by performing fewer DBT scans. The segmented images are necessarily different between CC and MLO with changes in the fibroglandular volume fraction sometimes noticeably different between the two. Examination of patient notes for the biopsy cohort may shed further light on this issue as

these women undergo DBT scans at two compression levels and in some cases were completely repositioned in between the two.

### ***Comparison of NIRST and DOSI Results***

DOSI imaging is performed primarily to ascertain scattering properties for the NIRST-DBT system; however, chromophore properties are also calculated for the DOSI measurements. The first 15 subjects were imaged with both DOSI and NIRST. Several of these subjects had unusable NIRST results, but for the remaining patients, it was possible to plot volume-weighted NIRST results vs. average DOSI results as shown in

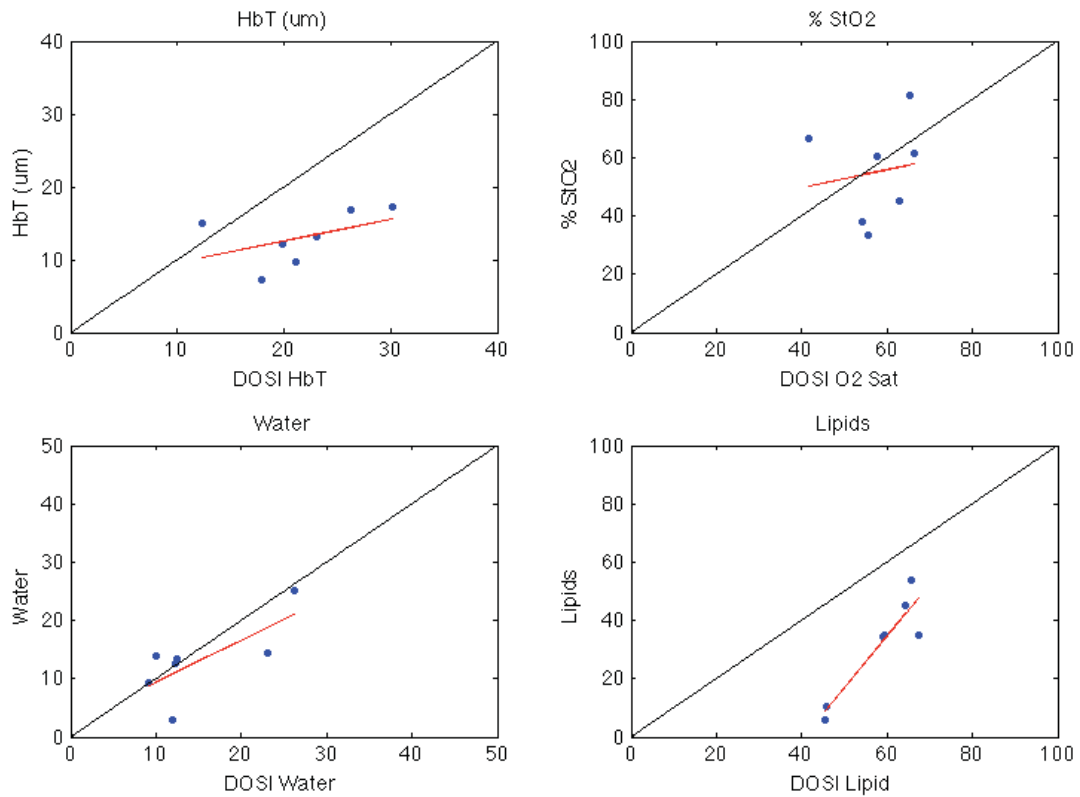


Figure 81.

### 6.1.12. Results

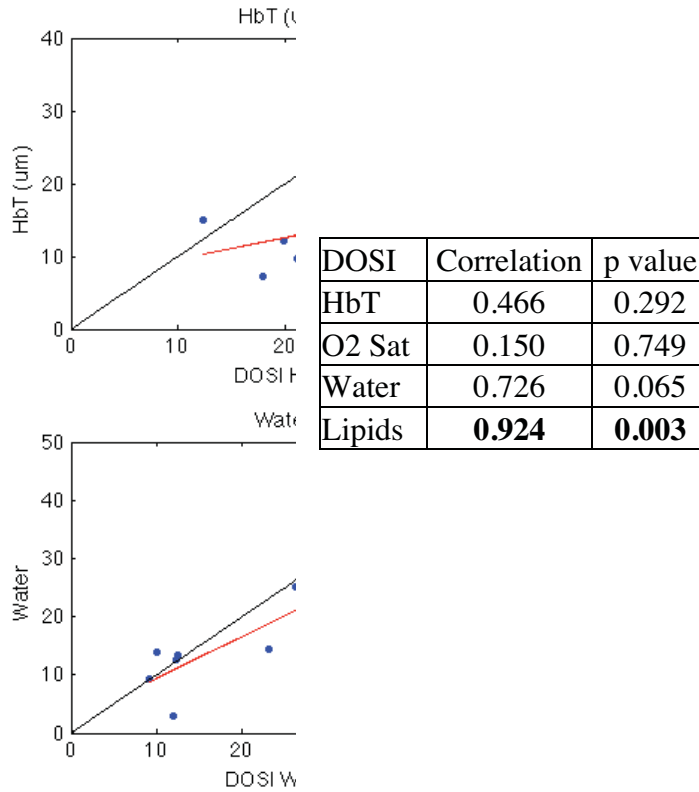


Figure 81: Comparison of NIRST and DOSI recovery of tissue chromophores. DOSI results are plotted on the x-axis with NIRST recovery on the y axis. Red lines show best fits of the data, while the black line depicts the 1:1 correlation between DOSI and NIRST results.

Table 10: Correlation between DOSI properties and NIRST for hemoglobin, oxygen saturation, water and lipids. Bold values indicate statistical significance ( $p < 0.05$ )

With the exception of lipids, DBT and DOSI results are not statistically similar for this small patient cohort. DBT recovery of HbT is generally below DOSI estimates by an average of 8 $\mu$ M or 50%. For oxygen saturation and water, values do not correlate, but the average value is similar between the two groups. Lipid fraction is the best matched chromophore with statistical correlation between NIRST and DOSI, but NIRST predicted lower lipid values in every case than those estimated by DOSI.

### **6.1.13. Discussion**

With only a handful of cases, there are no strong conclusions that can be drawn from the comparison of NIRST and DOSI recovery. Although it is surprising that HbT is lower in NIRST, there is a positive trend in that patients that recover low values in DOSI recover lower NIRST values. Oxygen saturation values are essentially incomparable due to differences in tissue geometry and a lack of compression during DOSI. Water values are similar on average. Higher estimates for DOSI lipid content are consistent with the more superficial tissue measured with the handheld reflectance geometry probe. However, if this is the cause, the opposite trend in HbT would be expected; a lower HbT would be found in DOSI measurements, which is not true here. Additional measurements are required before meaningful conclusions can be drawn about the differences in DOSI and NIRST but it is comforting to see that increases in chromophores across patients in DOSI (a broadband CW and FD hybrid system) are mirrored in NIRST (a limited, exclusively CW-based modality).

### ***Conclusions***

This chapter outlines the importance of healthy volunteers in validating a novel

NIRST-DBT combined imaging modality. The system was tested by a cohort of 32 volunteers with a wide range of breast sizes and shapes. The platform was carefully designed and detectable signals were obtained even at extreme thicknesses and densities. Only small tweaks to the hardware, software, and image reconstruction model were necessary. These iterative changes made fast and reliable imaging of women a reality.

Comparing the results obtained on the NIRST-DBT system with literature values and results from a well-researched existing optical system bolstered confidence in the new prototype. NIRST-DBT results showed expected trends relative to a wide array of patient characteristics, including BMI, breast density, and fibroglandular fraction and bra cup size. Examination of breast thickness under compression is not referenced in prior literature but shows strong correlation to oxygen saturation. HbT was correlated with BMI, breast density and fibroglandular fraction. Interestingly, oxygen saturation was not correlated with any of the patient demographics that were correlated for HbT, instead, bra cup size and breast thickness were significantly associated with oxygen saturation. Water was correlated with breast density, fibroglandular fraction and breast thickness. Lipids were correlated with the same patient features as noted for water but in the opposite direction, with an additional statistically significant correlation with BMI. Looking at aggregate values for all chromophores, mean HbT is 16  $\mu\text{m}$ , oxygen saturation is 54%, water is 11%, and lipids are 31%.

For a small subset of patients, comparison of NIRST and DOSI data recovered similar trends in chromophore values with significant correlation for water; however, absolute values were different in most cases. For this group, average values of HbT were higher for DOSI, with an average of 21  $\mu\text{M}$  (12-30  $\mu\text{M}$  range) for DOSI and 13  $\mu\text{M}$  for

NIRST (7-17  $\mu$ M range). For oxygen saturation, the average values were similar 57% (42-66%) for DOSI and 55% (33-8%) for NIRST. Results were also similar for water, 15% (9-26%) for DOSI and 13% (3-25%) for NIRST. Lastly, although lipid values were significantly correlated between DOSI and NIRST, DOSI lipid content was significantly higher 58% (45-67%) when compared to NIRST 31% (6-54%).

Assessments of the NIRST-DBT system reliability, segmentation methods, and effects of compression were possible by scanning each breast multiple times. Similar results were recovered when comparing adipose vs. fibroglandular and CC vs. MLO views with no statistically significant differences. Adipose and fibroglandular tissues may be more similar due to segmentation errors leading to partial volume averaging of these two areas. The only statistically significant result that came from the compressed vs. uncompressed breast scans is the lower oxygen saturation found in the compressed case ( $p=0.0427$ ) with 58% vs. 50% with higher saturation for the uncompressed case. Overall, individual patient correlations for the compression images are quite high, indicating that it may be possible to image women using NIRST at lower compression levels with DBT at typical mammographic compression.

It is important to note, however, that absolute quantification of absorption properties depends on scattering, here considered to be constant across patients. So any variation in scattering from this predetermined average for individual patients is manifested in differences in the absorption properties. Hence, what is recovered here is some combination of true absorption compounded by the scattering mis-estimation. Despite introduction of this unknowable scattering effect, trends in chromophore recovery follow expected results and prior literature values, providing some validation for

the exclusively CW system. Imaging of healthy volunteers is critical for the validation of new modalities and is the most realistic test that an imaging system can undergo before trying to scan abnormal tissue.

## **Chapter 7: NIRST-DBT Lesion Characterization Methods**

### ***Introduction***

Women with denser breasts have higher incidence of and mortality from breast cancer, and are the most difficult group to screen with mammography<sup>197-199</sup>. However, there is a high rate of false positive mammography results, leading to additional imaging and in some cases invasive biopsy procedures. Typically only about 1 in 5 biopsy results indicate breast cancer<sup>20,21</sup>. Improving the specificity of DBT, specifically the ability to non-invasively distinguish benign from malignant tissue, could spare many women from unnecessary biopsies.

The main purpose of building the NIRST-DBT system is to test the following hypothesis: NIRST-DBT can improve on the specificity of standalone DBT for diagnostic breast imaging. In order to test such a hypothesis, it is necessary to image women in the target group, those who have been recommended for biopsy screening due to the presence of a breast abnormality. This is not a particularly large cohort of women, as most women who participate in screening or diagnostic imaging possess normal or stable breast tissue. Hence, it was necessary to develop a recruiting strategy to target this population. Patient progression through the healthcare system prior to breast cancer diagnosis, as well as the anticipated niche for NIRST-DBT and time point for NIRST-DBT imaging is shown in Figure 82.

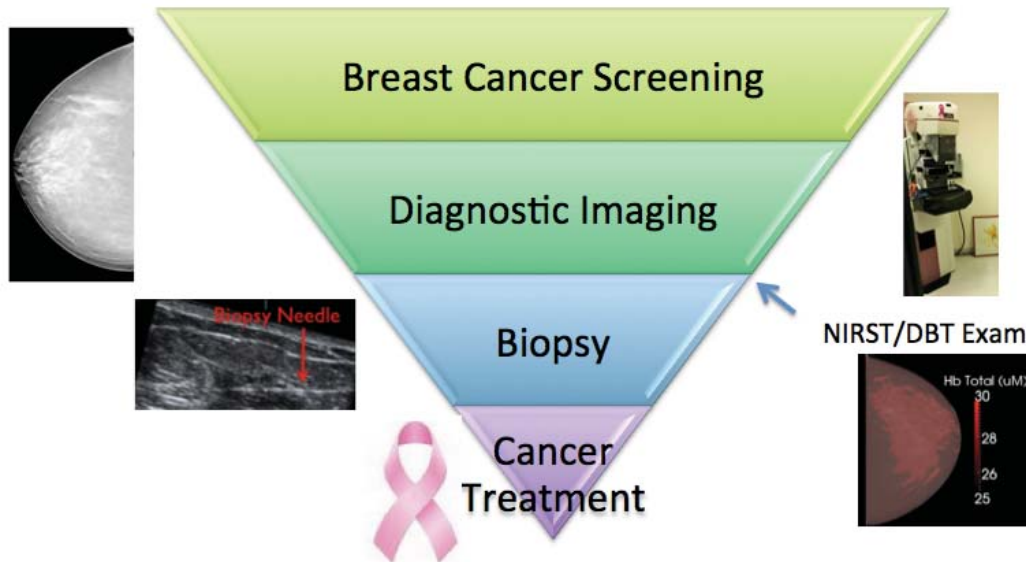


*Figure 82: Workflow chart for patients entering breast cancer screening showing the anticipated clinical niche for NIRST-DBT.*

This chapter describes patient recruitment strategies and shows anecdotal evidence of the ability of a combined NIRST-DBT imaging system to discriminate lesion types based on chromophore content. Imaging small ROIs can be more difficult than imaging normal subjects who generally have large swaths of adipose and fibroglandular tissue. Small areas have lower measurement sensitivity and are more prone to noise effects, increasing the importance of regularization in the non-linear reconstruction problem. In addition to presenting individual case studies and group statistics, this chapter describes several methods to improve the robustness in recovering chromophore content of small regions.

### ***Biopsy Patient Logistics***

Without a successful patient recruitment effort, it would be impossible to assess the ability of the NIRST-DBT system to improve sensitivity over standalone NIRST. Patient

recruitment necessitated careful coordination, planning, and organization of over a dozen people affiliated with DHMC and Thayer School. Thanks to these efforts, current recruitment stands at roughly one patient per week, with 13 patients imaged since active recruitment began on January 1<sup>st</sup> of 2014.

### **7.1.1. Patient Recruitment**

Patient recruitment is a team-based effort aimed at minimizing the effort required by potential participants, many of whom are anxious about the biopsy exam. From the patient's perspective, the recruitment process proceeds as shown in Figure 83. After the radiologist assesses the diagnostic images and makes the recommendation for biopsy, he informs the patient about the NIRST-DBT study. Women who are receptive to this idea are given the option to speak with an onsite nurse recruiter when scheduling their biopsy appointment. The nurse recruiter speaks to patients about the exam, even obtaining written consent of the patient and tentatively scheduling the exam if a subject is interested. If the patient has time constraints or wishes to think it over on her own first, she may provide permission to be contacted later on by the clinical research coordinator, who will call the patient to describe the study over the phone. Most women opt to schedule their NIRST-DBT imaging exam an hour prior to their biopsy appointment on the same day. The NIRST-DBT must be performed prior to biopsy, as the changes in the breast tissue after the invasive procedure would dominate the recovered chromophores. This process generally proceeds smoothly; no exams needed to be cut short so patients could make it to their biopsies, even in cases where the patient arrived late to the NIRST-DBT exam.

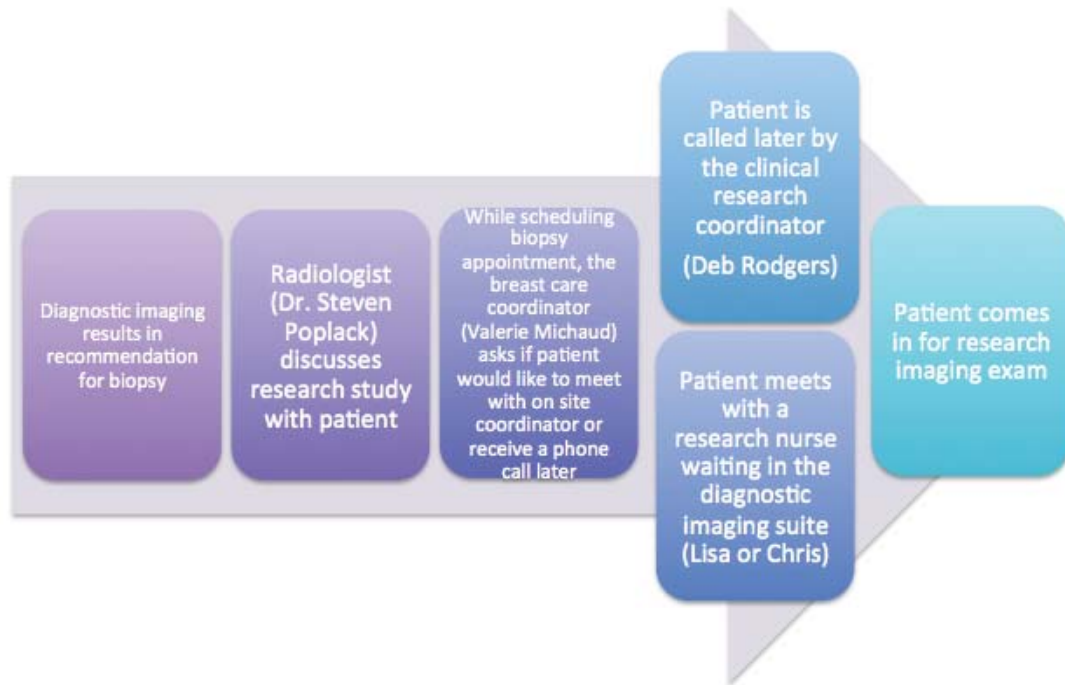


*Figure 83: Interactions with the research staff from the patient's perspective.*

There are many individuals working behind the scenes to ensure that the process goes smoothly for the patient. The primary people involved are described in Figure 84. In addition to these five individuals, three nurse recruiters discuss the study with patients and two additional researchers are typically involved in the NIRST exam - an assistant examiner and a hardware specialist waiting outside the exam room in case the equipment malfunctions. Additional details on patient exam procedures are included in the appendix. Without the dedication of all these individuals, successful patient recruitment for imaging biopsy subjects using NIRST-DBT would be impossible.

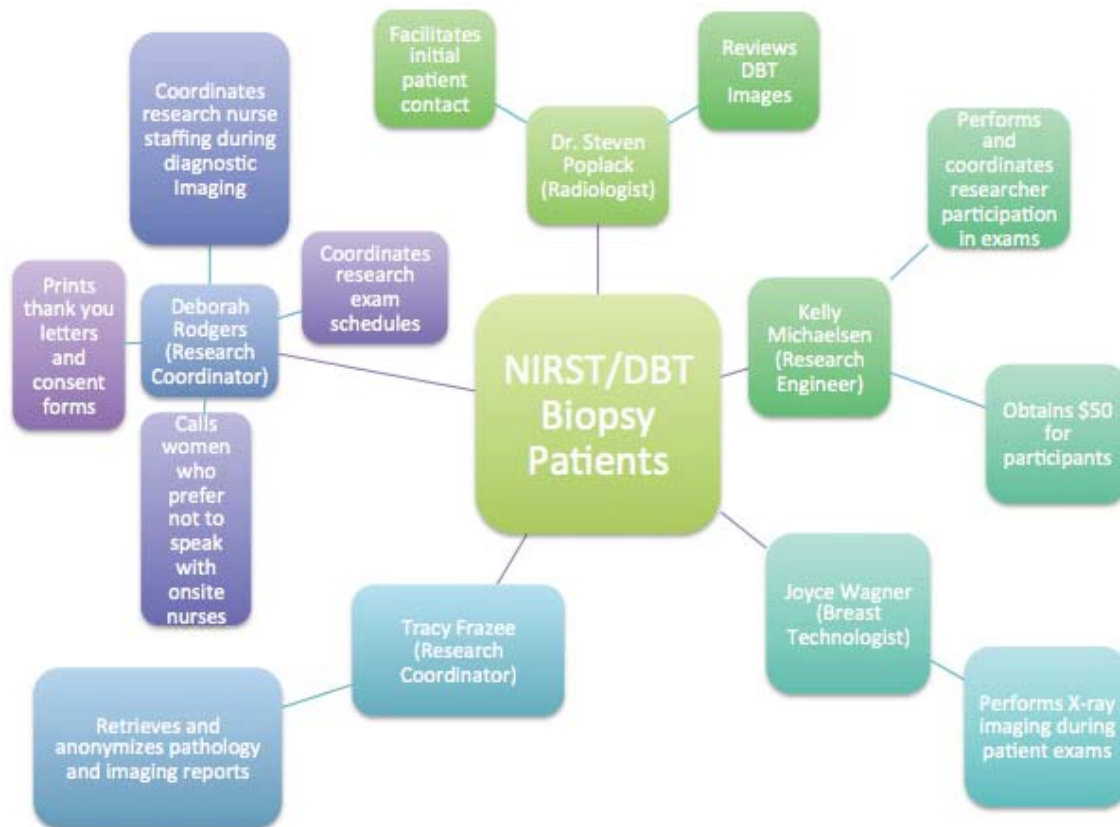


Figure 84: Workflow chart of steps required by the research team for imaging a biopsy patient with NIRST-DBT.

### 7.1.2. DBT Image Analysis

A radiologist (SPP) with extensive experience in DBT reads the images. As he is often involved in clinical care, image reads are unblinded. During DBT image reading for this research project, prior imaging studies and reports are accessed to aid in localization of the ROI. Additional information about the lesion is also recorded. This includes the plane of best visualization of the ROI as well as its extent in the z-plane, to help guide segmentation efforts. A screenshot is taken by the radiologist with the extent of the region of interest carefully highlighted in the x-y plane. This step is especially

important for calcification-based ROIs and guides the segmentation algorithm described in Chapter 3. Overall breast density is also assessed. Diagnostic, screening, and pathological reports are obtained for each patient as well. Each lesion is assigned a breast imaging-reporting and data system (BIRADS) category according to the following standard scale, which can be found in the diagnostic imaging report:

0 – incomplete, needs further evaluation

1 – normal dense breasts

2 – benign

3 – probably benign, recommend short-interval follow-up

4a – low suspicion for malignancy, biopsy should be considered

4b – intermediate suspicion for malignancy

4c – moderate concern but not classic for malignancy

5 – highly suggestive of malignancy, appropriate action should be taken<sup>200</sup>

All biopsy subjects in this study had at least one lesion rated 4 or higher; several had multiple lesions. Additional information about the breast is obtained from the segmented DBT slices, including segmented tumor volume, fibroglandular volume, and total breast volume.

### **7.1.3. Pathological Results**

The patient population to date includes three invasive cancers as well as one case of DCIS. The remaining lesions were benign, consisting of fibroadenomas, fibrocystic changes, adenosis, and cysts. One patient underwent bilateral biopsies for suspicious lesions in both breasts, while other patients had breast biopsies over a year prior and

known benign pathological outcomes, so the number of lesions probed via NIRST-DBT exceeds the number of patients included in the study.

Patient #	BIRAD	Diagnosis
201		5 left breast lesion 1 - invasive ductal carcinoma.
202	4C	left breast: ductal carcinoma in sita, extending into lobular ducts wth microcalcs identified in DCIS.
203	4A	left breast, lesion 1: stromal hyperplasia with focal features of duct cysts and adenosis. The microcalcifications are associated with adenosis. right breast lesion 1: fibropitheal lesion, suspicious. right breast lesion 2: benign.
204		4 duct microcysts and adenosis.
205		3 right breast lesion 1: cyst; right breast lesion 2: fibroadenoma, usual ductal hyperplasia and columnar.
206		4 left breast - benign breast tissue with focal fibrocystic changes and fat necrosis
207		4 sclerosing intraductal papilloma with usual ductal hyperplasia (right breast mass)
208	4A	no evidence of cancer on right breast. Left breast has calcifications. Left breast diagnosed with fibroadenomatous change.
209		4 right breast has clustered aprocrine cysts.
210		4 left breast has fibrocystic disease with cysts and adenosis
211		4 right breast is benign tissue with focal fibrocystic changes - stromal fibrosis, mild usual ductal hyperplasia
212	0 (incomplete)	left breast has invasive ductal carcinoma
213		5 left breast has invasive ductal carcinoma

*Table 11: BIRADS and pathology results from subjects in the biopsy cohort imaged to date.*

### 7.1.4. Patient Characteristics

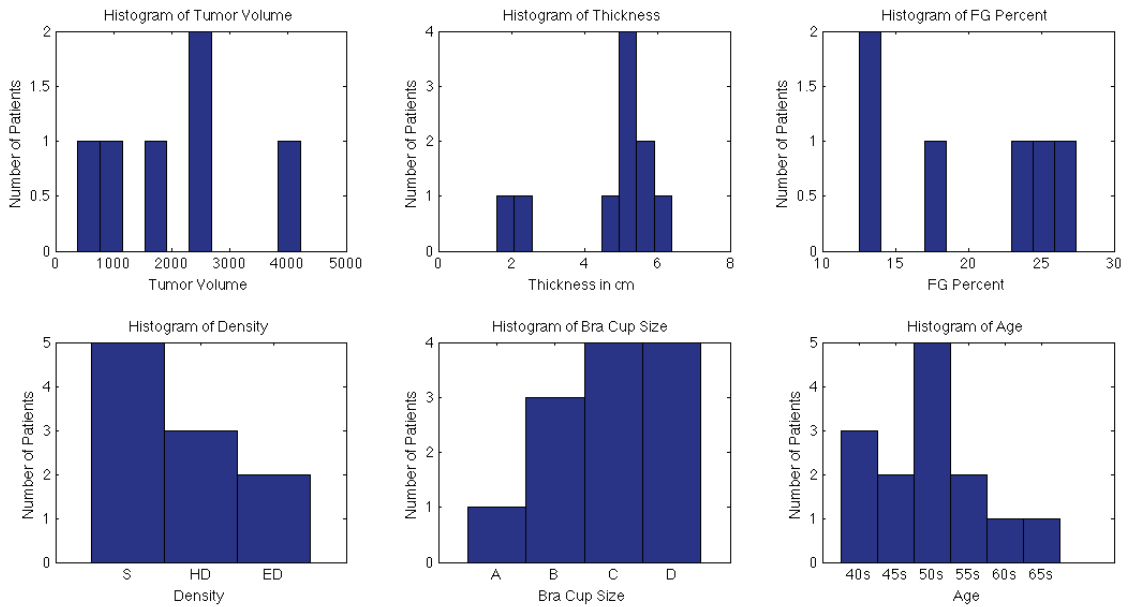


*Figure 85: Histograms of summary statistics for the biopsy cohort including tumor volume (in  $\text{mm}^3$ ), thickness (in cm), percent fibroglandular tissue, density category, bra cup size, and age.*

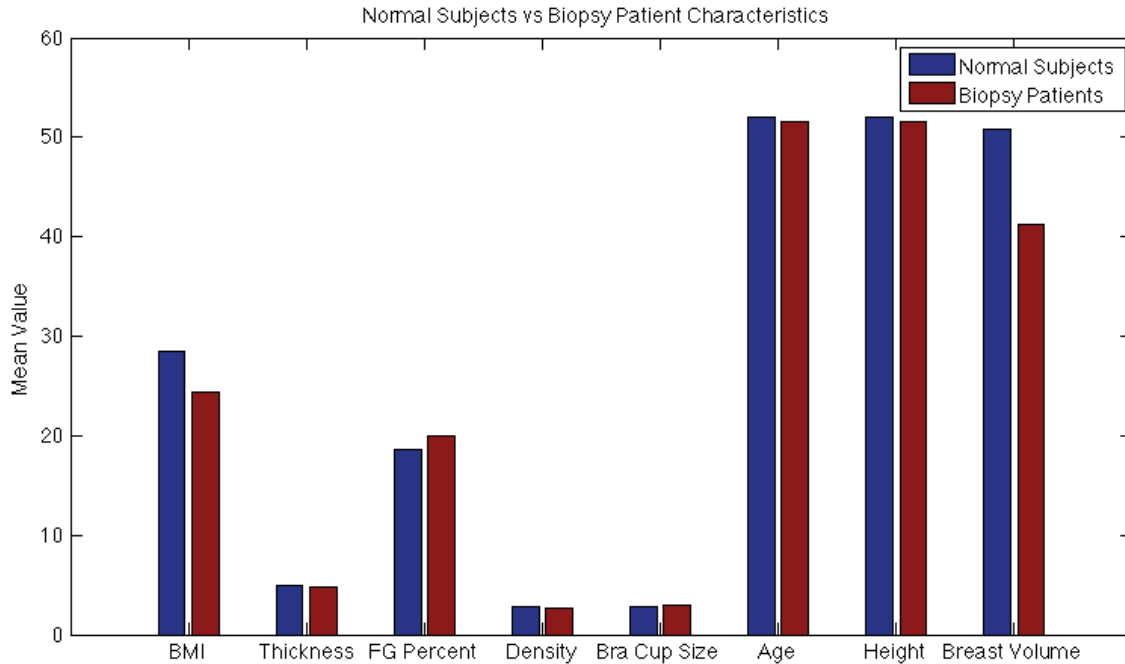


*Figure 86: Comparison of average patient characteristics for normal subject and biopsy subject cohort. The breast thickness is in cm, density and bra cup size have been converted to an ordinal scale, height is in inches and breast volume is in  $\text{cm}^3/10$ .*

Overall, the patient group had characteristics remarkably similar to the normal subjects described in the previous chapter, as shown in Figure 86. The property with the largest difference between the two groups was breast volume, which is calculated based on the DBT image stacks. Lower breast volumes generally correlate with a lower number of data points, as fewer detectors and sources are covered by the low-volume breast, which can be problematic. In one case, the breast was so small that all the light detectors were within 1.5 cm of a breast edge, the limit at which data is removed, so this patient could not be reconstructed using the existing scheme.

Concerted efforts are made prior to the exam to identify and localize breast ROIs in past imaging to ensure that regions are included in the NIRST-DBT exam.

Calcifications or masses are guided to the central aspect of the imaging plane by an expert breast technologist during NIRST-DBT exams in order to mitigate any potential edge effects. The patient must remain in place for much longer than a typical DBT scan, and when also imaging the uncompressed breast, there is more time and less force on the breast, so the patient may move a bit from her original position. In one case with a posteriorly located breast lesion, the ROI was not in the imaging field as it had been on the clinical DBT images. The positioning combined with patient movement afterwards made it impossible to reconstruct the NIRST-DBT images for one view due to a lack of visualization of the ROI. Steps to mitigate this issue have been taken; during detector panel and shroud removal and replacement, the breast technologist stands behind the patient, applying gentle pressure on the back to keep the patient in place.

### ***Increasing Sensitivity of Small Lesions***

Annual breast cancer screening improves breast cancer survival rate by detecting cancerous lesions at an earlier stage, typically before the lesion is palpable or the patient experiences any symptoms. By virtue of detection at this early stage, the lesions are typically quite small, averaging around 13-14 mm<sup>22,201</sup>. The biopsy cohort of this study displays a similarly small size of invasive cancers, just below 12mm in diameter on average.

Using NIRST to detect such small lesions is challenging in several ways. NIRST is effective at detecting changes in tissue chromophore levels. Larger tumors are associated with greater VEGF and microvessel density, hallmarks of angiogenesis<sup>202</sup>. Thus larger tumors often have higher contrast in total hemoglobin content, which is detectable via

NIRST. Inversely, smaller tumors will have lower contrast levels. In addition to more subtle shifts in the tissue metabolism, smaller tumors have lower NIRST sensitivity, which is determined by both the volume of the region of interest and locations of the light sources and detectors relative to that volume. Low NIRST sensitivity refers to the low probability of light from a source travelling to a particular location and then returning to a detector and has been demonstrated to have lower efficacy in distinguishing benign and malignant lesions<sup>203,204</sup>. In order to detect small inclusions with low sensitivity, data cannot be over-dampened through the use of a large regularization parameter or contrast will be lost, as demonstrated in Figure 87 for a phantom study for a large (15 mm diameter), medium (10 mm diameter) and small (7 mm diameter) cylindrical inclusion. Higher regularization values show no contrast in the inclusions, while the lesions were notable at successively smaller regularization values in size order such that the largest inclusion was apparent at higher regularization than the lowest.

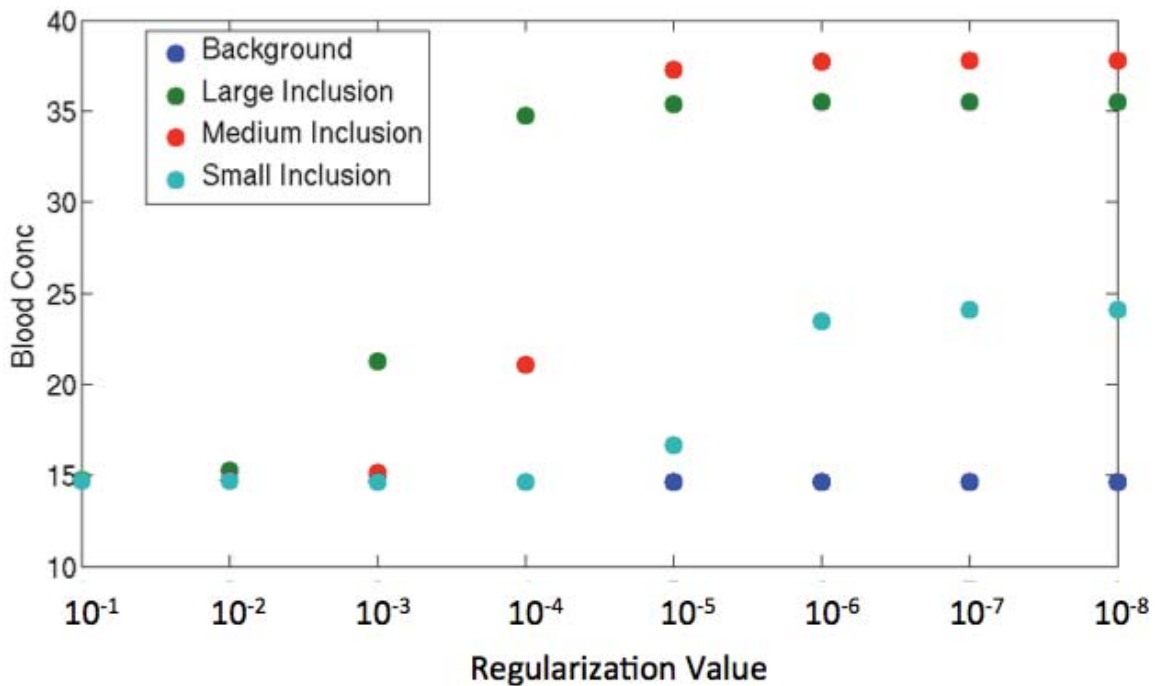


*Figure 87: Graph showing the dependence of inclusion size chromophore recovery on regularization. Smaller lesions require lower regularization values; in this case  $10^{-6}$  is necessary to fully recover the smallest inclusion while  $10^{-4}$  could recover HbT in the largest inclusion.*

Since this was a phantom study, noise within the data was extremely limited. Decreasing the noise in the reconstruction data was possible through the use of the same phantom for calibration and anomalous data, but with background-like hemoglobin levels in the inclusion to simulate a homogeneous medium in the calibration case. Clearly, such matching would be impossible when imaging humans. Additionally, patient data has inherently greater background or systematic error due to use of the breast shroud as well as innate tissue heterogeneity. In human subjects, a much larger regularization parameter is needed, even when using the highest regularization shown in Figure 87, where contrast was not observed in any of the inclusion phantom results. Non-physiological NIRST reconstruction values can be obtained, especially in breasts with particularly limited or noisy data sets, as shown in Figure 88.

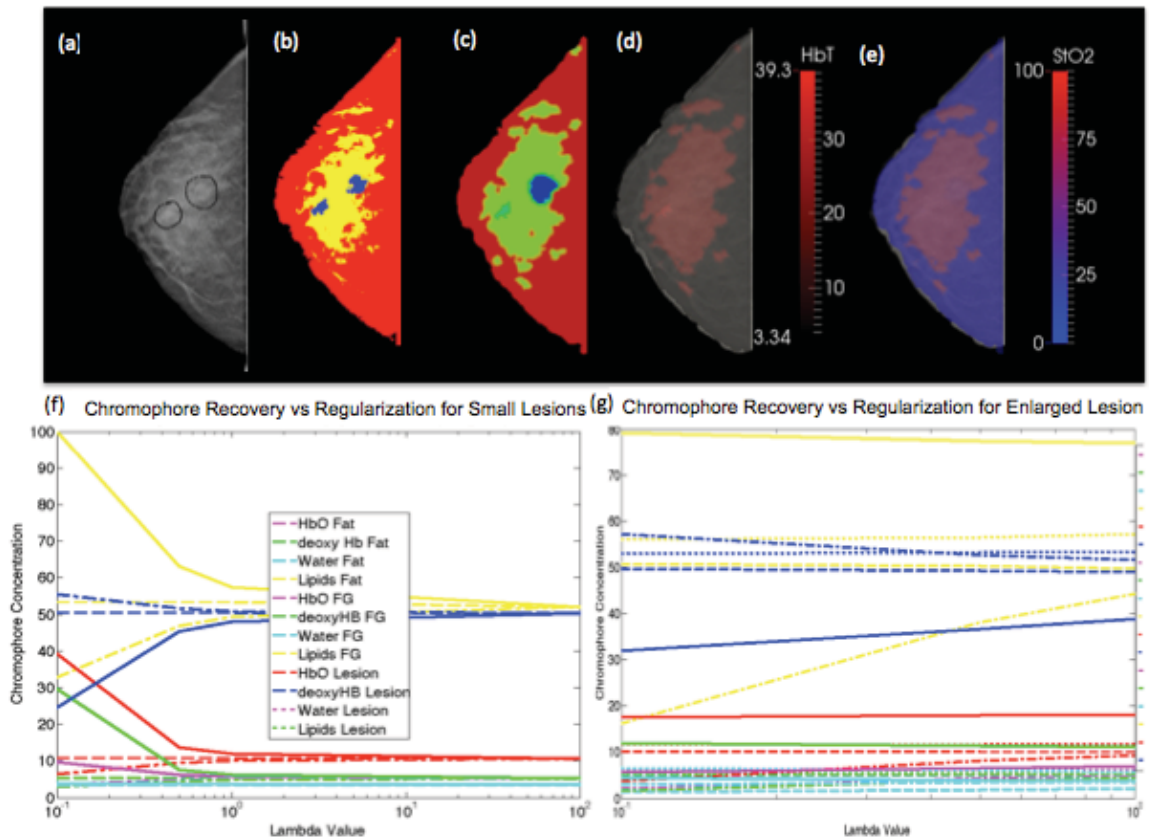


Figure 88: (a) Original processed DBT slice screenshot with circles drawn by the radiologist to indicate ROIs. (b) The segmented regions and (c) the resultant mesh with the right hand lesion enlarged to improve NIRST sensitivity while the left lesion was not enlarged. The resulting reconstruction for HbT (d) and oxygen saturation (e). The graphs depict the change in chromophore content vs. regularization for true-to-size lesions (f) and expanded lesions (g) for a different patient. Colors indicate different chromophores while line types represent different tissues regions. The solid lines represent the small lesion (f) and expanded lesion (g).

As seen in Figure 88(d) and (f), small lesions have a tendency to increase chromophore recovery to non-physiological levels as regularization is decreased for the reasons hypothesized above. One way to address this challenge is to enlarge the ROIs

above a certain sensitivity threshold, in this case, 2%. This percentage value refers to the sensitivity of the tumor region as a percent of the total sensitivity of the NIRST field and is described in detail in the literature<sup>203</sup>.

In short, using the complete CW Jacobian matrix,  $J$ , the sensitivity of the measurements to a given region identified by DBT,  $S_r$ , can be calculated using the equation  $S_r = \text{sum}[\log(J \cdot r)]$ , where  $r$  identifies nodes within the region of interest as a logical vector. Total sensitivity of the measurements to the domain,  $S_t$ , is calculated when  $r$  is entirely true. Sensitivity for a single region is calculated using an  $r$  vector that is true at points within the region of interest and null outside this. Regions are obtained from DBT images during segmentation and are used in creating the mesh from which the sensitivity measurement is derived. The relative sensitivity of the region to the total sensitivity is the ratio  $S_r/S_t$ .

After determination of the initial sensitivity of a region, if the sensitivity is below 2%, the region must be expanded. This occurs in incremental steps, expanding the tumor out from its original position one millimeter at a time, relabeling nodes of the mesh and increasing sensitivity until the threshold sensitivity is surpassed.

NIRST reconstructions with the enlarged lesions appear more stable, as shown in Figure 88 (f, g). At lower regularizations, small lesions can behave unpredictably, with chromophore levels exceeding physiological limits as noise dominates these regions during the reconstruction. However, the enlarged lesions maintain stability at the lowest tested regularization (0.1).

Of course, there are downsides to such an approach, most notably that more than just the tumor region is being sampled and there will be partial volume averaging that can

diminish contrast levels in the tumor. The evidence that this is be uniformly true is shown in Figure 89.

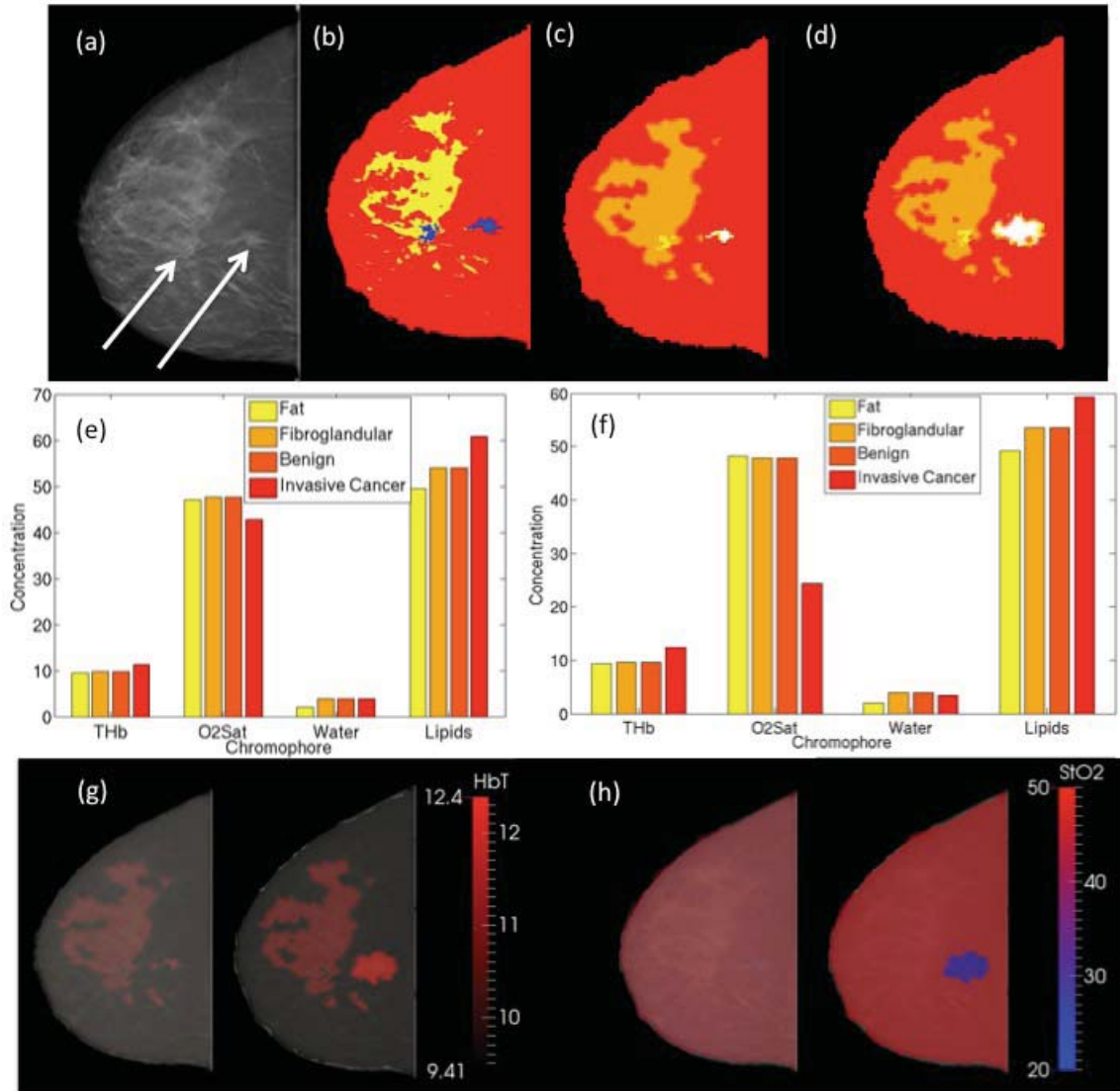


Figure 89: (a) DBT image slice with arrows pointing to a benign (left) and malignant lesion (right), as well as the DBT image segmentation (b) and visualization of the mesh before (c) and after (d) enlargement of the malignant lesion. (e) and (f) are the results of NIRST reconstruction for the smaller and larger lesion respectively. These results are displayed as DBT image overlays for total hemoglobin (g) and oxygen saturation (h).

For this patient, an invasive cancer is embedded in a largely fatty region, which generally has lower hemoglobin content than malignant or fibroglandular tissue. Upon expansion of the lesion size in the test mesh, some of this adipose tissue is invariably included in the reconstruction. It might be expected that such a maneuver decreases HbT. However, the opposite occurs; HbT is 12.4  $\mu\text{M}$  in the larger lesion, while it is 11  $\mu\text{M}$  in the smaller case, increasing the contrast with the fibroglandular region (9.5  $\mu\text{M}$ ) by 50%. There are several potential reasons for this improvement. As discussed above, improving lesion sensitivity can stabilize chromophore recovery and dampen noise effects. Additionally, studies using Doppler ultrasound have demonstrated that there is often much higher blood flow in regions adjacent to malignant tumors<sup>164</sup>. Also, it may be possible that DBT underestimates lesion size, as some studies examining final pathology specimens and screening images have shown, but generally these errors are on the order of a couple of mm<sup>161-163</sup>. It is unlikely that there is a sharp boundary between tumor blood supply and that of the surrounding tissue; as blood flow is a diffusive process in the smallest of vessels, there may be a high concentration of blood in the tumor central core, which levels off to that of the surrounding tissue some distance away.

### ***Lesion Characterization Using NIRST-DBT***

Thirteen biopsy patients have been imaged to date, although only the results of the first eight were available at the time of this writing. Two were excluded: one due to small breast volume and a second because the region of interest was not in the field of view of the DBT image. In total, nine lesions in the six remaining breasts have been analyzed.

### **7.1.5. Experimental Design**

As described above, small tumors were expanded about their tumor boundaries to improve sensitivity. All of the results presented in this section used the same regularization parameter, 0.5, which was chosen through testing after running a series of regularization values for all patients. This level provided sufficient contrast between regions without recovering non-physiologically acceptable chromophore values. Only compressed CC views have been analyzed to date. Future work will involve examining MLO, uncompressed, and contralateral breast images.

### **7.1.6. Case Examples**

The following cases shown in Figure 90 and Figure 91 depict a very small malignancy (DCIS) and a complex benign case including both a fluid-filled cyst and fibroadenoma. In the case of the DCIS, the original tumor volume was only  $.39 \text{ cm}^3$ , so tumor expansion increased the volume considerably. Despite increasing the size of the region of interest, a subtle elevation in HbT was present (10% over fibroglandular region value) along with lower oxygen saturation and higher water. As expected, fibroglandular tissue had more hemoglobin and water than the adipose, but surprisingly also higher lipids.

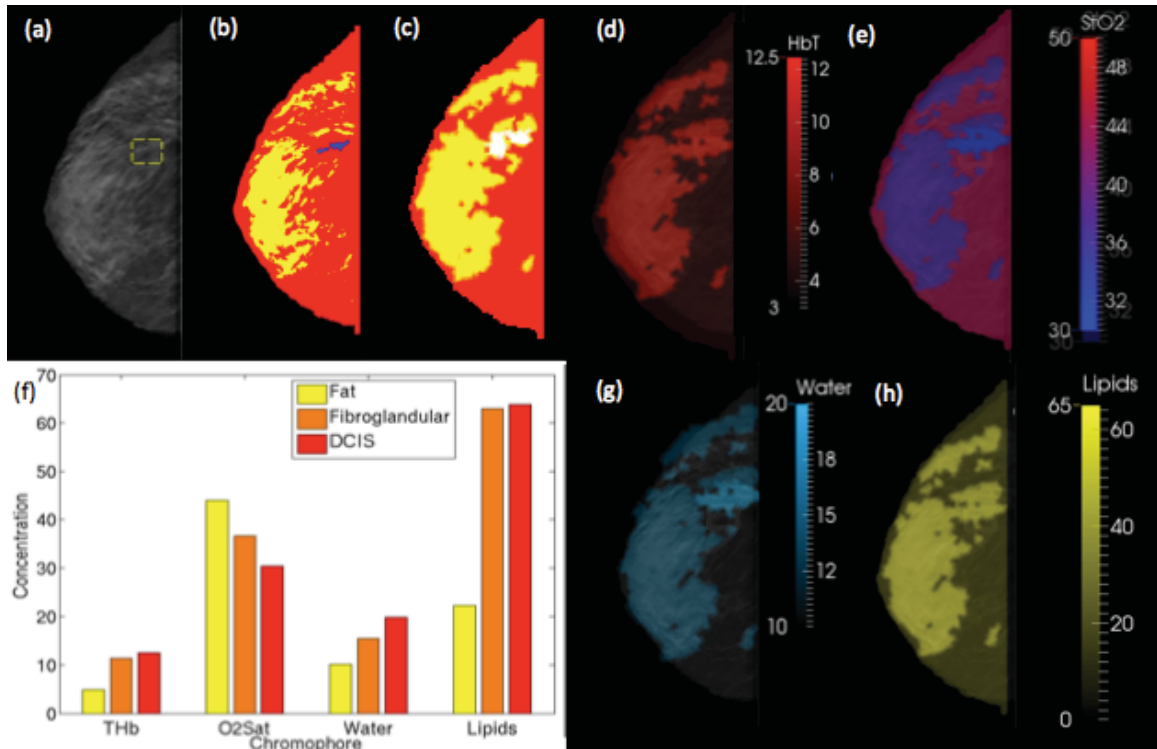


Figure 90: (a) Processed DBT slice with a cluster of tiny microcalcifications outlined with a yellow box. (b) The segmented image slice. (c) The mesh with the enlarged lesion. Overlays of total hemoglobin, oxygen saturation, water, and lipids are shown in (d, e, g, h) with a graphical summary in (f).

Figure 91 depicts a complex benign case including a fibroadenoma on the edge of the breast as well as a large fluid-filled cyst. Sensitivity of edge measurements is quite poor and modeling of tissue boundaries is inaccurate due to an inability to segment the natural breast curvature from DBT images. This would be an excellent case for expanding the lesion; however, doing so leads to merging of the two ROIs, with some of the cyst nodes relabeled. Expanding the tumor in this case would lead to partial volume averaging with the cyst, which is expected to have much different properties than any other type of tissue. The optical properties of the cystic region did in fact turn out to be

quite different from the others, with essentially no hemoglobin compared to the other breast tissues ( $8 \mu\text{M}$  vs.  $55 \mu\text{M}$ ). Surprisingly, the cyst did not recover much water, but did recover quite a lot of fat, perhaps due to cross talk between these two chromophores. The fibroadenoma, as expected, had properties similar to the fibroglandular tissue despite the low sensitivity and edge location of the lesion. One additional fact to note in this case is the incredibly low oxygen saturation in all but the adipose regions. This breast was very highly compressed, measuring only 2.6 cm thick, which likely contributed to these low values.

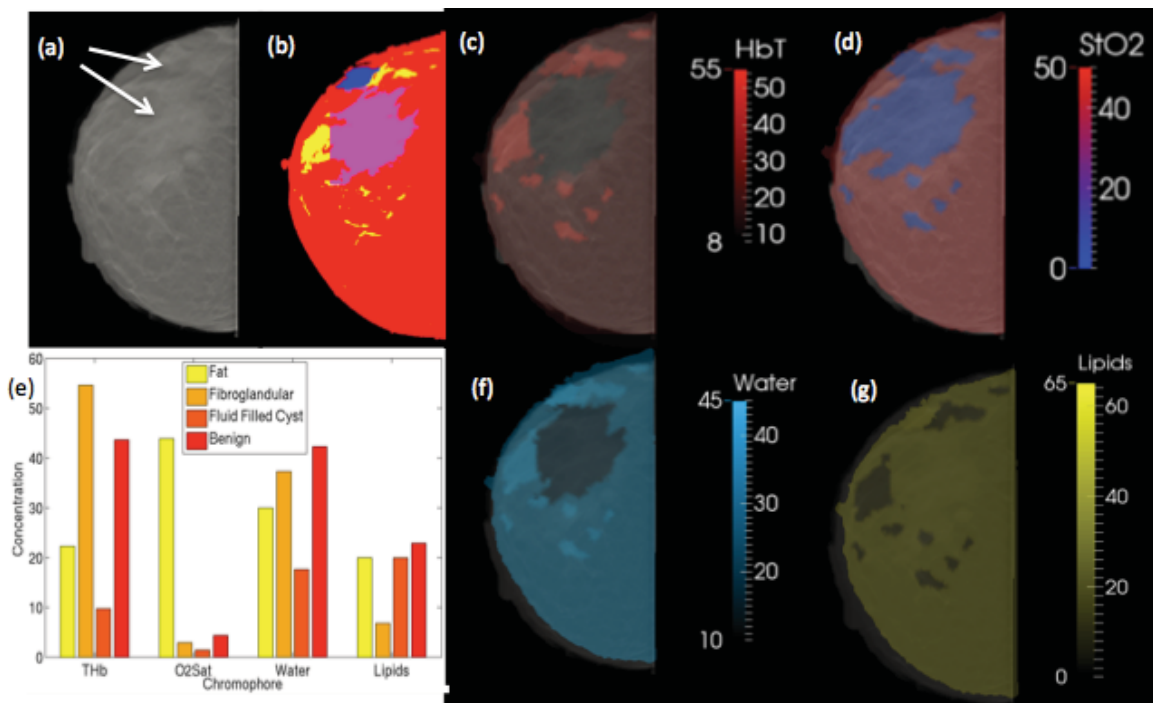


Figure 91: (a) Processed DBT image slice containing a fibroadenoma (top arrow) and large fluid-filled cyst (bottom arrow). (b) Segmented DBT image. DBT with NIRST overlays for tissue HbT, oxygen saturation, water, and lipids (c, d, f, g) as well as a graphical display of the same data (e).

### 7.1.7. Patient Summary

The results from all lesions and all patients have been aggregated to show total hemoglobin contrast in benign and malignant lesions, as shown in Figure 92. The results show the HbT in the region of interest divided by that of the fibroglandular, minus one, so that a 1:1 ratio means no contrast and appears as zero on the y axis. The two malignant lesions demonstrate positive contrast, with a 20% in HbT over the background. All benign lesions have lower HbT, 22% lower when all benign lesions are included but only 2.5% lower when only non-cystic lesions that are not directly on the tissue boundaries are considered. These results are not statistically significant due to the small patient population ( $p= 0.0967$  for all cases and  $p= 0.0548$  when edge cases are excluded).

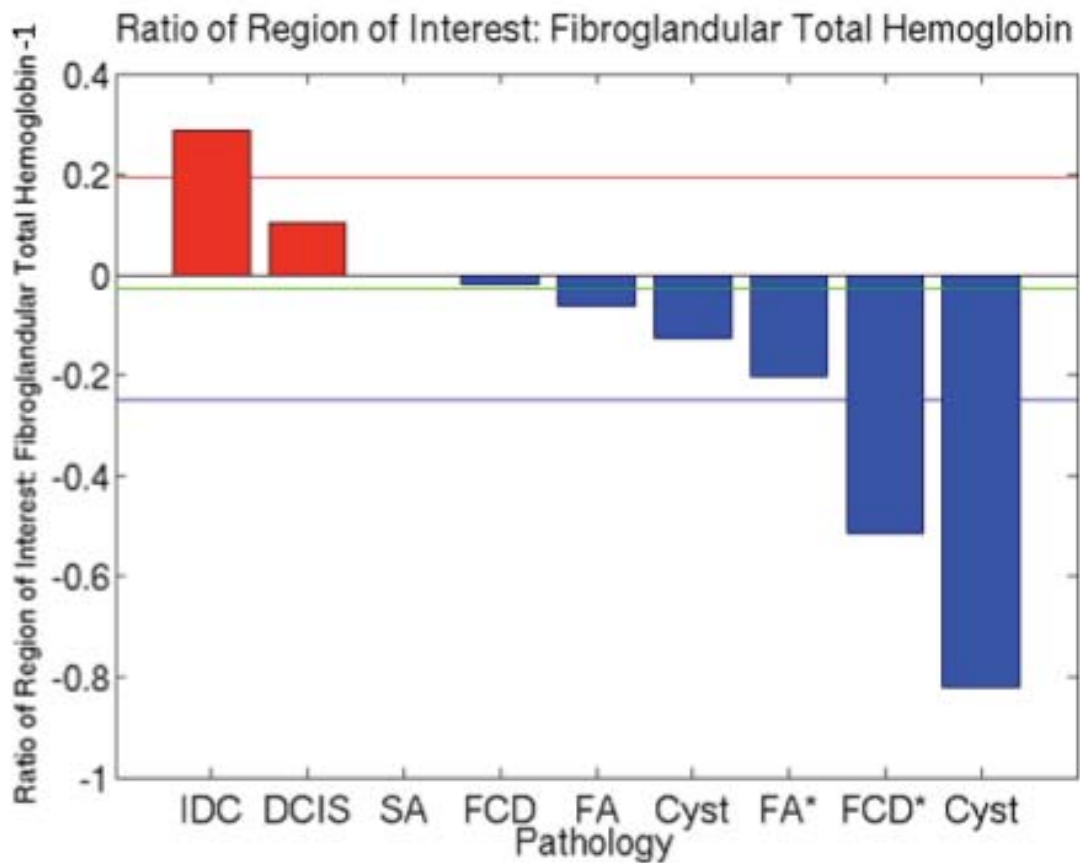


Figure 92: Summary slide showing the tumor to fibroglandular total hemoglobin ration minus one for all the benign and malignant lesions present in the first six patients of the biopsy cohort. Lesions shown here are invasive ductal carcinoma (IDC), ductal carcinoma in-situ (DCIS), sclerosing adenosis (SA), fibrocystic disease (FCD), fibroadenoma (FA), and cysts. The malignancies are depicted in red while benign lesions are blue. Lesions directly adjacent to the tissue boundaries are indicated by an asterisk on the x-axis. Mean contrast for malignancies is shown in the red line, while the mean contrast for benign lesions is shown in blue. When cysts and edge lesions are excluded from the benign lesion group, the mean contrast is shown in green.

## *Discussion*

The initial results from the biopsy cohort are promising but require extensive further validation with a larger group of women. There are some challenges that have been addressed already. The small size of the lesions has been mitigated through expansion, which has shown to be a robust technique in two cases, but a more systematic study is needed. Additionally, there are some cases where such expansion is not possible, as noted above when a breast contained two lesions in close proximity, one of which was a cyst.

Another notable challenge is lesions along the edge of the breast. Due to partial volume averaging of the DBT images, it is impossible to accurately determine the breast boundaries in x and y, so DBT-based breast models look like half cylinders with sharp edges. This results in poor reconstructions near these edges, with artificially low chromophore values as shown in the two cases in Figure 92. This edge model is not a good representation of tissue, as the breast maintains a level of curvature at the edges. Efforts to understand and more accurately model the tissue would be helpful for these cases, but for now, a workaround has been created. After explaining the undesirability of localizing lesions to tissue boundaries to the breast technologist, she has made a concerted effort to keep regions of interest near the center of the breast volume. This has been very successful so far, but this workaround is not possible for very small breasts like the benign case shown above, as these women do not have a lot of tissue available for manipulation.

Lastly, the level of contrast in the malignant lesions is not very high, only 20%. These values are a bit lower than previous studies demonstrating 2:1 contrast between

malignancy and background; however, many of the lesions included in these studies were much larger than the two presented here<sup>49-51</sup>. These difference in benign vs. malignant cases are not statistically significant due to the small patient population ( $p= 0.0967$  for all cases and  $p= 0.0548$  when edge cases are excluded). Extensive optimization and calibration may improve the signal-to-noise ratio of this system beyond the current capabilities.

One interesting consequence of expanding lesions is that less spatial prior information is used than in the small lesion case. This may lend credence to the ability of the NIRST-DBT system to image women at two separate compression levels, one for NIRST and a higher setting for DBT as the region of interest will shift a bit, but if the region of interest is going to be extended anyway, it may inconsequential. This can be examined further when the uncompressed data is reconstructed.

Lastly, although all patients here are compared using the same regularization, this may not be the best approach. The amount of noise in the data varies significantly, as does the number of data points collected per patient, which can change over an order of magnitude. Each case is unique and while applying a uniform approach is the easiest way to compare patients, a more nuanced experimentally-derived model that permits differences in reconstruction for each patient case may improve results.

### ***Conclusions***

In this section, approaches for DBT-guided near infrared spectroscopy of human subjects with regions of interest are discussed and early biopsy cohort results are presented. Thirteen women have been imaged to date with the NIRST-DBT system, only

two of which were unusable in our present reconstruction algorithm (one case may be salvageable with sufficient changes), with six presented here. Imaging a screening population is particularly challenging due to the small sizes of lesions. Incremental enlargement of tumor regions improved contrast recovery in case studies and improved chromophore stability over a range of regularization parameters.

Results from the preceding cases study will influence how future NIRST-DBT data are analyzed, particularly with regard to the role of sensitivity and tumor size. More subjects must be imaged and analyzed before the hypothesis presented through case studies here can be confirmed. Overall, these earliest results are promising, with a 20% non-significant difference in contrast between malignant and benign cases.

## **Chapter 8: The Role of Scattering in NIRST of the Breast**

### *The Importance of Scattering Information*

Developing an imaging modality for diagnostic imaging presents unique challenges. In order to be clinically successful, it must be simple to operate and interpret, have low cost per exam, and pose minimal risks to the individual. In an effort to keep cost and complexity low, we have pursued a NIRST system which projects light onto the breast surface at discrete locations with a motor-driven mirror and measures the resulting light signals with a fixed rectangular array of silicon photodiodes integrated into a detection panel placed on the opposite side of the breast. The design relies exclusively on continuous wave (CW) measurements for rapid, low-cost quantification of tissue absorption. Measuring optical scattering in tissue is more difficult and requires additional time- or frequency-domain (FD) elements that add to system cost, complexity, and examination time. Minimizing exam time is important both to limit the time the breast is subjected to compression and to maintain efficiency of workflow in the mammography clinic. Estimation of optical scattering properties is necessary in breast imaging because scattering events occur with about 100 times greater frequency than absorptive events, and there can be a lot of inter-patient variation in these values, which depends on breast composition and parenchymal density. Incorrect estimation of scattering alters estimates of optical absorption, especially hemoglobin concentration; hence, accurate scattering values are needed to characterize and quantify optical absorption properties of the breast.

Since the NIRST system measures exclusively CW data, scattering properties were necessarily estimated. In order to understand the impact of this decision, efforts were made to quantify scattering and to measure the effects of scattering mischaracterization as well as derivation of optical scattering properties from X-ray images to ensure the integrity of the absorption property results. This was done through simulation, phantom measurements and normal subject scattering derived from both an alternative optical modality and estimated from DBT slices.

### ***Simulation Results***

Early simulation studies examine the effects of using a single bulk tissue estimation of scattering values, which is possible by adding only six frequency domain channels to the existing system, as opposed to a two or three region estimation that would require a larger number of sources and detectors. Examination of the effects of using a single bulk tissue estimate of scattering were compared with using separate values for adipose tissue, fibroglandular, and tumor regions for eight subjects was performed. The bulk value produced greater error in absolute hemoglobin recovery when compared to two-region estimations of scattering for all three tissue types. The effect was most pronounced in the tumor, in which case using two regions instead of a single bulk estimate led to a 30.6% improvement in the accuracy of HbT concentration. Interestingly, a recent study of a combined NIRST/MRI system using bulk tissue estimates for a 60 patient cohort showed improved lesion detection when compared to the three-region estimate for a system comprised of 16 FD channels, presumably due to noisier data in low-sensitivity regions<sup>204</sup>. Hence, accurate three-region estimates of scattering would be the ideal case

but require a higher number of frequency domain channels. Inaccurate calculation of scattering in a small, less sensitive area is worse than using a bulk estimate of the entire tissue.

The effect of scattering mischaracterization on calculated hemoglobin values was examined in simulation as well. In this case, scattering values were assigned for the CW reconstruction rather than using FD data to estimate the scattering values. Two scattering estimates were assigned in each patient case: one for adipose and one for fibroglandular and malignant tissue. Fixed percentages of error were introduced into these scattering values. *Figure 93* depicts how errors in scattering propagate into inaccuracies in the reconstructed images of HbT concentration. Data for all tissue types for all patients are included in the plot and indicate certain trends. For example, underestimating scatter by 20% leads to an increase in the reconstructed HbT by 35.1%, while overestimating scatter by 20% leads to a reduction in the reconstructed HbT by 22.6%

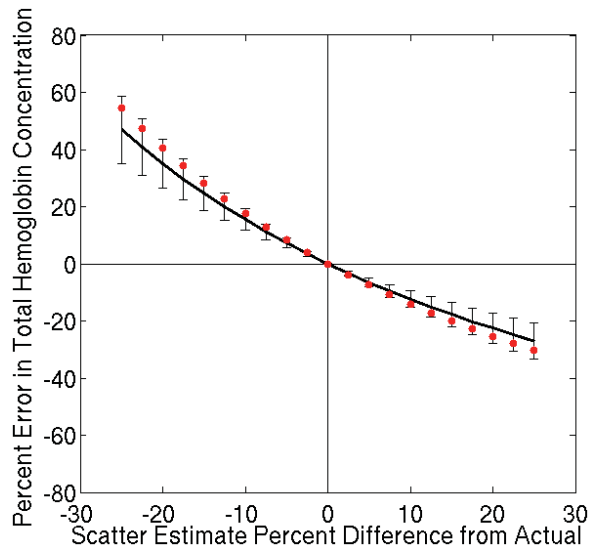


*Figure 93: Solid line shows the mean and the error bars show standard deviation of the average HbT, recovered in the image volumes from all patient cases as a function of*

*error in optical scattering. Red data points show the same analysis from the phantom experiments.*

Designing new multi-modal imaging systems typically presents tradeoffs and prototype simulations can guide hardware selection and implementation. Minimizing the number of wavelengths, sources, and detectors in a proposed FD imaging module decreases costs, complexity, and examination time in a multi-modality NIRST-DBT breast imaging platform. Simulations of NIRST data for eight subject-specific breast volumes based on DBT images highlight differences in results from each simulated system change.

Using two-region rather than single bulk tissue estimates of scattering had a large impact on the recovered HbT concentration. Mischaracterization of scattering led to errors in quantification of HbT. Significant differences in scattering are known to exist between adipose and fibroglandular tissue<sup>81,82</sup> and both contribute to a large fraction of breast composition by volume. Taking a single bulk estimate of these two tissues averages their scattering effects, leading to underestimation of hemoglobin concentration in the adipose region and overestimation in the fibroglandular and tumor regions. Bulk estimates of scattering can be obtained from as few as one measurement; however, quantitative recovery of chromophore levels in the different regions will not be as accurate as in the two region scattering case.

Although the inaccurate estimates in scattering may appear to be a serious flaw in system design, their impact can be mitigated. In our analysis, relative changes in scattering do not significantly depend on region size or shape or actual hemoglobin concentration. Hence, if scattering estimates are consistently inaccurate in different

regions, quantitative recovery of hemoglobin concentration will also be inaccurate, but contrast between regions should be maintained. This has been demonstrated for patient data in the next section. NIRST algorithms are known to have difficulty fully recovering absolute HbT<sup>57</sup>, yet analyzing relative contrast has proved to be a productive alternative<sup>51</sup>.

### ***Normal Subject DOSI Imaging***

We recognized the importance of using the simulation results as a guideline for obtaining scattering estimations for our first cohort of normal subjects. Realizing that scattering information could be important for patients, a total of 15 women were imaged using the combined NIRST-DBT system as well as the DOSI system, described in Chapter 5, which possesses both broadband and frequency domain imaging capabilities. As the women are imaged under vastly different geometries, it was not possible to obtain anything beyond simple bulk estimation for scattering for the entire breast. Averages of the scattering estimates obtained at twenty measurement sites were taken, with individual measurement variability between 5 and 7%.

#### **8.1.1. Patient Characteristics**

Normal subjects with a wide range of breast sizes, densities, BMI's, and ages from 46-60 were imaged on both the NIRST-DBT and DOSI systems. Despite directed recruitment efforts, no women were imaged in the lowest breast density category, fatty. There are relatively few women in this category, representing between 3 and 10% of the eligible screening population depending on age<sup>205</sup>. Additionally, they are the least likely to benefit from DBT imaging, as mammography has the highest specificity for this

group<sup>12</sup>. The women were roughly split between the other three categories, with six scattered breasts, five heterogeneously dense, and five extremely dense.

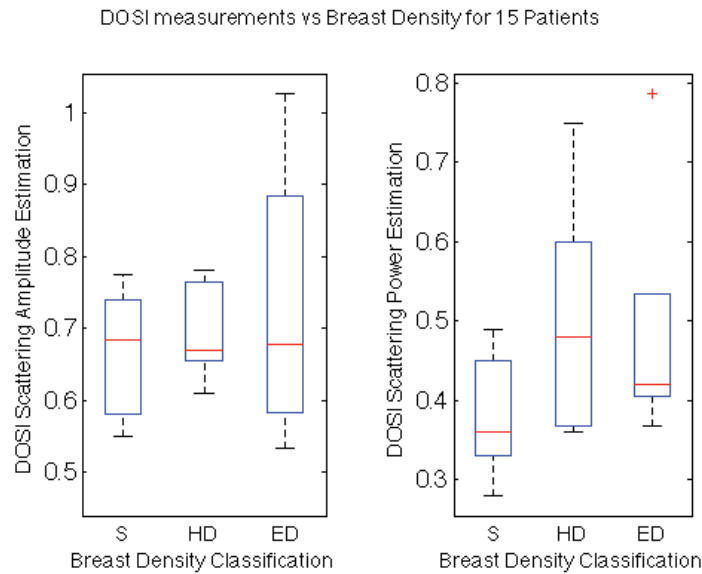
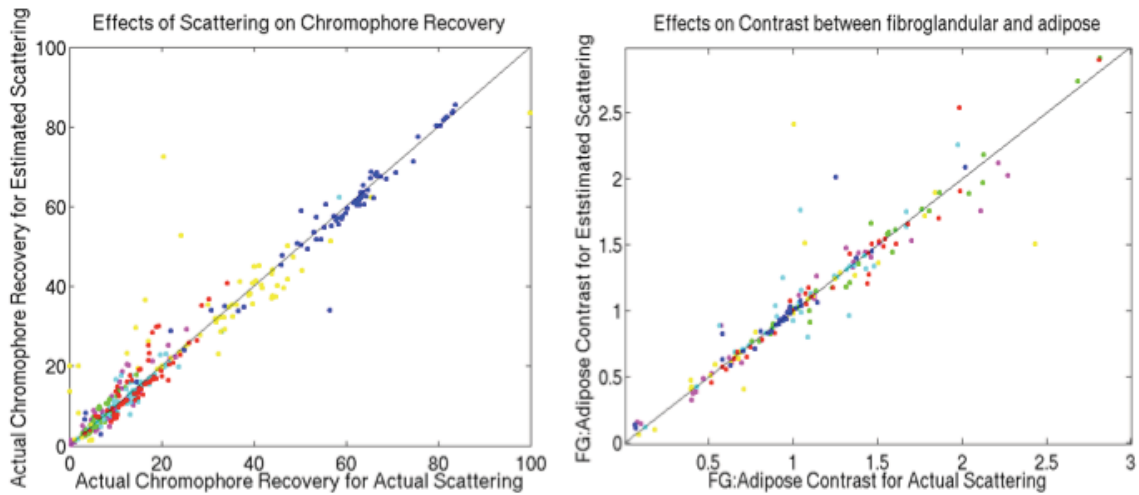


Figure 94: Boxplots showing the scattering amplitude (left) and scattering power (right) bulk tissue estimates for 15 patients as a function of BIRADS category.

### 8.1.2. Using Group Estimates

As shown in Figure 94, scattering amplitude and power measurements varied across individuals, from 0.55-1 for scattering amplitude and 0.3-0.75 for scattering power. Understanding the effects of scattering mischaracterization on absorption recovery is essential to confidently trust the results from an exclusively CW imaging system. In this case, the tissue chromophore recovery is compared for all 15 patients. In one case, the scattering properties used for the NIRST reconstruction are derived from the individual DOSI measurements. For the comparison case, average DOSI properties for all patients are used, specifically 0.7 for scattering amplitude and 0.45 for scattering power. The results of this comparison are shown in Figure 95.

In examining the correlation between absolute chromophore recovery and fibroglandular to adipose contrast, it is clear that most of the points follow along the 1:1 ratio line. Generally, the correlation fit is better for the contrast recovery case, as speculated during the simulation studies, but there is strong recovery in the absolute sense as well, as shown in Figure 95(b) and (c) respectively.



*Figure 95: Graphs comparing absolute chromophore recovery (left) and contrast ratios (right) for individual scattering estimate vs. uniform group scattering estimate as derived from DOSI. Each color in the graphs represents a different chromophore, with red representing total hemoglobin, magenta as oxygenated hemoglobin, green as deoxygenated hemoglobin, teal as water, yellow as fat, and dark blue as oxygen saturation. The black line in each graph represents 1:1 correlation.*

Correlation of specific chromophores is quantified through calculation of a correlation coefficient, shown in Figure 96. Overall quantification was excellent for hemoglobin parameters, demonstrably lower for water and lipid measurements, possibly due to lower sensitivity to these chromophores or greater noise in the higher wavelengths

in NIRST-DBT data, but all correlations were statistically significant. When comparing the absolute chromophore recovery to the contrast ratios, it is clear that for hemoglobin parameters, contrast is the superior metric, with an  $r$  value of .97 for HbT compared with 0.89 for the absolute quantification. However, for water and oxygen saturation, comparison of individual values is better. This may be due to the fact that oxygen saturation is already a ratio (HbO/HbT) so it is less affected by changes in scattering.

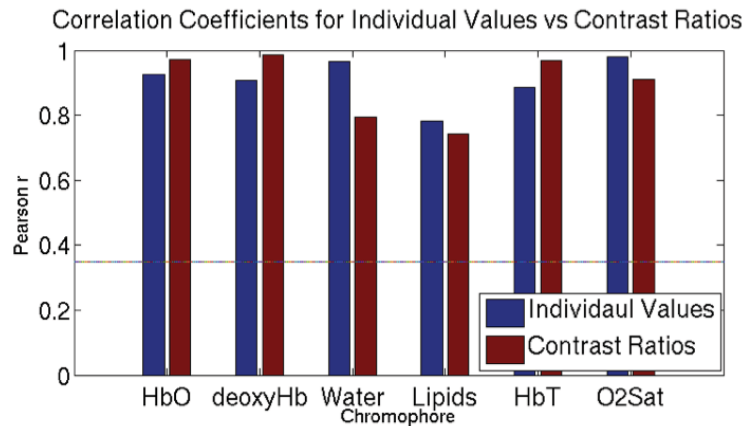


*Figure 96: Graph comparing absolute chromophore recovery (blue) and contrast ratio (red) correlation coefficients for individual scattering estimate vs. uniform group scattering estimate as derived from DOSI. The line shows the cutoff for statistical correlation, all cases are statistically correlated.*

Overall, mischaracterization in absolute chromophore recovery is less drastic than expected from simulation results, likely due to the overall similarity in recovered scattering amplitude and power measured by DOSI, with a coefficient of variation of 17.6%. Additionally, reconstructions of patient data are more heavily damped than phantom data due to the higher noise levels. This might also contribute to the relative similarity between data obtained using individual scattering estimations as compared to a

group value. The correlation of the recovered chromophores (over 0.97 for all hemoglobin parameters when using contrasting values) validates the use of a group scattering estimate across patients for exclusively CW imaging as opposed to measuring each patient individually.

### ***Normal Subject X-Ray Imaging***

Inaccurate quantification of light scattering can lead to significant errors when recovering tissue absorption<sup>84</sup>. Current normal subject imaging requires the use of two different platforms, NIRST-DBT and DOSI, which are located at separate ends of the hospital. The two techniques employ different geometries so region-based determination of optical scattering is not possible. Scattering information can be obtained via time or frequency domain components for the NIR imaging system, as has been done previously in a NIRST-DBT system built at Massachusetts General Hospital<sup>40,87-89</sup>. However, prior work in our group has shown a correlation between optical scattering and breast density, as seen in the bottom right hand side of Figure 97. In an effort to minimize the overall system complexity and to capitalize on the shared information obtained through completely co-registered NIR and DBT data sets, we propose to examine the feasibility of using X-ray pixel intensity as a surrogate marker for scattering in human subjects.

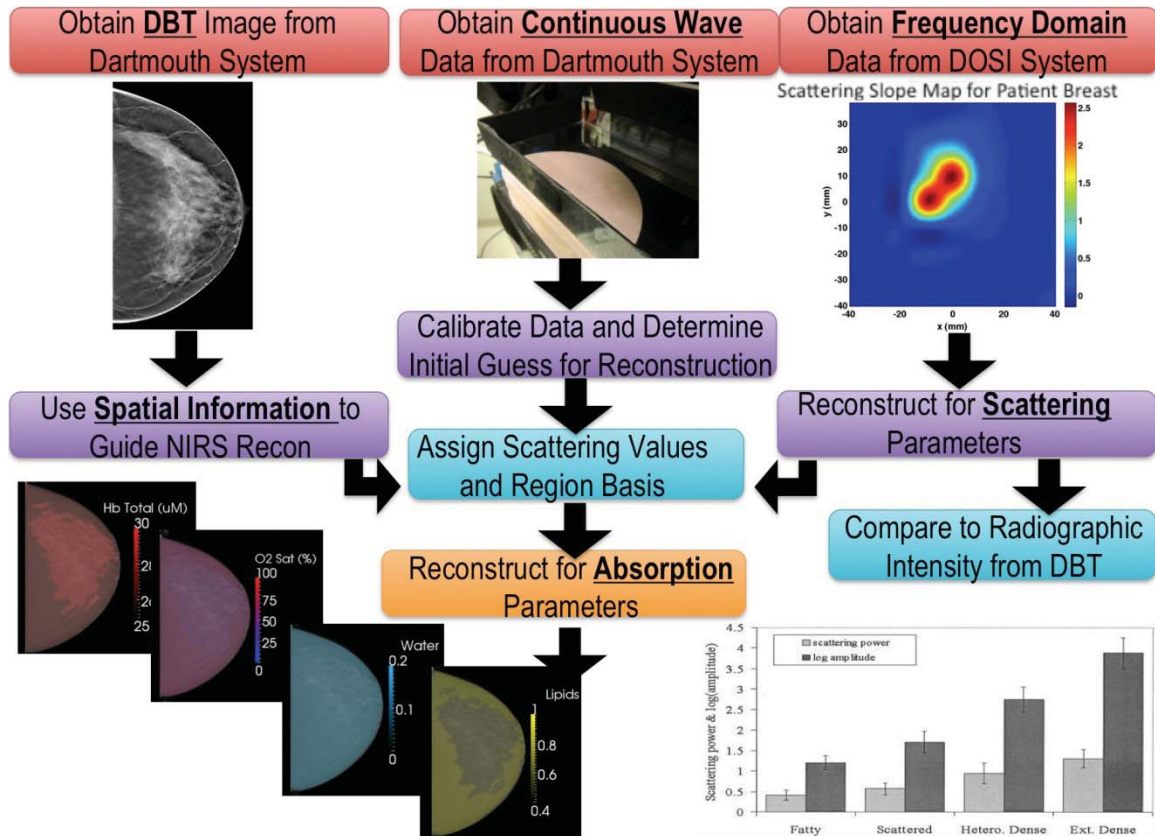


Figure 97: The workflow for normal subject imaging and chromophore recovery.

Current efforts are focused on comparing DBT pixel intensity to the optical scattering obtained from the DOSI system, encouraged by previously published work shown in the bottom right, indicating a correlation between breast density and optical scattering<sup>77</sup>.

### 8.1.3. Phantom Calibration

Estimation of breast density quantification has been extensively studied for mammography; we modified prior efforts for DBT<sup>206,207</sup>. In this case, the system takes images at several projections and different source angles. We examined the central projection image, when the source is directly above the detector, as this is most similar to mammography. We obtained a step wedge phantom consisting of 50% adipose and 50%

fibroglandular tissue mimicking breast tissue. The steps range from 0.5 to 6 cm in 0.5 cm increments, as shown in Figure 98. This phantom was imaged at the same kVp and mAs settings as each normal subject. The mean pixel intensity was recorded for the step corresponding most closely to the breast thickness. This value served as a calibration factor and was divided by the mean pixel intensity for each patient's raw central projection image. This technique facilitated inter-patient correlation as normal subjects were imaged at settings selected from a look-up table designed to minimize patient dose and maximize contrast.

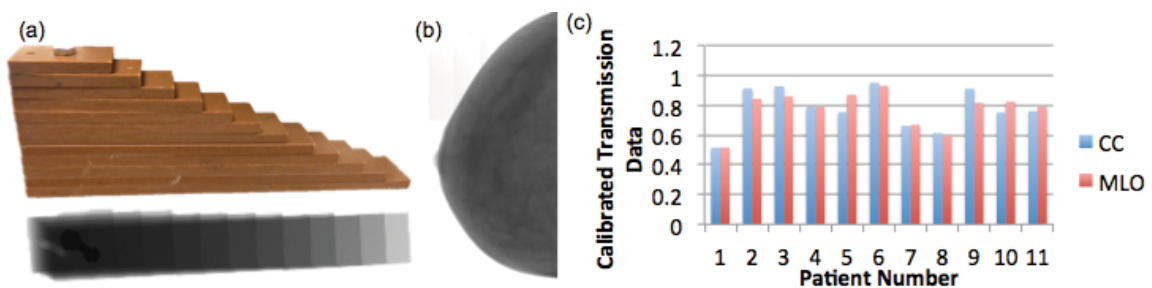


Figure 98: (a) The step wedge phantom used to calibrate the patient images and a sample X-ray image of the phantom. (b) An example of the raw central projection image from a normal subject breast. (c) Calibrated X-ray transmission data for all subjects<sup>208</sup>.

Pixel intensity values obtained from the central projection were averaged for the whole breast. These values were calibrated for kVp, mAs, and breast thickness using the results from the previous phantom experiments. The mean breast value was divided by the mean value for the step of the wedge phantoms to produce a rough estimate of calibrated X-ray transmission. These estimates were compared to measured tissue scattering using the DOSI system. Despite different imaging parameters, CC and MLO

views of a given breast are quite similar with less than 10% variation, and there is much greater variation between patients than between views as seen in Figure 98(c).

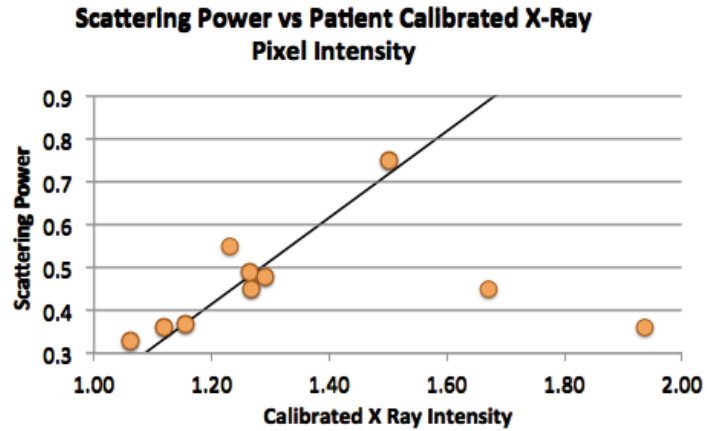


Figure 99: Graph showing the DOSI measured scattering power vs. the mean X-ray intensity after phantom calibration for all patients. Fit line was added after dropping patients with higher compression levels<sup>208</sup>.

CC and MLO X-ray transmission values were averaged and inverted, then compared to DOSI-obtained scattering properties, specifically scattering power and scattering coefficient at 850 nms. DOSI measurements at various points on the breast show minimal variation, between 7 and 9%, and this variation is not correlated to any specific quadrant. The results for scattering power are shown in *Figure 99*. A clear positive correlation is observed when comparing X-ray pixel intensity with DOSI scattering power; however, a couple of patients do not follow this trend. Further inspection of the data showed that these patients were more highly compressed than others. Specifically, the breast area as measured on the central projection view of the CC scan divided by the breast height measured on the compression paddle was higher. When

women with high compression ratios are removed from the analysis and a linear trend line is added, a good fit is observed with an r value of 0.92.

Scattering estimates from the fit for the scattering power and scattering coefficient at 850 nm were used in reconstructing a single normal subject and compared to a reconstruction of the same normal subject using the optical scattering data obtained from the DOSI system, as shown in Figure 100. The chromophore recovery in this subject was only 7-12% different (depending on the chromophores) using the DBT estimates instead of the measured values. Additionally, there was less than a 1% difference in the contrast between the fibroglandular and adipose in these two cases.

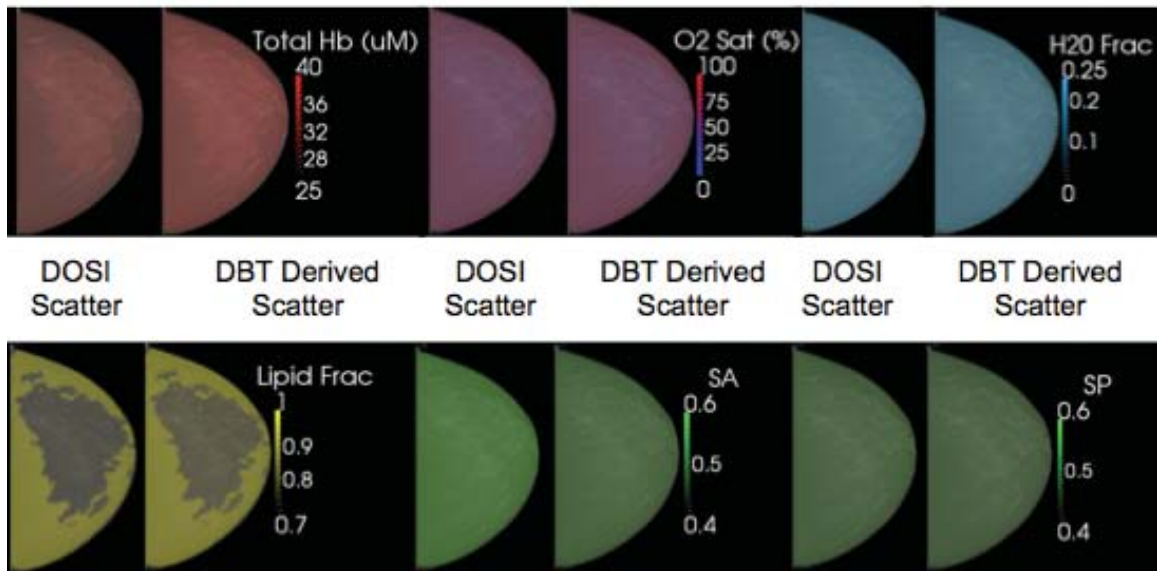


Figure 100: A normal subject reconstruction of total hemoglobin, oxygen saturation, water, and lipids for both adipose and fibroglandular regions for two cases: Scattering as determined from (top) the DOSI system and (bottom) the DBT-based estimate using the linear fit for scattering power and scattering coefficient at 850 nm.<sup>208</sup>

#### 8.1.4. Slope-Based Calibration

After obtaining these promising initial results, we have been working in consultation with an expert in X-ray imaging techniques, Dr. Srinivasa Vedantham at University of Massachusetts Medical Center, to develop a more sophisticated approach to analyzing the X-ray phantom data. This method takes into account more than just a single point of measurement, considering the rate of change in pixel intensity for different thicknesses in the hopes that this would improve the relationship between recorded optical scattering and X-ray pixel intensity.

Under mono-energy and parallel-beam approximation, the transmitted X-ray intensity follows Beer's law,  $I_t = I_0 \exp(-\mu t)$ . Using superscript  $b$  and  $p$  to represent breast and phantom images in  $(x, y)$  detector coordinates, and after log-transform:

$$\begin{aligned}\ln[I_t^b(x, y)] &= \ln[I_0^b] - \mu_b(x, y)t_b - \mu_s 2t_s + \ln[D_{offset}] \\ \ln[I_t^p(x, y)] &= \ln[I_0^p] - \mu_p t_p(x, y) + \ln[D_{offset}]\end{aligned}$$

In the above equation,  $\mu_b(x, y)$  represents the spatially-variant linear attenuation coefficient (LAC) of breast tissue excluding the skin,  $t_b$  represents the breast thickness excluding the skin in the uniform thickness region of the breast,  $\mu_s$  represents the linear attenuation coefficient of skin,  $2t_s$  represents the thickness of two skin layers (top and bottom),  $D_{offset}$  represents the detector signal offset,  $\mu_p$  describes the linear attenuation coefficient of the phantom material, and  $t_p(x, y)$  is the spatially variant step thickness of the phantom.

Images of the step phantom are acquired using identical technique factors as the breast, i.e.,  $I_0^p = I_0^b$ , then a calibration curve based on phantom step thickness  $t_p(x, y)$  can be generated.

Independent studies<sup>209,210</sup> have shown that the average breast skin thickness is 1.45 mm.

$$2t_s = 2 \times 0.145 = 0.29 \text{ cm}$$

$\overline{\ln[I_t^b]}$  represents the spatial average over the uniform thickness region of the breast. Let us represent the LAC of fibroglandular tissue as  $\mu_g$ . Over the energy range of 10-40 keV that encompasses most of the X-ray spectrum used in mammography and digital breast tomosynthesis, the LAC of the BR-12 material based step phantom approximates that of 50% fibroglandular breast tissue<sup>211,212</sup>. Also, the LAC of BR-12 is ~22% lower than that of skin over this energy range<sup>212</sup>. Hence,

$$\begin{aligned}\mu_p &= 0.5 \mu_g \\ \mu_s &= 1.285 \mu_p\end{aligned}$$

For a normal breast with no abnormalities (microcalcifications, cysts, masses, etc.), the breast tissue excluding the skin can be approximated as consisting of adipose and fibroglandular tissue. Hence,

$$\mu_b(x, y) = \mu_g k(x, y) + \mu_p (1 - k(x, y))$$

Where  $k(x, y) \in [0, 1]$ , where  $k = 0$  indicates adipose tissue and  $k = 1$  indicates fibroglandular tissue. We are interested in the location-averaged breast density, i.e.,

$$\mu_b = \overline{\mu_b(x, y)}$$

The method has limitations. It does not account for noise in the measurements or for X-ray scatter, important in DBT as no antiscatter grid is present. It has several sources of uncertainties including assumed thickness of skin layer, which can vary with location and between subjects (range: 0.8 to 2.3 mm). We can make further improvements by including the X-ray spectral model, but the aforementioned limitations would still be applicable.

This method was attempted using a logarithmic transform of the central projection image, and by taking the transform of the mean values from the original image. In both cases, no added benefit was seen by performing this more comprehensive analysis, but a persistent positive trend between calculated fibroglandular percent and optical scattering parameters is noted in Figure 101.

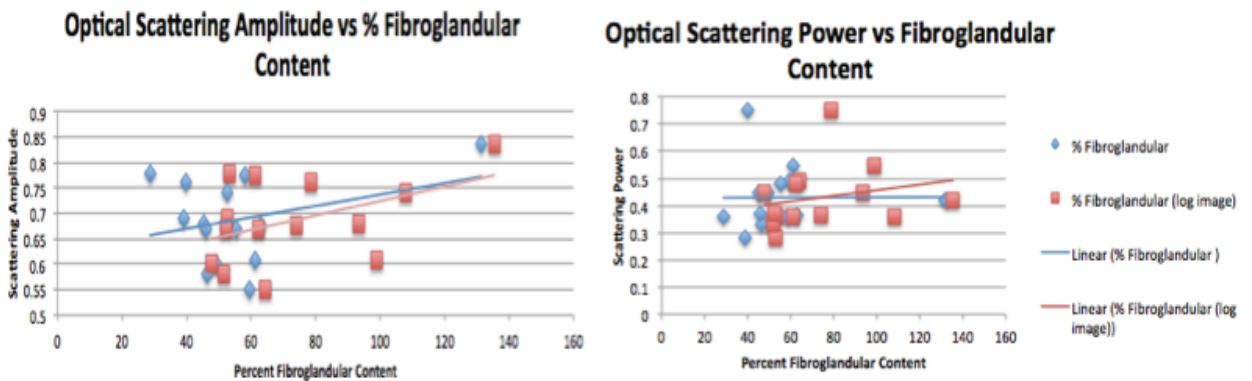


*Figure 101: These graphs show the relationship between calculated percent fibroglandular content and optical scattering amplitude (left) and power (right). Trend lines show a generally positive correlation between increasing fibroglandular content and optical scattering. Blue data points correspond to the log of the mean of the image, while red data points correspond to taking the average of the log of the image.*

Although a positive trend between increasing fibroglandular volume fraction and scattering amplitude and power is present, there is a lot of variability in the results. Most concerning was the non physiological fibroglandular percentages derived from this formula (over 100%), as seen in Figure 101.

This prompted the use of an alternative metric for fibroglandular percentage, the percent of tissue segmented as fibroglandular from the DBT image stacks, as described in Chapter 3. The results from the comparison of fibroglandular content and scattering properties is shown in Figure 102. In these cases, there is a statistically significant correlation between scattering properties and fibroglandular volume fraction ( $p < 0.02$ ). X-ray pixel intensity information was not used directly in this analysis but it is evaluated during the segmentation process. All the data points fall within 0.1 for scattering amplitude and 0.2 for scattering power. One downside of using the segmentation-based method is that unlike direct examination of pixel intensity values, it is not possible to assign scattering on a voxel by voxel basis, as the segmentation only produces two regions and DOSI only has a single scattering value. Further work with a tomographic FD imaging system that has at least two tissue regions and comparing the pixel intensity values from the two region segmentation of the DBT images would be helpful in understanding more about how pixel intensity affects optical scattering, but such a system is not available at Dartmouth. Overall, this is the most robust method that was developed

to ascertain scattering from DBT images.

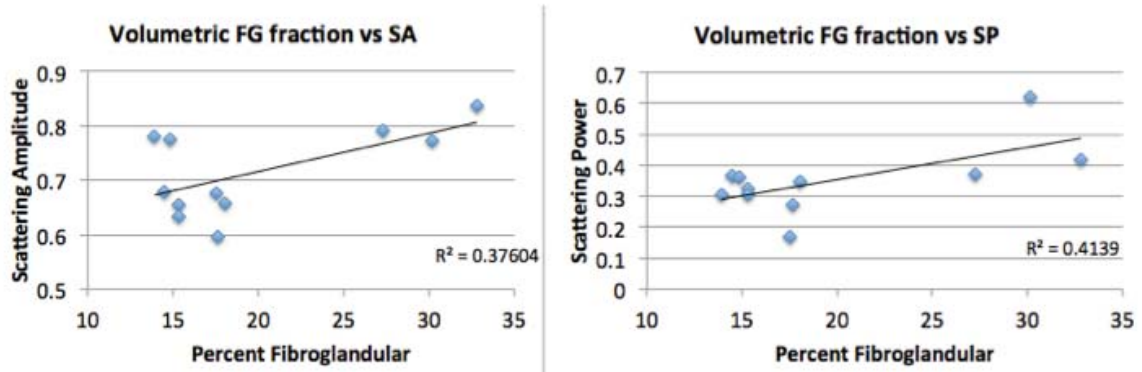


*Figure 102: These graphs show the relationship between volumetric fibroglandular fraction as determined from segmented DBT images and scattering amplitude (left) and power (right).*

### **Conclusions**

Through simulations, phantoms, and normal subject imaging, the effects of scattering estimation on recovered chromophores was explored in detail for this new exclusively CW imaging system. Results from simulations of normal patients showed lower accuracy in absolute chromophore recovery when using bulk tissue estimates of scattering as opposed to individual region estimates and also indicated that slight mischaracterization of scattering, for example, 20%, could cause a 22-35% change in the recovered hemoglobin levels. These results were worrisome and led to imaging women on both NIRST-DBT and DOSI systems to obtain scattering estimations for the first normal subjects.

The results from the normal subjects showed excellent correlation (r of .97) for comparing fibroglandular to adipose contrast in women using individualized scattering estimates vs. a group estimate based on the average for 15 patients. Looking at contrast

ratios instead of actual chromophore content may mitigate some of the errors induced by scattering mischaracterization. Additionally, optical scattering is greater in tissues with more changes in indices of refraction; typically, cells with extensive metabolic activity have greater scattering than adipocytes. Underestimation of scattering in these regions will lead to an overestimation of absorption to compensate. Hence, if a region of interest has a particularly high amount of scattering, it is more likely to be a tumor than a fluid-filled cyst, and will have higher absorption properties that will increase the contrast between the lesion and the background. In effect, bulk scattering estimation can enhance absorption contrast.

There are some problems with mis-estimation of scattering. It makes it challenging to compare both intra- and inter-patient absolute chromophore concentrations as scattering estimates will be off by a different amount in each patient. Additionally, scattering as a function of breast compression may cause some of the changes in breast absorption properties. An ideal solution would be estimation of tissue scattering from DBT images. This method could provide region- or voxel-based scattering estimates without any additional hardware or imaging time. Several methods for deriving optical scattering properties from DBT were examined, including point and slope based calibration methods as well as segmentation based efforts. Positive trends between increasing pixel intensity and fibroglandular volume as compared to optical scattering were noted, but non physiological calculated fibroglandular content was an issue in the slope based method and a few points quite far from the fit line were noted in the point based method.

Further examination of DOSI results demonstrated a correlation between fibroglandular volume as determined from the segmented breast images, and scattering properties. Using the segmentation of DBT images is the best method for patient-by-patient determination of scattering developed to date. An alternative method may be comparison of Quantra tissue estimates with scattering properties. This has not been tested yet due to the low number of subjects with Quantra data. However, based on the high correlation of contrast measurements, and demonstrated results with prior human subject imaging shown in Chapter 6, the benefit of improving the scattering with this additional tool is unknown at this time and difficult to assess in humans where true chromophore values are unknown. It is not possible to apply this method of segmentation to phantom models, making it challenging to evaluate further.

Overall, it appears that exclusive CW imaging may be useful when examining individual patients or for aggregate analysis, but caution is needed when attempting to draw conclusions from patient comparisons. Clear explanation that absorption properties measured are likely not the absolute values but some bundled effect of both absorption and scattering is necessary when looking at absolute chromophore values. Examination of contrast levels rather than absolute quantification of hemoglobin is likely the plan going forward, to allow CW only use, and mitigate the effects of limited scattering estimation.

## **Chapter 9: Conclusions and Future Directions**

### ***Completed Work***

This work concentrates on the development of instrumentation and methods to optimize a novel multimodal imaging platform for testing the hypothesis that NIRST could increase specificity above DBT alone to better distinguish malignant from benign lesions prior to biopsy. This was achieved by building a combined NIRST-DBT system with complete image co-registration. Hardware and software tools were developed simultaneously for successful imaging of phantoms, normal subjects and, finally, women directly prior to breast biopsy. Although it is not possible to draw significant conclusions due to the low number of biopsy patients imaged so far, two malignancies recovered ROI to fibroglandular total hemoglobin enhanced contrast, while all benign lesions had negative or neutral contrast relative to the background tissue, signaling promise for this modality in future large-scale patient studies. Each section of the study results are recapped here, highlighting what is most successful and which directions would be most profitable for future work.

### **9.1.1. System Design and Instrumentation**

Chapter 2 summarizes the process of simulating and building the hardware aspects of the NIRST-DBT imaging system. There were several unique considerations in building the combined NIRST-DBT system that guided crucial hardware decisions. Adding NIRST to an existing imaging technology considerably limited potential tissue geometries and source and detector locations. Typical DBT imaging is performed under breast compression for lower dose and better image contrast. In order to obtain co-

registered data sets for spatial prior guidance, the NIRST exam must be performed under compression as well and thus is necessarily quite short, less than one minute in length. As this system is designed for use after diagnostic X-ray imaging but prior to biopsy on many women, it was important to keep the additional costs of adding NIRST low. Lastly, this system should utilize a more comprehensive approach than the only other existing NIRST-DBT system, located at Massachusetts General Hospital<sup>40</sup>. A system was designed, operating with extensive CW components with a few FD channels based on the above specifications. Simulations of NIRST reconstruction based on existing clinical DBT dataset channels demonstrated the ability to distinguish benign and malignant lesions and were published as part of this thesis work (Michaelsen et al)<sup>151</sup>.

We built a system similar to the simulated design, but lacking FD channels for even greater simplicity. It employed eight wavelengths from 660-940 nm, with a raster scanning mirror system directing light onto the tissue at 77 different, configurable positions, with 75 1 cm x 1 cm photodiode detectors for light collection. One particularly difficult challenge was finding an acceptable material for covering the detector panel while minimally impacting both the near-infrared and X-ray transmissions. Polycarbonate was selected as the best option and when combined with extensive light blocking measures, produced clinical quality DBT images and usable NIRST data. Design of the system was published in a paper by Krishnaswamy et al.<sup>68</sup> and detailed materials analysis for the detector panel cover was published by Michaelsen et al<sup>91</sup>.

### **9.1.2. Image Formation Methods**

Chapter 3 provides background on the physics of light-tissue interaction and

explains NIR spectral region recovery from a mathematical point of view using prior information derived from the DBT images to improve optical reconstruction through synergistic combination of information streams. Spatial priors from the DBT image stack can be used to guide the NIRST estimation. Tissue volume and region basis are defined through the use of carefully segmented DBT images. This process improves spatial resolution of the optical data, aiding the reconstruction model through reduction in the number of unknowns by several orders of magnitude.

As there are currently no algorithms for DBT image segmentation due to the relative newness of this modality, extensive work was performed in collaboration with individuals at the University of Massachusetts Medical Center. Semi-automated segmentation algorithms were developed in MATLAB to separate adipose, fibroglandular, muscle, and tumor tissues. The fidelity of these techniques was tested by comparing calculated fibroglandular volume fraction from the new DBT segmentation technique to an FDA-approved tool for estimation of fibroglandular volume fraction from mammographic images, Quantra (Hologic, Inc). Statistically significant correlation was found between the segmented DBT volume and Quantra estimated the normalized fibroglandular volume fraction with a Pearson  $r$  value of 0.66 ( $p=0.004$ ) for 17 cases. Moreover, intra-modality normalized volumetric breast density assessed between two views of the same breast were better correlated with an  $r$  of 0.86 ( $p=0.03$ ) in DBT than in mammographic QUANTRA analysis, with an  $r$  of 0.57 ( $p=0.24$ ).

Finally, this chapter reviews the automated mesh creation process. This takes segmented DBT images and creates a mesh with the desired number of nodes, with additional capabilities to increase the mesh resolution in a small specific region of

interest. As source and detector positions are fixed for all subjects, their placement on the tissue volume was easily automated as well. This work is still to be written for publication, based upon collaboration with our UMass colleagues.

### **9.1.3. Phantom Imaging**

In Chapter 4, extensive phantom results from the development and optimization of the system are presented. Four different types of phantoms were tested, including a homogeneous phantom for calibration, a spectral slice phantom for assessing contrast recovery as a function of inclusion size and depth, hemoglobin phantoms for assessing linearity of contrast recovery of tissue chromophores, and finally anthropomorphic water- and lipid-based phantoms to more accurately represent breast tissue chromophore content.

Homogeneous calibration phantoms are used for the earliest NIRST reconstructions as well as during scanning of human subjects to account for model-data-mismatch and inter-source and detector variation as well as differences in virtual source strength in the model and real laser power at the time of imaging. This chapter describes a novel algorithm to calibrate NIRST data with respect to a known, absolute reference phantom, and generate an initial guess without the need for a large data set<sup>160</sup>.

The spectral slice phantom demonstrated HbT recovery in lesions as small as 7 mm. Recovery was similar for the largest two lesions across all depths. Mis-estimating the size or depth of a lesion affected the absolute recovery of HbT, especially relevant for a system relying on DBT images possessing poor z-resolution.

Noting a lack of phantom models that could truly represent the heterogeneity found in breast tissue or that included physiologically relevant water or lipid levels, we created a new phantom recipe described in Chapter 4 and in Michaelsen et al<sup>213</sup>. The resulting phantoms show consistent recovery within 5% of the actual value obtained on the DOSI system for the physiologically relevant range of 15-85% water content. They are also freestanding and can be molded into different regions, displaying excellent reproducibility and durability at a low cost in terms of time and materials.

#### **9.1.4. Methods for Combined NIRST-DBT Imaging**

In preparation for human subject imaging, examination procedures, software tools, and reconstruction strategies were developed for the new NIRST-DBT system. An acceptable patient workflow has been designed to allow full NIRST-DBT imaging in roughly a half an hour after patient consent has been obtained. Software tools using LABVIEW have been developed to control the hardware components. They are highly dependable and easy to use, facilitating quick training of new imagers. Additionally, the LABVIEW code is optimized to minimize examination time and includes graphical feedback of recovered signals for assessment during the exam.

Additional MATLAB software developments were created to help troubleshoot and distinguish problems caused by hardware, software, segmentation, data, or reconstruction efforts. Assigning data points to tissue types helps to identify address problems with reconstruction algorithms and data quality without waiting for complete reconstruction, which is particularly helpful for the large data set created in NIRST-DBT, which can take a day to reconstruct. Additionally, code has been developed for

converting LABVIEW output into reconstruction ready formats with bad data points removed based on experimentally-derived results. The data dropping procedures are robust and semi-automatic, providing inter-patient consistency. Development of these tools and methods provided greater understanding of system issues and was essential for patient imaging.

#### **9.1.5. Imaging Healthy Volunteers**

The use of healthy volunteers in validating a novel NIRST-DBT combined imaging modality is discussed Chapter 6. A total of 32 normal women with a wide range of breast sizes and densities participated. Usable data were obtained for all women except the first five cases. Iterative small tweaks were made to the hardware, software, and data post-processing steps, improving the speed and reliability of human subject imaging.

Aggregating results from over eighty scans showed expected trends relative to a wide array of patient characteristics including BMI, breast density, thickness, bra cup size, BMI and percent fibroglandular tissue. Significant correlations for all the major tissue chromophores, hemoglobin, oxygen saturation, water and lipids were found with one or more of the patient demographic categories. Additionally, results were consistent with published literature. This bolsters the argument that an exclusively CW system can produce reliable results in human breast imaging studies.

Since each breast was imaged multiple times, it was possible to assess the reliability of the NIRST-DBT system and segmentation methods, and gain an understanding of the effects of compression. As expected, there were no significant differences between CC and MLO views; more surprisingly there was no difference in

comparing adipose and fibroglandular tissue, likely due to partial volume averaging from poor segmentation. The only statistically significant result ( $p=0.0427$ ) was the difference in oxygen saturation between the compressed vs. uncompressed breast scans, with a lower saturation found in the compressed case. Overall, individual patient correlations for the images taken at compressed and uncompressed levels are quite high, indicating that it may be possible to obtain accurate chromophore recovery using NIRST at lower compression levels, with DBT at typical mammographic compression. Imaging of healthy volunteers provides information about the metabolic content of healthy breasts, is critical for the validation of new modalities and is the most realistic test that an imaging system can undergo before examination of abnormal tissue.

#### **9.1.6. NIRST-DBT Lesion Characterization Methods**

Chapter 7 presents recruitment strategies for DBT-guided near infrared spectroscopy of women recommended for biopsy, as well as individual case results. At the time of this writing, thirteen women have been imaged with the NIRST-DBT system, with six presented here. Data from two subjects were unusable in our present reconstruction algorithm (one case may be salvageable with proposed changes described in the future directions section, while the other has a lesion visible in only one view). The small size of lesions in this study, while a testament to the efficacy of annual breast screening, poses particular challenges for NIRST-DBT. By incremental enlargement of tumor regions, greater contrast and stability in the reconstruction was achieved.

Results from this study will influence how future NIRST-DBT data are analyzed, particularly with regards to regularization and the role of sensitivity, noise and tumor

size. More subjects must be imaged and analyzed before the hypothesis presented through case studies here can be confirmed. Overall, these earliest results are promising, with a 20% difference in contrast between malignant and fibroglandular tissue and only 2.5% difference in contrast between benign and fibroglandular tissue when cysts and edge lesions are excluded. This result was not statistically significant due to the low patient volume.

#### **9.1.7. The Role of Scattering in NIRST of the Breast**

Sprinkled throughout this entire thesis are issues related to optical scattering (a process 100 times more likely than absorption), which is not adequately recovered using an exclusively CW imaging modality such as the NIRST-DBT system. The final chapter in this thesis attempts to more cohesively discuss the issue of scattering as it relates to the ability of the NIRST-DBT platform to successfully distinguish between benign and malignant lesions, the ultimate goal of this project.

Results from simulations of normal patients showed lower accuracy in absolute chromophore recovery when using bulk tissue estimates of scattering as opposed to individual region estimates and also indicated that slight mischaracterization of scattering, for example, 20%, could cause a 22-35% change in the recovered hemoglobin levels. These results are worrisome and led to imaging women on both NIRST-DBT and DOSI systems to obtain scattering estimations for the earliest normal subjects.

Comparing normal subjects showed excellent correlation ( $r$  of .97 vs. .89) for using fibroglandular to adipose contrast in women using individualized scattering estimates vs. a group estimate based on the average for 15 patients. Looking at contrast ratios of

hemoglobin instead of actual chromophore content may mitigate some of the errors induced by scattering mischaracterization. For this reason, contrast ratios are used in examining the biopsy cohort.

There are some problems with misestimating scattering. It makes it challenging to compare both intra- and inter-patient absolute chromophore concentrations as scattering estimates can be off by a different amount in each patient. An ideal solution would be estimation of tissue scattering from DBT images. This method could provide region- or voxel-based scattering estimates without any additional hardware or imaging time. Several methods for deriving optical scattering properties from DBT were examined, including point and slope based calibration methods, as well as fibroglandular volume from DBT segmentation. Positive trends between increasing pixel intensity and fibroglandular volume as compared to optical scattering were noted but were hampered by high variability, the lowest of which was found in the case that used DBT segmentation to calculate the fibroglandular volume. These experiments pose a particular challenge in that human subject results have no true known value, just expected ranges, and phantoms do not display the same DBT pixel intensity heterogeneity found in patient scans. It may be possible to further examine the effects of using a single bulk estimate vs. individual DBT segmentation based values in subjects with tumors, examining how the difference scattering values changes contrast in benign and malignant lesions. This analysis, however, requires a larger patient cohort than is currently available.

## ***Future Directions***

The NIRST-DBT system has been tested, optimized, and successfully used for imaging healthy and diseased breasts. Based on this initial work, there are several areas for future development involving hardware changes for a second generation prototype, NIRST modeling for reconstruction, and phantom studies to further optimize the system.

### **9.1.8. Hardware Developments**

#### *9.1.8.1. New Detector Panel*

Ongoing normal subject studies have highlighted some areas for improvement for the next generation design. The current detector panel has two large SCSI connectors that are relatively short and do not securely attach to the PCB. This has limited our imaging efforts to the right breast only in many cases. In addition, these cables have loosened and detached from the detector panel during patient imaging sessions as the detector is removed for DBT imaging. Also, working with the optical cart in such close proximity to the patient interface limits the ability of the technologists to access this area for patient positioning.

The detectors in the current design output voltages that span about 2.5 orders of magnitude. This appears sufficient for chromophore recovery for the phantom with larger inclusions and normal subject studies performed to date. However, increasing this span will increase the amount of usable data and potentially improve imaging sensitivity. Our current design uses only half (0-10V) of the output available with the photodiode detectors (-10-10V). Using the full range of will increase the dynamic range of the system and may improve recovery of metabolic tissue markers.

A third area for improvement in the detector's arrangement is on the PCB board. Decreasing the space between detectors on the PCB and using a breast-shaped imaging pattern would allow for a greater number of detectors to collect usable data during an experiment, especially for small breasts. Currently there are about 1.2 cm of space between each detector; in the next generation this space will only be 0.5 cm. Additionally, the detectors should not be arranged in a rectangular pattern but in a breast shape, with a greater number of detectors in the rows closest to the chest walls. A radiologist has been consulted in development of the proposed design to ensure that adequate coverage for both CC and MLO views is possible in this scheme.

To address both the cable and range issues in the second-generation system, the analog-to-digital conversion will take place within the detector panel itself. This will eliminate the need for bulky cables; only a small USB connection will be required. This USB connector can be much longer than the current cables, easing the space constraints that currently hamper system usage and patient exam workflow. Also, direct connection with the digitization circuitry will double the range of measurable signal. This is accomplished via a voltage conversion from the -10 to 10V range of the detectors to +0-20V through an operational amplifier for each detector. These voltages are then digitally converted on a connected PCB contained within the same detector case. Adding these components to the detector panel will slightly increase its height, requiring modification to the detector panel case to accommodate the greater thickness. Mock-ups of the next generation detector panel and case are shown in Figure 103. This effort is spearheaded by Prof. Venkataramanan Krishnaswamy.

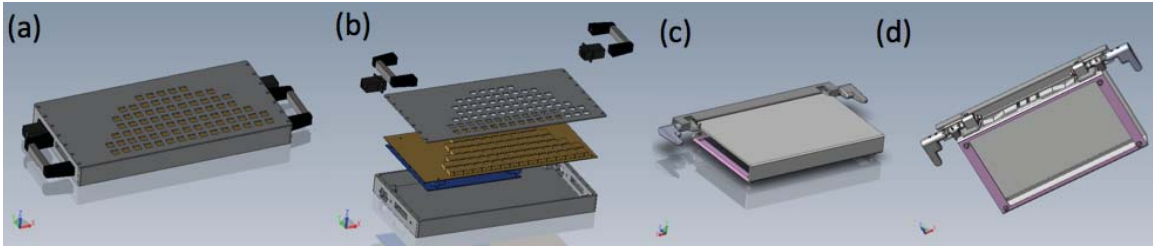
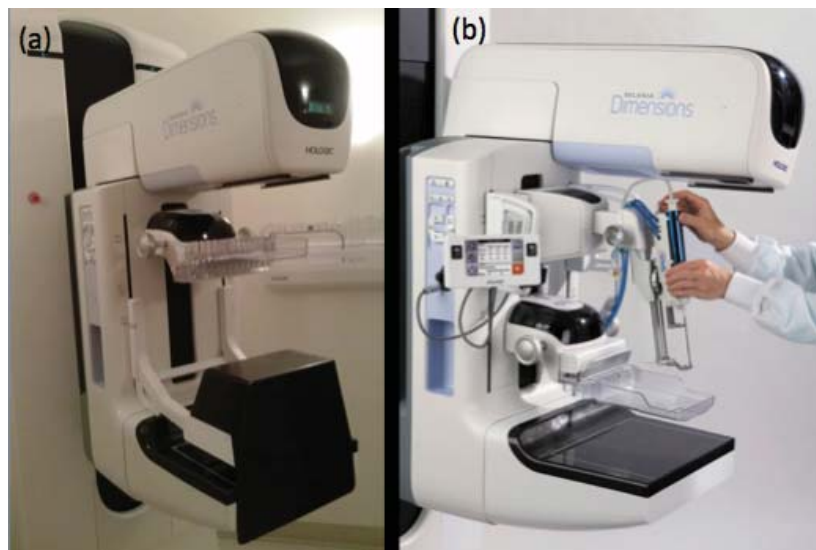


Figure 103: Mock-up images of the new detector (a, b) and detector case (c, d)

#### 9.1.8.2. Clinical Unit Attachment

In preparation for a multi-center clinical study with the broadest possible appeal, the next generation prototype NIRST-DBT system is designed to attach to clinical Hologic Dimensions 2D/3D breast screening platforms. Versatility and the ability to perform NIRST-DBT scans anywhere a Dimensions unit exists were the main drivers behind this decision. Space is at a premium in most hospital environments and the NIRST-DBT unit requires a specialized and dedicated room for its use, which may not be justifiable without a large stream of research participants. By operating as a removable attachment, NIRST-DBT imaging could be performed while still meeting current clinical DBT needs.



*Figure 104: Clinical Hologic Dimensions unit at Dartmouth (a) and unit with biopsy plate attachment (b).*

The ease of use of this attachment is essential to ensure the success of this NIRST-DBT prototype. Currently, we plan to use a commercially available biopsy attachment modified to hold the new detector panel and case, as shown in Figure 104. The light source will be attached to the X-ray gantry using a mechanism that allows for repeated, precise positioning in the same location and does not otherwise affect operation of the DBT unit.

There are other benefits to using a newer DBT imaging system beyond facilitating trials at other institutions. The Dimensions unit is capable of taking both 2D and 3D images; 2D is not possible on the current Genesis unit. Additionally, the new clinical DBT has a much larger detector so that women with the largest breasts can be fully imaged in one scan. As we currently exclude women with breast that require more than one DBT scan for full coverage out of dose concerns, this larger detector panel will increase our potential population for study enrollment. Lastly, a force sensor is present on the Dimensions unit, which will strengthen our understanding of the effects of compression on chromophore recovery.

#### *9.1.8.3. Source Strength Measurement*

When imaging small sized phantom inclusions, variations in the laser source strength can be of the same magnitude as signal attenuation from contrast, diminishing the signal to noise ratio, as noted in chapter 4. A simple solution, feasible on the current prototype as well as in future designs, has been created and is nearly ready use. A small

portion of the laser light output is tapped before the laser scanning mirrors. The optical fiber is embedded directly in the back left corner photodiode of the detector panel (which is most infrequently covered with breast tissue during a scan). This is accomplished through a small fixed enclosure that keeps out all other light sources and is only 2 mm higher than detector panel itself, so it doesn't impede detector removal during the scan. The photodiode is a real-time monitor of the source signal strength and can be used to calibrate out random fluctuations, decreasing noise.

#### *9.1.8.4. Elimination of Breast Shroud*

Without black-covered foam and wire breast shroud that cups the breast during the NIRST scan, data would be unusable. The shroud blocks light transmission to detectors that are not covered by the breast tissue, limiting signals from impinging on the polycarbonate detector cover and channeling spurious light signals to far off detectors as shown in Figure 105. The shroud works fairly well, although lipid recovery may be depressed in cases where positioning is not perfect and some detectors are still exposed, as mentioned in Chapter 6, because channeling is strongest at the highest wavelengths. There are some challenges associated with the shroud, however. It can be difficult to position; asking patients to hold the shroud can help in some cases, but there are just some positions where the shroud cannot obtain close enough contact with the breast. A second-generation shroud has been built to potentially ameliorate this situation, but completely getting rid of the shroud would be an even greater improvement for several reasons. First, it takes time to position the shroud. We estimate that about four minutes of the thirty-minute exam are spent trying to get the shroud in an optimal position.

Secondly, breast technologists often use finger pressure on the breast to assert whether or not a compression level is sufficient. This is not possible with the shroud in place.

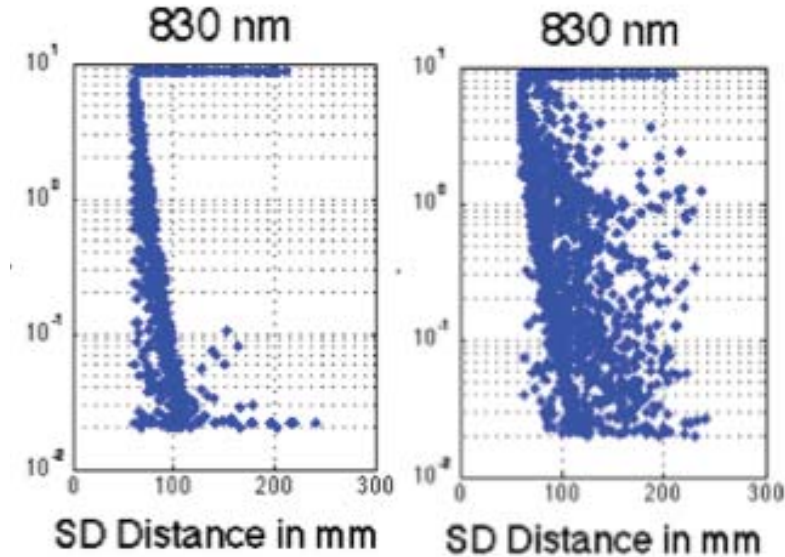


*Figure 105: Signal from all detectors for a phantom scan imaged (a) with the shroud and (b) without the shroud.*

Efforts to eliminate the shroud involve a short survey scan using NIRST, in which detector signals can be used to determine the extent of the breast tissue; detectors that are not covered are not read during the DAQ readout, as their signals are not useful. This survey scan could also be useful for on-the-fly configuration of light source positions to maximize sensitivity and minimize exam time.

#### **9.1.9. Software Developments**

From a software standpoint, there are many areas for further study that could improve NIRST recovery. With a large cohort of normal and abnormal NIRST-DBT breast data sets (over 150 to date), it may be possible to improve lesion detection and sensitivity along the breast edges as well as contrast in regions of interest.

#### *9.1.9.1. Regularization, Noise and Lesion Size*

Noise in NIRST data sets is considerably variable, depending on shroud breast contact, source and detector variation, and other factors that vary in a unique way for each case. Regularization is important for noise suppression, so rather than a uniform regularization value, it may be possible to determine an optimal regularization value on a patient-by-patient basis. Utilization of correct regularization is important because data over-smoothing can eliminate contrast while under-smoothing can cause spurious noise domination. An analogous argument can be made for expanding tumor boundaries, as too large an expansion will diminish the impact of the actual tumor signal when averaged with the background. Perhaps some measurement of data noise (based on the standard deviation off the slope of the log amplitude vs. source detector distance graph) and tumor sensitivity could predict optimal tumor volume and regularization. An especially helpful method would dictate optimal values prior to reconstruction, saving computational time currently spent running multiple tumor sizes or regularization values.

#### *9.1.9.2. Estimation of Optical Scattering*

As described extensively in Chapter 8, deriving optical scattering properties from DBT images was moderately fruitful when using DOSI as the known scattering values, but there was still some variation in the data even while using the best DBT segmentation based method. Comparing DBT images and tomographic optical FD reconstructions with different regions is one alternative approach but difficult to achieve approach. A second option would be to use some basic guidance from the DBT imaging as well as the physiological constraints of water and lipids in the breast to calculate optical scattering

and power. More specifically, this involves using the breast density categorization from the radiologist to determine the expected water-to-lipid ratio from literature data or the results of Chapter 6 on water and lipid content by density. Using expected lipid-to-water contrast, as well as a second equation (total water and lipid fraction should equal 1), it is possible to solve for both scattering amplitude and power. This could be a viable alternative that is more patient specific than a singular scattering estimation used across all subjects.

#### *9.1.9.3. Inclusion of Chest Wall Data*

In the current reconstruction scheme, all data points less than 1.5 cm from the tissue boundary are discarded despite the important additional information they possess because the tissue boundaries are not adequately modeled. For the chest wall side in particular, an end to the tissue is modeled when clearly the patient's actual body continues. The other edges are not representative either as they do not mimic breast curvature. Instead of creating precise volumetric breast models, we would consider a semi-infinite slab model, or at least a breast model with edges extended beyond the true tissue edges. It may be possible to include previously discarded detectors by placing the sources and detectors spaced as before, but well away from the mesh edges, and labeling the regions within imaged DBT volume, leaving the rest of the nodes to be a part of a separate region. In some cases, it may be possible to reconstruct previously unreconstructable data from patients with small breasts, but at the cost of additional computation time due to the increased size of the mesh.

#### *9.1.9.4. Source Position and Scan Optimization*

The raster scanning source is highly configurable. Currently, there are three source patterns that are used depending on breast shape. Additional patterns, specifically those that are optimized for MLO views would improve our sensitivity to lesions in the upper quadrant. Further optimization is possible on a patient-by-patient basis through a survey NIRST scan that determines the breast extent and positions the source only at locations within the tissue. Additional studies could optimize the number and spacing of source positions, possibly decreasing the examination time without adversely affecting the NIRST chromophore recovery.

#### *9.1.9.5. Distributed Sources and Detectors*

In all cases reconstructed in this thesis, sources and detectors were modeled as points, a clear deviation from the actual geometry, which has source diameters of  $1 \text{ cm}^2$  and detector active areas of  $1 \text{ cm}^2$  as well. We could approximate light detectors as centimeter squares, but the code was not optimal; it considered each tetrahedral element covered by the detector to be separate, adding the contributions of all elements after the fact. It also took a long time to run and did not appear to greatly alter the data. With actual NIRST-DBT data, it would be a good idea to reexamine the impact of distributed sources and detectors using a more optimized code.

#### **9.1.10. Phantom Experiments**

As detailed in Chapter 4, significant work went in to the creation of anthropomorphic breast phantoms with accurate water and lipid quantities. The main purpose of doing so was to test the ability of the NIRST-DBT system to appropriately

quantify water and lipid content; however, time constraints and a focus on patient imaging prevented this from happening. It is clear from the results shown in Chapter 6 that the NIRST system does detect changes in breast composition, with higher water and lower lipids found in denser breasts. However, as documented in case examples in Chapter 7, it is unclear how well this is accomplished in small lesions. Phantoms containing physiologically relevant water and lipid content have been imaged on the NIRST-DBT system for homogeneous cases and will be reconstructed in the future to assess the ability of our limited high wavelength dataset to discriminate water and lipid content in both large regions and small inclusions.

#### **9.1.11. Final Remarks**

This new multimodality imaging platform has successfully imaged women of all kinds and shown some ability to distinguish benign from malignant lesions in limited early trials. The biggest technical challenge for NIRST-DBT is detection of contrast for lesions of a small size, in some cases not even masses but collections of microcalcifications only a millimeter or two in diameter. This is difficult because small deviations from normal tissue will only slightly perturb the light signal, both on account of their size and the smaller in vivo metabolic changes when compared to a more fulminant tumor. Improving the signal-to-noise ratio is of the utmost importance for optimizing the NIRST-DBT system. Many experiments and processes described in this thesis are aimed at decreasing signal noise levels, but there are still several areas for future improvement, such as implementation of a source strength measurement or more accurate breast volume and source and detector modeling. An alternative approach

would be to augment the existing signal through exogenous contrast agents such as indocyanine green. For the short term, imaging a larger cohort of biopsy patients will assist in determining if current signal-to-noise levels are sufficient for accurate discrimination of benign and malignant lesions.

## Appendices

### Appendix A: Original Settings for DBT Images



#### Genesis Technique Table

#### 2. TOMO TECHNIQUE CHART

Standard paddle operation

Thickness (mm)	Fatty			Normal			Dense		
	filter	kV	mAs	filter	kV	mAs	filter	kV	mAs
20	Al	26	26	Al	25	36	Al	25	42
25	Al	27	28	Al	26	36	Al	26	44
30	Al	28	28	Al	27	38	Al	27	46
35	Al	28	34	Al	28	38	Al	27	54
40	Al	28	42	Al	28	48	Al	28	58
<b>42</b>	<b>Al</b>	<b>29</b>	<b>38</b>	<b>Al</b>	<b>29</b>	<b>44</b>	<b>Al</b>	<b>29</b>	<b>56</b>
45	Al	29	44	Al	29	52	Al	29	62
50	Al	29	52	Al	29	60	Al	30	66
55	Al	29	64	Al	30	66	Al	32	64
60	Al	29	76	Al	30	80	Al	32	78
65	Al	30	82	Al	31	86	Al	35	68
70	Al	30	98	Al	32	90	Al	37	68
75	Al	31	98	Al	32	106	Al	37	78
80	Al	31	112	Al	35	86	Al	39	76
85	Al	32	114	Al	35	98	Al	39	86
90	Al	32	130	Al	37	92	Al	39	98

Dose Value of **145mrad (1.45mGy)** for a 4.2cm Normal Breast

*Appendix B: Modified Settings for DBT Images*

mm	Fatty		Normal		Dense	
	kV	mAs	kV	mAs	kV	mAs
50	30	52	31	48	32	47
55	30	62	31	58	32	55
60	30	62	32	60	33	57
65	32	63	33	60	33	65
70	32	72	33	68	34	65
75	33	71	34	68	35	67
80	34	69	35	71	36	70
85	34	77	36	72	37	69
90	35	79	36	80	37	78

## *Appendix C: Patient Imaging Checklist*

### Before the exam:

- Calibrate the system with the sliced phantom
- Make sure there is \$50 in the envelope with the patient's name
- Place the shroud
- Make sure there is an appropriate gown in the room

### With the patient:

- Bring the patient in from the waiting area
- Consent the patient and explain the procedure
- Give the patient the gown and wait outside as she changes

### Running the test:

- Help the technician to position the patient
- Read the paddle height
- Enter the data into the computer – start the threshold at 3
- Tell the patient that the lights will be turned off
- Run the test

### Transition to TOMO:

- Remove the shroud and the detector panel
- Stand behind the protective glass

### Increasing the Compression:

- Slide the detector panel and the shroud back in
- Help the technician to increase the compression
- Check the paddle height
- Change the information on the computer and rerun the test

### Transition to TOMO:

- Remove the shroud and the detector panel
- Stand behind the protective glass

Transition period:

- Ask the patient for age, height, weight and bra cup size
- Position the detector panel and the shroud

Repeat procedure for either the other breast or for MLO.

## *Appendix D: Detailed Steps for Patient Imaging*

### Imaging a Normal Patient:

1. Calibrate with the sliced phantom:
  - a. Create the folder with the current date
  - b. The settings should be on the “homed” attenuator settings
  - c. Make sure the black cloth is on the plastic top
  - d. Make sure to bring the plastic plate to the top of the phantom
  - e. Run the phantom under the large, medium and small settings – making sure to change the name each time
2. Prepare for the patient
  - a. Make sure the envelope has the money, letter and the patient’s name
  - b. Make sure there is a gown in the room
  - c. Place the (cleaned) shroud on the panel – usually start with the medium size
  - d. Change the threshold to 3
  - e. Change the file name to CC
3. Consent the patient
4. Give the patient the gown, say that it should be open in the front
5. Help Joyce to position the patient, making sure that the shroud is as close to the body as possible so that it covers most of the exposed panel
6. Read the paddle height
7. Make sure that the correct size – small, medium or large is selected
8. Turn off the lights and run the test
9. Turn the lights back on and help Joyce with increasing the compression
10. Record the new paddle height and change the threshold to the past highest threshold
11. Run the test
12. Remove the detector panel and the shroud
13. Step back behind the shield as the X-ray is being taken
14. Intermission – ask about the:
  - a. Age
  - b. Height
  - c. Weight
  - d. Bra cup size
  - e. Whether still has periods
15. Put the detector panel back on and the shroud – help Joyce as she rotates
16. Change the file name to MLO
17. Equalize again
  - a. For MLO, always use size medium or larger!
18. Run the test

19. Help with the increased compression
20. Patient is done! Let her change and then give the envelope.

Imaging a biopsy patient:

1. Calibrate with the sliced phantom:
  - a. Create the folder with the current date
  - b. The settings should be on the “homed” attenuator settings
  - c. Make sure the black cloth is on the plastic top
  - d. Make sure to bring the plastic plate to the top of the phantom
  - e. Run the phantom under the large, medium and small settings – making sure to change the name each time
2. Prepare for the patient
  - a. Make sure the envelope has the money, letter and the patient’s name
  - b. Make sure there is a gown in the room
  - c. Place the (cleaned) shroud on the panel – usually start with the medium size
  - d. Change the threshold to 3
  - e. Change the file name to (right/left)CC
3. Consent the patient
4. Give the patient the gown, say that it should be open in the front
5. Help Joyce to position the patient, making sure that the shroud is as close to the body as possible so that it covers most of the exposed panel
6. Read the paddle height
7. Make sure that the correct size – small, medium or large is selected
8. Turn off the lights and run the test
9. Take out the shroud and the detector panel – Joyce will take the X-ray.
10. Put the detector panel and shroud back on.
11. Increase the compression.
12. Record the new paddle height and change the threshold to the past highest threshold
13. Run the test
14. Remove the detector panel and the shroud – Joyce will take the X-ray.
15. Intermission – ask about the:
  - a. Age
  - b. Height
  - c. Weight
  - d. Bra cup size
  - e. Whether still has periods
16. Do the same thing on the other side, but be sure to change the file name to (left/right) cc!
17. Patient is done! Let her change and then give the envelope.

### Collection of Data for Analysis:

1. Copy the NIRST files from that day onto a hard drive and then put that on Jumbo in a folder that has the Patient Number → NIRST → Left vs. Right → CC vs. MLO → Compressed vs. Uncompressed
2. Open the data on the other computer and reconstruct the images:
  - a. Open MView on both the left and right monitors.
  - b. Search for the files under the aws drive. (You should have the numbers that Joyce will give you that correspond to the patient from that day).
  - c. Once the images have finished loading, click on Tomo → Reconstruct. This takes a while to load.
  - d. When the reconstruction is finished, go to File → Save all w/o gain map. Click on Desktop → shortcut to patient scans. Create a folder with the patient number. Inside that patient folder, make another folder for CC and another folder for MLO. Save the images in the appropriate folder.
3. Put that data on a hard drive, and then put that on Jumbo in a folder Patient Number → DICOMS → Left vs. Right → CC vs. MLO

\*Note – the organization of the folders to save the files may be different depending on whether the patient is a biopsy patient or a normal patient. Look at patient 10 for an example of how to organize a normal patient, and patient 201 for how to organize a biopsy patient.

### Data Analysis:

#### **Running the Program**

1. Make sure the files are organized correctly on Jumbo!
2. Login in to isotope.
3. ssh into the Jumbo server.
4. In matlab, open up the “new\_raw2nirfast\_jumbo” file
5. Change the patient number and the file name
  - a. The file name should say “left/right” and “compressed/uncompressed” depending on which one you want.
6. It is usually useful to run the code by section so that if there is an error, you don't have to rerun the whole code
7. Once the first section is done running, run the second section. An image of the breast will come up
  - a. Look for areas of the breast that appear to completely thin out along the top and bottom. (This will basically appear as a thin line of red pixels toward the top and bottom).

- b. Use the “clicker” tool at the top to zoom in and note where the line starts forming from the breast
8. Press the right arrow on your keyboard (as if you were scrolling) and it will ask you if you want to delete pixels, above or below a certain value. Enter in the pixel values that you noted above. This will black out the thin lines.
9. Take a screen shot of the image at slice 0.
10. Scroll through the images with the right arrow on your keyboard. It will run through all the images once as you click through, and then once on its own much faster.
11. Run the next section of code. Possible issues that may come up:
  - a. If the breast is really small, sometimes it is necessary to change the edges value. Scroll through the code and find where it asks for inner edges. It usually says 50, but for a smaller breast, change it to a smaller number. (I usually decrease to 40, then 30 depending on whether it works or not).
12. While this part of the code is running, 6 figures will be produced. Take a screen shot of each of these figures.
13. Put the figures in a PowerPoint with the screen shot of slice 0. Make sure to note which side of the breast, whether it is CC or MLO and whether it is compressed or uncompressed. Also note whether the edges were changed.
14. Check to see if the graphs look good! You want to see good linear fits. Especially for smaller breasts, sometimes the program gets rid of too much data (the data that is kept is in blue; the data that is not kept is in red). In that case, go back and make sure the edges value is small enough.
15. Run the last section of the code: this should delete the files from the side in MatLab (you want these to be cleared so that the next patient doesn't use the images from the previous patient). Check to make sure it is saved properly – there should be a folder on Jumbo under the patient name → NIRST → Processed.

### **Reconstruction:**

1. resave the “testcalcallproperties” code as a new script with the name “testcalcallproperties\_pt#” for each patient that you want to reconstruct. You can run up to 5 at a time.
2. Open a non interactiv terminal
3. Type “screen”
4. Type “matlab<testcalcallproperties\_pt#.m> date\_pt#.log
5. Press Cntl + a + d
6. Logout
7. Repeat for each of the new scripts that you made. (Each new script should correspond to a different patient).
8. Once you logout, you can leave the computer. It will run overnight.
9. The next day, check to see if the reconstructions worked. On jumbo, open the patient number → NIRST → reconstructions.

10. Open up the text files. The one with more numbers is the wavelength-by-wavelength data for standard reconstructions, each column is a region, typically fat, then fibroglandular, then tumor. The final column is the values used for calibration.
11. In the spectral text file the data displays:
  - a. The first row shows fat (or whatever is labeled region 1)
  - b. The second row shows fibroglandular (or whatever is labeled region 2)
  - c. The third row will show the tumor if there is one
  - d. The first column is oxygenated hemoglobin, then deoxygenated hemoglobin, then water and lipid percentages.
  - e. Check to make sure that the percentages are all less than 1 and that there are no zero or negative values in any of the data points.
  - f. Check this data against the figures in the powerpoint that were previously created to see if they make sense. Keep in mind that hemoglobin usually absorbs at a lower wavelengths than fat and water.

## Citations

1. Cancer Facts & Figures 2013. at <http://www.cancer.org/research/cancerfactsfigures/cancerfactsfigures/cancer-facts-figures-2013>>
2. SEER Cancer Statistics Review, 1975-2009 - Previous Version - SEER Cancer Statistics Review. at [http://seer.cancer.gov/csr/1975\\_2009\\_pops09/](http://seer.cancer.gov/csr/1975_2009_pops09/)>
3. Siegel, R., Naishadham, D. & Jemal, A. Cancer statistics, 2013. *CA. Cancer J. Clin.* 63, 11–30 (2013).
4. Shapiro, S., Strax, P. & Venet, L. Periodic breast cancer screening in reducing mortality from breast cancer. *JAMA* 215, 1777–85 (1971).
5. Tabar, L. *et al.* Efficacy of breast cancer screening by age. New results from the Swedish Two-County Trial. *Cancer* 75, 2507–17 (1995).
6. Thurfjell, E. L. & Lindgren, J. A. Breast cancer survival rates with mammographic screening: similar favorable survival rates for women younger and those older than 50 years. *Radiology* 201, 421–6 (1996).
7. Duffy, S. W. *et al.* Reduction in breast cancer mortality from organized service screening with mammography: 1. Further confirmation with extended data. *Cancer Epidemiol. Biomarkers Prev.* 15, 45–51 (2006).
8. Carney, P. A. *et al.* Individual and combined effects of age, breast density, and hormone replacement therapy use on the accuracy of screening mammography. *Ann Intern Med* 138, 168–75 (2003).
9. Poplack, S. P., Tosteson, A. N., Grove, M. R., Wells, W. A. & Carney, P. A. Mammography in 53,803 women from the New Hampshire mammography network. *Radiology* 217, 832–40 (2000).
10. Elmore, J. G. *et al.* Ten-year risk of false positive screening mammograms and clinical breast examinations. *N Engl J Med* 338, 1089–96 (1998).
11. Burgess, A. E., Jacobson, F. L. & Judy, P. F. Human observer detection experiments with mammograms and power-law noise. *Med Phys* 28, 419–37 (2001).
12. Rosenberg, R. D. *et al.* Effects of age, breast density, ethnicity, and estrogen replacement therapy on screening mammographic sensitivity and cancer stage at diagnosis: review of 183,134 screening mammograms in Albuquerque, New Mexico. *Radiology* 209, 511–8 (1998).

13. Andersson, I. *et al.* Breast tomosynthesis and digital mammography: a comparison of breast cancer visibility and BIRADS classification in a population of cancers with subtle mammographic findings. *Eur. Radiol.* 18, 2817–2825 (2008).
14. Chiu, S. Y. *et al.* Effect of baseline breast density on breast cancer incidence, stage, mortality, and screening parameters: 25-year follow-up of a Swedish mammographic screening. *Cancer Epidemiol Biomark. Prev* 19, 1219–28 (2010).
15. Kopans, D. B. Beyond randomized controlled trials: organized mammographic screening substantially reduces breast carcinoma mortality. *Cancer* 94, 580–1; author reply 581–3 (2002).
16. Lewin, J. M. *et al.* Clinical comparison of full-field digital mammography and screen-film mammography for detection of breast cancer. *AJR Am J Roentgenol* 179, 671–7 (2002).
17. Lewin, J. M. *et al.* Comparison of full-field digital mammography with screen-film mammography for cancer detection: results of 4,945 paired examinations. *Radiology* 218, 873–80 (2001).
18. Pisano, E. D. *et al.* Diagnostic performance of digital versus film mammography for breast-cancer screening. *N Engl J Med* 353, 1773–83 (2005).
19. Olivotto, I. A., Kan, L. & Coldman, A. J. False positive rate of screening mammography. *N Engl J Med* 339, 560; author reply 563 (1998).
20. Gur, D. *et al.* Trends in recall, biopsy, and positive biopsy rates for screening mammography in an academic practice. *Radiology* 235, 396–401 (2005).
21. Hubbard, R. A. *et al.* Cumulative Probability of False-Positive Recall or Biopsy Recommendation After 10 Years of Screening Mammography: A Cohort Study. *Ann. Intern. Med.* 155, 481–492 (2011).
22. Ciatto, S. *et al.* Integration of 3D digital mammography with tomosynthesis for population breast-cancer screening (STORM): a prospective comparison study. *Lancet Oncol.* 14, 583–589 (2013).
23. Rafferty, E. A. *et al.* Assessing Radiologist Performance Using Combined Digital Mammography and Breast Tomosynthesis Compared with Digital Mammography Alone: Results of a Multicenter, Multireader Trial. *Radiology* 266, 104–113 (2013).
24. Zuley, M. L. *et al.* Digital Breast Tomosynthesis versus Supplemental Diagnostic Mammographic Views for Evaluation of Noncalcified Breast Lesions. *Radiology* 266, 89–95 (2013).

25. Michell, M. J. *et al.* A comparison of the accuracy of film-screen mammography, full-field digital mammography, and digital breast tomosynthesis. *Clin. Radiol.* 67, 976–981 (2012).
26. Skaane, P. *et al.* Comparison of digital mammography alone and digital mammography plus tomosynthesis in a population-based screening program. *Radiology* 267, 47–56 (2013).
27. Park, J. M., Franken, E. A., Garg, M., Fajardo, L. L. & Niklason, L. T. Breast tomosynthesis: present considerations and future applications. *Radiographics* 27 Suppl 1, S231–40 (2007).
28. Feng, S. S. J. & Sechopoulos, I. Clinical digital breast tomosynthesis system: dosimetric characterization. *Radiology* 263, 35–42 (2012).
29. Robinson, M. & Kotre, C. J. Trends in compressed breast thickness and radiation dose in breast screening mammography. *Br J Radiol* 81, 214–8 (2008).
30. Corlu, A. *et al.* Diffuse optical tomography with spectral constraints and wavelength optimization. *Appl Opt* 44, 2082–93 (2005).
31. Srinivasan, S. *et al.* Near-infrared characterization of breast tumors in vivo using spectrally-constrained reconstruction. *Technol Cancer Res Treat* 4, 513–26 (2005).
32. Srinivasan, S., Pogue, B. W., Jiang, S., Dehghani, H. & Paulsen, K. D. Spectrally constrained chromophore and scattering near-infrared tomography provides quantitative and robust reconstruction. *Appl Opt* 44, 1858–69 (2005).
33. Chance, B. *et al.* Breast cancer detection based on incremental biochemical and physiological properties of breast cancers: a six-year, two-site study. *Acad Radiol* 12, 925–33 (2005).
34. Grosenick, D. *et al.* A multichannel time-domain scanning fluorescence mammograph: performance assessment and first in vivo results. *Rev Sci Instrum* 82, 024302 (2011).
35. Shah, N. *et al.* Noninvasive functional optical spectroscopy of human breast tissue. *Proc. Natl. Acad. Sci. U. S. A.* 98, 4420–4425 (2001).
36. Spinelli, L. *et al.* Characterization of female breast lesions from multi-wavelength time-resolved optical mammography. *Phys Med Biol* 50, 2489–502 (2005).
37. Intes, X. Time-domain optical mammography SoftScan: initial results. *Acad Radiol* 12, 934–47 (2005).
38. Poellinger, A. *et al.* Near-infrared laser computed tomography of the breast first clinical experience. *Acad Radiol* 15, 1545–53 (2008).

39. Culver, J. P. *et al.* Three-dimensional diffuse optical tomography in the parallel plane transmission geometry: evaluation of a hybrid frequency domain/continuous wave clinical system for breast imaging. *Med Phys* 30, 235–47 (2003).
40. Fang, Q. *et al.* Combined optical and X-ray tomosynthesis breast imaging. *Radiology* 258, 89–97 (2011).
41. Zhu, Q. *et al.* Benign versus malignant breast masses: optical differentiation with US-guided optical imaging reconstruction. *Radiology* 237, 57–66 (2005).
42. Brooksby, B. *et al.* Combining near-infrared tomography and magnetic resonance imaging to study in vivo breast tissue: implementation of a Laplacian-type regularization to incorporate magnetic resonance structure. *J Biomed Opt* 10, 051504 (2005).
43. Ntziachristos, V., Yodh, A. G., Schnall, M. D. & Chance, B. MRI-guided diffuse optical spectroscopy of malignant and benign breast lesions. *Neoplasia* 4, 347–54 (2002).
44. Connolly, D. T. *et al.* Tumor vascular permeability factor stimulates endothelial cell growth and angiogenesis. *J. Clin. Invest.* 84, 1470–1478 (1989).
45. Dvorak, H. F., Brown, L. F., Detmar, M. & Dvorak, A. M. Vascular permeability factor/vascular endothelial growth factor, microvascular hyperpermeability, and angiogenesis. *Am. J. Pathol.* 146, 1029–1039 (1995).
46. Guidi, A. J. *et al.* Vascular permeability factor (Vascular endothelial growth factor) expression and angiogenesis in patients with ductal carcinoma in situ of the breast. *Cancer* 80, 1945–1953 (1997).
47. Chia, S. *et al.* Human Epidermal Growth Factor Receptor 2 Overexpression As a Prognostic Factor in a Large Tissue Microarray Series of Node-Negative Breast Cancers. *J. Clin. Oncol.* 26, 5697–5704 (2008).
48. Weidner, N., Semple, J. P., Welch, W. R. & Folkman, J. Tumor angiogenesis and metastasis--correlation in invasive breast carcinoma. *N. Engl. J. Med.* 324, 1–8 (1991).
49. Cerussi, A. *et al.* In vivo absorption, scattering, and physiologic properties of 58 malignant breast tumors determined by broadband diffuse optical spectroscopy. *J Biomed Opt* 11, 044005 (2006).
50. Grosenick, D. *et al.* Time-domain scanning optical mammography: II. Optical properties and tissue parameters of 87 carcinomas. *Phys Med Biol* 50, 2451–68 (2005).

51. Poplack, S. P. *et al.* Electromagnetic breast imaging: results of a pilot study in women with abnormal mammograms. *Radiology* 243, 350–9 (2007).
52. Wells, W. A., Wang, X., Daghlian, C. P., Paulsen, K. D. & Pogue, B. W. Phase contrast microscopy analysis of breast tissue: differences in benign vs. malignant epithelium and stroma. *Anal Quant Cytol Histol* 31, 197–207 (2009).
53. Bartek, M., Wang, X., Wells, W., Paulsen, K. D. & Pogue, B. W. Estimation of subcellular particle size histograms with electron microscopy for prediction of optical scattering in breast tissue. *J Biomed Opt* 11, 064007 (2006).
54. Cerussi, A. E. *et al.* Sources of absorption and scattering contrast for near-infrared optical mammography. *Acad Radiol* 8, 211–8 (2001).
55. Kukreti, S. *et al.* Characterization of metabolic differences between benign and malignant tumors: high-spectral-resolution diffuse optical spectroscopy. *Radiology* 254, 277–84 (2010).
56. Zhu, Q. *et al.* Breast cancer: assessing response to neoadjuvant chemotherapy by using US-guided near-infrared tomography. *Radiology* 266, 433–442 (2013).
57. Pogue, B. W. *et al.* Image analysis methods for diffuse optical tomography. *J Biomed Opt* 11, 33001 (2006).
58. Brooksby, B. *et al.* Spectral priors improve near-infrared diffuse tomography more than spatial priors. *Opt Lett* 30, 1968–70 (2005).
59. Brooksby, B. *et al.* Imaging breast adipose and fibroglandular tissue molecular signatures by using hybrid MRI-guided near-infrared spectral tomography. *Proc Natl Acad Sci U A* 103, 8828–33 (2006).
60. Carpenter, C. M. *et al.* Image-guided optical spectroscopy provides molecular-specific information in vivo: MRI-guided spectroscopy of breast cancer hemoglobin, water, and scatterer size. *Opt Lett* 32, 933–5 (2007).
61. Jacques, S. L. & Pogue, B. W. Tutorial on diffuse light transport. *J Biomed Opt* 13, 041302 (2008).
62. Pogue, B. W., Leblond, F., Krishnaswamy, V. & Paulsen, K. D. Radiologic and near-infrared/optical spectroscopic imaging: where is the synergy? *AJR Am. J. Roentgenol.* 195, 321–332 (2010).
63. Bevilacqua, F., Berger, A. J., Cerussi, A. E., Jakubowski, D. & Tromberg, B. J. Broadband absorption spectroscopy in turbid media by combined frequency-domain and steady-state methods. *Appl. Opt.* 39, 6498–6507 (2000).

64. No, K. S., Kwong, R., Chou, P. H. & Cerussi, A. Design and testing of a miniature broadband frequency domain photon migration instrument. *J Biomed Opt* 13, 050509 (2008).
65. Delpy, D. T. & Cope, M. Quantification in tissue near-infrared spectroscopy. *Philos. Trans. R. Soc. Lond. Ser. B-Biol. Sci.* 352, 649–659 (1997).
66. Intes, X. *et al.* In vivo continuous-wave optical breast imaging enhanced with Indocyanine Green. *Med. Phys.* 30, 1039–1047 (2003).
67. Choe, R. *et al.* Differentiation of Benign and Malignant Breast Tumors by In-Vivo Three-Dimensional Parallel-Plate Diffuse Optical Tomography. *J. Biomed. Opt.* 14, 024020 (2009).
68. Krishnaswamy, V. *et al.* A digital X-ray tomosynthesis coupled near infrared spectral tomography system for dual-modality breast imaging. *Opt. Express* 20, 19125–19136 (2012).
69. Taroni, P. *et al.* Optical identification of subjects at high risk for developing breast cancer. *J. Biomed. Opt.* 18, 060507 (2013).
70. Enfield, L. C. *et al.* Three-dimensional time-resolved optical mammography of the uncompressed breast. *Appl Opt* 46, 3628–38 (2007).
71. Taroni, P. *et al.* Seven-wavelength time-resolved optical mammography extending beyond 1000 nm for breast collagen quantification. *Opt. Express* 17, 15932–15946 (2009).
72. Yates, T. *et al.* Optical tomography of the breast using a multi-channel time-resolved imager. *Phys. Med. Biol.* 50, 2503–2517 (2005).
73. Nissilä, I. *et al.* Comparison between a time-domain and a frequency-domain system for optical tomography. *J. Biomed. Opt.* 11, 064015 (2006).
74. Nissilä, I. *et al.* Instrumentation and calibration methods for the multichannel measurement of phase and amplitude in optical tomography. *Rev. Sci. Instrum.* 76, 044302 (2005).
75. Zhu, Q. *et al.* Noninvasive monitoring of breast cancer during neoadjuvant chemotherapy using optical tomography with ultrasound localization. *Neoplasia N. Y.* N 10, 1028–1040 (2008).
76. Zhu, Q. *et al.* Early-stage invasive breast cancers: potential role of optical tomography with US localization in assisting diagnosis. *Radiology* 256, 367–378 (2010).

77. Srinivasan, S. *et al.* Interpreting hemoglobin and water concentration, oxygen saturation, and scattering measured in vivo by near-infrared breast tomography. *Proc Natl Acad Sci U A* 100, 12349–54 (2003).
78. Jiang, S. *et al.* Evaluation of Breast Tumor Response to Neoadjuvant Chemotherapy with Tomographic Diffuse Optical Spectroscopy: Case Studies of Tumor Region-of-Interest Changes. *Radiology* 252, 551–560 (2009).
79. Poplack, S. P., Tosteson, T. D., Kogel, C. A. & Nagy, H. M. Digital breast tomosynthesis: initial experience in 98 women with abnormal digital screening mammography. *AJR Am J Roentgenol* 189, 616–23 (2007).
80. Carpenter, C. M. *et al.* Image-guided optical spectroscopy provides molecular-specific information in vivo: MRI-guided spectroscopy of breast cancer hemoglobin, water, and scatterer size. *Opt Lett* 32, 933–5 (2007).
81. Cerussi, A. *et al.* In vivo absorption, scattering, and physiologic properties of 58 malignant breast tumors determined by broadband diffuse optical spectroscopy. *J Biomed Opt* 11, 044005 (2006).
82. Brooksby, B. *et al.* Imaging breast adipose and fibroglandular tissue molecular signatures by using hybrid MRI-guided near-infrared spectral tomography. *Proc Natl Acad Sci U A* 103, 8828–33 (2006).
83. Cerussi, A. E. *et al.* Spectroscopy enhances the information content of optical mammography. *J. Biomed. Opt.* 7, 60–71 (2002).
84. Michaelsen, K., Krishnaswamy, V., Pogue, B. W., Poplack, S. P. & Paulsen, K. D. Near-infrared spectral tomography integrated with digital breast tomosynthesis: Effects of tissue scattering on optical data acquisition design. *Med Phys* 39, 4579–87 (2012).
85. Dehghani, H. *et al.* Near infrared optical tomography using NIRFAST: Algorithm for numerical model and image reconstruction. *Commun Numer Methods Eng* 25, 711–732 (2008).
86. Moon, J. A., Mahon, R., Duncan, M. D. & Reintjes, J. Resolution Limits for Imaging through Turbid Media with Diffuse Light. *Opt. Lett.* 18, 1591–1593 (1993).
87. Fang, Q. *et al.* Combined optical imaging and mammography of the healthy breast: optical contrast derived from breast structure and compression. *IEEE Trans Med Imaging* 28, 30–42 (2009).
88. Carp, S. A. *et al.* Dynamic functional and mechanical response of breast tissue to compression. *Opt Express* 16, 16064–78 (2008).

89. Carp, S. A. *et al.* Compression-induced changes in the physiological state of the breast as observed through frequency domain photon migration measurements. *J Biomed Opt* 11, 064016 (2006).
90. Bouchard, J. P. *et al.* Reference optical phantoms for diffuse optical spectroscopy. Part 1--Error analysis of a time resolved transmittance characterization method. *Opt Express* 18, 11495–507 (2010).
91. Michaelsen, K. *et al.* Characterization of materials for optimal near-infrared and X-ray imaging of the breast. *Biomed. Opt. Express* 3, 2078 (2012).
92. Mark, J. E. Polymer Data Handbook (2nd Edition). at [http://www.knovel.com/web/portal/browse/display?\\_EXT\\_KNOVEL\\_DISPLAY\\_bookid=2620](http://www.knovel.com/web/portal/browse/display?_EXT_KNOVEL_DISPLAY_bookid=2620)
93. Bolin, F. P., Preuss, L. E., Taylor, R. C. & Ferenec, R. J. Refractive index of some mammalian tissues using a fiber optic cladding method. *Appl. Opt.* 28, 2297–2303 (1989).
94. Kasarova, S. N., Sultanova, N. G., Ivanov, C. D. & Nikolov, I. D. Analysis of the dispersion of optical plastic materials. *Opt. Mater.* 29, 1481–1490 (2007).
95. Vogel, A. & Venugopalan, V. Mechanisms of Pulsed Laser Ablation of Biological Tissues. *Chem. Rev.* 103, 577–644 (2003).
96. Pogue, B. W. *et al.* Three-dimensional simulation of near-infrared diffusion in tissue: boundary condition and geometry analysis for finite-element image reconstruction. *Appl Opt* 40, 588–600 (2001).
97. Schweiger, M., Arridge, S. R., Hiraoka, M. & Delpy, D. T. The finite element method for the propagation of light in scattering media: Boundary and source conditions. *Med. Phys.* 22, 1779–1792 (1995).
98. Dehghani, H., Brooksby, B. A., Vishwanath, K., Pogue, B. W. & Paulsen, K. D. The effects of internal refractive index variation in near-infrared optical tomography: the finite element modeling approach. *Phys. Med. Biol.* 48, 2713–2727 (2003).
99. Dehghani, H. *et al.* Near infrared optical tomography using NIRFAST: Algorithm for numerical model and image reconstruction. *Commun. Numer. Methods Eng.* 25, 711–732 (2008).
100. Arridge, S. R. Photon-measurement density functions. Part I: Analytical forms. *Appl Opt* 34, 7395–409 (1995).
101. Patterson, M. S., Chance, B. & Wilson, B. C. Time resolved reflectance and transmittance for the non-invasive measurement of tissue optical properties. *Appl Opt* 28, 2331–6 (1989).

102. Jacques, S. L. and W. in *Opt.-Therm. Response Laser Irradiat. Tissues* (Welch, A. and can G.) (Springer, 1995).
103. Arridge, S. R. & Hebden, J. C. Optical imaging in medicine: II. Modelling and reconstruction. *Phys. Med. Biol.* 42, 841–53 (1997).
104. Lynch, D. *Numerical Partial Differential Equations for Environmental Scientists and Engineers: a first practical course.* (Springer, 2005).
105. Arridge, S. R. & Schweiger, M. Photon-measurement density functions. Part 2: Finite-element-method calculations. *Appl Opt* 34, 8026–8037 (1995).
106. Pogue, B. W. *et al.* Implicit and explicit prior information in near-infrared spectral imaging: accuracy, quantification and diagnostic value. *Philos. Trans. R. Soc. Math. Phys. Eng. Sci.* 369, 4531–4557 (2011).
107. Fang, Q. Q. *et al.* Combined Optical Imaging and Mammography of the Healthy Breast: Optical Contrast Derived From Breast Structure and Compression. *Ieee Trans. Med. Imaging* 28, 30–42 (2009).
108. Basevi, H. R. A. *et al.* Compressive sensing based reconstruction in bioluminescence tomography improves image resolution and robustness to noise. *Biomed. Opt. Express* 3, 2131–2141 (2012).
109. Yalavarthy, P. K., Pogue, B. W., Dehghani, H. & Paulsen, K. D. Weight-matrix structured regularization provides optimal generalized least-squares estimate in diffuse optical tomography. *Med. Phys.* 34, 2085–2098 (2007).
110. Jermyn, M *et al.* Integrated tool for segmentation and 3D volume mesh creation from medical images for diffuse optical tomography. *Biomed. Opt. Express* (2013).
111. Brooksby, B. *et al.* Spectral priors improve near-infrared diffuse tomography more than spatial priors. *Opt Lett* 30, 1968–70 (2005).
112. Srinivasan, S., Pogue, B. W., Jiang, S., Dehghani, H. & Paulsen, K. D. Spectrally constrained chromophore and scattering near-infrared tomography provides quantitative and robust reconstruction. *Appl Opt* 44, 1858–69 (2005).
113. Eker, C. Optical Characterization of Tissue for Medical Diagnosis. *PhD Thesis Dep. Phys. Lund Inst. Technol.* (1999).
114. Prah, S. A. & Jacques, S. L. Oregon Medical Laser Center. (2012). at <http://omlc.ogi.edu/spectra/>
115. Van Staveren, H. J., Moes, C. J. M., van Marle, J., Prah, S. A. & van Gemert, M. J. C. Light Scattering in Intralipid-10% in the wavelength range of 400-1100nm. *Appl. Opt.* 30, 4507–4514 (1991).

116. Mourant, J. R., Fuselier, T., Boyer, J., Johnson, T. M. & Bigio, I. J. Predictions and measurements of scattering and absorption over broad wavelength ranges in tissue phantoms. *Appl. Opt.* 36, 949 (1997).
117. Li, A., Zhang, Q., Culver, J., Miller, E. & Boas, D. Reconstructing chromosphere concentration images directly by continuous-wave diffuse optical tomography. *Opt. Lett.* 29, (2004).
118. Tromberg, B. J. *et al.* Assessing the future of diffuse optical imaging technologies for breast cancer management. *Med Phys* 35, 2443–51 (2008).
119. Carpenter, C., Srinivasan, S., Pogue, B. & Paulsen, K. Methodology development for three-dimensional MR-guided near infrared spectroscopy of breast tumors. *Opt. Express* 16, 17903–17914 (2008).
120. Pogue, B. W. *et al.* Implicit and explicit prior information in near-infrared spectral imaging: accuracy, quantification and diagnostic value. *Philos Trans. Math Phys Eng Sci* 369, 4531–57 (2011).
121. Yalavarthy, P. K. *et al.* Structural information within regularization matrices improves near infrared diffuse optical tomography. *Opt Express* 15, 8043–58 (2007).
122. Pogue, B. W. Image analysis methods for Diffuse Optical Tomography. *J. Biomed. Opt.* 11, (2006).
123. Garrison, J. B., Grant, D. G., Guier, W. H. & Johns, R. J. Three dimensional roentgenography. *Am. J. Roentgenol. Radium Ther. Nucl. Med.* 105, 903–908 (1969).
124. Dobbins, J. T., 3rd & Godfrey, D. J. Digital X-ray tomosynthesis: current state of the art and clinical potential. *Phys. Med. Biol.* 48, R65–106 (2003).
125. Smith, A. Fundamentals of Breast Tomosynthesis: Improving the Performance of Mammography. *Hologic Inc* (2008).
126. Dobbins, J. T., 3rd. Tomosynthesis imaging: at a translational crossroads. *Med. Phys.* 36, 1956–1967 (2009).
127. Sechopoulos, I. & Ghetti, C. Optimization of the acquisition geometry in digital tomosynthesis of the breast. *Med. Phys.* 36, 1199–1207 (2009).
128. Chawla, A. S., Samei, E., Saunders, R. S., Lo, J. Y. & Baker, J. A. A mathematical model platform for optimizing a multiprojection breast imaging system. *Med. Phys.* 35, 1337–1345 (2008).
129. Zhang, Y. *et al.* A comparative study of limited-angle cone-beam reconstruction methods for breast tomosynthesis. *Med. Phys.* 33, 3781–3795 (2006).

130. Webber, R. L., Horton, R. A., Tyndall, D. A. & Ludlow, J. B. Tuned-aperture computed tomography (TACTTM). Theory and application for three-dimensional dento-alveolar imaging. *Dentomaxillofacial Radiol.* 26, 53–62 (1997).
131. Mertelmeier, T., Orman, J., Haerer, W. & Dudam, M. K. Optimizing filtered backprojection reconstruction for a breast tomosynthesis prototype device. in 6142, 61420F–61420F–12 (2006).
132. Dobbins, J. T. & McAdams, H. P. Chest Tomosynthesis: Technical Principles and Clinical Update. *Eur. J. Radiol.* 72, 244–251 (2009).
133. Wu, T., Moore, R. H., Rafferty, E. A. & Kopans, D. B. A comparison of reconstruction algorithms for breast tomosynthesis. *Med. Phys.* 31, 2636–2647 (2004).
134. Chen, Y., Lo, J. Y. & Dobbins, J. T., 3rd. Importance of point-by-point back projection correction for isocentric motion in digital breast tomosynthesis: relevance to morphology of structures such as microcalcifications. *Med. Phys.* 34, 3885–3892 (2007).
135. Smith, S. M. & Brady, J. M. SUSAN—A New Approach to Low Level Image Processing. *Int J Comput Vis.* 23, 45–78 (1997).
136. Chen, J., Paris, S. & Durand, F. Real-time Edge-aware Image Processing with the Bilateral Grid. in *ACM SIGGRAPH 2007 Pap.* (ACM, 2007). doi:10.1145/1275808.1276506
137. Tomasi, C. & Manduchi, R. Bilateral filtering for gray and color images. in *Sixth Int. Conf. Comput. Vis. 1998* 839–846 (1998). doi:10.1109/ICCV.1998.710815
138. Vedantham, S. *et al.* Semi-automated segmentation and classification of digital breast tomosynthesis reconstructed images. *Conf Proc IEEE Eng Med Biol Soc* 2011, 6188–91 (2011).
139. Sahiner, B. *et al.* Image feature selection by a genetic algorithm: Application to classification of mass and normal breast tissue. *Med. Phys.* 23, 1671–1684 (1996).
140. Bezdek, J. C., Pal, M. R., Keller, J. & Krisnapuram, R. *Fuzzy Models and Algorithms for Pattern Recognition and Image Processing.* (Kluwer Academic Publishers, 1999).
141. Chan, H. P. *et al.* Computer-aided classification of mammographic masses and normal tissue: linear discriminant analysis in texture feature space. *Phys. Med. Biol.* 40, 857–876 (1995).

142. Chen, W., Giger, M. L. & Bick, U. A fuzzy c-means (FCM)-based approach for computerized segmentation of breast lesions in dynamic contrast-enhanced MR images. *Acad. Radiol.* 13, 63–72 (2006).
143. Linxi, S. *et al.* Volumetric Breast Density: Comparison of estimates from tomosynthesis reconstructions with mammography. *AAPM Annu. Meet. Submitt.*
144. Jermyn, M. *et al.* Fast segmentation and high-quality three-dimensional volume mesh creation from medical images for diffuse optical tomography. *J. Biomed. Opt.* 18, 086007–086007 (2013).
145. Pogue, B. W. & Patterson, M. S. Review of tissue simulating phantoms for optical spectroscopy, imaging and dosimetry. *J. Biomed. Opt.* 11, 041102–041102–16 (2006).
146. Hwang, J., Ramella-Roman, J. C. & Nordstrom, R. Introduction: Feature Issue on Phantoms for the Performance Evaluation and Validation of Optical Medical Imaging Devices. *Biomed. Opt. Express* 3, 1399–1403 (2012).
147. Thomsen, S. & Tatman, D. Physiological and Pathological Factors of Human Breast Disease That Can Influence Optical Diagnosis. *Ann. N. Y. Acad. Sci.* 838, 171–193 (1998).
148. Michels, R., Foschum, F. & Kienle, A. Optical properties of fat emulsions. *Opt. Express* 16, 5907–5925 (2008).
149. McBride, T. O. *et al.* Spectroscopic Diffuse Optical Tomography for the Quantitative Assessment of Hemoglobin Concentration and Oxygen Saturation in Breast Tissue. *Appl. Opt.* 38, 5480–5490 (1999).
150. Mastanduno, M. A., Jiang, S., DiFlorio-Alexander, R., Pogue, B. W. & Paulsen, K. D. Automatic and robust calibration of optical detector arrays for biomedical diffuse optical spectroscopy. *Biomed. Opt. Express* 3, 2339–2352 (2012).
151. Michaelsen, K., Krishnaswamy, V., Pogue, B. W., Poplack, S. P. & Paulsen, K. D. Near-infrared spectral tomography integrated with digital breast tomosynthesis: Effects of tissue scattering on optical data acquisition design. *Med Phys* 39, 4579–87 (2012).
152. Jiang, S. *et al.* Near-infrared breast tomography calibration with optoelastic tissue simulating phantoms. *J Electron. Imag* 12, 613–620 (2003).
153. Pogue, B. W., Paulsen, K. D., Abele, C. & Kaufman, H. Calibration of near-infrared frequency-domain tissue spectroscopy for absolute absorption coefficient quantitation in neonatal head-simulating phantoms. *J. Biomed. Opt.* 5, 185–93 (2000).

154. Jiang, S. D. *et al.* Near-infrared breast tomography calibration with optoelastic tissue simulating phantoms. *J. Electron. Imaging* 12, 613–620 (2003).
155. Poplack, S. P. *et al.* Electromagnetic Breast Imaging: Results of a Pilot Study in Women with Abnormal Mammograms. *Radiology* 243, 350–359 (2007).
156. Arridge, S. R. Photon-Measurement Density-Functions: I. Analytical Forms. *Appl. Opt.* 34, 7395–7409 (1995).
157. Arridge, S. R. & Schweiger, M. Photon-measurement density functions. Part 2: Finite-element-method calculations. *Appl Opt* 34, 8026–8037 (1995).
158. McBride, T. O., Pogue, B. W., Jiang, S., Osterberg, U. L. & Paulsen, K. D. Development and Calibration of a Parallel Modulated Near-Infrared Tomography System for Hemoglobin Imaging In Vivo. *Rev Sci Instr* 72, 1817–1824 (2001).
159. Dehghani, H., Pogue, B. W., Poplack, S. P. & Paulsen, K. D. Multiwavelength three-dimensional near-infrared tomography of the breast: initial simulation, phantom, and clinical results. *Appl. Opt.* 42, 135–45 (2003).
160. Mastanduno, M. A. *et al.* Absolute calibration for complex-geometry biomedical diffuse optical spectroscopy. in 8578, 85780W–85780W–10 (2013).
161. Bosch, A. M. *et al.* Preoperative estimation of the pathological breast tumour size by physical examination, mammography and ultrasound: a prospective study on 105 invasive tumours. *Eur. J. Radiol.* 48, 285–292 (2003).
162. Fasching, P. A. *et al.* Influence of mammographic density on the diagnostic accuracy of tumor size assessment and association with breast cancer tumor characteristics. *Eur. J. Radiol.* 60, 398–404 (2006).
163. Gruber, I. V. *et al.* Measurement of tumour size with mammography, sonography and magnetic resonance imaging as compared to histological tumour size in primary breast cancer. *BMC Cancer* 13, 328 (2013).
164. Huang, Y.-H. *et al.* Diagnosis of solid breast tumors using vessel analysis in three-dimensional power Doppler ultrasound images. *J. Digit. Imaging* 26, 731–739 (2013).
165. Michels, R., Foschum, F. & Kienle, A. Optical properties of fat emulsions. *Opt Express* 16, 5907–25 (2008).
166. Wang, J. *et al.* In vivo quantitative imaging of normal and cancerous breast tissue using broadband diffuse optical tomography. *Med Phys* 37, 3715–24 (2010).

167. Brooksby, B. Near-infrared tomography breast image reconstruction with a priori structural information from MRI: algorithm development for reconstructing heterogeneities. *IEEE JSTQE* 9, 199–209 (2003).
168. Wang, J. *et al.* In vivo quantitative imaging of normal and cancerous breast tissue using broadband diffuse optical tomography. *Med. Phys.* 37, 3715–3724 (2010).
169. Merritt, S. *et al.* Comparison of water and lipid content measurements using diffuse optical spectroscopy and MRI in emulsion phantoms. *Technol. Cancer Res. Treat.* 2, 563–569 (2003).
170. Nachabé, R., Hendriks, B. H. W., van der Voort, M., Desjardins, A. E. & Sterenborg, H. J. C. M. Estimation of biological chromophores using diffuse optical spectroscopy: benefit of extending the UV-VIS wavelength range to include 1000 to 1600 nm. *Biomed. Opt. Express* 1, 1432–1442 (2010).
171. Quarto, G. *et al.* Comparison of organic phantom recipes and characterization by time-resolved diffuse optical spectroscopy. in 8799, 879905–879905–6 (2013).
172. Nelson, T. R., Cervino, L. I., Boone, J. M. & Lindfors, K. K. Classification of breast computed tomography data. *Med. Phys.* 35, 1078–1086 (2008).
173. Graham, S. J., Stanchev, P. L., Lloyd-Smith, J. O. A., Bronskill, M. J. & Plewes, D. B. Changes in fibroglandular volume and water content of breast tissue during the menstrual cycle observed by MR imaging at 1.5 t. *J. Magn. Reson. Imaging* 5, 695–701 (1995).
174. Tanamai, W. *et al.* Diffuse optical spectroscopy measurements of healing in breast tissue after core biopsy: case study. *J. Biomed. Opt.* 14, 014024 (2009).
175. Cerussi, A. E. *et al.* Diffuse optical spectroscopic imaging correlates with final pathological response in breast cancer neoadjuvant chemotherapy. *Philos Trans. Math Phys Eng Sci* 369, 4512–30 (2011).
176. Cerussi, A. E. *et al.* Tissue phantoms in multicenter clinical trials for diffuse optical technologies. *Biomed. Opt. Express* 3, 966–971 (2012).
177. Kou, L., Labrie, D. & Chylek, P. Refractive indices of water and ice in the 0.65- to 2.5- $\mu\text{m}$  spectral range. *Appl. Opt.* 32, 3531–3540 (1993).
178. Eker, C. Optical characterization of tissue for medical diagnostics. (1999).
179. Zijlstra, W. G., Buursma, A. & Assendelft, O. W. van. *Visible and Near Infrared Absorption Spectra of Human and Animal Haemoglobin: Determination and Application.* (VSP, 2000).
180. Kawamura, Y. Guar Gum: Chemical and Technical Assessment. (2008).

181. Van Veen, R. L. P. *et al.* Determination of visible near-IR absorption coefficients of mammalian fat using time- and spatially resolved diffuse reflectance and transmission spectroscopy. *J. Biomed. Opt.* 10, 054004 (2005).
182. Tsai, C.-L., Chen, J.-C. & Wang, W.-J. Near-infrared Absorption Property of Biological Soft Tissue Constituents. *J. Med. Biol. Eng.* 21, 7–14 (2001).
183. Koch, D. E., Pearson, A. M., Magee, W. T., Hoefler, J. A. & Schweigert, B. S. Effect of Diet on the Fatty Acid Composition of Pork Fat. *J. Anim. Sci.* 27, 360–365 (1968).
184. Rieder, R. F. Hemoglobin stability: observations on the denaturation of normal and abnormal hemoglobins by oxidant dyes, heat, and alkali. *J. Clin. Invest.* 49, 2369–2376 (1970).
185. Ayyala, R. S., Chorlton, M., Behrman, R. H., Kornguth, P. J. & Slanetz, P. J. Digital Mammographic Artifacts on Full-Field Systems: What Are They and How Do I Fix Them? *RadioGraphics* 28, 1999–2008 (2008).
186. Carpenter, C. M., Srinivasan, S., Pogue, B. W. & Paulsen, K. D. Methodology development for three-dimensional MR-guided near infrared spectroscopy of breast tumors. *Opt Express* 16, 17903–14 (2008).
187. Jiang, S. *et al.* Evaluation of breast tumor response to neoadjuvant chemotherapy with tomographic diffuse optical spectroscopy: case studies of tumor region-of-interest changes. *Radiology* 252, 551–60 (2009).
188. Srinivasan, S. *et al.* In Vivo Hemoglobin and Water Concentrations, Oxygen Saturation, and Scattering Estimates From Near-Infrared Breast Tomography Using Spectral Reconstruction. *Acad. Radiol.* 13, 195–202 (2006).
189. Brooksby, B. *et al.* Quantifying adipose and fibroglandular breast tissue properties using MRI-guided NIR tomography. in *Optical Tomography and Spectroscopy of Tissue VIII*, (in press) (2005).
190. Tromberg, B. J. *et al.* Imaging in breast cancer: Diffuse optics in breast cancer: detecting tumors in pre-menopausal women and monitoring neoadjuvant chemotherapy. *Breast Cancer Res.* 7, 279 (2005).
191. Pogue, B. W. *et al.* Characterization of hemoglobin, water, and NIR scattering in breast tissue: analysis of intersubject variability and menstrual cycle changes. *J. Biomed. Opt.* 9, 541–552 (2004).
192. Advance Data from Vital and Health Statistics, Number 347 (October 27, 2004) - CDC\_1960\_2002.pdf. at <[http://loristalter.com/wp-content/uploads/CDC\\_1960\\_2002.pdf](http://loristalter.com/wp-content/uploads/CDC_1960_2002.pdf)>

193. Nie, K. *et al.* Age- and race-dependence of the fibroglandular breast density analyzed on 3D MRI. *Med. Phys.* 37, 2770–2776 (2010).
194. Sullivan, D. C., Beam, C. A., Goodman, S. M. & Watt, D. L. Measurement of force applied during mammography. *Radiology* 181, 355–357 (1991).
195. Helvie, M. A., Chan, H. P., Adler, D. D. & Boyd, P. G. Breast thickness in routine mammograms: effect on image quality and radiation dose. *Am. J. Roentgenol.* 163, 1371–1374 (1994).
196. Jiang, S., Pogue, B. W., Laughney, A. M., Kogel, C. A. & Paulsen, K. D. Measurement of pressure-displacement kinetics of hemoglobin in normal breast tissue with near-infrared spectral imaging. *Appl. Opt.* 48, D130–136 (2009).
197. Chiu, S. Y.-H. *et al.* Effect of baseline breast density on breast cancer incidence, stage, mortality, and screening parameters: 25-year follow-up of a Swedish mammographic screening. *Cancer Epidemiol. Biomark. Prev. Publ. Am. Assoc. Cancer Res. Cosponsored Am. Soc. Prev. Oncol.* 19, 1219–1228 (2010).
198. Boyd, N. F., Lockwood, G. A., Byng, J. W., Tritchler, D. L. & Yaffe, M. J. Mammographic densities and breast cancer risk. *Cancer Epidemiol. Biomarkers Prev.* 7, 1133–1144 (1998).
199. Lam, P. B., Vacek, P. M., Geller, B. M. & Muss, H. B. The association of increased weight, body mass index, and tissue density with the risk of breast carcinoma in Vermont. *Cancer* 89, 369–75 (2000).
200. American College of Radiology. Breast Imaging Reporting and Data System (BI-RADS) 4. (2003).
201. Dummin, L. J., Cox, M. & Plant, L. Prediction of breast tumor size by mammography and sonography—A breast screen experience. *The Breast* 16, 38–46 (2007).
202. Valković, T. *et al.* Correlation between vascular endothelial growth factor, angiogenesis, and tumor-associated macrophages in invasive ductal breast carcinoma. *Virchows Arch. Int. J. Pathol.* 440, 583–588 (2002).
203. Mastanduno, M. *et al.* Methods for Whole Breast MRI Guided Near-Infrared Spectroscopy.
204. Mastanduno, M. A. *et al.* Whole-Breast MRI-guided Optical Spectroscopy for Increased Diagnostic Specificity. *Radiol. Prep.*
205. Vacek, P. M. & Geller, B. M. A Prospective Study of Breast Cancer Risk Using Routine Mammographic Breast Density Measurements. *Cancer Epidemiol. Biomarkers Prev.* 13, 715–722 (2004).

206. Pawluczyk, O. *et al.* A volumetric method for estimation of breast density on digitized screen-film mammograms. *Med. Phys.* 30, 352–364 (2003).
207. Kaufhold, J., Thomas, J. A., Eberhard, J. W., Galbo, C. E. & Trotter, D. E. G. A calibration approach to glandular tissue composition estimation in digital mammography. *Med. Phys.* 29, 1867–1880 (2002).
208. Michaelsen, K. E., Krishnaswamy, V., Pogue, B. W., Poplack, S. P. & Paulsen, K. D. Scattering estimation from digital breast tomosynthesis guiding near infrared spectral tomographic reconstruction. 857811–857811 (2013). doi:10.1117/12.2002465
209. Shi, L., Vedantham, S., Karellas, A. & O’Connell, A. M. Technical note: Skin thickness measurements using high-resolution flat-panel cone-beam dedicated breast CT. *Med. Phys.* 40, 031913 (2013).
210. Huang, S.-Y., Boone, J. M., Yang, K., Kwan, A. L. C. & Packard, N. J. The effect of skin thickness determined using breast CT on mammographic dosimetry. *Med. Phys.* 35, 1199–1206 (2008).
211. White, D. R., Martin, R. J. & Darlison, R. Epoxy resin based tissue substitutes. *Br. J. Radiol.* 50, 814–821 (1977).
212. Vedantham, S. & Karellas, A. X-ray phase contrast imaging of the breast: Analysis of tissue simulating materials. *Med. Phys.* 40, 041906 (2013).
213. Michaelsen, K. E. *et al.* Anthropomorphic Breast Phantoms with Physiological Water, Lipid and Hemoglobin Content for Near Infrared Spectral Tomography. *J. Biomed. Opt.* (2014).